Selected Methods for Field-Controlled Reconfiguration of Soft-Matter Electrical Contacts

Submitted in partial fulfillment of the
requirements for the degree of
Doctor of Philosophy
in
Mechanical Engineering

James P. Wissman

B.S., Mechanical Engineering, University of Maryland

Carnegie Mellon University
Pittsburgh, PA

May, 2017

Acknowledgments

First and foremost, I would like to thank my advisor, Carmel Majidi, for his support and guidance over the past several years. I have greatly enjoyed working in the Soft Materials Lab and watching it mature, even to the point of changing names! It was truly a unique experience that allowed me to grow both as a researcher and as a person. Thank you also to my thesis committee members Gary Fedder, Maarten de Boer, and Gianluca Piazza for their time and counsel.

I would also like to thank the past and present members of the Soft Materials Lab for their comradery and constant collaboration. May your candy bucket remain full, and may your Tuesdays and Fridays produce many fails. Special thanks to Lauren for her support from beginning to end of my graduate career, to Bugra for spotting me both in the gym and in the lab, and to Vivek for sharing in late night discussions on beam mechanics.

Many thanks to my parents, Kim and Pat, for their encouragement. Perhaps this was many more years of education than you had anticipated when sending me off to University of Maryland back in 2008. Also thanks to my brothers Andrew, Paul, and Thomas for keeping my spirits up with silly Facebook chats and GIF exchanges.

Last, but not least, I would like to thank my funding sources for the financial support throughout my PhD career. In particular, thanks to the Office of Naval Research (Grant #N000141612301 and Grant #N000141210614; PM: Dr. Tom McKenna; Bio-Inspired Autonomous Systems).

Abstract

Just as conventional mechatronic systems rely on switches and relays, machines that are soft and elastically deformable will require compliant materials that can support field-controlled reconfiguration. In this dissertation, I present several novel approaches to shape programmability that primarily rely on condensed soft matter and are stimulated by electric or magnetic fields. I begin with electric-field-driven methods for achieving shape programmability of elastomer-based systems. These include dielectric elastomer actuators and electrostatic beams that undergo extreme stretch. Classical theories in elasticity and electrostatics are used to examine the mechanical responses and instabilities of these soft, hyperelastic systems. Such modeling techniques are also used to examine another switching mode based on the snap through behavior of a buckled ferromagnetic beam under magnetic load. I will then discuss a unique approach to shape programmability that is based on electrochemistry and exploits the coalescence and separation of anchored liquid metal drops. In this case, electrical signals under 10V are utilized to manipulate surface energies and transition between bi-stable states. Experiments and Surface Evolver simulations show that oxidation and reduction on opposing poles of the coalesced drops create an interfacial tension gradient that eventually leads to limit-point instability. Theory derived from bipolar electrochemistry and vertical electrical sounding predicts droplet motion and separation based on geometry and bath conductivity, facilitating the optimization of reconfigurable devices using this phenomenon. I conclude with the application of the bi-stable droplets to a simple toggle switch capable of changing circuit conductivity by over three orders of magnitude.

Contents

List of Tables

List of Figures

Chapter 1

Introduction

In recent years, the engineering community has taken an interest in developing soft and stretchable electronics, actuators, and sensors. Devices fabricated with compliant materials offer many benefits over those created with rigid materials like metals, silicon, and hard plastics. In particular, this technology strives to expand functionality, to increase durability, and to mimic or comply with biology - characteristics that pair particularly well with co-robotics, medical equipment, and wearable electronics. Mechanical "impedance matching" can prevent injuries during human-machine interaction, while the soft, stretchable nature prevents wearable devices from interfering with movement and can allow for life-like motions when actuated. As these devices become increasingly complex, there is need for "programmable" materials which can reconfigure and change system functionality, particularly for electrical switching and tuning.

1.1 Materials for Stretchable Electronics

A key objective in developing stretchable circuits and switches/relays is to replace rigid materials with soft alternatives (fig. 1.1). Mechanical properties of human biological tissue, such as muscle (elastic modulus ∼10 kPa), provide a reasonable

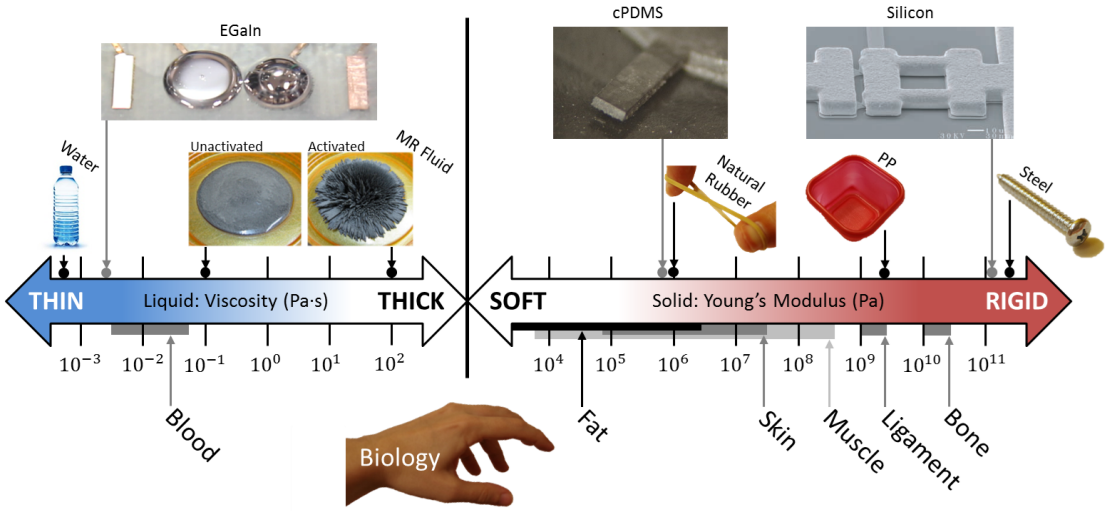

Figure 1.1: Rigidity/viscosity distribution of materials and devices. The left side represents the distribution of liquids and the right side represents the distribution of solids. Directly above the scale are engineering type materials, including water, natural rubber, polypropylene (PP), and steel. Magnetorheological fluid (MR fluid) is also included in its unactivated and activated states (Credit: [7]). Directly below the scale are biological materials, including blood, fat, skin, muscle, ligament, and bone. Value ranges were taken from literature [8–12]. It should be noted that these material constants are approximations as biology often exhibits viscoelasticity and anisotropy. Values varied widely based on factors such as testing method, strain rate, and subject age. The top right image is a conventional microelectromechanical switch (credit: Analog Devices and [13]). The top left and top center image represent alternative soft-matter switching technologies from this work.

benchmark that reflects the application areas described above. Elastic polymers (elastomers) and gels are commonly employed as structural materials for soft-matter engineering due to their hyperelasticity (often displaying strains over 100%) and low elastic moduli (< 1 MPa). Additionally, fluids may be utilized as they conform and flow, preventing significant changes in the overall mechanical properties of the host system. However, desirable qualities in mechanical compliance are often (without further material customization, as discussed below) accompanied by poor electrical conductivity. Some degree of stretchability has been achieved with traditional rigid metals and silicon by applying thin films in serpentine or "wavy" patterns on elastomeric substrates [14, 15]. Geometry limits strain on the films while the entire body can undergo tensile strains on the order of 100%. However, because the film material is not truly stretchable, there is an increased risk of failure through plastic deformation, fracture, or mechanical-mismatch-induced delamination. Instead, soft electronics can be achieved by applying conductive materials which are inherently stretchable.

1.1.1 Conductive Polymers

One method for creating stretchable circuits is to utilize conductive elastomers that consist of conductive particles loaded into a polymer matrix (fig. 1.2). In contrast to wavy electronics and similar technologies, conductive rubbers are inherently soft and can bond extremely well with surrounding elastomer. Carbon black [16], exfoliated graphite [17, 18], carbon nanotubes [19, 20], and silver micro- and nano- particles [16] are just a few examples of fillers chosen to create soft-matter electronics such as sensors and electrodes. It should be noted, however, that because a significant volume of filler must be used to achieve percolation for electrical conductivity (varying from case to case based on factors such as particle shape [20]), the particles can have an adverse effect on the physical properties of the bulk material. Specifically, the elastic

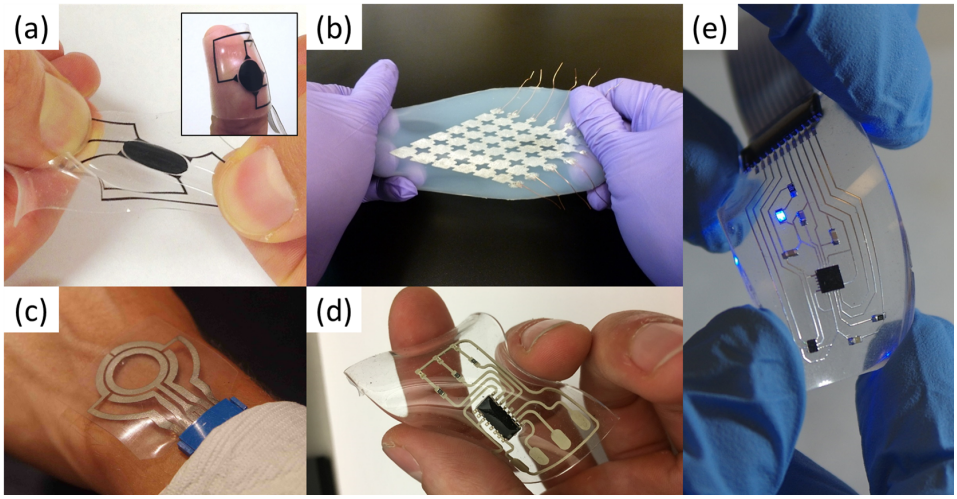

Figure 1.2: Examples of stretchable electronics. (a) Conductive polydimethylsiloxane (PDMS) composed of carbon black embedded in elastomer to create a tactile sensor [6]. (b) Eutectic gallium-indium (EGaIn) embedded in silicone to create a capacitive grid [21]. (c) EGaIn interfaced with anisotropic conductive elastomer to create a tactile sensor [26]. (d) Conventional surface mount chips interfaced with conductive silver PDMS. Credit: Alexi Charalambides (Soft Materials Laboratory). (e) Conventional surface mount chips interfaced with liquid metal traces [27].

modulus tends to increase with filler concentration, and the material often develops increased viscoelastic behavior. Furthermore, electrical conductivity is limited and will often fluctuate undesirably, sometimes failing altogether, with factors such as excessive forces and humidity [21]. Typical conductivity values include 10^4 S-m^{-1} for high concentrations of silver in polydymethylsiloxane (PDMS) [16] and 10^1 S-m^{-1} for carbon black in PDMS [16] as compared to 5.96*10^7 S-m^{-1} for copper. Blends of conductive polymers such as poly(3,4-ethylenedioxythiophene) polystyrene sulfonate (PEDOT:PSS) [22–24] or polyaniline (PANI) [25] offer high conductivity ($\sim 10^5$) and strains over 100%. PEDOT:PSS also provides high transparency, though it tends to be more rigid ($\sim$ 1 GPa) and inelastic [24]. PANI is not transparent, but maintains a modulus of $\sim$700 kPa [25].

1.1.2 Liquid Metal

Another compelling option is liquid conductors. In particular, liquid-phase metals have attracted a lot of attention in the soft robotics and sensors community. The benefit of liquid metal is high conductivity and robustness as it can flow within channels without losing connection despite large deformations, as shown in fig. 1.2. While early designs made use of mercury [28], researchers have most recently turned towards gallium alloys because of their low toxicity. Eutectic gallium-indium (EGaIn) and Galinstan, a gallium-indium-tin alloy, are common choices and are only about 20 times less conductive than copper [29]. In addition, when exposed to oxygen these gallium alloys tend to form a thin skin of gallium oxide which provide structural integrity and increase stickiness and wettability [30]. These liquid metals have already been successfully employed stretchable devices such as curvature sensors [31] and antennae [32]. With the development of these soft electronics, numerous methods for patterning and depositing liquid metal architectures have been explored. This includes injection-based techniques [31–33], microcontact printing [34], direct writing [35, 36], and liquid metal embedded elastomers (LMEE) [37–39]. I, with colleagues, have also explored liquid metal stencil lithography [21], CO_2 laser patterning [6], interfacing with anisotropic conductors [26], and selective wetting to copper traces [27].

1.2 Programmable Structures

Functionality beyond stretchable wiring and sensing can be achieved with the implementation of programmable structures. Conventionally, programmable structures may refer to modular robots [40–42] which use rigid materials. Rather than having a fixed design and purpose like traditional robots, these devices are capable of rearranging themselves to achieve new capabilities and to produce a wide variety of

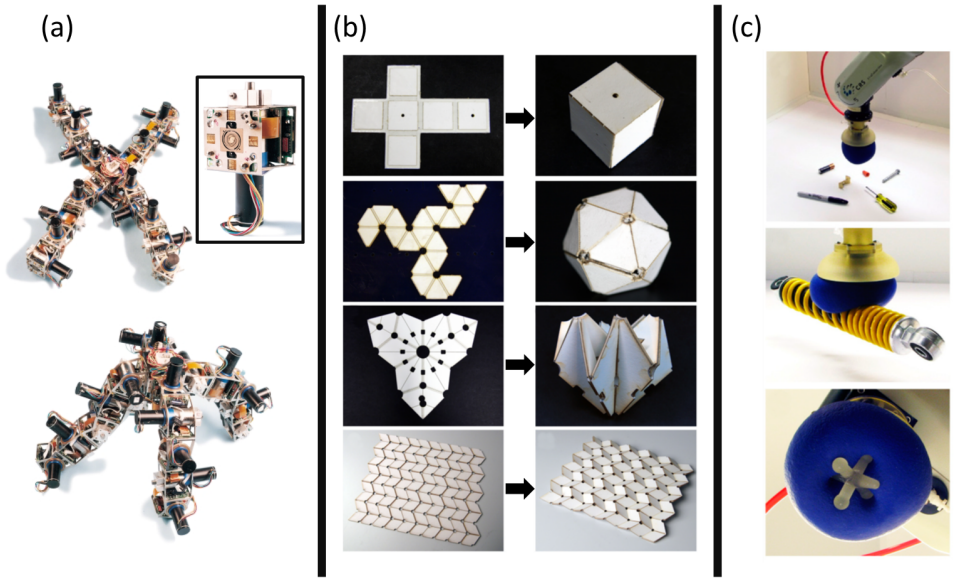

Figure 1.3: Programmable structures. (a) Modular robot. Inset: A single module. Credit: [40]. (b) Self-folding origami designs using shape-memory composite. Credit: [43]. (c) Particle jamming gripper. Credit: [45].

locomotion methods (fig. 1.3a). This has been accomplished by developing multiple relatively simple robotic modules that physically and electrically interact. Each module may contain joints, actuators, and/or sensors, contributing to shape change, such as extension [41], and locomotion, such as rolling and walking [40]. Approaching the materials level, recent developments in tunable origami structures has also contributed to increasing the programmability of rigid systems. Self folding systems (fig. 1.3b) typically use shape memory polymer [43] or shape memory alloy [44] to fold into new structures [43] or to do mechanical work [44].

1.2.1 Rigidity Tuning

Moving towards soft programmable materials, phase changes and microparticle interaction can be leveraged for tunable properties, such as rigidity, though do not necessarily involve shape change. Magnetorheological fluids, generally consisting of ferrous micro-particles suspended in a liquid such as oil, can effectively increase in

viscosity with the application of a magnetic field. This behavior is caused by the alignment of the ferrous particles as they orient themselves within the field. The major application for this technology is damping and clutching [46–48], though it has also been applied to rigidity tuning [49]. Electrorheological fluid functions similarly, though with the application of an electric field [46, 50, 51]. A more dramatic change in rigidity takes place during particle jamming [45], where "flowing" granules in an air-tight bladder become "solid" as a vacuum is introduced (fig. 1.3c). Prior to jamming, the bladder can conform to a wide variety of objects. After applying the vacuum, the bladder becomes locked in whatever shape it currently holds, allowing it to grasp enclosed objects.

1.2.2 Shape Change

Other tunable soft materials allow for shape morphing, often accompanied by changes in rigidity. Liquid crystal elastomers, for example, exhibit various strains depending on how their molecules are ordered. The application of heat or light can trigger the transition between nematic and isotropic reversibly, allowing for muscle-like behavior [52–55]. While usually presented as actuators [52–54], liquid crystal elastomers have also been applied as a transforming surface [55]. Hydrogels can exhibit similar behavior, swelling due to factors such as heat and solution concentration. As with liquid crystals, hydrogels are often marketed as actuator material, though they can be used for transitioning between material shapes [56] and continuously manipulating a surface profile [57].

1.2.3 Soft Actuators

In particular, this work focuses on programming the shape of soft condensed matter with the goal of achieving switch/relay behavior. The key difference between shape programmability and actuation is that the former performs very little work.

This allows for low energy activation and high efficiency. However, the methods to achieve shape programmability and the methods to achieve actuation for work are not mutually exclusive.

Pneumatic Actuators

When considering potential manipulation methods for soft reconfigurable devices, it is also useful to consider methods of actuation used for existing soft machines. The most popular method is pneumatic. In general, air is used to inflate pockets (PneuNets) within elastomer bodies or to simply expand a balloon-like structure (fig. 1.4). Examples include crawling robots [58], rolling robots [59], and tentacles [60]. McKibben actuators are also popular and make use of meshed inextensible cords to control actuation [61, 62]. McKibben actuators are commonly referred to as artificial muscles and have been applied to wearable orthotic devices [63]. Pneumatic actuators have the benefit of large, fast deformations, but are limited by the need for bulky hardware and/or compressed air.

Shape Memory Alloy Actuators

Shape memory alloy (SMA), such as nickel-titanium (Nitinol), is another popular material for actuation that changes shape and rigidity in response to phase transitions [64, 65]. For most SMA actuators, there is a twinned martensite phase at room temperature, and the material can then be deformed easily. Once heated, however, a highly ordered austenite phase develops, and the material returns to some pre-programmed shape. Conveniently, Joule heating can be used through the material itself to induce this transformation. Applications of SMAs have included rolling robots [66] and bio-mimetic fins [67]. Like pneumatics, SMAs can produce large deformation. While they do not require high voltages or bulky hardware, they are relatively slow and are not energy efficient nor inherently soft.

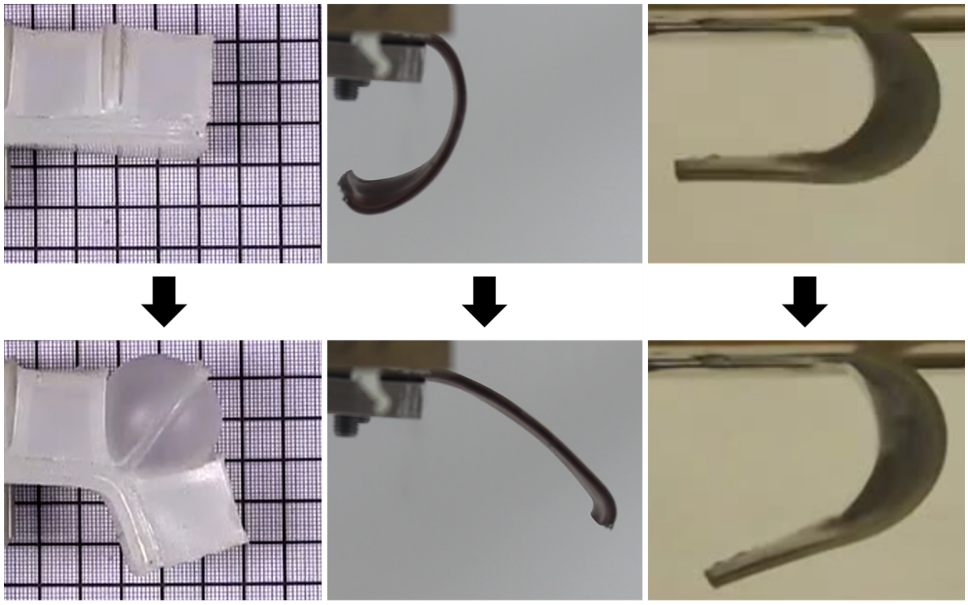

Figure 1.4: Examples of soft actuators. Left: Pneumatically actuated joint (unpublished). Center: Shape memory alloy actuator. Credit: Xiaonan Huang (Soft Materials Laboratory). Right: Curved dielectric elastomer actuator. Credit: Carmel Majidi (Soft Materials Laboratory).

Ionic Polymer-Metal Composite Actuators

Ionic polymer-metal composites (IPMCs) are created by layering a polymer electrolyte between to metallic electrodes - an anode and a cathode. When charges are applied, ions migrate to the appropriate electrode causing an asymmetric swelling within the polymer and forcing the device to bend. Subsequent diffusion of ions causes the IPMC to gradually relax [65, 68]. These actuators have been used for grippers [68], fins [68], and robotic legs [69]. It should be noted that IPMCs can also act as sensors [68]. IPMCs have the benefit of low actuation voltage and bi-directional motion by switching anode and cathode, but application is limited by low work density, low strains, poor electromechanical coupling, and the need to remain hydrated.

Dielectric Elastomer Actuators

Lastly, dielectric elastomer actuators (DEAs), consisting of a soft dielectric layer sandwiched between two compliant electrodes, are an area of interest for researchers in soft-matter-engineering. An example is shown in fig. 1.4. When a large potential is applied across the electrodes, electrostatic "Maxwell Stress" compresses the dielectric layer, causing expansion in the transverse directions [65, 70, 71]. Theory is further discussed in Chapter 2. Dielectric elastomer actuators have been used to create robots capable of walking [72], arm wrestling [73], and peristaltic motion [74]. DEAs have the benefit of high efficiency and fast actuation. Drawbacks include the requirement of a high voltage source and the possibility of dielectric breakdown or arcing.

1.2.4 Liquid Metal Electrochemistry

A more recent development has been the electrochemical manipulation of gallium-indium (fig. 1.5) in electrolytic solutions. In general, these methods fall into two categories: continuous electrowetting (CEW) and oxide-driven spreading. The former is a result of electrocapillarity, following the Young-Lippmann equation, and allows

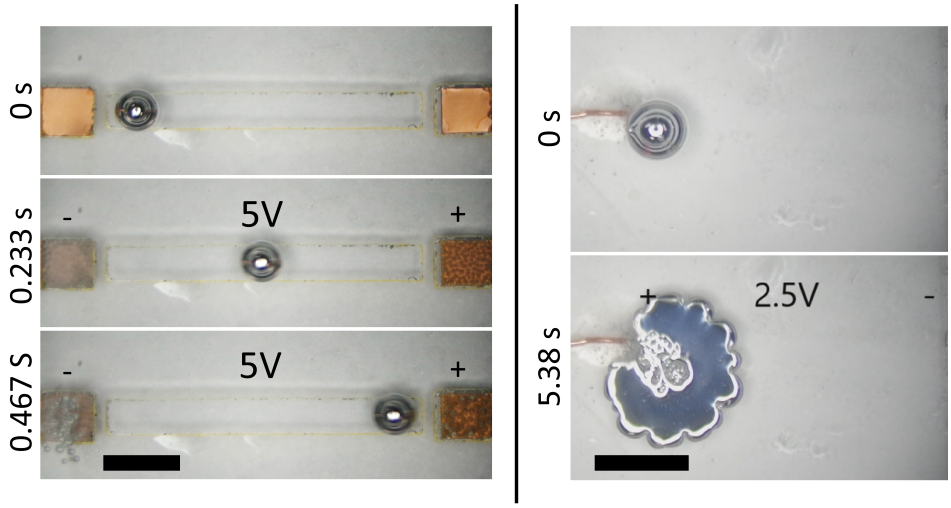

Figure 1.5: Continuous electrowetting and oxide-induced liquid metal spreading in 30% (weight per volume) NaOH. Left: Continuous electrowetting in NaOH solution. Right: Oxidation of EGaIn in 1% (weight per volume) NaOH. Black scale bars are 5 mm.

for the locomotion of liquid metal droplets [75] or the movement of surrounding fluid [76]. In contrast, the latter is a result of dramatic decreases in effective interfacial tension as oxide grows, behaving like a surfactant [77]. This has been used to direct GaIn through particular channels and exhibits fingering instabilities under certain conditions [77]. These methods are further discussed in Chapter 4.

1.3 Presented Work & Objectives

Electronics with soft and stretchable physical properties have increased in popularity with the rise of robotics, wearable technology, and bio-mimetic machines. As an alternative to wavy electronics, conductive rubbers and liquid metal alloys have been used to create truly all-soft-matter circuits. Although advances have already been published on pressure-sensing skins [78], soft, pneumatic robots [58], and artificial octopus arms [79], these devices are generally tethered to rigid hardware that handle most of the electrical and, in the case of the pneumatic robot, actuating functionality. This may be undesirable for some applications, such as a fully untethered artificial octopus, and so effort has been invested in developing elastic electronic components such as wires [80], capacitors [81], inductors [81], and diodes [82]. However, there is a lack of designs for physically reconfigurable components that maintain a soft-bodied nature. In particular, I aim to develop devices that are

- Constructed of soft, condensed matter for use in stretchable electronics.
- Capable of low-energy shape programmability for the purpose of achieving electrical switching and reconfiguration.
- Activated by low voltages (<10V) for use with standard microcontrollers and power supplies.

Thesis Overview:

Chapter 2: Given its previous success, efficiency, and excellent scaling, I begin by looking at electrostatic devices. My first contribution is the modeling of a curved actuator consisting of a prestretched DEA attached to an unstrained polydimethylsiloxane (PDMS) substrate. The DEA itself is constructed of a PDMS dielectric layer and a pair EGaIn electrodes that were applied using a simple stencil lithography fabrication technique. When actuated, the DEA relieves some of the residual strain within the body, causing it to flatten out. Given electromechanical instabilities and the chance of dielectric breakdown under high voltages, it is important to understand the behavior of these devices. I present a simple plane strain model and solve for the bending angle as a function of voltage using energy minimization and a Neo-Hookean constitutive law. When this approach fails to capture the experimentally measured response of the actuator, I introduce a specialized elastic shell theory that produces predictions in much stronger agreement with experimental data. Next, I report MEMS-inspired work for fabricating and modeling an electrostatic cantilever for all-soft-matter electronics. To begin, small angle beam approximations are used in conjunction with parallel plate theory to derive a fourth order governing equation for the cantilever shape as a function of dimensions, material properties, and applied voltage. Prototype beams are created to operate on the millimeter scale and are composed of carbon-filled conductive PDMS (cPDMS) created with carbon black. A novel fabrication method is utilized which consists of patterning layers of PDMS, cPDMS, and sacrificial poly(acrylic acid) layers with a CO_2 laser. Strong agreement is shown between experimental pull-in values and theory, supporting the use of traditional beam and electrostatic equations with stretchable materials.

Chapter 3: A fixed-fixed beam is studied next to further examine field-induced deformation of a millimeter-scale elastic element. Specifically, the behavior of the beam when simultaneously under extreme stretch and electrostatic actuation is of

interest. The beam is modeled as a Cosserat directed rod with an extensible arc length. By assuming small bending strains, an effective flexural rigidity can be defined based on the spatial cross-sectional area and the slope of the stress-strain curve. A fourth-order ordinary differential equation can then be produced which is essentially the Euler-Bernoulli beam equation with an additional correction term for axial forces. To verify the theory, centimeter scale silicone beams are stretched and placed under point load. With a 3-parameter Ogden constitutive model, the theory agrees well with the experimental values even for strains of 200%. The theory is then used to model the behavior of an electrostatic fixed-fixed beam under various stretches. The results indicate that an electrostatic fixed-fixed beam could remain functional under large stretches without extreme voltage variation. Complimenting the above work, I examine the case of pre-buckled beams under distributed load. A Raleigh-Ritz approach is applied, using two shape functions, and a simplified analytic model is derived. The theory is then applied to the case of a magnetic load and compared to experimental values with good qualitative agreement. The bi-stable behavior allows for on/off toggling of a soft-matter circuit when a critical magnetic load is reached and rapid temporary switching when sub-critical load is applied.

Chapter 4: Lastly, I examine the manipulation of liquid metals in electrolytic solutions. By introducing oxidative currents directly to the liquid metal, oxide grows on its surface, lowering the effective interfacial tension. This effect is leveraged to cause spreading and coalescence of neighboring droplets that are anchored to copper pads. Separation is then achieved by applying current across the coalesced drops. A bipolar electrochemical phenomenon results in the growth of oxide on the anodic pole and reduction on the cathodic pole, creating an interfacial tension gradient. If the gradient is substantial enough, the droplets separate to minimize the total energy of the system. This problem is examined with Surface Evolver simulations and bipolar electrochemistry theories, resulting in equations capable of predicting the onset of

droplet motion and the critical current required for droplet separation. The system is applied to create a simple bi-stable switch capable changing conductivity by 3 orders of magnitude. Further, the device can function on less than 10V.

Chapter 5: This dissertation concludes with a section discussing possible future directions. Soft lithographic techniques and new methods for patterning liquid metals may allow the miniaturization of DEA and electrostatic beam type switches to MEMS scales. Obstacles such as adhesion and contact resistance are further discussed. The manipulation of liquid metal also holds further promise. Challenges include maintaining droplet coalescence during stretching, gravitational influences, and gas formation at electrodes. However, using pH-neutral solutions, catered channel and pad geometries, miniaturization, and the use of alternating currents may overcome these and improve the overall functionality.

Chapter 2

Field-Responsive Fixed-Free Elastomer Beams

I begin by examining voltage-controlled deflection of elastomer beams that have one end fixed and the other end free. The first section presents an approach that incorporates a dielectric elastomer actuator (DEA), which has been popular within the soft robotics community. Specifically, I model the actuation of a pre-curved DEA beam that could be used to create and break electrical connections within a soft circuit. The second section presents a method inspired by the electrostatic cantilevers used in microelectromechanical systems (MEMS). Theoretical models of both examples are presented, and predictions are compared to experimental measurements. The experimentally-validated theories furnish relationships between material properties, geometry, applied voltage, and flexural response that can inform design and highlight limitations of these architectures.

2.1 Response of a Dielectric Elastomer Actuator Embedded with Liquid Gallium-Indium Electrodes [1, 2]

Dielectric elastomer actuators (DEAs) represent a promising alternative to conventional actuator technologies for powering soft bio-inspired robots, assistive wearable technologies, and other systems that depend on mechanical "impedance matching" with soft biological tissue. In contrast to electrical motors and hydraulics, DEAs can be made entirely out of soft elastic materials and fluids and remain functional under extreme bending and stretching. Moreover, they operate with very little electrical power and can exhibit as much as 90% efficiency of electrical energy input to mechanical work output [65, 70]. While there have been significant improvements since early studies in the late 1990s, progress in DEA performance and robotics implementation continues to depend on advancements in materials selection, design, and predictive theoretical modeling of the underlying elasticity and electromechanical coupling.

Here, we introduce a DEA composed of liquid-phase gallium-indium (GaIn) alloy electrodes embedded between layers of poly(dimethylsiloxane) (PDMS)[83]. In contrast to existing DEA designs, which contain inextensible (but flexible) frames [84], springs [85], or solid electrodes [86], the mechanics of the GaIn-embedded composite is governed entirely by the elasticity of the surrounding PDMS elastomer. Moreover, we observe that the cHomposite forms a saddle-shape and exhibits a relationship between longitudinal bending curvature and voltage that cannot be predicted with a classical bending beam model (see e.g. Sect. 4.2.2 of [87]). Instead, we use a kinematically parameterized shell theory and use the Rayleigh-Ritz technique for minimum potential energy to estimate the shape of the DEA at static equilibrium. We find that the theoretical predictions are in strong agreement with experimental measurements (without the aid of data fitting) so long as we allow for negative Gaussian curvature

($\mathcal{K} < 0$). In addition to furnishing an accurate prediction for the GaIn-PDMS composite, we are confident that this modeling approach can be extended to other DEA materials and designs.

DEAs are composed of a soft insulating elastomer film coated with conductive fluid or rubber electrodes. Applying a potential difference Φ to the electrodes induces an electrostatic pressure (Maxwell stress) on the embedded dielectric layer. As with a capacitor, nearly no current is drawn by the DEA, and thus very little power is expended. The dielectric is frequently created with a soft elastomer, such as acrylic-based VHB tape (3M$^{\text{TM}}$) or PDMS. DEA designs include diaphragms [88], bimorphs [70, 89], rolls [70, 90], and reinforced planar stacks [91, 92] and exhibit a variety of of motions, load capacities, and electromechanical coupling.

A central challenge in DEA development is the selection of "stretchable" electrodes that do not constrain the elastic deformation of the embedded dielectric layer [93]. Typically, the surfaces of the dielectric are coated with metallic particles [94], graphite powder [70], carbon fibers [70], carbon black [92], or carbon grease [90, 95]. Alternatively, DEAs may comprise conductive electrode materials such as electrolytic elastomers (hydrogels) [96] or electrodes made conductive by direct filling with conductive particles [89] or through low-energy ion implantation [88]. Fabrication methods include include spraying, stamping, printing, laser-cutting and spin-coating, or creating thin-film metal trace electrodes of copper, silver or gold using electroplating, sputtering, evaporation and patterning with photolithography [93]. While carbon based electrodes are relatively cheap and easy to fabricate, they have inherently high electrical resistivity and are often grainy and inconsistent at thinner layer thicknesses. In contrast, thin film metallic electrodes are highly conductive and easily patterned, but add to the stiffness of the DEA and require clever fabrication to undergo stretching (eg. pre-buckling and wavy electronics[97]).

Liquid-phase GaIn alloys represent a promising alternative to existing carbon

based and solid electrode materials [98, 99]. Like carbon grease, it does not interfere with the mechanics of the surrounding elastomer and remains conductive during stretching. However, it exhibits 3-6 orders of magnitude lower electrical resistance, with a conductivity only $1/20^{\text{th}}$ that of conventional copper wiring. Liquid GaIn has already been used for soft and stretchable wiring [80], sensors [100], and electronics [101]. Microfluidic channels of liquid alloy are typically produced with replica molding and needle injection using techniques adapted from "soft" lithography and microfluidics [29]. However, DEAs require a thin film coating of liquid alloy that cannot be produced using needle injection. Instead, they must be produced with techniques like laser machining[6], masked deposition[102], or stencil lithography[21, 103].

The dielectric in a DEA is typically modeled as an incompressible elastic solid subject to a Maxwell stress $\sigma_M = \epsilon_r \epsilon_0 \mathbf{E}^2$, where ϵ_0 is the permittivity of free space, ϵ_r is a dielectric constant, and $\mathbf{E}$ is the electric field strength [70, 104–106]. Recently, researchers have examined dynamics [107], resonance [108, 109], and failure of thin film dielectrics [110, 111] and the effect of viscoelasticity on electric instabilities and fracture [112]. In most cases, the elastomer in a DEA undergoes elastic strains and bending curvatures that are beyond the scope of linearized theories for elastic plates and shells. Instead, we must use a non-classical shell theory that treats the elastomer as an incompressible hyperelastic solid. For moderate stretch, we can model the PDMS layers with a NeoHookean constitutive law that only requires a single coefficient of elasticity [113]. For larger strains, we must use a Mooney-Rivlin[114, 115], Ogden[116], or any other model that allows for nonlinear elasticity with two or more coefficients.

2.1.1 Experimental Methods

Stencil Lithography [21]

Many methods exist for embedding liquid metal within elastic polymers. Channels can be created by using soft lithography techniques [32, 33] or by casting elastomers within 3D printed molds [31]. The liquid alloy can then be injection-filled, though care must be taken to allow paths for air to escape. Recently, gallium-indium (GaIn) circuits [117] and 3D structures have been produced by depositing individual liquid droplets with microcontact printing [34], direct writing [35, 36], and micro-transfer [118].

Here, we present a fabrication method based on stencil lithography. A mask is used to selectively deposit liquid metal on a substrate before encasing it in elastomer. This has been performed with both 3D printed masks [119] and copper masks [103]. Contributing to this class of fabrication techniques, we found that generic printer paper also works well as a stencil. While GaIn easily wets to various elastomers, it resisted adhering to paper. Selective wetting and clean liquid metal placement can thus be achieved via inexpensive, easily handled material. It should be noted that the lyophobic nature of paper has been independently discovered by other groups [120] and has been explained in terms of Caussie's law and surface texturing [121]. Recently, PDMS has been textured to mimic paper physically by molding and nanoparticle coating and by chemical reaction with acids to create a surface less wettable by GaIn alloys [121].

Fig. 2.1 from provides some examples of stencil lithography fabrication: a capacitive grid and a planar capacitor. Masks were created with printer paper which was patterned with a CO_2 laser engraver (VLS3.50, Universal Laser Systems). The mask was placed on a silicone elastomer substrate. The tackiness of the silicone rubber helps keep the mask in place throughout fabrication. A pen with an silicone rubber

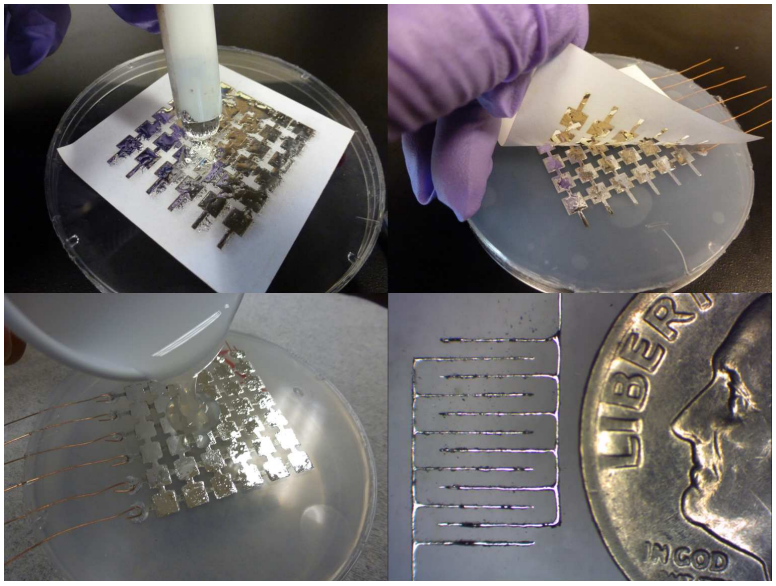

Figure 2.1: Stencil lithography [21]. Top Left: Using an silicone rubber-tipped pen to apply eutectic gallium-indium (EGaIn) over a paper mask. Top Right: Removing the paper mask. Bottom Left: Safely pouring uncured elastomer over exposed EGaIn traces. Bottom Right: Small features for a planar capacitor achieved with CO_2 laser cut printer paper stencil lithography.

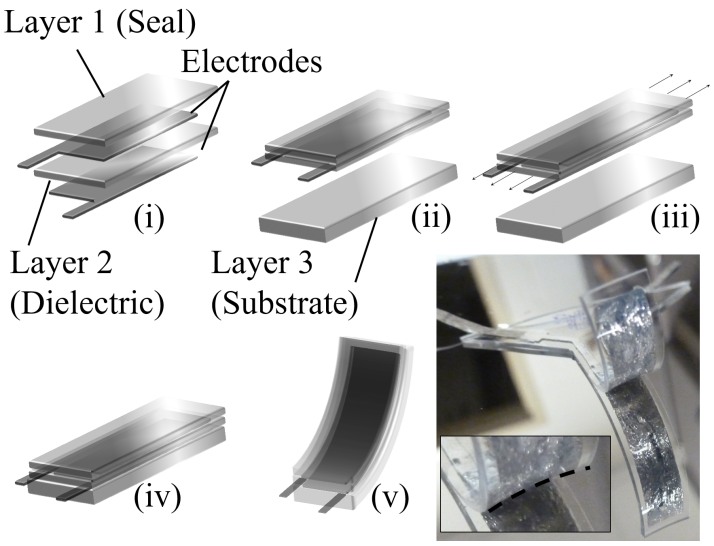

Figure 2.2: Illustration of DEA layer components during fabrication showing (i) encapsulated electrodes and compliant electrode layers, (ii-iv) straining of DEA composite and bonding to an initially unstrained substrate polymer layer and (v) curved configuration of released actuator with picture of actual device. Inset: Lower edge highlighting the negative Gaussian curvature.

tip was used to pick up and apply liquid metal, though scrap pieces of rubber work well, too. Because eutectic gallium-indium (EGaIn) wets more strongly to the elastomer than to the paper, minimal liquid metal transfers to the mask, requiring little to no cleanup after the mask is removed. Thanks to the structural strength of EGaIns oxide skin, the encasing elastomer could simply be poured on the existing structures.

Using laser-cut printer paper, we have achieved conductive traces approximately 250 μm wide. The limiting factor has been paper thickness and the singeing of the paper during cutting, which can create rough edges. Further, for small devices, the mask may consist of strips of paper which can easily be folded, ripped, or misaligned. This may be remedied by finding an alternate mask material or by using paper in conjunction with a more rigid supporting layer. Regardless, the stencil lithography method with the use of paper has been demonstrated as a quick and low-cost means to create functional soft-matter electronics and was used in the following section to fabricated electrodes for a DEA.

Actuator Fabrication and Testing

The GaIn-PDMS composite is produced using the steps presented in fig. 2.2 [83]. The design and fabrication were primarily performed by Lauren Finkenauer of the Soft Materials Laboratory (PI: C. Majidi). The PDMS dielectric layer (SYLGARD®184; Dow Corning) is first applied on a flat substrate using a 5 μm resolution thin film applicator (ZUA 2000 Universal Applicator, Zehntner GmbH). After curing on a hot plate, eutectic GaIn (EGaIn, $\geq$ 99.99%; Sigma-Aldrich) electrodes are manually deposited using an elastomeric blotter and laser-patterned (VLS3.50, Universal Laser Systems) stencil[21]. After deposition, the mask is carefully removed and an encapsulating layer of PDMS is applied over the exposed liquid electrodes. Before this sealing step, a thin strip of adhesive-backed conductive paper (3M$^{\text{TM}}$ Fabric Tape CN-3490) is placed in contact with each patterned liquid metal electrode for eventual interfacing with external electronics. Following another cure on the hot plate, the composite PDMS-EGaIn-PDMS film is carefully peeled and flipped in order to expose the other side of the dielectric layer, and a second set of electrodes is applied in the same way. The pre-strain required for inducing curvature is achieved by manually stretching the DEA by 6% and allowing it to naturally adhere to a substrate. Lastly, a thicker layer of PDMS elastomer is applied over the stretched DEA. The sealing layer, dielectric layer (separating the embedded electrodes), and substrate layer have thicknesses of $H_1 = 163$ μm, $H_2 = 85$ μm, and $H_3 = 490$ μm, respectively.

The resulting curved DEA (fig. 2.3) is connected to a 10 kV high voltage transformer (Q101-5, EMCO High Voltage Corporation) via conductive paper leads and placed on an isolated substrate. A high voltage probe (PR 28A HV DMM Probe, B&K Precision) attenuates by 1000$\times$ the voltage across the actuator for real-time recording via an Arduino UNO R3 microcontroller with a custom MATLAB GUI interface. Recorded footage of the device actuating as the voltage is slowly ($\approx$0.02 Hz) ramped up and down from $0.0 - 5.0$ kV is evaluated using a video analysis

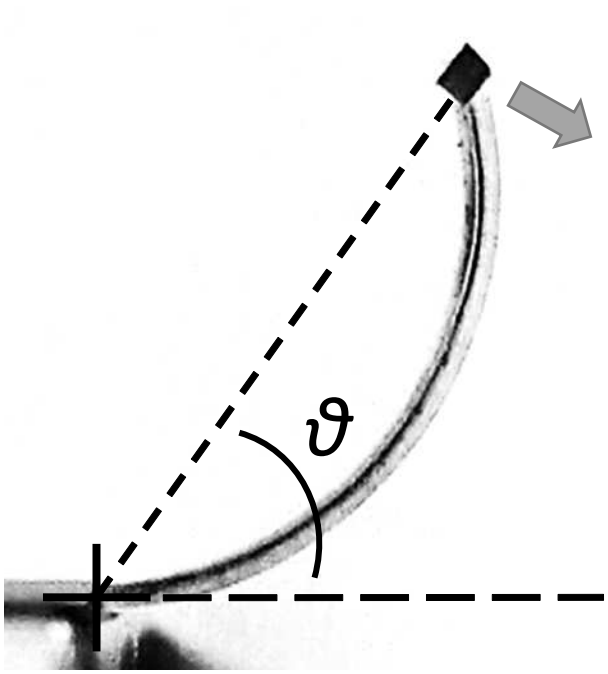

Figure 2.3: Side view of soft-matter PDMS-GaIn DEA composite during testing.

and modeling software (Tracker; http://physlets.org/tracker/). We extract data on deformation (bending) as a function of time by monitoring the changing beam tip deflection with the aid of the automated object tracking tool. The voltage can then be interpolated and correlated with the Tracker output based on time stamps for a complete description of actuation in response to voltage.

2.1.2 Theory

In its *natural* (i.e. mechanically isolated, stress-free) state, each PDMS layer of the DEA is a right rectangular prism with length L_i, width W_i, and thickness H_i as shown in fig. 2.4. As illustrated in fig. 2.2, the index $i \in \{1, 2, 3\}$ identifies the layer (*layer 1* – sealing layer; *layer 2* – dielectric layer coated with electrodes on the top and bottom surfaces; *layer 3* – thick elastomer substrate). In order to induce residual bending curvature in the DEA, layers 1 and 2 have dimensions $L_1 = L_2 < L_3$ and $W_1 = W_2 \geq W_3$. To assemble the DEA, layers 1 and 2 are bonded together and

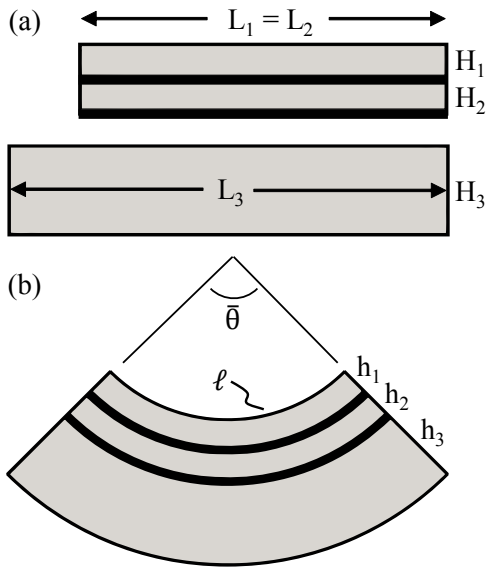

Figure 2.4: (a) Actuator cross-section with dimensions before assembly (electrodes marked by black lines shown only for illustrative purposes and are not included in the thickness dimensions). (b) Actuator cross-section after assembly.

then stretched so that they share the same length and width as layer 3. When the third layer is bonded, the composite deforms in order to relieve the residual strains in the pre-stretched layers. In general, this deformation involves changes in the width, length, and bending curvature(s) of the composite. Moreover, the shape of the DEA at static equilibrium changes when electrical voltage Φ is applied to the electrodes. Fig. 2 shows the direction of beam deflection with applied voltage Φ, which results in a changing ϑ (defined as half of the arc angle $\bar{\theta}$ shown in fig. 2.4). We observe that in addition to bending about its intermediate (width-wise) axis, the GaIn-PDMS composite also bends in the opposite direction about its major (length-wise) axis to form a saddle-like shape. Pure bending (zero Gaussian curvature, i.e. $\mathcal{K} = 0$ and saddle-like deformation ($\mathcal{K} < 0$) are examined separately in the following subsections. In both cases, the bending curvature about the intermediate axis decreases as the applied voltage Φ increases.

Model I: Pure Bending

One method for modeling the device is to simplify the kinematics by ignoring saddle formations and assuming a plane strain condition. Under this description, each layer is of equal width W regardless of deformation. The result is pure bending where the DEA curls into a circular arc with an inner radius of ρ and an arc angle of $\bar{\theta}$ (see fig. 2.4). Alternatively, the inner radius can be described in terms of curvature κ and length ℓ. Furthermore, the liquid metal electrodes are assumed to be infinitely thin, and a NeoHookean constitutive model is employed for the PDMS elastomer. (NeoHookean is deemed appropriate because strains are less than 10%.) The strain energy density shown below can be determined with the three principal stretches (λ_i) and a material coefficient of elasticity $C_1 = Y/6$, where Y is the Young's modulus for uniaxial loading.

$$\psi = C_1(\lambda_1^2 + \lambda_2^2 + \lambda_3^2 - 3). \tag{2.1}$$

We define λ_θ, λ_n, and λ_z as principal stretches. The symbol λ_θ refers to the stretch along the the arc length ($\mathbf{e}_\theta$), λ_n to the width ($\mathbf{e}_n$), and λ_z to the thickness ($\mathbf{e}_z$). Incompressibility dictates that the product of these three stretch values must be equal to 1, and so the plane strain condition implies $\lambda_n = 1$ and $\lambda_z(z) = 1/\lambda_\theta$. The stretch $\lambda_\theta(z)$ can be quantified as $\ell(1 + \kappa z)/L_i$, where z the position of material radially from the inner surface. The elastic strain energy Ω can then be determined by plugging the stretch values into the NeoHookean energy density equ. (2.1) and integrating over the unstrained, material volume: $\Omega = \Omega_1 + \Omega_2 + \Omega_3$.

$$\psi_i = C_1 \left\{ \left(\frac{\ell}{L_i}(1 + \kappa z) \right)^2 + \left(\frac{\ell}{L_i}(1 + \kappa z) \right)^{-2} - 2 \right\} \tag{2.2}$$

$$\Omega_1 = \int_0^{H_1} \psi_1 W L_1 \, dz \tag{2.3}$$

$$\Omega_2 = \int_{H_1}^{H_1+H_2} \psi_2 W L_2 \, dz \tag{2.4}$$

$$\Omega_3 = \int_{H_1+H_2}^{H_1+H_2+H_3} \psi_3 W L_3 \, dz. \tag{2.5}$$

Equivalently, the stretch $\lambda_\theta(z)$ can be quantified as $\bar{\theta}(\rho+z)/L_i$. As before, $\lambda_n = 1$ and $\lambda_z(z) = 1/\lambda_\theta$. Because the elastomer is incompressible, the elastic strain energy can be calculated by integrating over the dimensions in the final configuration, where h_i refers to the deformed thickness of each layer which can be determined based on the stretch definitions and the actuator geometry (See Appendix A.1).

$$\psi_i = C_1 \left\{ \left(\frac{\bar{\theta}(\rho+z)}{L_i} \right)^2 + \left(\frac{\bar{\theta}(\rho+z)}{L_i} \right)^{-2} - 2 \right\} \tag{2.6}$$

$$\Omega_1 = \int_0^{h_1} \psi_1(\rho+z) W \bar{\theta} \, dz \tag{2.7}$$

$$\Omega_2 = \int_{h_1}^{h_1+h_2} \psi_2(\rho+z) W \bar{\theta} \, dz \tag{2.8}$$

$$\Omega_3 = \int_{h_1+h_2}^{h_1+h_2+h_3} \psi_3(\rho+z) W \bar{\theta} \, dz. \tag{2.9}$$

For the electrostatic energy, the electric field as a function of ρ can be determined using Maxwell's equations. To begin, we assume no charge builds within the elastomer, so the divergence of the electric field (gradient of the potential φ) is known to be zero between and outside the electrodes. The result is the following differential equation with respect to z: $\varphi_{,zz} + (1/(\rho+z))\varphi_{,z} = 0$. Furthermore, we can describe the potential at the electrodes as $\Phi/2$ and $-\Phi/2$, where Φ is the applied voltage drop. The change in potential with respect to z is assumed to be negligible outside of the electrodes. This boundary value problem yields the following solution for the electric

field:

$$\mathbf{E} = \frac{\Phi}{(\rho + z)\ln\left[(\rho + h_1 + h_2)/(\rho + h_1)\right]}. \tag{2.10}$$

The electrostatic contribution U_ϕ to the total potential energy is

$$U_\phi = -\int_{h_1}^{h_1+h_2} \frac{1}{2}\epsilon_r \epsilon_0 \mathbf{E}^2 (\rho + z)\bar{\theta}(W - 2b)dz\,, \tag{2.11}$$

which corresponds to an "electrical enthalpy." Here, $\epsilon_0 = 8.85 \times 10^{-12}$F/m is the vacuum permittivity and ϵ_r again is the relative electrical permittivity (i.e. dielectric constant). Also, the dimension b (0.75 μm) represents the width of the PDMS border in the plane of the liquid GaIn electrodes. Electrostatic energy can also be approximated by assuming that the electrodes form a parallel plate capacitor. The width of this capacitor is W_e, the electrode separation h_2, and the length is approximated as $\ell_D = L_2\lambda_\theta$ where λ_θ is evaluated at $z = h_1 + h_2/2$. The capacitance C is then determined and used to calculate U_ϕ:

$$C \approx \frac{\epsilon_r \epsilon_0 W_e \ell_D}{h_2} \tag{2.12}$$

$$U_\phi = -\frac{1}{2}C\Phi^2 = -\frac{\epsilon_r \epsilon_0 W_e \ell_D \Phi^2}{2h_2}\,. \tag{2.13}$$

Lastly, at static equilibrium, the combined energy $\Pi = \Omega + U_\phi$ must be minimized with respect to the free kinematic parameters ρ and $\bar{\theta}$. Note that $\{\rho, \bar{\theta}\}$ and $\{\ell, \kappa\}$ are geometrically related and can be interchanged. This can be performed numerically with a multivariable optimization or by finding the solution to the two linearly independent equations $\partial\Pi/\partial\rho = 0$ and $\partial\Pi/\partial\bar{\theta} = 0$. For the work presented here, the combination of current volume strain energy and Maxwell's solution and the combination of material volume strain energy and capacitor approximation result in nearly equivalent results.

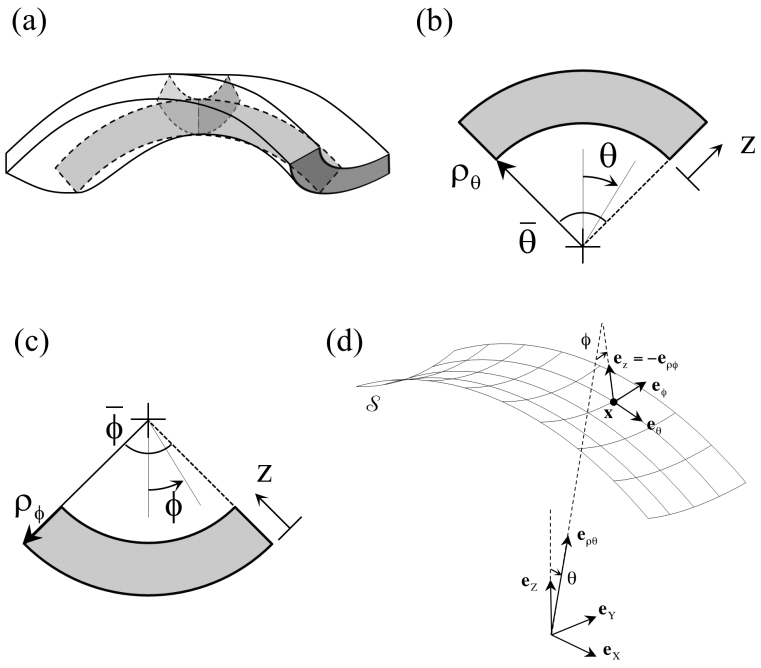

Figure 2.5: (a) DEA composite deforms to form a saddle-like geometry. (b) Deformation in the $\mathbf{e}_\theta - \mathbf{e}_z$ plane shows bending with radius $\rho_\theta = {\kappa_\theta}^{-1}$ in the longitudinal direction. (c) Deformation in the $\mathbf{e}_\phi - \mathbf{e}_z$ plane shows bending with radius $\rho_\phi = {\kappa_\phi}^{-1}$ in the width-wise direction. (d) Position of a point $\mathbf{x}$ within a saddle surface $\mathcal{S}$.

Model II: Saddle-Like Deformation

In practice, we observe that the DEA deforms into a saddle-like shape (see fig. 2.2 inset) with negative Gaussian curvature $\mathcal{K} = -\kappa_\theta \kappa_\phi$, where κ_θ and κ_ϕ are the principal curvatures along the length ($\mathbf{e}_\theta$) and width ($\mathbf{e}_\phi$), respectively. In order to examine the dependency of $\{\kappa_\theta, \kappa_\phi\}$ on Φ, we consider three representations (placements) of the elastic layers. In the *natural* placement, each layer is isolated and has dimensions $\{L_i, W_i, H_i\}$. In the *reference* placement the pre-stretched layers (1 & 2) are bonded to the thick substrate (layer 3) and the composite relaxes into a rectangular prism of length ℓ and width w. Here, each point has Euclidean coordinates $\{X, Y, Z\}$ where the tangent bases $\{\mathbf{e}_X, \mathbf{e}_Y, \mathbf{e}_Z\}$ are oriented along the composite length, width, and thickness, respectively. Lastly, in the *current* placement, the composite deforms such that the top of layer 1 (sealing layer) forms a *saddle surface* $\mathcal{S}_1$ with dimensions $\{\ell, w\}$ and principal curvatures $\{\kappa_\theta, \kappa_\phi\}$ as defined below. Here, each point has "inverted" spherical coordinates $\{\theta, \phi, z\}$ and the coordinate lines have tangent (covarient) vectors $\{\mathbf{e}_\theta, \mathbf{e}_\phi, \mathbf{e}_z\}$. The coordinates $\{\theta, \phi, z\}$ along with the arcangles $\{\bar{\theta}, \bar{\phi}\}$ and radii of curvature $\rho_\theta = {\kappa_\theta}^{-1}$ and $\rho_\phi = {\kappa_\phi}^{-1}$ for the $\mathcal{S}_1$ centerlines are defined in fig. 2.5.

Assuming that points in the $\mathbf{e}_X - \mathbf{e}_Z$ and $\mathbf{e}_Y - \mathbf{e}_Z$ planes of the reference placement remain plane, the $\mathbf{e}_\theta - \mathbf{e}_\phi$ surfaces in the reference placement form saddles $\mathcal{S}$. For each z, $\mathcal{S}$ has centerlines with arcangles $\bar{\theta} = \kappa_\theta \ell$ and $\bar{\phi} = \kappa_\phi w$ and radii of curvature $\rho_\theta + z$ and $\rho_\phi - z$. The coordinate lines along the $\mathbf{e}_\theta$ and $\mathbf{e}_\phi$ directions have total lengths of $\ell_\theta = \{(\rho_\theta + z) + (1 - \cos\phi)(\rho_\phi - z)\}\bar{\theta}$ and $w_\phi = (\rho_\phi - z)\bar{\phi}$, respectively. Referring to fig. 2.5, a point in $\mathcal{S}$ has a position

$$\mathbf{x} = \mathbf{x}(\theta, \phi, z) = (\rho_\theta + \rho_\phi)\mathbf{e}_{\rho\theta}(\theta) + (\rho_\phi - z)\mathbf{e}_{\rho\phi}(\theta, \phi)\,, \tag{2.14}$$

where $\mathbf{e}_{\rho\theta} = \sin\theta \mathbf{e}_X + \cos\theta \mathbf{e}_Z$ and $\mathbf{e}_{\rho\phi} = \sin\phi \mathbf{e}_Y - \cos\phi \mathbf{e}_{\rho\theta}$.

For each z, the saddle surface $\mathcal{S}$ has an area (see Appendix A.2) of

$$a(z) = \left\{ [\rho_\theta + \rho_\phi]\bar{\phi} - 2\,(\rho_\phi - z)\sin\left(\frac{\bar{\phi}}{2}\right) \right\} \bar{\theta}(\rho_\phi - z)\,. \tag{2.15}$$

Each layer of the composite is assumed to be incompressible and so the final thicknesses h_i can be estimated by dividing the initial volume by the final area of its top surface: $h_i \approx W_i L_i H_i / a_i$, where $a_1 = a(0)$, $a_2 = a(h_1)$, and $a_3 = a(h_1 + h_2)$. The final layer thicknesses h_i are only approximations because they are calculated using the area of the top surface rather than mid-plane of each layer. Moreover, the exact layer thickness will be non-uniform since the principal stretch λ_θ in the $\mathbf{e}_\theta$ direction increases with $|\phi|$. Nonetheless, the above approximations are used since it allows the thickness to be estimated *explicitly* by calculating a_1, h_1, a_2, ... , h_3 in sequence.

Each layer is treated as a *hyperelastic* solid with principal stretches $\{\lambda_\theta, \lambda_\phi, \lambda_z\}$ in the $\{\mathbf{e}_\theta, \mathbf{e}_\phi, \mathbf{e}_z\}$ directions and a strain energy density $\psi = \psi(\lambda_\theta, \lambda_\phi, \lambda_z)$. The stretches λ_θ and λ_ϕ are calculated by dividing the arclength of each convecting coordinate line by its original length in the natural placement: $\lambda_\theta(\phi, z) = \ell_\theta / L_i$ and $\lambda_\phi(z) = w_\phi / W_i$, where $i = 1$, 2, and 3 for $z \in [0, h_1)$, $[h_1, h_1 + h_2)$, and $[h_1 + h_2, h_1 + h_2 + h_3]$, respectively. Incompressibility implies $\lambda_z = 1/\lambda_\theta\lambda_\phi$ and that the total elastic strain energy $\Omega = \sum_{i=1}^{3} \Omega_i$ can be calculated by integrating ψ in the current placement where now Ω_i are evaluated as follows:

$$\Omega_1 = \int_0^{h_1} \int_{-\bar{\phi}/2}^{\bar{\phi}/2} \psi \ell_\theta (\rho_\phi - z)\, d\phi\, dz \tag{2.16}$$

$$\Omega_2 = \int_{h_1}^{h_1+h_2} \int_{-\bar{\phi}/2}^{\bar{\phi}/2} \psi \ell_\theta (\rho_\phi - z)\, d\phi\, dz \tag{2.17}$$

$$\Omega_3 = \int_{h_1+h_2}^{h_1+h_2+h_3} \int_{-\bar{\phi}/2}^{\bar{\phi}/2} \psi \ell_\theta (\rho_\phi - z)\, d\phi\, dz\,. \tag{2.18}$$

For a pre-strain of <10% in layers 1 and 2, we expect only moderate stretches at

static equilibrium. Therefore, we again treat the composite as a NeoHookean solid and let

$$\psi = 2C_1 \left({\lambda_\theta}^2 + {\lambda_\phi}^2 + \frac{1}{{\lambda_\theta}^2 {\lambda_\phi}^2} - 3 \right) , \tag{2.19}$$

where $C_1 = Y/6$ is the coefficient of elasticity as before.

When voltage Φ is applied, the DEA has a total potential energy $\Pi = \Omega + U_\phi$, where U_ϕ is the electrical enthalpy. Since the electrodes are surrounded by a border that is $b = 0.75$ mm wide, the final area is approximately χa_2, where $\chi = (W_2 - 2b)(L_2 - 2b)/W_2 L_2$. In the current placement (i.e. saddle-shape configuration), the capacitance between the two electrodes is estimated as $C \approx \chi \epsilon_r \epsilon_0 a_2 / h_2$ and the electrical enthalpy is

$$U_\phi = -\frac{1}{2} C \Phi^2 = -\chi \frac{\epsilon_r \epsilon_0 a_2 \Phi^2}{2 h_2} . \tag{2.20}$$

Lastly, the unknown kinematic parameters $\{w, \ell, \kappa_\theta, \kappa_\phi\}$ are determined by minimizing the total potential energy Π. This may be accomplished either by performing a multivariable optimization or finding the solution to the stationary conditions $\partial\Pi/\partial w = \partial\Pi/\partial\ell = \partial\Pi/\partial\kappa_\theta = \partial\Pi/\partial\kappa_\phi = 0$. While both approaches are valid, numerical minimization is more convenient since it eliminates the additional step of calculating the partial derivatives of Π.

2.1.3 Results and Discussion

Results from the experiments and theory are presented in fig. 2.6. The grey dots correspond to experimental measurements collected from a single DEA sample and the dash-dot curve are theoretical predictions from the simplified pure bending model. The pure bending theory (Model I) overestimates the angle of deflection by approximately 9^o. Furthermore, it exaggerates the change $\Delta\vartheta$ in arcangle $\vartheta = \bar{\theta}/2$ as a function of applied voltage Φ. This is most likely because the plane strain assumption underestimates the final thickness of the dielectric, causing an overestimate of

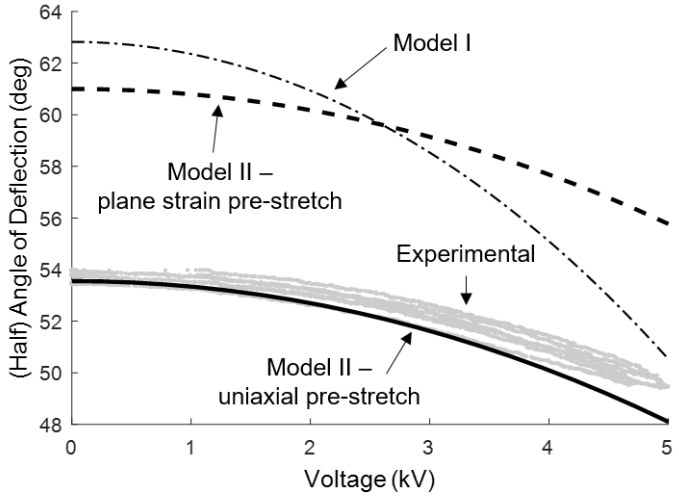

Figure 2.6: Comparison of experimental measurements and theoretical predictions for the arcangle $\vartheta = \bar{\theta}/2$ as a function of applied voltage Φ: (gray dots) experimental data collected from repeated measurements on a single DEA sample; (dash-dot) the theoretical prediction based on Model I; (solid) prediction from Model II assuming uniaxial pre-stretch; (dashed) prediction with Model II assuming plane strain pre-stretch.

the electrostatic component of the potential (particularly at higher strains and voltages). The lack of saddle formation may also play a role in the misrepresentation of $\Delta\vartheta$ since the effective area moment of inertia is underestimated.

The thin shell presented (Model II) predictions, represented by the solid curve with circular markers, that are in much stronger agreement with the experimental measurements. These predictions correspond to a uniaxial pre-stretch of layers 1 & 2 during the DEA assembly. As discussed above, the two layers are first bonded together and stretched so that they share the same width and length of layer 3. For pure uniaxial loading, the two layers stretch by an amount $\hat{\lambda}_X = L_3/L_1 = L_3/L_2$ in the $\mathbf{e}_X$ direction and $\hat{\lambda}_Y = \hat{\lambda}_Z = \hat{\lambda}_X^{-1/2}$ in the $\mathbf{e}_Y$ and $\mathbf{e}_Z$ directions. This requires an initial width $W_1 = W_2 = W_3/\hat{\lambda}_Y = W_3\sqrt{L_3/L_1}$. We use the term "uniaxial" since the elastomer is under uniaxial stress during pre-stretch with the condition $\sigma_Y = \sigma_Z = 0$ implying $\hat{\lambda}_Y = \hat{\lambda}_Z$.

The theoretical prediction appears to be in strong agreement with the experimental measurements (without the aid of data fitting). While the resulting observed change in bending curvature is less than has been demonstrated by other unimorph type DEAs [94], our device both takes into account saddling due to pre-stretch and also displays no obvious degradation of the electrode material throughout testing (though a much more extensive study is necessary to verify this claim). However, the theory suggests that even greater bending can be achieved by imposing a "plane strain" loading condition during pre-stretch. To accomplish this, layers 1 & 2 should be constrained such that $\hat{\lambda}_Y = 1$ during pre-stretch. Theoretical predictions based on this case where $W_1 = W_2 = W_3$ are presented by the dashed curve in fig. 2.6. This prediction preserves the dependency of $\Delta\vartheta$ on Φ but increases the absolute angle of deflection by approximately 7^o. The greater bending angle is attributed to a dramatic reduction in transverse curvature (see fig. 2.7), which allows for almost pure bending deformation. Here, "plane strain" refers to the constraint that strain only

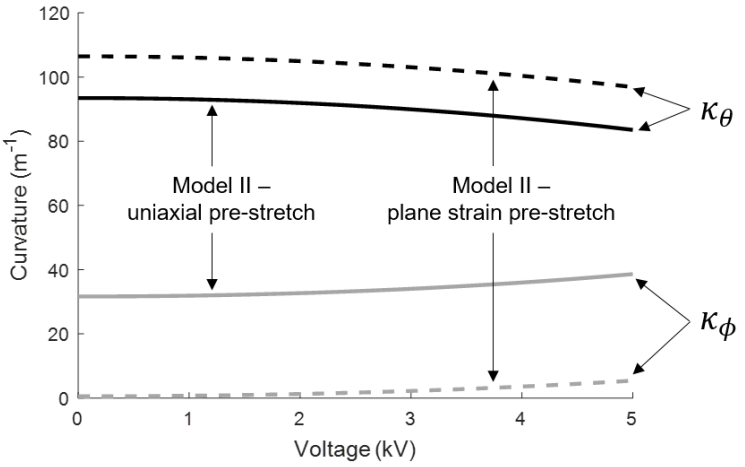

Figure 2.7: Comparison of predicted bending curvatures κ_θ (black) and κ_ϕ (grey) in the $\mathbf{e}_\theta - \mathbf{e}_z$ and $\mathbf{e}_\phi - \mathbf{e}_z$ planes: (solid) uniaxial pre-stretch; (dashed) plane strain pre-stretch.

in the $\mathbf{e}_X - \mathbf{e}_Z$ plane. However, this could also be interpreted as a "plane stress" assumption where stress is restricted to the $\mathbf{e}_X - \mathbf{e}_Y$ plane (i.e. $\sigma_Z = 0$).

Fig. 2.7 compares curvatures in the two bending planes of the saddle-shaped DEA. For uniaxial pre-stretch, the bending curvatures in the $\mathbf{e}_\theta - \mathbf{e}_z$ (open circles) and $\mathbf{e}_\phi - \mathbf{e}_z$ (open triangles) planes are approximately $\kappa_\theta \sim$ 84-93 m^{-1} and $\kappa_\phi \sim$ 32-39 m^{-1}, respectively. This relatively high degree of negative Gaussian curvature can be explained by the Poissons effect as the actuator bends. Although the DEA layer is generally in tension while the initially unstrained layer is in compression, the uniaxial pre-stretch results in an approximately constant width with respect to z ($\kappa_\phi \approx 0$) if κ_θ is forced to zero by some external moment. However, as the beam bends, material towards the inner surface experiences more compression and width expansion, causing the saddle formation ($\kappa_\phi > 0$). Unlike an external moment, which lengthens the DEA layer but shortens its width, electrostatic pressure during actuation leads to an increase in both width and length. As a result of the width expansion, actuation induces an increase in κ_ϕ.

For plane strain pre-stretch, bending in the $\mathbf{e}_\theta - \mathbf{e}_z$ plane (filled circles) is greater

($\kappa_\theta \sim$ 97-107 m^{-1}), however the curvature in the $\mathbf{e}_\phi - \mathbf{e}_z$ plane (filled triangles) is almost negligible ($\kappa_\phi \sim$ 0.5-5 m^{-1}). Unlike the uniaxial case, one would expect a negative κ_ϕ to form if κ_θ were reduced to zero by an external moment; due to the plane strain, the DEA layer would attempt to contract to a smaller width than the initially unstrained layer. As the beam bends, the inner material experiences the same phenomenon described for the uniaxial case, favoring a more positive κ_ϕ. At equilibrium under no voltage, the negative κ_ϕ caused by the plane strain and the positive κ_ϕ caused by the beam bending nearly cancel out. As with the uniaxial case, actuation with an applied voltage tends to increase the DEA width, further increasing κ_ϕ in the positive direction.The minimal saddling in the plane strain pre-stretch case explains why its 0 voltage predictions are similar to those of the pure bending model. The saddling has the greatest effect on the effective area moment of inertia in comparison to overall width or thickness.

The theoretical predictions presented in figs. 2.6 and 2.7 are obtained for geometries and materials constants based on the experimental DEA sample: $L_1 = L_2 = 20$ mm, $L_3 = 1.06L_1 = 21.2$ mm, $W_3 = 6.5$ mm, $b = 0.75$ mm, $H_1 = 163$ μm, $H_2 = 85$ μm, and $H_3 = 490$ μm. The Young's modulus, $E = 1$ MPa, was determined through tensile tests with an Instron® materials testing system (Model 4467; Instron) and is similar to values found in the literature [122–126]. A dielectric constant $\epsilon_r = 2.72$ is reported in the product data sheet of the materials supplier (Dow Corning, Inc.). The double integrals for computing Ω_i are performed in MATLAB R2016b using an adaptive Simpson quadrature (*dblquad*) and Π is minimized for $\{w, \ell, \kappa_\theta, \kappa_\phi\}$ using a direct simplex search method (*fminsearch*). Complete code for Model I and Model II can be found in Appendices B and C, respectively.

Fig. 2.8 shows the reversible switching of a liquid metal circuit using a curved DEA to create and break electrical contacts. This demo was prepared by Lauren Finkenauer of the Soft Materials Laboratory and is described in greater detail within

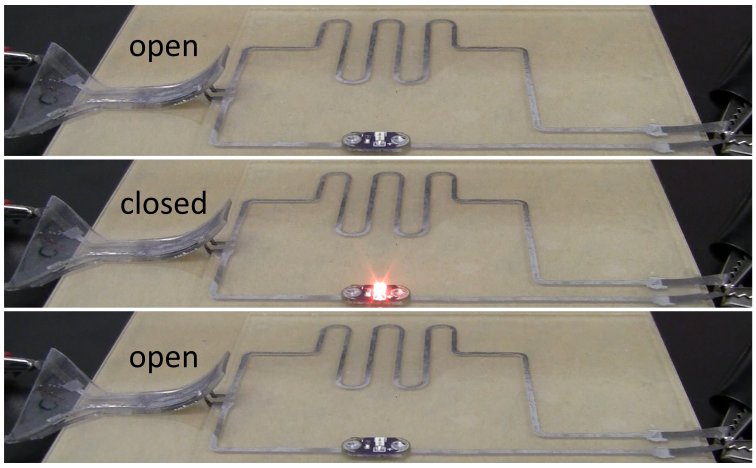

Figure 2.8: Demonstration of a circuit open and closed by a curved DEA switch. Credit: Lauren Finkenauer [83].

[83]. The implementation here reflects the feasibility of using these actuators as switching elements.

2.1.4 Concluding Remarks

I have introduced an entirely soft DEA that contains no rigid or inextensible materials. It is composed of PDMS embedded with a liquid-phase GaIn alloy. After assembly, the GaIn-PDMS spontaneously deforms into a saddle-shape that changes curvature when voltage is applied to the liquid electrodes. This shape is accurately predicted with an elastic shell theory based on the principle of minimum potential energy and hyperelastic constitutive model. Since the materials undergo only moderate strains ($< 10\%$), good agreement between theory and experiment can be achieved with a NeoHookean constitutive law, which only requires a single coefficient of elasticity. In general, DEAs with large pre-stretch and bending curvature should be modeled with a more accurate nonlinear constitutive law. However, even in these cases, the proposed 4-parameter kinematic representation for a saddle-shaped shell with negative Gaussian curvature is sufficient for predicting the shape at static equilibrium for prescribed pre-stretches and voltage. While we focused on two types of pre-stretch (so-called uniaxial and plane strain loading), the theory is sufficiently general for any biaxial loading condition on the dielectric layer prior to bonding and release.

High energy efficiency is perhaps the most appealing characteristic of dielectric elastomer actuators. In soft MEMS, these devices could create and break electrical connections with nearly zero power consumption. However, relatively high voltages are required, particularly because the dielectric layer must be compressed. Furthermore, there is no inherent pull-in instability as seen in traditional electrostatic MEMS switches, such as cantilever and fixed-fixed beams. This can be seen as either a pro or a con depending on the application, though, for switching, DEAs lack the extra force that exists just after pull-in could be detrimental. This study has provided in-

sight into the importance of accurate modeling - both with regards to hyperelasticity and with regards to kinematic approximations. Furthermore, the stencil lithography rapid prototyping described in this chapter expands the range of methods with which liquid metal films can be patterned.

2.2 Soft-Matter Electrostatic Cantilevers

To further decrease the required voltage for actuation, we examine the possibility of using an electrostatic cantilever beam (fig. 2.9). Unlike the DEA in the previous section, the device presented here makes use of an air gap, eliminating the extra voltage required to compress an elastomer dielectric layer while maintaining the high energy efficiency and low current usage. This resembles traditional microelectromechnical systems (MEMS) (see Appendix D) and may be subject to pull-in instability. The design can be relatively simple, and the actuation is rapid, even at the length scale used for the prototypes here. Electrostatic switches generally consist of a stationary pull-in electrode which is charged and attracts a floating fixed-free [127, 128] or fixed-fixed beam [129]. This actuation can be used to directly complete a connection [127, 128] or to form a capacitor [129]. The work presented here focuses on electrostatic pull-in of rubber beams for eventual application to a soft-matter switch. Theory is discussed and compared with good agreement to experimental studies.

2.2.1 Theory

A rectangular cantilever beam with a length of L, thickness of H, and width of W is considered. It is expected that, as the beam deflects, the electrostatic force will increase as the distance between it and the pull-in electrode decreases. One method to estimate the cantilever deformation due to electrostatic forces is to apply small angle beam bending approximations. In conjunction with this, the electric field is

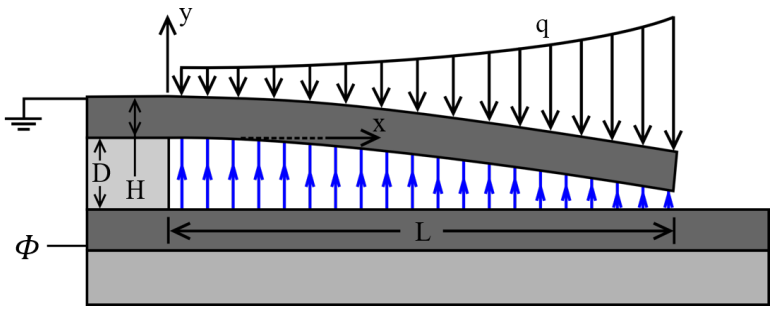

Figure 2.9: The electrostatic cantilever beam visualization. The lines and arrows under the beam represent the electromagnetic field.

assumed to project orthogonally from the pull-in electrode to the cantilever. Fig. 2.9 is a visualization of the beam with the assumed electric field and expected force distribution. With small angles, the system can be modeled as a series of dx by W parallel plate capacitors, ignoring fringing fields. The value of one of these capacitors is

$$\delta C = \frac{\epsilon_0 \epsilon W dx}{D + y(x)}, \tag{2.21}$$

where $\epsilon 0$ is the permittivity of free space, ϵ is the relative permittivity of air ($\sim$1), and D is the initial gap between the cantilever and the pull-in electrode. The position along the beam is indicated with x and $y(x)$ is the location in the bending direction. The potential energy of each capacitor as a function of applied voltage Φ is

$$U = \frac{1}{2}\delta C \Phi^2. \tag{2.22}$$

Deriving this potential energy with respect to $y(x)$ provides the force (2.23) from each capacitor.

$$dF = \frac{\epsilon_0 W \Phi^2 dx}{2(D + y(x))^2}. \tag{2.23}$$

The distributed load q along the beam as a function of $y(x)$ is dF/dx. Small angle beam theory states that this load is proportional to the fourth order differentiation of $y(x)$ with respect to x. The final governing equation is thus

$$EIy'''' = -q = -\frac{\epsilon_0 \Phi^2 W}{2(D + y(x))^2}, \tag{2.24}$$

where E is the elastic modulus of the cantilever and I is the moment of inertia. By imparting boundary conditions, this equation can be solved numerically to acquire a beam shape for given dimensions and voltages. In this case, the four boundary

conditions the following:

$$y(0) = 0, \tag{2.25}$$

$$y'(0) = 0, \tag{2.26}$$

$$M(L) = y''(L) = 0, \tag{2.27}$$

$$v(L) = y'''(L) = 0. \tag{2.28}$$

In addition to zero displacement and slope at the base of the beam, both the internal moment M and the shear stress v at the end of the beam are zero. Similar approaches to modeling this problem can be found in the literature, sometimes using methods such as finite differencing [130]. In particular, we are interested in the voltage at which electrostatic forces overcome elastic restoring forces, causing the beam to spontaneously collapse into the pull-in electrode. This is known as the pull-in voltage (Φ_{PI}). In general, assumptions are made regarding the equivalent spring constants [131] or beam shape [132] to acquire a close-formed solution. [132] makes the following assumption for the beam shape as a function of tip position $y(x)$:

$$y(x) \approx \left(\frac{x}{L}\right)^2 y(L). \tag{2.29}$$

A closed-form solution for the beam tip position as a function of voltage can then be acquired. When plotted, the pull-in voltage can be found where the system is semi-stable. [132] approximates this voltage (assuming a rectangular cross-section) as

$$\Phi_{PI}(x) \approx \sqrt{\frac{18EID^3}{5\epsilon_0 L^4 W}} = \sqrt{\frac{3EH^3D^3}{10\epsilon_0 L^4}}. \tag{2.30}$$

Despite the additional approximations, (2.30) provides insight into the key metrics for designing a simple electrostatic cantilever.

2.2.2 Beam Fabrication

In order to test the electrostatic theory, our goal was to fabricate prototype fixed-fixed beams on millimeter scale in length outside of the cleanroom. Again, we turn to MEMS, where sacrificial and release layers enable tiny, delicate structures to be fabricated. However, to avoid harsh developing chemicals that could damage elastomers or otherwise be inconvenient, we opt for water-soluble materials. Three options include polyacrylic acid (PAA) [133], polyvinyl alcohol (PVA) [133, 134], and gelatin [135]. For the work presented here, we used PAA.

Poly(dimethylsiloxane) (PDMS) (Sylgard 184) was chosen as the structural material for the device because it offers a low modulus, it is easy to spin coat or mold, and it is well-documented in the literature. Further, extensive research has been invested in creating conductive PDMS (cPDMS) by loading it with carbon black [6, 16], carbon nanotubes [19], exfoliated graphite [18], and silver micro-particles [16]. The PDMS and cPDMS can be bonded easily, making them ideal for this project. Carbon black was chosen as the conductive filler for the samples constructed in this paper because of its low cost and ease of use.

Fig. 2.10 demonstrates the process used to fabricate the fixed-free beams experimentally tested in this work. To prepare the substrate from step i in 2.10, 11 g of 10:1 PDMS was poured on a 3.5" x 3.5" stainless steel sheet and allowed to cure for over 2 hours on a hotplate at 75°C. Afterwards, 10.5 g of 20:1 PDMS was mixed with 1.85 g of carbon black (Alfa Aesar Carbon black 100% compressed, 45527) to create a 15% weight ratio of cPDMS. Mixing was performed for 1 minute in a centrifugal mixer (Thinky) without the debubbling step. The mixture is pasty and had be applied with a thin film applicator (ZUA 2000 Universal Applicator, Zehntner GmbH), creating a layer of about 600 microns in thickness. This, too, was cured on a hotplate at the same temperature for over 2 hours. Finally, PAA was applied. PAA can be applied with a thin film applicator or with a spin coater directly to a PDMS or conductive

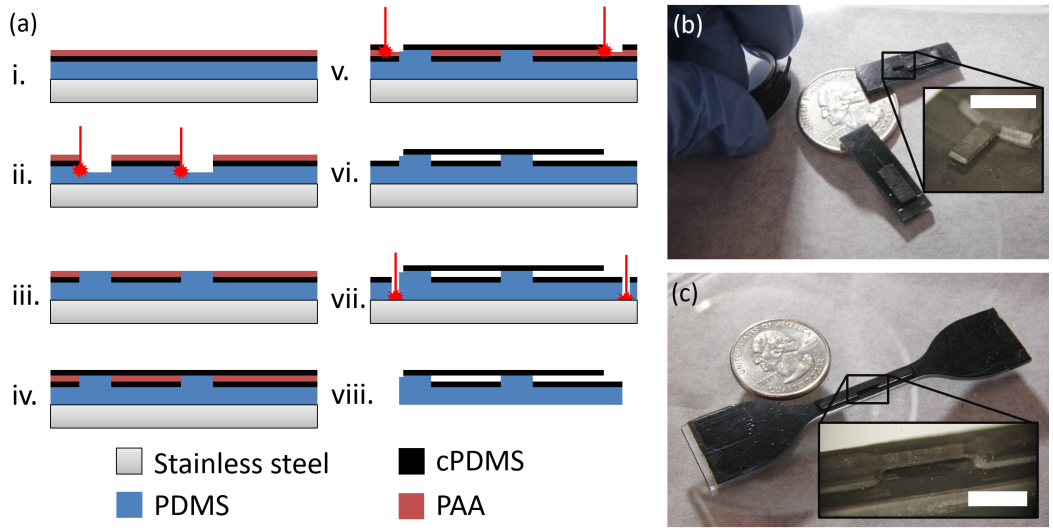

Figure 2.10: PAA fabrication steps for suspended cPDMS beams. i) Coat PAA on cPDMS/PDMS surface after oxygen plasma treatment. ii) Pattern through the PAA (and cPDMS if desired). iii) Fill in trenches with PDMS as anchors. iv) Coat with an additional layer of cPDMS. v) Pattern outlines for releasing beams and for allowing water to reach the PAA. vi) Submerge in water to dissolve PAA and remove from metal plate. vii) Laser pattern or manually cut out the structures. viii) Remove from substate. b) Some cantilever examples. c) A fixed-fixed beam on a dogbone body. All scale bars represent 3 mm.

PDMS (cPDMS) substrate. However, given the 30% aqueous solution, pouring about 8 g of the solution on the cPDMS surface and allowing it to spread was adequate.

Because the PAA solution is aqueous, it is helpful to treat the elastomer surface with oxygen plasma turn it from hydrophobic to hydrophilic. We used an SPI Plasma Prep III in atmosphere at 30W for about 45 seconds. The mechanism behind this is the replacement of methyl groups with polar silanol groups and has been widely researched [136–140]. The water was allowed to evaporate on the hotplate (same temperature) for over 2 hours. After the PAA hardens , it can be patterned with the CO2 laser.

A CO_2 laser (VLS3.50, Universal Laser Systems) was used to pattern through the PAA into the PDMS/cPDMS substrate (ii). Around 5 raster passes at 70% power, 100% speed, 1000 PPI, and highest quality (lowest throughput) were required with

the HPDFO lens. It should be noted that the cPDMS is particularly messy to ablate and had to frequently be wiped/rinsed clean with isopropyl alcohol. PDMS was then filled into the patterned areas (iii) to act as insulating anchor points for the conductive beams. Curing was done on the hotplate at 75°C for over 2 hours.

For step iv, the same cPDMS recipe described above was used to create a second batch, which was again applied with the thin-film applicator and cured with the same parameters. The CO_2 laser was again used to pattern this surface (v), though only until the PAA layer (careful not to damage the cPDMS layers underneath. This patterning step outlines the beams and other structures which will be released. It also allows access points for water to reach the PAA. After patterning, the entire body was submerged in water (overnight) to allow PAA to dissolve (vi). Finally, the components can be cut out with the CO_2 laser or by hand (vii) with a blade and peeled off the substate (viii). The ordering of vi through viii were sometimes rearranged depending on the types of samples created. The samples were rinsed thoroughly with water and isopropyl alcohol and allowed to dry.

2.2.3 Results and Discussion

Using the process described above, cPDMS electrostatic cantilevers were fabricated at lengths of approximately 2, 2.5, 3, 3.5, 4, and 4.5 mm. For each length, 3 widths were fabricated: averaging 0.46, 0.94, and 1.43 mm. Due to uneven surfaces (particularly hotplates) and other fabrication imperfections, beam thickness ranged from around 0.104 mm to 0.233 mm, and air gap height ranged from around 0.310 to 0.626 mm. To account for this when comparing to theoretical values, equ. (2.30) was rearranged to acquire a new function dependent solely on length:

$$\hat{\Phi}_{PI} = \frac{10\epsilon_0 \Phi_{PI}^2}{3EH^3D^3} = \frac{1}{L^4} \tag{2.31}$$

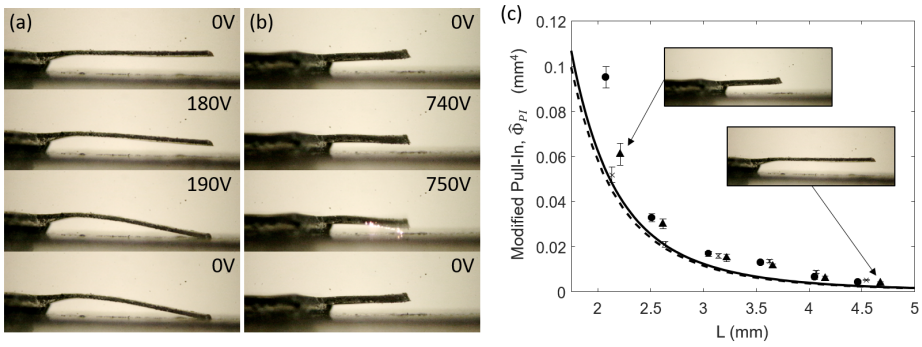

Figure 2.11: Pull-in results. Sequences (a) (∼4.676 mm long, 0.899 mm wide) and (b) (∼2.213 mm long, 1.004 mm wide) show images of beams before voltage was applied, just prior to pull-in, just after pull-in, and after pull-in at 0V. The plot (c) compares experimental results to theory. Widths of 0.46 (circles), 0.94 (triangles), and 1.43 mm (crosses) are plotted separately. The theory from equ. (2.31), $1/L^4$, is plotted as a solid line. Numeric results are plotted as a dashed line.

Pull-in experiments were performed by quasi-statically increasing the voltage (Stanford Research Systems, PS375) applied across the cantilever and the pull-in substrate by 10V increments. This was continued until the beam snapped down or exhibited a spark 6 times for each beam. Sample images are shown in fig. 2.11a,b. Note that the spark shown in fig. 2.11b occurs after pull-in has initiated (also see literature on Paschen's law and related phenomena on sparks [141, 142]). Prior to each trial (6 times per beam), images were taken to collect data on air gap height. The voltages and other beam data were plotted as the left side of equ. (2.31) and theory was plotted as the right side. The elastic modulus of the cPDMS was determined to be about 840 kPa based on tensile data from an Instron (Model 5969).

The numeric and analytic predictions (see Appendix E for MATLAB 2016b code) for pull-in were very similar, only deviating slightly at short beam lengths where small angle approximations begin to suffer. Both tended to underestimate the required voltage, though agreement with experimental data was still strong. Conductive polymers rely on conductive paths of particles, which could lead to deviation from theory if areas of no conductivity exist. Further, conductive rubbers (and cured elastomers in

general) tend to vary in stiffness based on factors such as age and curing temperature. These factors all introduce deviations into the system. However, it seems apparent that, especially at short beam lengths, the wider beams require less voltage for pull-in. This is most likely due to fringing electric fields. The theory assumes electric fields only pass directly between the beam and the substrate, but in reality, field lines lead off the sides and top, as well. These fringing fields have a large impact for beams that are smaller width-wise. Additional material testing, simulation, and pull-in data is included in Appendix F.

This study has shown that for deformations with small strains, traditional beam mechanics and electrostatic theories can be applied to devices constructed of conductive rubbers. While this is useful for designing devices and predicting behavior, cPDMS has other characteristics which limit its use in soft electronics. In particular, the low conductivity (0.7 Ω-m) is not sufficient for the most switching applications. According to [13], it is generally considered a failure for a MEMS switch when the contact resistance rises above 5 Ω. While this level of conductivity may not be needed for all applications, it is a useful benchmark.

One solution for the high resistance may be to replace the carbon black with a more conductive alternative. PDMS with silver micro-particles has been reported [16] providing resistivity as low as 0.0001 Ω-m, though concentrations of about 86% were required. Similar conductivities were shown for spray-on carbon nanotubes [78]. Another option is eutectic gallium-indium, a liquid allow with a resistivity of about $2.9*10^{-7}$ Ω-m [29].

Adhesion has presented another potential obstacle. Typical direct contact switches do not suffer from this issue [13]. However, in the case of the elastic materials used in this paper, the same low modulus which allows for lower pull-in voltages creates a greater possibility for permanent stiction. Careful adhesion modeling, such as that presented in [143], may provide a geometry which can solve this problem. Alterna-

tively, an antagonistic electrode could be placed on the opposite side of the beam to oppose adhesion. A similar problem would present itself if an EGaIn design were implemented where the surface tension, amplified by EGaIn's oxide layer, would be of concern.

2.2.4 Conclusions

This study focuses on understanding the mechanics behind creating electrostatically actuated switches composed entirely of soft-matter. A simple theory was derived and solved numerically to compare with experimental results and a closed-form approximation found in the literature. While the comparison was favorable, there was room for design, fabrication, and theoretical improvement to further miniaturize the devices and address concerns with adhesion. Further, while the cPDMS was acceptable for electrostatic actuation, it failed to meet requirements for completing circuits due to high resistances. Additional information on fabrication is reported in Appendices G and H. Future work will focus on implementing materials with higher conductivities. Additionally, cantilever beams have the benefit of being free from the influence bulk material stretch or compression. However, behavior under hyperelastic stretch and compression is of interest in the context of soft MEMS, and so fixed-fixed beams will be examined as they can be tested while placed under axial stress. This will have the added benefit of paving the way for stretchable diaphragms that can act as pumps and valves.

Chapter 3

Manipulation of Hyperelastic and Buckled Fixed-Fixed Structures

The previous chapter considered the case of fixed-free devices under the manipulation of electrostatic loading. Here, we instead consider fixed-fixed elastomer beams with the target of creating a more robust soft electrical switch that responds to field stimulation. Although pull-in requirements will be increased with respect to the fixed-free condition, analyzing this case expands the variety of possible device designs for factors such as resonant frequency. Furthermore, a fixed-fixed design has a higher tolerance for internal stresses formed during fabrication and for deformation of the host body; these two factors may cause a fixed-free beam to develop excessive gap distances or to unintentionally contact the pull-in electrode, whereas a second fixed end would help to maintain the desired off-state shape. For the sake of generality, we consider cases where the device is either stretched or compressed. The first section discusses the behavior of fixed-fixed beams under hyperelastic stretch, concluding with a discussion on the effect of this stretch on possible electrostatic devices. The second section considers a soft ferromagnetic beam that buckles under compression and changes its buckled deflection in response to magnetic field.

3.1 Nonlinear Deflection of a Fixed-Fixed Elastomer Beam under Extreme Stretch [3]

In chapter 2, Euler-Bernoulli beam equations with Hooke's law were adequate for describing cantilever behavior, but these models are insufficient when deformations are large or when significant strains are involved. While cantilever beams have the benefit of isolation from outside forces, fixed-fixed beams under large stretches have the potential to exhibit interesting behavior. Here one must utilize more rigorous elastic rod theories (see Appendix I) combined with hyperelastic constitutive laws. When considering incompressible, isotropic materials, one of the earliest and most commonly used hyperelastic constitutive relations was proposed by Mooney in 1940 [114] and further discussed by Rivlin in 1948 [115]. Materials that follow this model are commonly referred to as Mooney-Rivlin solids, and their energy density can be described in terms of the first and second invariants of the left Cauchy stretch tensor and two material constants:

$$\psi = C_1(\lambda_1^2 + \lambda_2^2 + \lambda_3^2 - 3) + C_2(\lambda_1^{-2} + \lambda_2^{-2} + \lambda_3^{-2} - 3) \tag{3.1}$$

In the above relation, λ_i represent the principle stretches and C_1 and C_2 are coefficients of elasticity.

Perhaps the most popular constitutive law in hyperelasticity, due to its simplicity, is Neo-Hookean, which Treloar introduced using statistical mechanics in 1943 and 1944 [144, 145] and later compared to work by Rivlin [113]. The energy density of a Neo-Hookean solid is described as Mooney-Rivlin material where C_2 is set to 0 in (3.1). C_1 is often set to $E/6$, where E is Young's Modulus, to coincide with Hooke's Law when the strain is small. A more general constitutive equation was described by Ogden in 1972 [116]. The energy density of the Ogden solid can also be determined

with principle stretches and material constants:

$$\psi = \sum_{m=1}^{N} \frac{\mu_m}{\alpha_m}(\lambda_1^{\alpha_m} + \lambda_2^{\alpha_m} + \lambda_3^{\alpha_m} - 3) \tag{3.2}$$

The above constitutive laws are common and frequently compared [146, 147].

3.1.1 Theory

The model in this paper takes a similar approach to previous work examining Cosserat curves with hyperelastic constitutive laws [148]. In particular, I use a small-on-large theory, where the initial pre-stretch is substantial and nonlinear, and the subsequent deflection is minimal, allowing for linearization and small angle approximations (about the large pre-stretch condition) to simplify the theory further. The model is then compared to experimental data for stretched beams under point loads. This model describes an incompressible, isotropic beam under a fixed force pre-stretch and planar loading conditions. Later, adjustments are made to accommodate fixed end positions. Specifically, we will focus an initially straight fixed-fixed beam and loading which is normal to the direction of pre-stretch (fig. 3.1). The theory is based upon the condition that the beam is thin relative to its length and that deflections are small, resulting in minimal bending strains.

Derivation of Governing Equation

The above conditions give rise to several important assumptions. First, the deformation is dominated by axial stress, tangent to the length of the beam. Second, the cross-section is affected by the overall lengthening of the beam but not by the bending strains such that the cross-section remains perpendicular to the centerline of the beam. The bending moment at any cross-section can then be approximated with the curvature, the spatial area moment of inertia, and an effective elastic modulus.

The effective modulus assumes that the axial stress-strain curve is linear for the small changes in strain induced by bending. Finally, we assume that that that the strain along the centerline remains constant along the length of beam and is only influenced by the pre-stretch loading (the planar loading conditions do not lengthen the beam). This assumption is valid only for small deflections. Given the above assumptions, we can break the problem into three conditions: 1) the initial configuration, 2) the reference configuration during pre-stretch, and 3) the final spatial configuration during deflection.

In the initial configuration, the beam has a length L, thickness H, and a width W. In both the the reference and final configurations, the centerline length becomes l, the thickness becomes h, and the width becomes w. For the pre-stretches, we define $\lambda_t = l/L$ (along the length), $\lambda_n = h/H$ (along the thickness), and $\lambda_z = w/W$ (along the width). Incompressibility dictates that the Jacobian, $J = \lambda_t\lambda_n\lambda_z$, must be equal to 1, so $\lambda_n = \lambda_z = 1/\lambda_t$. Again, take note that λ_t describes the only stretch due to pre-stretch and can be large compared to any additional strain due to bending. The fixed force pre-stretch and lack of cross-sectional deformation during bending means that the cross-section is identical between the reference and final configurations and that the center-line length of the beam does not change between these states. Axial stress due to bending can be superimposed on the pre-stretch by adding κy, where y is the distance from the center-line in the n direction. These assumptions lead to the following stretch tensor:

$$\mathbf{B} = (\lambda_t - \kappa y)e_t \otimes e_t + \frac{1}{\sqrt{\lambda_t}}e_n \otimes e_n + \frac{1}{\sqrt{\lambda_t}}e_z \otimes e_z. \tag{3.3}$$

The principal stresses are defined using the same nomenclature as the stretch: σ_t, σ_n, and σ_z. Using the stretches above, it is easy to determine the associated stress

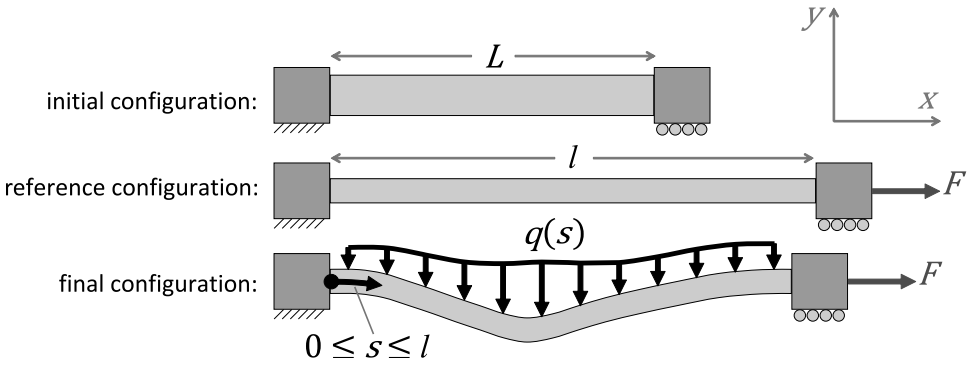

Figure 3.1: Model diagram with constant stretching force F and arbitrary loading q.

by using hyperelastic constitutive equations of the form

$$\sigma_i = \lambda_i \frac{\partial \psi}{\partial \lambda_i} - P. \tag{3.4}$$

Here, W is an energy density function, which will depend on the choice of hyperelastic constitutive model – such as Mooney-Rivlin (3.1) or Ogden (3.2) – and P is a hydrostatic pressure associated with incompressibility. Since the beam is only subject to axial load and electrostatic body forces, the surfaces are traction free, which implies $\sigma_n \approx \sigma_z \approx 0$. The condition set by (2.4) makes it easy to solve for the unknown hydrostatic pressure, P. For a Ogden material, one finds that

$$\sigma_t = \sum_{m=1}^{N} \mu_m (\lambda_t^{\alpha_m} - \lambda_t^{-0.5\alpha_m}). \tag{3.5}$$

The equivalent elastic modulus, E^*, is determined by taking the derivative of the tangential stress with respect to the tangential stretch. For an Ogden material,

$$E^* = \frac{d\sigma_t}{d\lambda_t} = \sum_{m=1}^{N} \mu_m (\alpha_m \lambda_t^{\alpha_m - 1} - \frac{\alpha_m}{2} \lambda_t^{-0.5\alpha_m - 1}). \tag{3.6}$$

This equivalent elastic modulus is useful for estimating changes in stress when small strains are applied to a beam already stretched by λ_t. We use it here to simplify the expressions for axial force and moment within the beam:

$$\sigma = \sigma(\lambda_t, \kappa) \approx \sigma_t - E^* \kappa y, \tag{3.7}$$

$$F \approx \int_{-H/(2\sqrt{\lambda_t})}^{H/(2\sqrt{\lambda_t})} \sigma \frac{W}{\sqrt{\lambda_t}} dy = \sigma_t \frac{WH}{\lambda_t}, \tag{3.8}$$

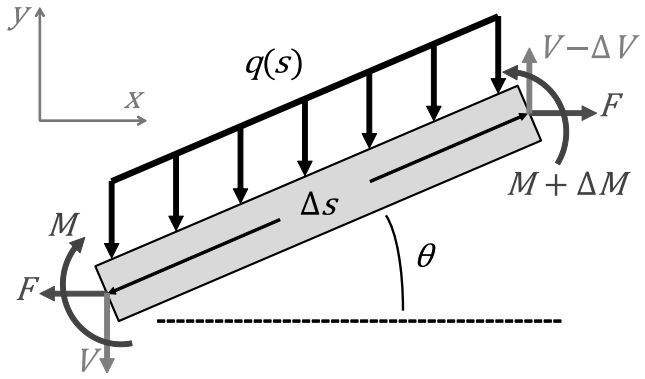

Figure 3.2: Spatial free body diagram of a beam section of length Δs.

$$M \approx -\int_{-H/(2\sqrt{\lambda_t})}^{H/(2\sqrt{\lambda_t})} \sigma y \frac{W}{\sqrt{\lambda_t}} dy = E^* \kappa \frac{H^3 W}{12\lambda_t^2}. \tag{3.9}$$

Note that these integrals must be performed in the final configuration. From (3.9), we can define the effective area moment of inertia in the reference configuration: $I^* = (H^3 W)/(12\lambda_t^2)$. One might notice that this is essentially the normal area moment of inertia for a rectangular beam modified with the stretch value to pull it from the initial to reference/current configuration. Analogous to Euler-Bernoulli theory, curvature can then be calculated as

$$\kappa = \frac{d\theta}{ds} = \frac{M}{I^* E^*}. \tag{3.10}$$

Next, we can isolate out an infinitesimally long line segment of the beam and perform force and moment balances. Due to the significant forces cause by the lengthening of the beam, one must apply the balance laws in the spatial configuration (Eulerean description), as shown in fig. 3.2, even if deflections are small. The force caused by lengthening is given by (3.8). By balancing the forces in the y-direction,

one finds that

$$\frac{dV}{ds} = -q(s). \tag{3.11}$$

The moment balance results in

$$\Delta M - F\Delta s \sin(\theta) + V\Delta s \cos(\theta) + O(\Delta s^2) = 0. \tag{3.12}$$

In the limit as $\Delta s \to 0$, it becomes clear that

$$\frac{dM}{ds} = F \sin(\theta) + V \cos(\theta). \tag{3.13}$$

Combining (3.13) with (3.10), one acquires the following second order differential equation:

$$\frac{d^2\theta}{ds^2} = \frac{F}{I^*E^*} \sin(\theta) + \frac{V}{I^*E^*} \cos(\theta). \tag{3.14}$$

With the definition of two boundary conditions, such as $\theta(s = 0) = \theta(s = l) = 0$ for a fixed-fixed beam, this equation can be solved numerically. Alternatively, this equation can be further adjusted by assuming small deflection angles. In this case we retrieve an expression very similar Timoshenko's differential equation for describing a column being deflected while under compression (see equation (1-5) in [149]).

$$\frac{d^4y}{dx^4} = \frac{F}{I^*E^*}\frac{d^2y}{dx^2} - \frac{q}{I^*E^*}. \tag{3.15}$$

Numerical Analysis

As mentioned above, the equ. (3.14) and (3.15) assume that the horizontal pre-stretch force remains constant. However, for many situations, including the experiments described in this paper, a fixed end position must be enforced. In this case, the

beam lengthens as it is deflected. To simplify this phenomenon, we assume that any increase in length is spread equally throughout the beam, effectively increasing the pre-stretch by some amount δ. The new pre-stretch value, $\lambda_f = \lambda_t + \delta$, thus refers to the overall axial stretch in the final configuration with fixed ends. The distance δ can be adjusted numerically such that the appropriate final beam length is achieved to satisfy the fixed end position condition.

Equ. (3.14) is in terms of s and θ, where ds remains constant for each infinitesimal line segment. When solved, the x-direction end-to-end distance of the final configuration is shorter than that of the reference configuration (in contrast to what would be expected for a fixed force condition). To achieve the fixed end condition, the reference length is increased (by δ) to $l_f = \lambda_f L$ such that the final configuration end-to-end distance contracts to $l = \lambda_t L$ under the applied load (also see Appendix K.1). Since l_f describes the overall length under the fixed position condition, the force F, effective modulus E^*, and final width w and height h are all in terms of λ_f instead of λ_t, and (3.14) is solved for s ranging from 0 to l_f. Essentially, we want to satisfy the isoperimetric constraint

$$l = \int_0^{l_f} \sqrt{1 - \left(\frac{dy}{ds}\right)^2}\, ds. \tag{3.16}$$

In the case of (3.15), the simplification into terms of x rather than s forces the curve to have fixed end positions because dx (rather than ds) remains constant for each infinitesimal line segment. However, it does not account for the stretching required to maintain this fixed position condition. The same occurs with Euler-Bernoulli beam theory. To compensate for the additional stretching, the reference length is increased to l_f (also see Appendix K.2). Again, the force, effective modulus, and final width and height must be calculated in terms of λ_f instead of λ_t. However, because (3.15) forces the end positions to remain constant, the differential equation should still be

solved for x ranging from 0 to l (not l_f). When solved, the overall length in the final configuration is equal to the new reference length, l_f:

$$l_f = \int_0^l \sqrt{1 + \left(\frac{dy}{dx}\right)^2}\, dx. \tag{3.17}$$

Due to the complexity of the governing equations and of the methods for achieving fixed end positions, it is easiest to acquire the solutions numerically. In this work, the numerical analysis was performed using MATLAB R2016b. The differential governing equation was solved using *bvp4c*, and δ was solved for using *fsolve* using the above two equations. For the point load experiments presented here, the solutions from equ. (3.14) and equ. (3.15) were nearly identical. Only results from equ. (3.15) is presented here, with the code for both included in Appendix M.

3.1.2 Experimental Methods

The following experiment was designed to test the accuracy of the theory developed above. In particular, we aim to verify the "correcting" term, $Fy''/(I^*E^*)$ from (3.15). To accomplish this, a rubber beam is stretched and subjected to a point load. No distributed load is assumed, and the force versus displacement curve is recorded for comparison to the theory.

Ecoflex 0030 (Smooth-On, Inc.), a two-part silicone rubber, was studied as the hyperelastic material for the following tests. After thoroughly mixing, the uncured elastomer was cast into a 100 mm x 20 mm x 4 mm 3D printed (Objet24, Stratasys Ltd.) molds, degassed, and cured. For testing purposes, flat 3D printed plates were adhered (Loctite® Super Glue Gel Control) to the ends, allowing the beam to be secured with a pin and clamp without compressing and deforming the elastomer, as seen in fig. 3.3. The same pin and clamp system was used to secure the elastomer for material characterization and for the deflection tests. A 70 mm x 20 mm x 4 mm

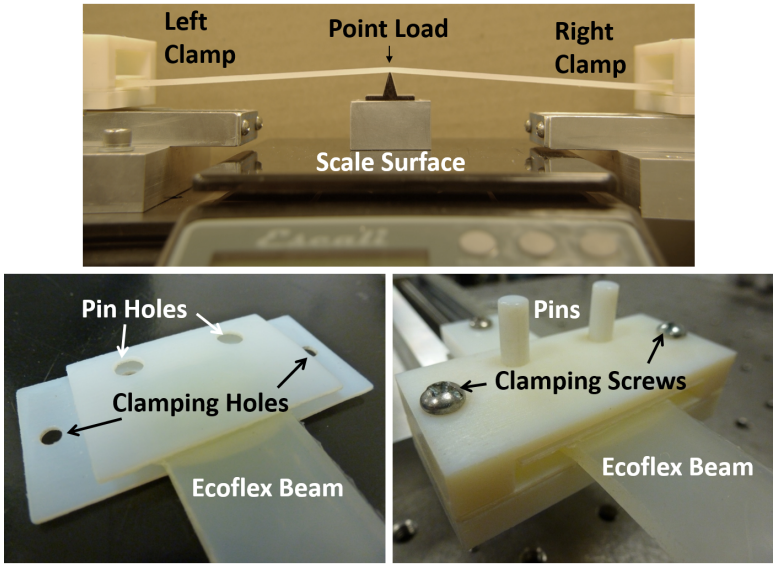

Figure 3.3: Top: Overall setup. Bottom left: Flat plates adhered to Ecoflex beam. Bottom right: Clamping and pinning setup.

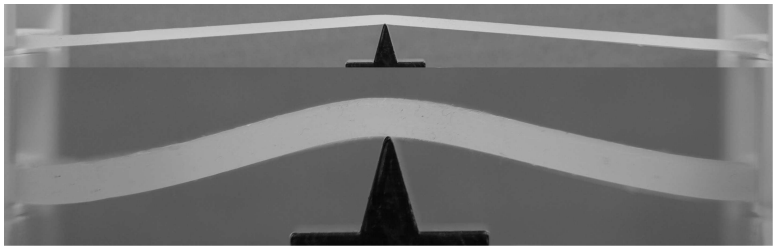

Figure 3.4: Top: 7 mm deflection at 250% stretch. Bottom: 7 mm deflection at 102% stretch. (Scales differ in each image.)

section of Ecoflex 0030 was left exposed between the secured ends. Three separate samples were tested.

Material characterization was performed using an Instron tensile tester (33R 4442) in order to acquire a stress versus stretch curve. To test the theory for deflection under extreme stretches, the ends of the beams were secured to translating blocks. A 3D printed wedge raised and lowered with a vertical stage to impart point loads, monitored by a scale (L-600, Escali Corp). Displacements were tracked with a digital dial gauge from 0 mm to 7 mm. The translating blocks were adjusted to test samples under stretches from 100% to 300%. fig. 3.4 Indentation data was gathered by analyzing photographs of deflected beams with a software called Tracker (http://physlets.org/tracker/).

3.1.3 Results and Discussion

Fig. 3.5 shows the true stress versus stretch for Ecoflex 0030. The data is an average taken from three samples for the purpose of determining parameters for hypereleastic constitutive models. Neo-Hookean (elastic modulus of $E = 50kPa$)fails to capture a slight softening effect as the stretch approaches 150% and the more extreme strain hardening at stretches above 250%. Mooney-Rivlin and Ogden models were fit to the data using MATLAB's *fittype* and *fit* functions. Mooney-Rivlin ($\{C_1, C_2\}$ set as $\{6882, 1451\}$ Pa) follows the softening behavior, improving the accuracy until 200%

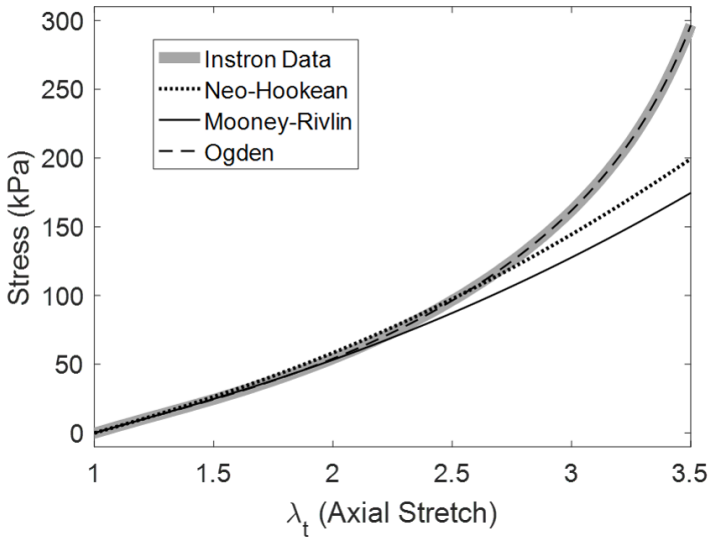

Figure 3.5: Instron data compared to Neo-Hookean, Mooney-Rivlin, and Ogden constitutive models for Ecoflex 0030. See Appendix J.

but again failing to demonstrate significant hardening. The curve is captured well by a 3-parameter Ogden model ($\{\alpha_1, \alpha_2, \alpha_3\}$ set as $\{1.214, -8.1327, 16.9936\}$ and $\{\mu_1, \mu_2, \mu_3\}$ set as $\{22889, -956.2, 2.6390 * 10^{-5}\}$ Pa). Fewer or more parameters could be used to increase or decrease the accuracy of the model. One might notice that because the theory only focuses on uniaxial strain, the Instron data (which was also uniaxial) could be used numerically with the theory in place of a hyperelastic constitutive law. It is also important to note that a true material characterization should at least include additional equibiaxial testing. As discussed in [150], multiple optimal fitting parameters may work for either axial and biaxial, but only certain values will work well for both simultaneously. Despite this, only uniaxial characterization was required here since experiments introduced mainly axial loading.

The experimental results are compared with theory in fig. 3.6. As expected, the Neo-Hookean model (not plotted in fig. 3.6 for the sake of brevity) fails to capture the behavior completely, especially at stretches of 150% or greater. Mooney-Rivlin improves the accuracy up to about 200% stretch. The Ogden model, however, provides

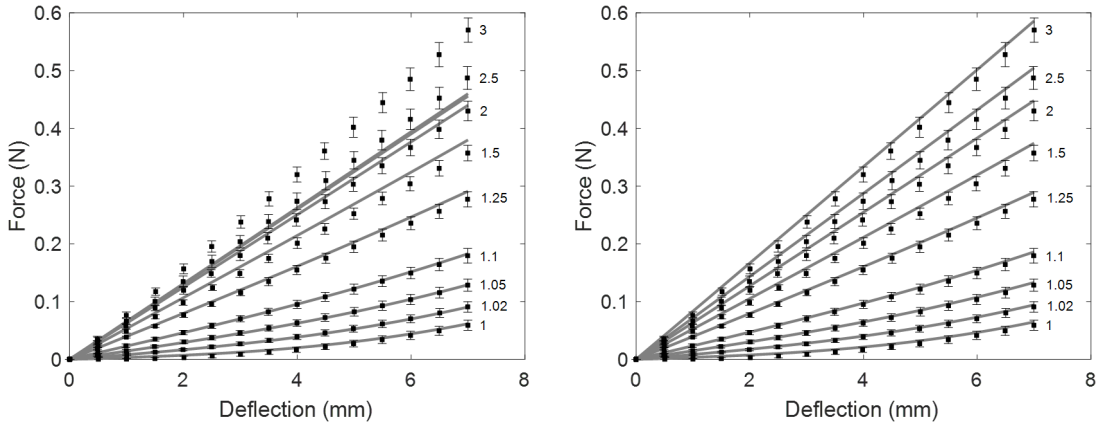

Figure 3.6: Left: Mooney-Rivlin compared to measured data. Right: Ogden compared to measured data.

theoretical results which compare well to the experiments, even at larger stretches. At low pre-stretches ($< 105\%$) the force versus vertical displacement curve features a positive curvature. This is associated with the beam bending aspect of the theory. At greater pre-stretches, the curve is nearly linear, indicating a more membrane-like response associated with the correcting factor of the theory. Essentially, as pre-stretch is increased, we see a transition between a beam bending and a membrane response. Larger vertical displacements would more prominently feature this transition even at low pre-stretches, although a more robust theory would have to be developed for this case since small angle assumptions would no longer be valid.

Although the theory with the Ogden constitutive model shows strong agreement with the experimental data, it generally overestimates forces, particularly at large stretches. Some error could be expected as changing humidity and temperature have an effect on the rigidity of elastomers, though this is expected to be minimal. Error in the experimental setup, such as deformation of the end clamps or flexing of the scale, is expected to be greater at larger pre-stretches due to the increasing forces and could contribute to the observed discrepancy. However, even at high pre-stretches, the forces are small and would not have a large enough impact on the testing structure

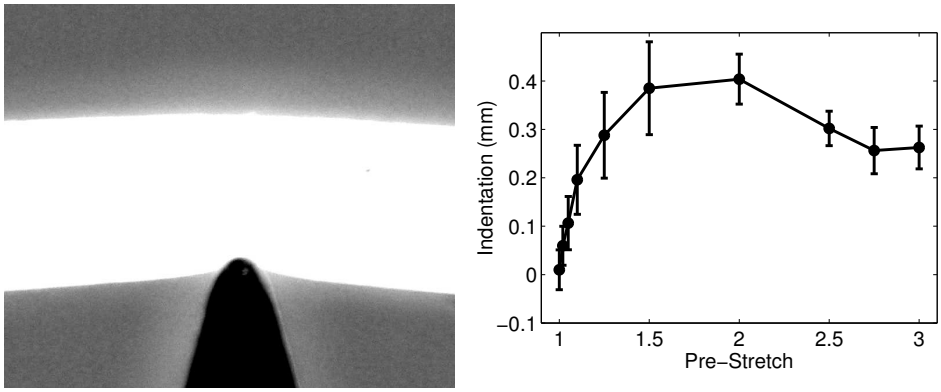

Figure 3.7: Left: Indentation at 200% pre-stretch and 7 mm vertical displacement. Right: Plot for indentation as a function of pre-stretch at 7 mm displacement.

to explain what is observed. The most likely culprit is the indentation formed at the point of contact between the point load wedge and the elastomeric beam.

Fig. 3.7 provides an example and a set of data for indentation at various pre-stretches at a vertical displacement of 7 mm. At low pre-stretches, there is too little force to cause a significant indentation. Pre-stretch between 150% and 200% results in the greatest indentation. Despite the continued increase in force, the impact decreases at higher stretches and appears to level off as 300% stretch is approached. This is evidently due to the strain hardening of the elastomer. Contact mechanics could be included in the theory to account for the indentation. To get a quick approximation of the effect of the indentation, we instead take the Ogden theory value at vertical displacement $y_d = 7mm - y_{ind}$, where y_{ind} is the average indentation distance. Fig. 3.8, showing force as a function of pre-stretch at max displacement, includes the adjustments for the effects at the contact. The adjusted Ogden theory effectively bound the experimental data, showing great agreement with the theory.

3.1.4 Application to Electrostatic Beams

Modeling has been performed for electrostatic actuation of a fixed-fixed beam. To accomplish this, the equations defined above 3.14 and 3.15 are applied with the elec-

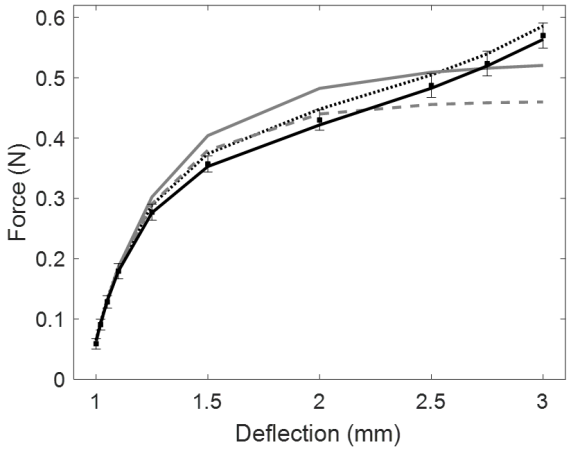

Figure 3.8: Measured force as a function of pre-stretch when vertical displacement is fixed at 7 mm. The grey solid line is Neo-Hookean theory, the grey dashed line is Mooney-Rivlin, the black dotted line is Ogden, and the black solid line is Odgen adjusted based on the average measured indentation.

trostatic forces defined in Chapter 2. Specifically,

$$q = -\frac{\epsilon_0 \Phi^2 w}{2(d + y(x))^2}. \tag{3.18}$$

Simulations were run for an Ecoflex 0030 beam of length L =700 μm, width W =500 μm, and height H =50 μm. The initial height between the beam and pull-in electrode was D =50 μm. MATLAB 2016b code is included in Appendix N, and an example re-formulation is shown in Appendix L. These dimensions were chosen as they would be the approximate dimensions achieved using the fabrication methods described previously. The simulations presented here assumed that the ends were not fixed (fixed force F applying longitudinal stretch). Simulations for fixed ends showed nearly the same results for the given dimensions. (Alternative dimensions and simulations are reported in Appendix O.) Also, note that the electrostatic force distribution is calculated based current configuration width (w) and gap (d). Electrostatic forces were calculated as though the beam were entirely conductive. Simulations have indicated that varying the width of the beam has no significant bearing on the pull-in voltage, regardless of pre-stretch. Indifference to width is characteristic of electrostatic beams. Also noteworthy is the displacement of the center of the beam just before pull-in is reached. At least for the dimensions tested here, this value remains nearly constant ($\sim 2/5d$) even at pre-stretches ranging from 100% to 300%. This is demonstrated in fig. 3.9, where the beam described above is actuated at various pre-stretches. Here, the dimension d remained constant regardless stretch ($d = D$).

Fig. 3.10 demonstrates how the pull-in voltage changes as a function of pre-stretch. When d is held constant regardless of pre-stretch ($d = D$), the pull-in voltage increases but begins to level off around 300%. As the beam is stretched, the flexural rigidity increases, requiring additional voltage to cause pull-in. However, increased stretch also tends to increase the surface area over which electrostatic forces accumulate. The

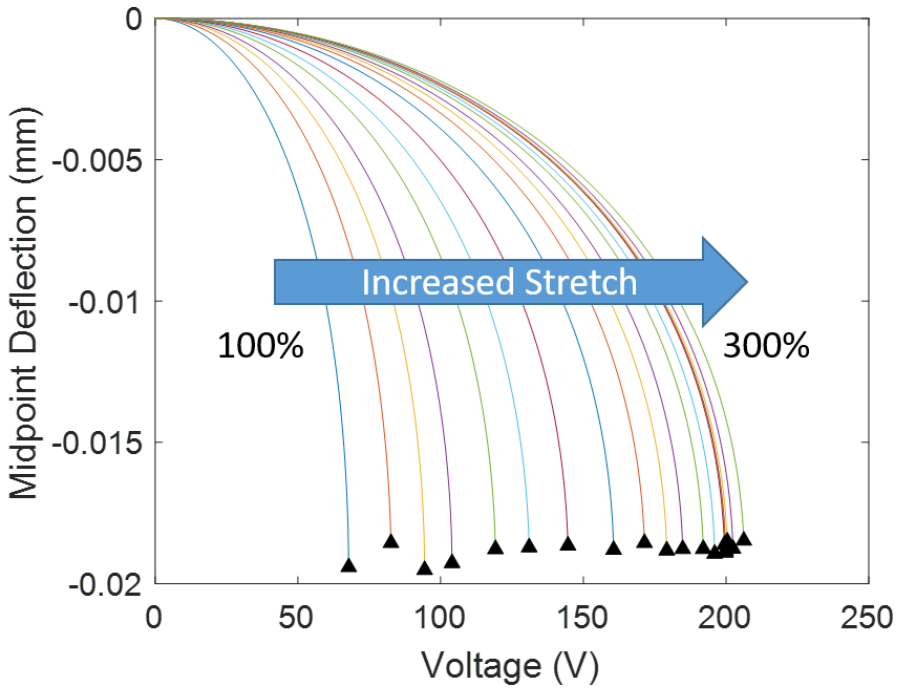

Figure 3.9: Pull-in data from MATLAB simulations for $d = D$. Each line represents the same beam at a different pre-stretch value. The pull-in voltage/displacement is marked by black rectangles.

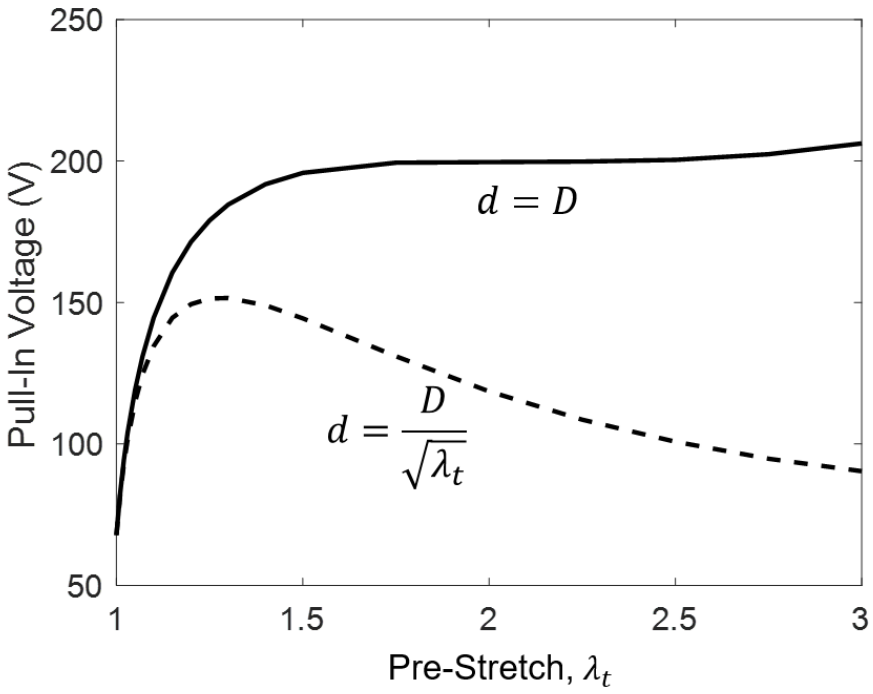

Figure 3.10: Pull-in voltage as a function of pre-stretch for when dimension d remains constant ($d = D$) and for when dimension d changes with pre-stretch ($d = D/\sqrt{\lambda_t}$).

balancing of these forces causes the leveling off of pull-in values. When d is allowed to decrease with pre-stretch ($d = D/\sqrt{\lambda_t}$), the pull-in voltage actually decreases after some stretch value. The decrease of d supplies the extra electrostatic force required to make this happen when compared to the constant d scenario. The sharp increase in pull-in voltage at the beginning is, again, an indicator of the transition from bending to membrane behavior. Experimentally, we could expect to see either case depending on how the sample is fabricated. In any case, this data suggests that it may be beneficial to fabricated fixed-fixed electrostatic beams that are pre-stretched (when the rest of the body is relaxed). Any additional stretch will result in little change or a decrease in pull-in voltage. Furthermore, there may exist an optimal elastomer which has the appropriate stress-strain curve such that the pull-in voltage can remain nearly constant.

The fabrication methods performed so far in this document (see Chapter 2) generally result in structures as small as 1000s of microns in length and 100s of microns in thickness. When testing fixed-fixed cPDMS beams on this scale, we generally saw arcing prior to any pull-in instability. In contrast, traditional MEMS, such as those shown in [13] are often an order of magnitude smaller in scale. Future work will include developing equivalently sized soft switches. Before proceeding, it is wise to check the scaling laws. From 3.19 found in [132], it is easy to see that pull-in voltage scales linearly with size. Furthermore, linear beam theory indicates that the effect of gravity on the cantilever vanishes at small scales. Both of these points are supported with our own simulations based on equations above and provide more incentive to shrink the devices.

$$\Phi_{PI}(x) \approx \sqrt{\frac{18EID^3}{5\epsilon_0 L^4 W}} = \sqrt{\frac{3EH^3D^3}{10\epsilon_0 L^4}}. \tag{3.19}$$

Simulations for scaling has been performed for the fixed-fixed beam design. Like the cantilever, the effect of gravity vanishes at small scales. Additionally, as indicated by fig. 3.11, pull-in voltage roughly scales linearly with size. This data seems to indicate that, regardless of stretch, these electrostatic beams scale favorable when shrunk in size. It should be noted that the smaller scale would not solve correctly when using the governing equation in terms of y and x. Instead, the equation in terms of θ and s was used. The reason for this simulation failure at smaller sizes is not clear, but the likely culprit is numeric limitations within MATLAB.

3.1.5 Concluding Remarks

We have presented a theory that combines rod theory with hyperelastic constitutive models to predict the behavior of pre-stretched beams under various loading conditions. The simplest form of the theory includes a beam bending term and a correction

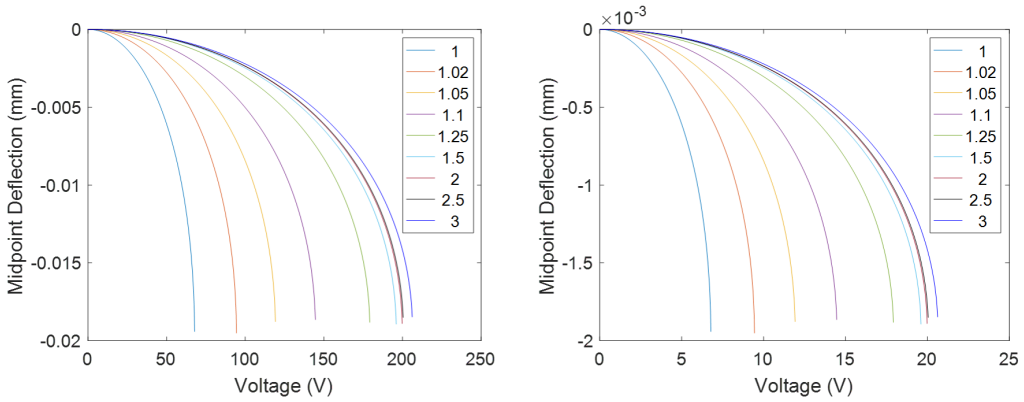

Figure 3.11: Position of the center of a beam as a function of voltage. Left: 700 μm x 500 μm x 50 μm fixed-fixed beam. The gap is held constant at 50 μm regardless of stretch ($d = D$). Elastic behavior is that of Ecoflex 0030. Right: Same setup with dimensions scaled down by 10 times. The legends represent input pre-stretch values.

term accounting for longitudinal forces. We specify that this theory is specifically for small deflections and small angles and shows good agreement between the model and point load experimental data. The model successfully captures a gradual transition from beam bending behavior to a membrane response. Furthermore, we show that much of the error can be accounted for by the indentation at the point of contact. Future work may examine this in the context of contact mechanics, though it will not be necessary for the current goal of applying this theory to electrostatic pull-in of hyperelastic beams. When applied to electrostatic pull-in, we see interesting behavior indicating that fabricating a pre-stretched beam may be the best option when fabricating an easy to use device. Further miniaturization of these beams is necessary for truly testing these theories on electro-mechanical coupling. Regardless, the second regime that is of interest for these devices is the condition of compression. In this case, the buckling of the beams must be considered.

3.2 Instabilities of Buckled Ferroelastomer Beams [4]

3.2.1 Introduction

Wearable computing and soft bio-inspired robotics depend on elastically deformable electronics that match the mechanical properties of natural biological tissue [151, 152]. Stretchable circuit wiring and "artificial skin" sensing is currently accomplished with soft elastomer composites[153], soft microfluidics[80], and a variety of deterministic architectures involving wavy patterns and microscale geometries[154]. The latter approach typically exploits elastic instabilities such as buckling and wrinkling[151]. In addition to stretchable electronics, these elastic instabilities have also been used for adhesion and wetting control[155–157], shape-programmable origami[158, 159],

valves for manipulating fluid flow[160], reversible fluidic encapsulation[161], and elastocapillary snapping[162]. The dynamic loss of elastic stability and beam snapping has provided opportunities for pneumatic actuation[163], voltage-controlled dielectric elastomer actuators[1, 164], and the control of optical properties through snapping microlens structures[165]. Moreover, buckling and snap-through govern dynamic elasto-morphological coupling in a variety of biological mechanisms. These include morphogenesis of the *Volvox* embryo[166], catapult-like ejection of fern sporangia[167], and the thigmonastic movement of the Venus flytrap (*Dionea* plants)[168]. For these engineered and biological systems, elastic instabilities have a central role in enabling stretchable functionality or reducing the energetic barrier for achieving dramatic changes in shape or morphology.

In this section, I show the ability to exploit elastic instability for physically reconfigurable soft electronics. This is accomplished with a soft elastic switching element (fig. 3.12a) that undergoes a buckling instability in response to an external magnetic field (fig. 3.12b). The switch is composed of a pre-buckled ferromagnetic elastomer beam that reversibly controls the electrical conductivity between a source and drain electrode. External magnetic field is used to induce either temporary deflection or snap-through between bistable states, allowing for two modes of electrical switching behavior. We examine both through a combination of experimental observations and theoretical modeling based on elastic beam theory and variational techniques. The theory furnishes stability criteria that not only inform switch design but also allows us to predict the influence of subsequent stretch and external mechanical loading on switch response.

This work builds on previous studies on snap-through buckling instabilities [169–174] as well as the magneto-elastostatics of so-called magnetorheological (MR) elastomers. MR elastomers are composed of a dispersion of ferromagnetic microparticles (typically Fe, Ni, Co, or their alloys) suspended in an elastomeric matrix[175–179].

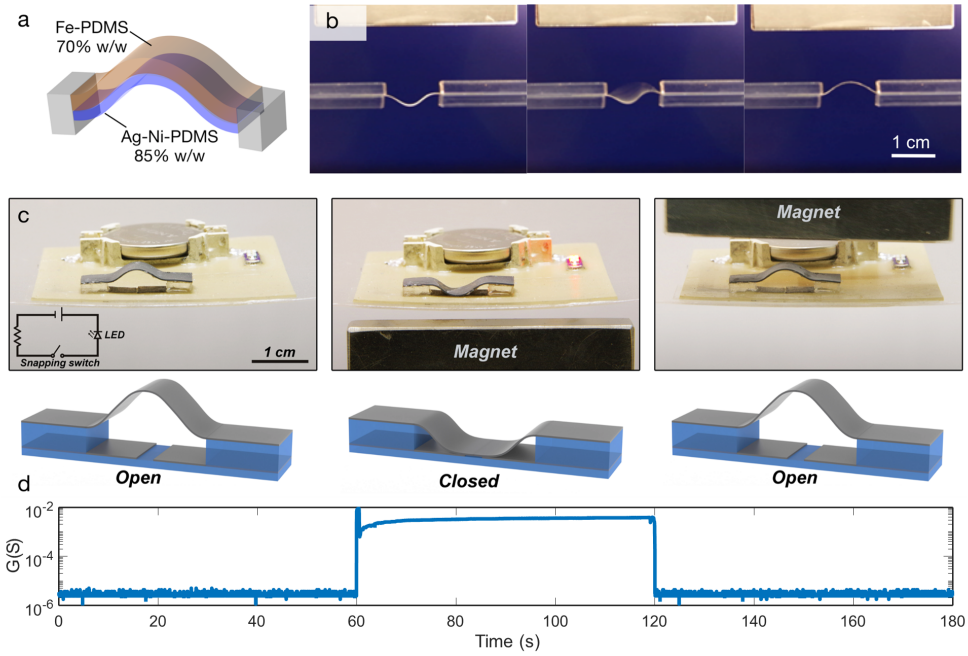

Figure 3.12: **a)** Model of the bilayered ferroelastomeric beam in a pre-buckled state **b)** Doubly clamped bistable ferroelastic beam undergoing snap through (left to right) from one stable configuration to the other under the influence of an increasing external magnetic field. **c)** Demonstration of a soft, flexible switch by magnetically snapping a ferroelastomer beam to open and close a circuit, as illustrated by turning on and off an LED. The schematics show the open and closed circuit states. **d)** Conductance (G) of the circuit as the beam is snapped in and out of a closed configuration.

In this study, a prismatic strip of MR elastomer is coated with a layer of elastomer embedded with a percolating network of Ag-coated Ni microparticles. This conductive layer functions as a "gate" electrode that controls electrical connectivity between a pair of "source" and "drain" leads. The influences of composition on the magnetic, electrical, and mechanical properties of both the ferromagnetic and conductive elastomer composites are well understood[180–183]. There has also been growing interest in applying ferromagnetic elastomers for soft robotic sensing and actuation. This includes flexural elements for bending actuation, magnetically-powered origami, and a crawling soft robot cable of field-activated "self-locomotion" [184].

We begin by presenting the methods for fabricating an MR elastomer composite and field-activated switch in which the composite beam forms reversible electrical contact with a pair of source/drain leads (fig. 1c,d). The leads are composed of liquid-phase eutectic gallium-indium (EGaIn) alloy sealed with an anisotropically conductive "z-film" elastomer that is only conductive through its thickness [185]. The response of the ferromagnetic beam to external magnetic field is found to be in reasonable agreement with theoretical predicitions based on elastic rod theory and principle of minimum potential energy. In particular, the theory can be used to predict the proximity of the magnet at which snap-through instability occurs. The following work was done in collaboration with Vivek Ramachandran and Michael D. Bartlett (then part of the Soft Materials Laboratory).

3.2.2 Experimental

The swiching element shown in fig. 1a is composed of two layers of elastomer composite. The top layer is a 80 μm thick strip of polydimethylsiloxane (PDMS) elastomer (Sylgard 184; 10:1 base-to-catalyst ratio; Dow Corning) embedded with 70% w/w Fe microparticles (spherical, diameter $<10\mu$m; Alfa Aesar). The bottom layer is 30 μm thick and composed of PDMS embedded with 85% w/w Ag-coated Ni microparticles

($\sim$15μm; Potters Industries). Both layers are prepared by shear mixing the uncured PDMS and microparticles with a stirring rod for 5 minutes. The Fe-PDMS layer is deposited using a thin-film applicator (ZUA 2000; Zehntner Testing Instruments). The elastomer is then partially cured at 70$^{\mathrm{O}}$C for 20 minutes. Next, a layer of Ag-Ni-PDMS is deposited over the Fe-PDMS film and the composite is then fully cured at 70$^{\mathrm{O}}$C for 90 minutes. The composite sheet is patterned into strips using a CO_2 laser (VLS 3.50; Universal Laser Systems). Each strip has total dimensions of $t = 110\mu$m (thickness), $L_0 = 15.4$ mm (length), and $b = 5$ mm (width). It is assumed that the dispersion of the particles is random but statistically uniform throughout the volume. Both layers are ferromagnetic and only the Ag-Ni-PDMS layer is electrically conductive. The Fe-PDMS layer functions as the magnetically-powered actuator layer while the Ag-Ni-PDMS is used as the gate electrode for electrical switching.

Switch Fabrication

The layup and fabrication method of the switch is presented in fig. 3.13. First, we prepare a thin film substrate of PDMS (300 μm) and allow it to cure at 70° C. Next, we lay down green masking tape (LaserTape; IKONICS Imaging Inc.) that is patterned with a CO_2 laser and deposit a thin film of liquid-phase eutectic gallium-indium alloy (EGaIn, 99.99% pure; Sigma-Aldrich). Removing the masking tape leaves behind 4 mm wide EGaIn traces that will function as a pair of source/drain electrodes. To prevent leakage, these liquid electrodes are sealed with a layer of Ag-Ni-PDMS conductive elastomer. Prior to curing, laser-patterned squares of conductive non-woven fabric (3M CN-3490) are placed on the surface of the elastomer, directly above the lead terminals. These will function as contact pads that make reversible electrical contact with the Ag-Ni-PDMS layer of the composite beam.

To prevent electrical conductivity between the elastomer-embedded EGaIn electrodes, a magnetic field is applied as the Ag-Ni-PDMS seal cures. This is accom-

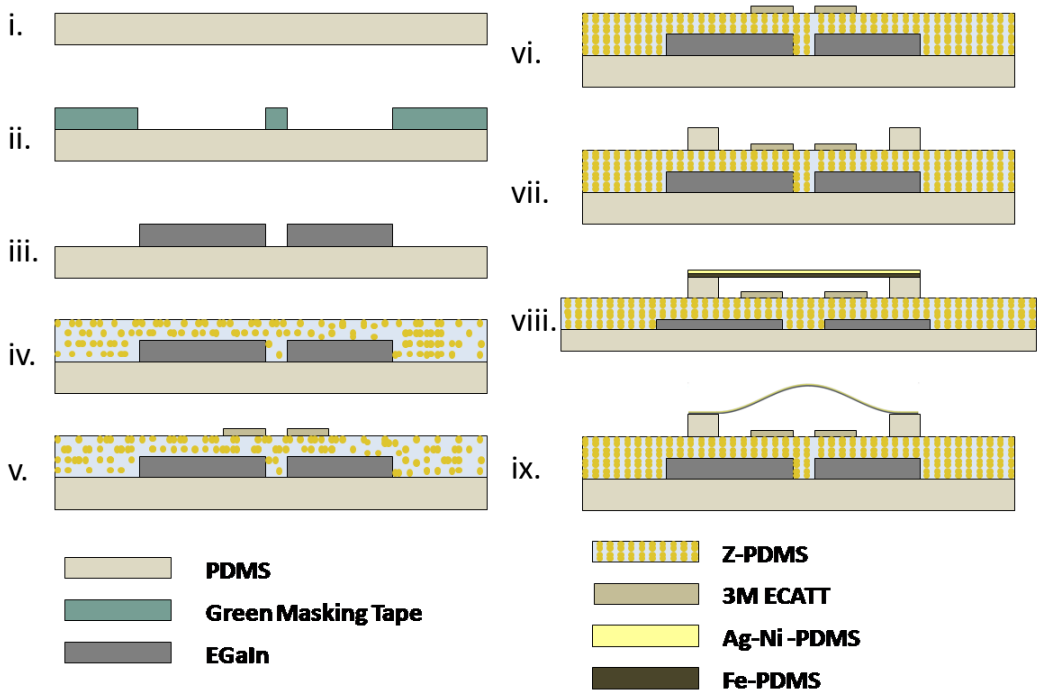

Figure 3.13: Layup and fabrication method for the switch implementation. i. Created PDMS substrate; ii. Lay down mask; iii. Apply GaIn and remove mask; iv. Apply uncured PDMS with microparticles; v. Before curing, place conductive fabric contacts; vi. Cure on magnet for particle alignment; vii. Attach PDMS posts to the substrate with Sil-Poxy; viii. Stretch the body and attach the beam to the PDMS posts with Sil-Poxy; ix. Release after Sil-Poxy has properly bonded.

plished by placing the sample above a permanent magnet (NdFeB; K&J Magnetics, Inc.) while it cures in an oven for 45 minutes at 70°C. The magnetic field causes the Ag-coated Ni particles to self-assemble into vertically aligned columns. This results in an anisotropically conductive "z-film" elastomer that is only conductive through its thickness ($\mathbf{e}_z$). A coin cell battery holder (BU2032SM-HD-G, Digi-Key Electronics Inc.) and LED (DEV-10754 ROHS, LilyPad LED Micro - Red, Sparkfun Inc.) is mounted to the surface of the Ag-Ni-PDMS seal during curing. After the seal is cured, the substrate is stretched and bonded to the ferroelastomer switch. The switch itself is composed of the ferroelastomer strip supported by two vertical PDMS posts. The posts are bonded to the pre-stretched substrate using a silicone adhesive (Sil-Poxy; Smooth-On Inc.). Once the beam is bonded firmly onto the posts, the substrate is released and the beam undergoes compression and buckling.

Critical Magnet Distance for Snap-Through

Snap-through occurs when the vertical distance d between the supports of the ferroelastic beam and the surface of an external magnet (2"x2"x1/4" NdFeB magnet; K&J Magnetics, Inc.) reaches a critical value d_{cr}. This critical separation is determined by vertically lowering the magnet towards the beam, which is initially buckled away from it. The magnet is mounted on to the travel head of a materials testing system (Instron 5969) and is lowered at a rate of 10 mm/min. The d_{cr} values are measured from a video analysis and modeling software (Tracker; http://physlets.org/tracker/) of video recordings of the beam as it transitions from one stable state to the other.

3.2.3 Principles & Theory

The snap-through instability demonstrated in fig. 3.12 can be explained by an analytic model based on elastic rod theory and the principal of minimum potential. Referring to fig. 3.14, the beam is initially straight with the supports separated by the natural

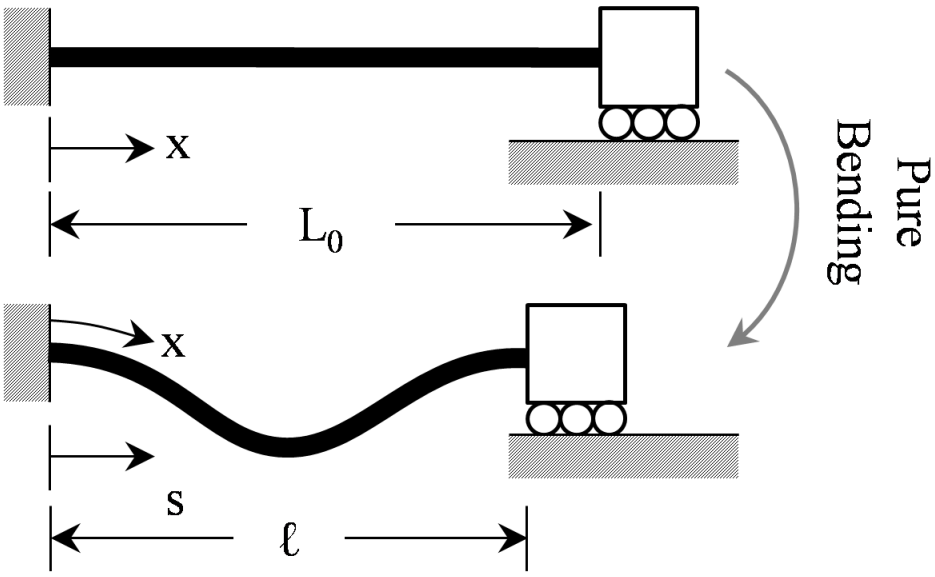

Figure 3.14: Beam deformation is described by pure bending.

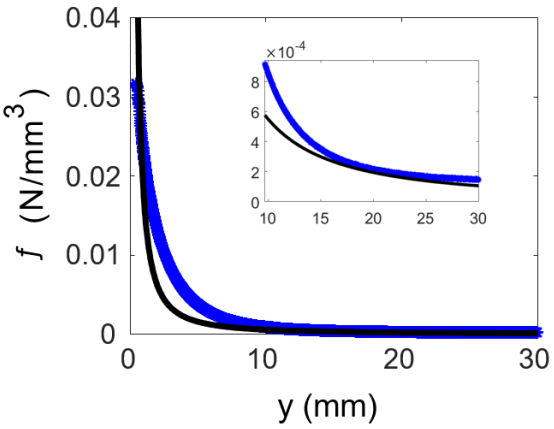

Figure 3.15: Variation in the magnetic force density f of the permanent magnet with vertical distance y from the testing face to the point of measurement, $\beta = 550$ N $\cdot$m$^{-3/2}$ is the fitting parameter. Inset: Zoomed-in region focusing on the distances in which snap-through generally occurred.

length L_0 of the beam. Next, the separation is reduced to $\ell < L_0$, which causes the beam to compress and buckle. From this pre-buckled reference state, the deflection of the beam is controlled with an external force-inducing field (eg. gravitational, magnetic, electrostatic). At each point in the beam, this field exerts a force density $\mathbf{f} = f\mathbf{e}_z$, where $\mathbf{e}_z$ is the unit vector along the beam's minor axis and f has units of N/mm^3. When the field source is located at a nominal distance y above the supports, the force density is expected to scale with y^n, i.e. $f = \beta y^n$, where β is a fitting parameter associated with the choice of the field source. In this study, a magnet is centered a distance d above the beam supports, has a N/S orientation aligned with the beam's minor axis ($\mathbf{e}_z$), and the force density is measured to scale as $y^{-3/2}$ (fig. 3.15). The value for β was determined to be 550 N $\cdot$m$^{-3/2}$ based on snap-through results. Fig. 3.15 demonstrates how this value fits with direct measurements of the distributed load (see Appendix P). Although the overall fit is not perfect, the region of interest where snap-through occurs is in good agreement.

Kinematics

Prior to buckling, the beam has a natural length L_0, width b, thickness t, and cross-sectional area $A_0 = bt$. The variable $x \in [0, L_0]$ represents the axial coordinate in the Lagrangian (natural, undeformed) description. Although the beam is composed of two layers, it is convenient to treat it as a uniform elastic rod with uniform density ρ, Young's modulus E, and flexural rigidity $D = Ebt^3/12$. Referring to fig. 3.14, beam deformation is descibed by pure bending, during which the arclength L_0 remains fixed and cross-sectional elements along the beam have a vertical deflection $w = w(x)$. For a given end-to-end separation ℓ, it is convenient to define a horizontal stretch $\hat{\lambda} := \ell/L_0$. In this way, $\hat{\lambda}$ and $w(x)$ can be related by the following isoperimetric constraint:

$$\hat{\lambda} = \frac{\ell}{L_0} = \frac{1}{L_0}\int_0^{L_0} \sqrt{1 - w_{,x}^2}\, dx\,. \tag{3.20}$$

The clamped-clamped supports also prevent vertical displacement and rotation at the ends:

$$w(0) = w_{,x}(0) = w(\ell) = w_{,x}(\ell) = 0\,. \tag{3.21}$$

The subscript $_{,x}$ denotes the derivative w.r.t. the coordinate x.

We restrict w to approximations of the form $w \approx \alpha_1\phi_1 + \alpha_2\phi_2$. Here, $\{\phi_1,\, \phi_2\}$ are linearly independent basis functions and $\{\alpha_1,\, \alpha_2\}$ are the corresponding weighting coefficients. For the basis functions, we selected mode shapes that are in qualitative agreement with experimentally observed deflections (see Appendix Q):

$$\phi_1 = \frac{1}{2}\left\{1 - \cos\left(\frac{2\pi x}{L_0}\right)\right\}, \tag{3.22}$$

$$\phi_2 = \frac{4}{3\sqrt{3}}\sin\left(\frac{2\pi x}{L_0}\right)\left\{1 - \cos\left(\frac{2\pi x}{L_0}\right)\right\}. \tag{3.23}$$

Substituting this approximation for w into (3.20) yields a relationship between the unknown coefficients α_1 and α_2.

Potential Energy

In general, the load per unit length (f_t) and total potentially energy (U) associated with the external force-inducing fields have the form

$$f_t = \sum_{\xi} q_{\xi}(d-w)^{p_{\xi}}, \tag{3.24}$$

$$U = \sum_{\xi} \int_0^{L_0} \frac{q_{\xi}}{p_{\xi}+1}(d-w)^{p_{\xi}+1} dx\,. \tag{3.25}$$

Here, q_{ξ} is the coefficient of the field load which is dependent on the flexural and material properties of the beam, d is the distance between the source of the field and the beam mid-plane, and p_{ξ} describes the dependency between the force density and the distance between the source and each point on the beam. For our system, the beam is subject to only gravitational and magnetic loading. The coefficient of the gravitational load can be represented as $q_g = \rho A_0 g$, where $\rho = k\rho_m + (1-k)\rho_e$ is the average specific density of the composite and g is the gravitational acceleration. Here, k is the mass fraction of the ferromagnetic particles and ρ_m and ρ_e are the specific density of the particles and elastomer, respectively. The coefficient of the magnetic load is defined as $q_m = \beta A_0$, which is independent of the beam deflection. For the gravitational load and the magnetic load, the values of p_g and p_m are 0 and $-3/2$, respectively.

At static equilibrium, the elastic deformation of the beam is determined by extremizing the total potential energy functional $\Pi = \Pi(\lambda, w)$. The potential Π is composed of the elastic strain energy (from bending), and the energy associated with gravity and magnetic field.

$$\Pi = \int_0^{L_0} \left\{ \frac{1}{2} D w_{,xx}^2 + q_g w - \frac{2q_m}{(d-w)^{1/2}} \right\} dx\,. \tag{3.26}$$

To obtain an approximate solution for w, we first apply the isoperimetric constraint

in order to eliminate α_1 and express w and Π only in terms of α_2. Next we determine the value of α_2 at which Π is stationary (i.e. $\mathrm{d}\Pi/\mathrm{d}\alpha_2 = 0$. Lastly, we compute the second variation ($\mathrm{d}^2\Pi/\mathrm{d}\alpha_2^2$ to determine whether the solution is stable (i.e. Π is locally minimized). Numerical solutions are obtained in MATLAB (R2016b; The Mathworks, Inc.) and an analytic approximation is obtained by performing Taylor series expansions on (3.20) and Appendix Q).

Approximation

To obtain an approximate scalar function for the potential $\Pi \approx \Pi(\alpha_1, \alpha_2)$, we substitute the expression for $w = w(\alpha_1, \alpha_2)$ into (3.26) and perform a Taylor series expansion (see Appendix Q):

$$\begin{aligned}\Pi \approx\ & \frac{D\pi^4}{L_0^3}(\alpha_1^2 + \frac{320}{27}\alpha_2^2) + \frac{L_0 q_g \alpha_1}{2} \\ & -\frac{L_0 q_m}{d^{3/2}}\left\{\frac{\alpha_1}{2} + \frac{1}{288d}\left(81\alpha_1^2 + 80\alpha_2^2\right)\right. \\ & \left. +\frac{5\alpha_1}{1152d^2}\left(45\alpha_1^2 + 112\alpha_2^2\right)\right\}. \end{aligned} \tag{3.27}$$

Next, α_1 is estimated from a Taylor series approximation of the unilateral constraint (3.20):

$$\tilde{\alpha}_1 = \pm 2\left\{\left(\frac{L_0}{\pi}\right)^2(1-\hat{\lambda}) - \frac{32}{27}\alpha_2^2\right\}^{1/2}. \tag{3.28}$$

For our analysis, the beam is initially buckled away from the source of the magnetic field and therefore, we consider the beam to have a negative value of $\tilde{\alpha}_1$.

Substituting (3.28) in (3.27), we obtain $\Pi = \tilde{\Pi}(\alpha_2)$, which must be locally convex at stable equilibrium. In the absence of magnetic and gravitational load, $d^2\tilde{\Pi}^*/d\alpha_2^2 \approx 128\pi^4 EI/9L_0^3 > 0$, which implies that the buckled shape $\alpha_1 = \tilde{\alpha_1}$, $\alpha_2 = 0$ is elastically stable. However, applying an increasing magnetic loading in the direction opposite of the deflection will cause the second variation to decrease until the stability criterion

is no longer satisfied. Of particular interest is the critical separation of the magnet from the midplane (d_{cr}) at which snap-through occurs. This is obtained by finding the solution of d to the condition $d^2\tilde{\Pi}^*/d\alpha_2^2 = 0$:

$$\begin{aligned}
&-\frac{32\pi}{27}\frac{q_m}{d^{3/2}}(1-\hat{\lambda})^{-1/2} + \frac{19}{9}\frac{q_m}{d^{3/2}}\frac{L_0}{d} \\
&-\frac{65}{18}\frac{q_m}{\pi d^{3/2}}\left(\frac{L_0}{d}\right)^2(1-\hat{\lambda})^{1/2} \\
&+\frac{32}{27}\frac{Ebt^3\pi^4}{L_0^3} + \frac{32\pi}{27}q_g(1-\hat{\lambda})^{-1/2} = 0\,.
\end{aligned} \tag{3.29}$$

3.2.4 Results

To understand the behavior of the bistable beam as it changes configuration from one stable state to the other after undergoing snap-through, it helps to examine the following cases separately: (i) deflection under low magnetic loading, and (ii) snap-through instability. For this analysis (see fig. 3.16), we used the following system parameters: $\rho_m = 8000$ kg. m^{-3}, $\rho_e = 965$ kg. m^{-3}, $k = 0.8$, $E = 5.0$ MPa (see Appendix R), $\beta = 550$ N $\cdot$m$^{-3/2}$, $q_m = 0.303$ mN m$^{1/2}$, $L_0 = 15.4$ mm, $b = 5$ mm, $t = 110$ μm, and $\hat{\lambda} = 0.9$. In fig. 3.16, the curve corresponding to the numerical solution was generated by solving (3.20) in MATLAB (R2013a; The Mathworks, Inc.) using the native *integral* and *fsolve* functions (see Appendix S). In contrast, the curve corresponding to the analytical solution was generated from the approximation for α_1 given in (3.28). Corresponding values for q_m and d are provided in the figure caption.

Sub-critical load

Prior to introducing the magnet, the beam is observed to either deflect up or down and adopt the first mode shape ϕ_1 (i.e. $\alpha_2 = 0$). This corresponds to the conventional bifurcation instability associated with compressive preload and buckling. Next,

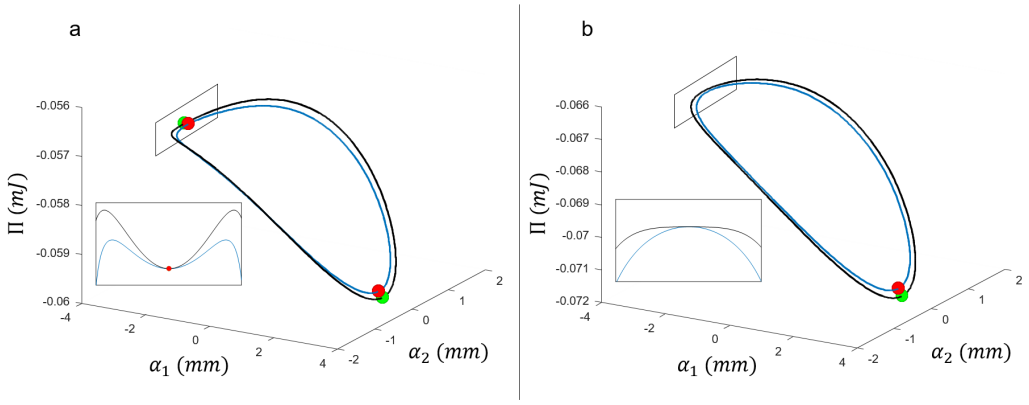

Figure 3.16: Numerical (blue) and analytical (black) results for the relative variation in the potential energy along the "valley" under **a)** sub-critical magnetic load (d = 25 mm) and **b)**post-critical magnetic load (d = 18 mm), with local and global minima indicated (numerical (red dot) and analytical (green dot)). The value of the coefficient of magnetic load is $q_m = 0.303$ mN m$^{1/2}$.

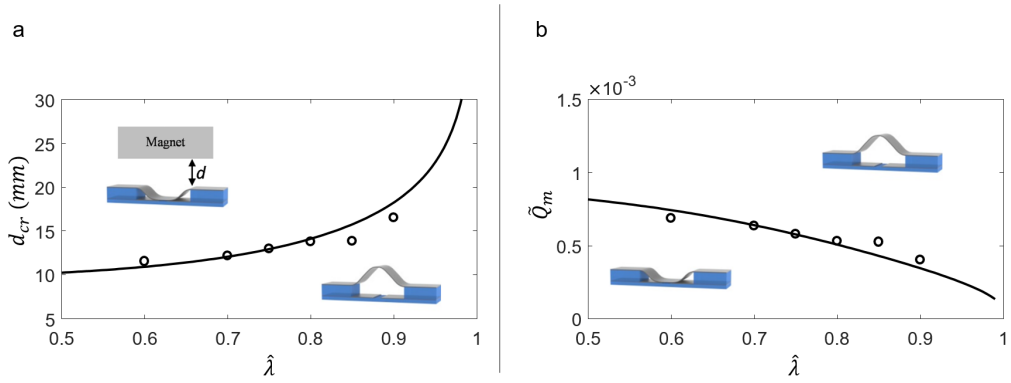

Figure 3.17: **a)** Critical distance d_{cr} versus $\hat{\lambda} = \ell/L_0$ and **b)** critical non-dimensional magnetic loading $\tilde{Q}_m := q_m L_0/EA_0 {d_{\text{cr}}}^{3/2}$ versus $\hat{\lambda} = \ell/L_0$for the analytical model (solid) and experimental calculations (markers).

suppose that a magnet is placed on the side opposite the direction of deflection. According to the approximate theory the beam will not deflect from its pre-buckled state so long as $d > d_{\text{cr}}$. However, in practice we observe a modest decrease in amplitude $|\alpha_1|$ due to the elastic compressibility of the magnetically loaded beam. Such deformation is reversible and the beam will spring back to its original deflection when the magnet is removed. As described below in Sec. 3.2.4, this sub-critical loading can be exploited for a high frequency relay in which electrical contact between the source/drain electrodes is only temporarily broken when a magnet is applied. It is important to recognize that for such applications, the theory will need to be modified to account for the unilateral contact with the electrodes.

Post-critical load

Again suppose that the beam is initially deflected away from the magnet. As the magnet is brought closer to the beam, d will eventually reach the critical separation d_{cr} necessary to induce a snap-through instability. During snap-through, α_2 becomes non-zero and the beam exhibits a linear combination of the first and second bending modes. Referring to fig. 3.16b, these transitional values of α_1 and α_2 correspond to the path along which the decrease in Π is steepest. An analogous behavior is observed

in the study of diatomic molecules, where such a transition is referred to as the lowest-energy pathway or intrinsic reaction coordinate (IRC) curve [186]. These correspond to physical "transition states" or configurations that the beam momentarily adopts as it approaches its stable state.

Fig. 3.17a shows the dependency of d_{cr} on $\hat{\lambda} = \ell/L_0$ for the analytical model. We also consider the influence of $\hat{\lambda}$ on the non-dimensionalized critical magnetic load,

$$\tilde{Q}_m := \frac{q_m L_0}{E A_0 {d_{\text{cr}}}^{3/2}} \tag{3.30}$$

where the material parameters and dimensions are prescribed (see fig. 3.17b). For given beam dimensions (L_0, A_0), elastic modulus E, and magnet distance d, it follows that stretching the beam from its buckled state (thereby decreasing the compression and consequently, increasing $\hat{\lambda}$) reduces the magnetic load required to induce snap-through instability. Also, a more rigid beam (i.e. larger EA_0/L_0) will require a greater nominal load $q_m/{d_{\text{cr}}}^{3/2}$. As shown in fig. 3.17b, the curve intersects the x-axis at $\hat{\lambda} = 1$. This arises from the assumption that the rod is inextensible/incompressible and only undergoes flexural deformation.

Switch Implementation

A principle feature of the pre-buckled ferroelastomer switch is its ability to exhibit either reversible or snap-through responses when subject to magnetic loading (fig. 3.18a). When snapping between the two stable configurations, we demonstrate the ability to reversibly switch between closed and open circuit states. In this case, the magnetic field is only necessary for switching. However, when a low oscillatory magnetic field is applied, the beam exhibits temporary and reversible deformation. In this case, removing the field causes the beam to spring back to its original deflection. This response corresponds to a higher frequency switching mode that rapidly oscillates

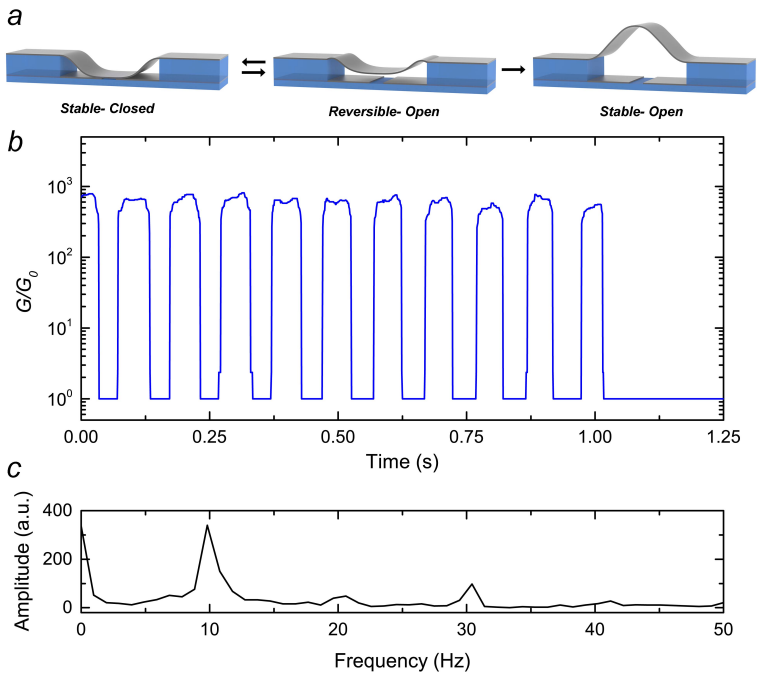

Figure 3.18: **a)** Schematic representation of the three states during fast switching. **b)** Experimental data showing fast switching between the stable-closed and reversible-open states for 1 s followed by a snap through transition to the stable-open configuration. Normalized by $G_0 = 2.44 * 10^{-6}$ S. **c)** FFT of the data in part b showing the strong peak at 10 Hz switching frequency.

between an open and closed circuit. This fast switching behavior is demonstrated in fig. 3.18b, where the switch is activated with a sub-critical magnetic field. After one second of reversible switching, the magnetic field is increased such that $d < d_{\text{cr}}$. This causes snap-through to the permanently open circuit. By taking a Fast Fourier Transform (FFT) of the conductivity data (fig. 3.18c), we see a strong peak at 10 Hz, which corresponds to the magnetically-controlled switching frequency. This frequency was limited by our experimental setup, and further investigated into the limits of the high frequency switching could be explored by varying geometry and material parameters.

3.2.5 Discussion

In this work, we demonstrate an implementation of a switching element in a flexible circuit by utilizing the buckling instabilities of a bistable ferroelastomer beam. For a given set of material and dimensional properties, the behaviour of the beam is studied for a variety of magnetic loading conditions. Depending upon the operational requirements of the switch, there are certain considerations that need to be accounted for while designing and fabricating the beam for the switching element. For example, the elastic modulus E of the beam is influenced by the volume fraction of rigid microparticles and the modulus of the elastomer matrix. In particular, it follows from (3.29) that d_{cr} decreases with modulus. This is consistent with physical observation – more rigid beams are more resistant to snap-through instability.

It is also expected that as $\hat{\lambda}$ decreases, the amount of magnetic load required to induce snap-through also increases for the same nominal gap. This is supported by the experimental results shown in fig. 3.17 and suggests that a switch will become less resistant to snap-through as the buckling induced compression is reduced. When the non-dimensional magnetic load exceeds $\tilde{Q}_m$, the beam will undergo snap-through. Below this value, the deflection is reversible, i.e. the beam will return to its original

shape when the magnetic field is removed. This has important implications when selecting thresholds for the magnetic loads used to excite reversible and permanent switching responses.

The pre-buckled ferroelastomer beam bears some resemblance to switch designs used in the microelectromechanical systems (MEMS). In MEMS, actuation schemes can broadly be classified into the following categories: electrostatic, piezoelectric, thermomechanical, and electromagnetic. Despite its immense popularity and low power consumption, electrostatic actuation requires high pull-in voltages and generally results in small displacements. Alternatively, thermomechanical loading is capable of generating large displacements with high forces, but its power requirements are correspondingly large for slow response rates. Piezoelectric actuation is promising but required rigid materials that are no capable of being strtetchable. In contrast, electromagnetic actuators are capable of rapidly producing adequate forces and displacements with relatively low mechanical work input and can be produced with soft materials. Here, we show that such low power functionality can be accomplished with bistability and the use of a permanent magnet.

3.2.6 Conclusion

I have introduced a soft reconfigurable electrical contact that utilizes magneto-flexural coupling and snap-through instability. This switch is composed of a pre-buckled ferroelastomer strip that deforms in response to an external magnetic field. It exploits snap-through mechanics in order to transition between an open and closed-circuit configuration. For low magnetic loads, there is a second switching mode – the circuit is only temporarily opened when field is applied and returns to being closed when field is removed. The switch response is explained with an analytic model derived by applying the Rayleigh-Ritz method to examine the static equilibrium of a ferromagnetic elastic rod. A key result of this analysis is a stability criterion that

relates a non-dimensional critical magnetic load for snap-through $\tilde{Q}_m$ with the ratio $\hat{\lambda} = \ell/L_0$ of the support separation and beam length. Despite the success shown here and in the previous sections, electrostatic and magnetic actuation have limitations which make them less practical for switch implementation. Particularly at the scales presented in this work, the former still require hundreds of volts and the later requires power-hungry electromagnets or bulky magnets (which then have to be actuated). Approaching the problem from a new angle, the next chapter discusses an electrochemical solution to soft-matter switching.

Chapter 4

Field-controlled electrical switch with liquid metal [5]

The devices shown in the previous sections required high voltages for electrostatic actuation or bulky/power-hungry field sources for magnetic actuation. Furthermore, stiction, capillary forces, and other surface energies may be detrimental to many soft switches due to scaling. However, these surface phenomena can be leveraged for liquid-based systems to achieve actuation. The most prevalent is electrowetting on dielectric, but more recently the application of voltages to liquid metal droplets in electrolytic solution has emerged as a unique method for reconfiguration at voltages often below 10V [75, 77, 187, 188]. Here, we apply such manipulation to create a bistable switch. The first section discusses the driving factors and provides a theory for prediction system behavior. Second, the phenomena is applied to multiple droplets in a single bath and to a switching circuit.

4.1 Coalescence and Separation of Liquid Metal

Coalescence and separation of liquid droplets are typically governed by fluidic instabilities that arise under static [189, 190] (e.g. liquid bridge separation) or hydro-

dynamic [191–194] (Rayleigh instability) conditions. While much is already known about their role in fluid mechanics (e.g. capillary bridges, continuous jets, droplet-to-droplet impacts), there has been relatively little study of how these instabilities can be harnessed to control droplet interactions in electrochemical systems. Of special interest is the reversible coalescence and separation of liquid droplets through electrowetting or electrochemistry under voltages of ∼1-10V. Such an ability could enable field-programmable microfluidics that can be directly operated with conventional microelectronics and power supplies. Moreover, it provides an opportunity to further explore the interplay between interfacial tension, geometry, and fluidic instabilities through spatial control of interfacial energies.

Several examples of digital microfluidics and liquid-based switches exist in the literature, though most demand high voltages for conventional electrostatic techniques [195–199] or activate under outside influences such as environmental corrosion of oxide [200]. Referring to fig. 4.1, low-voltage-controlled coalescence and separation is accomplished with a pair of liquid metal (LM) droplets immersed in a basic aqueous electrolytic solution. The droplets are anchored to copper pads (referred to as the gate and drain) via alloying. Voltages are applied at these electrodes as well as at two outer copper pads (referred to as the counter and gate) to achieve switching behavior. Like traditional field-effect transistors, on/off states can be manipulated with the input of electric fields, and a gate-source threshold voltage must be met to achieve off-to-on switching (coalescence). In contrast to transistors, this system involves the physical reconfiguration of LM contacts rather than the rearrangement of electrons and holes, and separation requires a fourth (counter) electrode that likewise has gate-source-counter voltage requirements. Conductance between the source and drain changes by over 3 orders of magnitude depending on whether or not the droplets are coalesced.

The LM is a eutectic Ga-In (EGaIn) alloy, which forms a Ga_2O_3 surface oxide in

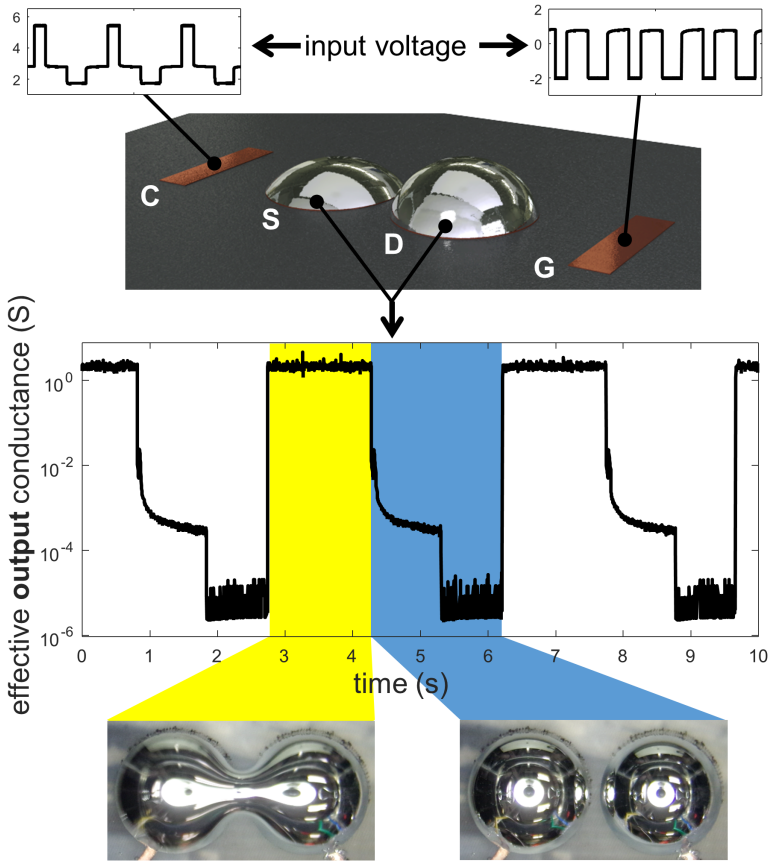

Figure 4.1: Overview of the "liquid metal transistor". Top image: Layout of key electrodes, including the counter (C), the source (S), the drain (D), and the gate (G). The source and source are wetted with EGaIn. The inset plots refer to the input voltage (relative to the source at ∼0.85V) to achieve coalescence and separation. Bottom plot: The measured equivalent conductance across the source and drain, varying by over 3 orders of magnitude depending on whether or not drops are coalesced (bottom left) or separate (bottom right).

aqueous basic environments when placed under an oxidative potential. When such a potential is applied directly to the source electrode (relative to the gate), the associated LM spreads, contacts, and coalescences with the neighboring droplet (fig. 4.2a). On the other hand, a voltage applied across the gate and counter causes separation under the influence of an oxide-controlled gradient in interfacial tension (fig. 4.2b). The latter involves two stages – geometrically-constrained droplet deformation during electrochemical oxidation (fig. 4.2c) followed by capillary bridge separation. This fluidic instability corresponding to a limit-point in the locus of solutions to the governing Laplace equ. (fig. 4.2d). Such solutions represent the critical point of an energy functional (Π) that accounts for both the interfacial gradient and the incompressibility of the fluid.

This unique approach to controlling liquid droplet interactions builds on new insights in EGaIn electrochemistry and LM-fluid interactions. When immersed in a 1M NaOH(aq) solution, voltage-controlled (<10V) oxidation leads to a dramatic decrease in effective interfacial tension [77]. Under gravity, the droplet will flatten, which we harness here to bring the droplets closer together and ultimately coalesce. Previously, these and similar low-voltage electrochemical methods for manipulating LM have been studied for achieving drastic surface area changes [201–203], device reconfiguration [187, 204], tunable antennas [205], and light valving [206]. While LM droplet coalescence has been studied in water with reductive voltages [202] and in NaOH solution without applied current (spontaneous coalescence) [207], this work focuses on the controlled use of oxidative potentials to achieve this goal. Furthermore, the method for separation harnesses a novel electro-capillary instability driven by oxide-induced interfacial tension gradients that has not before been demonstrated in the literature. In addition to providing experimental evidence and insights into these interface phenomena, we show how such field-controlled droplet interactions can be used for gated logic. This "liquid metal transistor" (Fig. 4.1) represents the first demonstration of

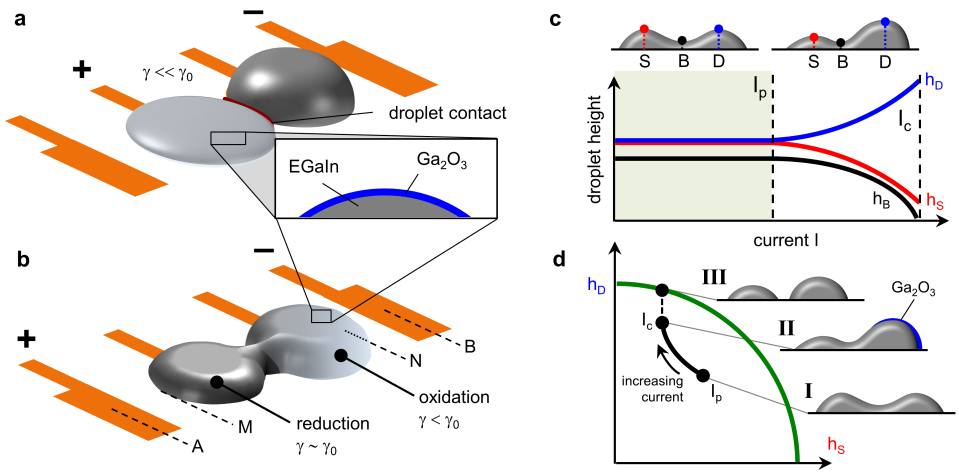

Figure 4.2: Summary of droplet coalescence and separation behavior. A) An oxidative potential is applied at the source electrode while the gate is negative. This causes spreading of the source EGaIn. Contact and coalescence occur between the source and drain. Positions A, B, M, and N are relevant for equ. (4.2). B) A positive voltage is applied at the counter relative to the gate. Oxidation occurs on the anodic pole of the EGaIn and reduction occurs on the cathodic pole, causing a gradient of interfacial tension which eventually makes the system unstable. C) Droplet and bridge height as a function of current when voltage is applied across the counter and gate electrodes. Blue (h_D) is the drain side, red (h_S) is the source side, and black (h_B) is the bridge. D) Heights of LM over the source and drain pads. The green curve follows the heights when drops are separated (limited by volume), and the black curve follows the heights when the drops are coalesced and as current is applied across the outer electrodes.

a reversible, bistable fluidic switch that conducts DC electricity and can be operated with low voltage (<10V). Although not practical as a replacement for solid-state transistors, it nonetheless demonstrates the ability to create field-programmable fluidics that are controlled by conventional electrical circuitry.

4.1.1 LM interfacial tension

The phenomena in fig. 4.1 and 4.2 are governed by underlying principles of LM interfacial tension and electrochemistry. In an oxygenated environment, droplets of EGaIn form a self-passivating Ga_2O_3 skin[30]. When removing the oxide in a bath of NaOH(aq) or HCl(aq), the liquid metal becomes a Newtonian fluid with high interfacial tension ($\gamma^* \sim 0.5$ J/m^2). In this reduced state, a droplet of EGaIn will equilibrate into an energetically stable shape (volume Γ [m^3]) that minimizes a free energy potential Π [J] subject to geometric constraints. Of special interest here is the case when the droplet wets the surface of a copper electrode through metallic alloying – this alloyed region remains of constant area and interfacial energy. The EGaIn-NaOH solution interface $\mathscr{S}$ [m^2] is then the only surface relevant for calculating potential energy. The equilibrium shape Γ corresponds to a critical point of the energy functional

$$\Pi = \oint_{\mathscr{S}} \gamma \, dA + \int_{\Gamma} (\rho_G - \rho_S) g z \, dV, \tag{4.1}$$

which accounts for interfacial and gravitational energy while remaining subject to the isoperimetric constraint $\int_\Gamma dV \equiv \mathscr{V}$. Here, γ is the interfacial tension at the LM-solution interface, ρ_G is EGaIn density, ρ_S is surrounding solution density, g is gravitational acceleration, z is the height of a point inside the droplet, and $\mathscr{V}$ is the prescribed fluid volume.

The surface oxide is restored when a voltage (Φ) that exceeds the oxidative poten-

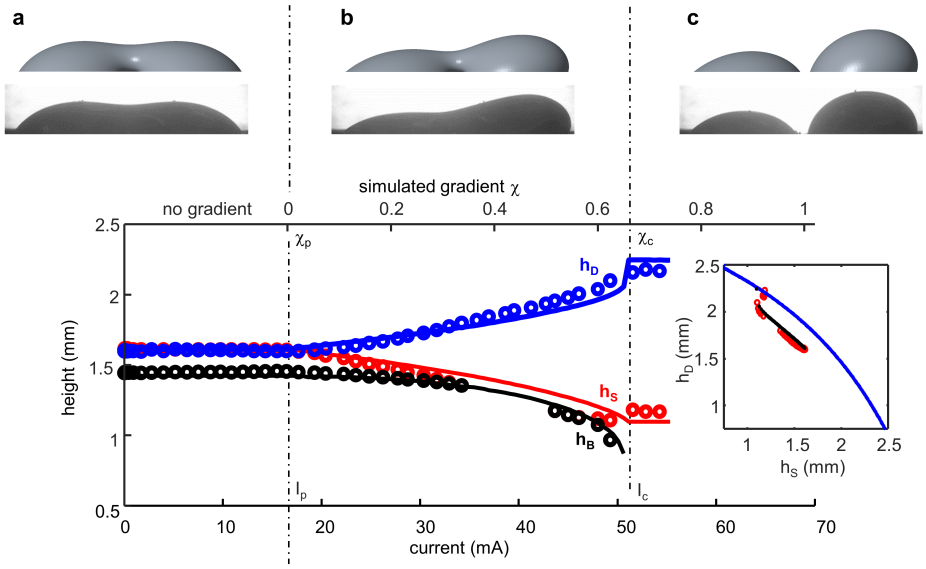

Figure 4.3: Comparison of Surface Evolver surface tension gradient simulation (plotted as solid lines) to experimental photos (plotted as circular points). a) No gradient. b) Just prior to separation. c) Just after separation.

tial (Φ_O) is applied across the LM-solution interface. This occurs during coalescence (figs. 4.2a). Oxide deposition lowers the interfacial tension, which can be roughly approximated by the scaling $\gamma \sim \gamma^* e^{-\Phi/\Phi_O}$. In addition to drastically lowering the tension, surface oxidation increases with greater proximity to the counter electrode due to increased current flow. This results in an interfacial tension gradient and spatial dependency $\gamma = \gamma(\mathbf{X}; \Phi)$, where $\mathbf{X} \in \mathscr{S}$ represents the coordinates of points at the LM-solution interface. Substitution into equ. (4.1) results in a Dirichlet energy functional that can be minimized using computational techniques. We utilize Surface Evolver[208], which uses a gradient descent method to solve this functional and has previously been used to study liquid metal solder[209–211]. For our problem, $\gamma(\mathbf{X}; \Phi)$ must be input manually since the software does not model voltage gradients or electrochemical interactions.

When brought into contact, EGaIn droplets wetted to two separate electrodes can coalesce and form a stable liquid bridge. For the configuration shown in fig. 4.2,

this requires adequate fluid volume for a given center-to-center electrode spacing s and pad diameter D. To initiate contact, an oxidative potential is applied between one of the droplets and the gate electrode, located opposite the neighboring droplet. This voltage drop causes the oxidizing droplet to preferentially spread towards the gate and thus towards the neighboring EGaIn wetted to the drain pad. Once the two droplets are in nominal contact, they coalesce under the influence of interfacial tension. With the oxidative potential switched off and in the presence of NaOH solution, oxide will be removed and the interfacial tension will increase, though this process can be hastened with a brief ($\leq$ 1s) reductive potential applied directly to the metal droplet.

Gradients in interfacial tension can also be induced by applying a current across the EGaIn from two outer electrodes that are not in direct contact with the LM (fig. 4.2b). Oxidation and reduction occur on the anodic and cathodic poles of the metal, respectively, once a critical end-to-end (point M to point N in fig. 4.2b) voltage drop ($\Delta\Phi_p$) is achieved. Beyond this point, the levels of oxidation and reduction can be tuned by adjusting the applied potential. This phenomenon is referred to as bipolar electrochemistry[212, 213]. It is not limited to liquid metal and has largely been studied with solid metals for creating janus and striped particles[214], generating motion via gas production[215], and growing gradients of material[216, 217]. This bipolar redox has been previously observed with GaIn as a growth of gallium oxide on the anodic pole, though it typically behaves as a hindrance to droplet motion [75, 218] and pumping [76].

Since the experiments were performed in a bath, the voltage drop ($\Delta\Phi$) from M to N and the current (I) across the outer electrodes are related by the following impedance law:

$$\Delta\Phi = \frac{I}{2\pi\sigma}\left(\frac{1}{\ell_{AM}} - \frac{1}{\ell_{BM}} - \frac{1}{\ell_{AN}} + \frac{1}{\ell_{BN}}\right). \tag{4.2}$$

This model accounts for Faradaic impedances at the electrodes, caused by mass trans-

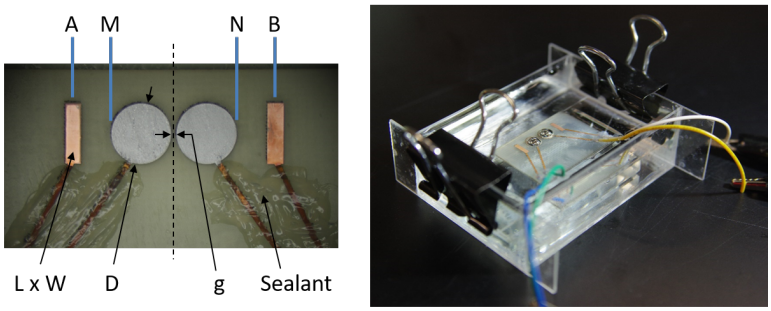

Figure 4.4: Sample layout and general testing bath. (a) Electrode orientation and dimensions. (b) Testing bath.

port and electron transfer [219]. Here, σ is the solution conductivity and ℓ_{ij} for $i \in A, B$ and $j \in M, N$ represent the distances between the outer electrodes (A,B) and an intermediate pair of points (M, N), as marked in fig. 4.2b. This approach is adapted from techniques in geophysics to interpret vertical electrical sounding data [220–222] (also used for measuring resistivity of semiconductor germanium [223]). With equ. (4.2), one can predict the required current to achieve the necessary potential drop $\Delta\Phi$ for a specific level of bipolar redox. The use of current also avoids any ambiguities related to the dramatic voltage drops near the electrode interfaces due to Faradaic impedances.

4.1.2 Methods

Sample Layout and Fabrication

Test samples were fabricated on standard copper clad board (0.5 oz. FR4) using a commercial UV laser patterning system (LPKF, ProtoLaser U3). As seen in fig. 4.4, samples are symmetric and consist of two outer rectangular pads of dimensions L x W and two inner circular pads of diameter D. Note that the two circular pads are silver/gray due to alloying with GaIn. Conductive pathways leading away from the electrodes were insulated with Sil-Poxy (Smooth-On) or Loctite Quick Set Epoxy. Standard wiring was soldered to copper contact pads (also insulated with adhesive)

for interfacing with external electronics. The base design comprised the following dimensions: D = 5.642 mm (pad surface area of 25 mm^2), W = 1.5 mm, L = 5.642 mm, G = 0.5 mm, and length from A to B l_{AB} = 19 mm. Two droplets of GaIn from an 18G dispensing needle and one drop from a 25G needle, amounting to a volume of approximately 51 mm^3 (droplet volume methods are described in Appendix T), were used for the base design. Parametric testing consisted of varying only lAB (outer electrode separation) and scaling the entire device (including GaIn volume) while keeping the NaOH weight to volume concentration constant at 1%. When testing for NaOH concentration effects, the base dimensions were used.

Testing baths were constructed out of four 25 x 75 mm and one 50 x 75 mm glass slides. Sil-Poxy or Loctite Epoxy was used to adhere and seal the edges, forming a box (fig. 4.4) suitable for taking side profile videos and images without distortion. The FR4 samples were adhered to 50 x 75 glass slides, allowing a snug fit in the baths, preventing twisting. A 2" x 1" x 0.25" streak plate (United Scientific) was used as a spacer between the bottom of the bath and the sample (preventing poor alignment due to sealant along the edges of the box). Binder clips were used to pin the sample in place. To create the appropriate solution concentration of sodium hydroxide, NaOH pellets (BDH9292, VWR) were added to deionized water (3190K731 , McMaster-Carr), mixed, and allowed to dissolve.

Droplet Control and Electrical Monitoring

For the characterization experiments, an Arduino UNO R3 microcontroller was used in conjunction with three shields (see fig. 4.5). Voltage was supplied by a dual DC power supply (Hewlett Packard) and controlled (V_{in}) with a Power Digital to Analog Converter (DAC) Shield (Visgence, Inc.). Second, an Extended Analog to Digital Converter (ADC) Shield (Mayhew Labs) was used to measure voltages (A#). Lastly, a custom shield was designed and fabricated to provide additional control and signal

conditioning. The custom shield contains 3 solid state relays (SSR#) (CS128, Coto Technology) for directing voltage application to 3 of the 4 electrodes (Counter C, Source S, Drain D, and Gate G) associated with the liquid metal switch (the gate is always grounded). To acquire data on current, the voltage across a 1 ohm shunt resistor (R4) was amplified by an instrumentation amplifier (IA) (AD623BRZ-R7, Analog Devices Inc.). The associated gain could be adjusted during testing with a digital rheostat (AD5270BRMZ-100, Analog Devices Inc.). The DAC, ADC, and rheostat were all controlled using serial peripheral interface (SPI) communication through the Arduino. Simple digital signals (d#) from the Arduino controlled the chip (LTC1859, Linear Technology) associated with the Extended ADC Shield allowed for 16-bit resolution and a range of $\pm$10V but was limited by an internal input resistance of 42kΩ for unipolar measurements and 31kΩ for bipolar. As a result, a quad operation amplifier (op amp) buffer (AD8244BRMZ, Analog Devices Inc.) was added to the custom shield to produce low impedance outputs, thus avoiding measurement inaccuracies due to voltage divider effects within the ADC. The entire system was controlled with a custom MATLAB graphical user interface.

Voltage was first applied to the source electrode ($\sim$2.5V) to induce spreading and coalescence (while the gate was always grounded). In most cases, a brief ($\sim$1 sec) reductive voltage ($\sim$-3V) was applied to the source electrode to hasten the removal of oxide immediately after coalescence. This was especially useful for low NaOH concentrations (0.1% or 0.5%) but was detrimental to successful coalescence at higher concentrations (5%) as the snap back motion was rapid enough to cause separation. Next, the voltage applied to the counter was increased in approximately 0.1V increments every second until the droplets separated or until the upper limit of the equipment ($\sim$8.5V for $\pm$10V input to the DAC) was reached. After, the voltage applied to the counter was reduced to 0V. The voltages applied at all 4 electrodes and the supplied currents were recorded at 250Hz.

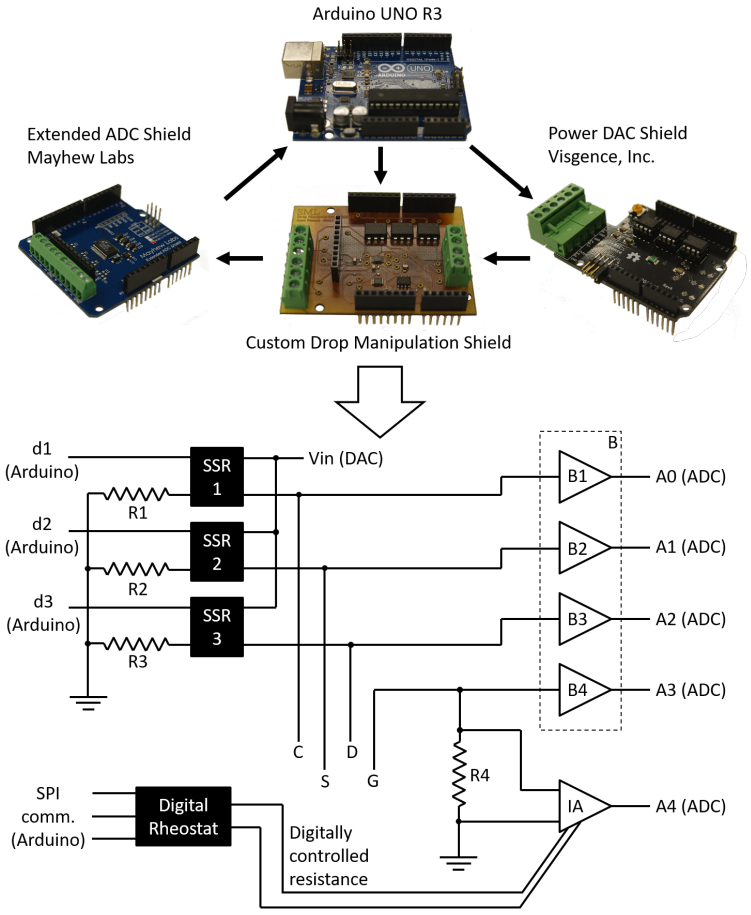

Figure 4.5: Top: Photographs of the Arduino and three shields. Bottom: Simplified circuit diagram of the custom shield. SSR Solid state relay. B Quad op amp buffer. IA Instrumentation amplifier. d# Digital input from Arduino. A# Voltage to be measured. R1-3 330Ω current limiting resistors. R4 1Ω shunt resistor. C Counter electrode. S Source electrode. D Drain electrode. G Gate electrode.

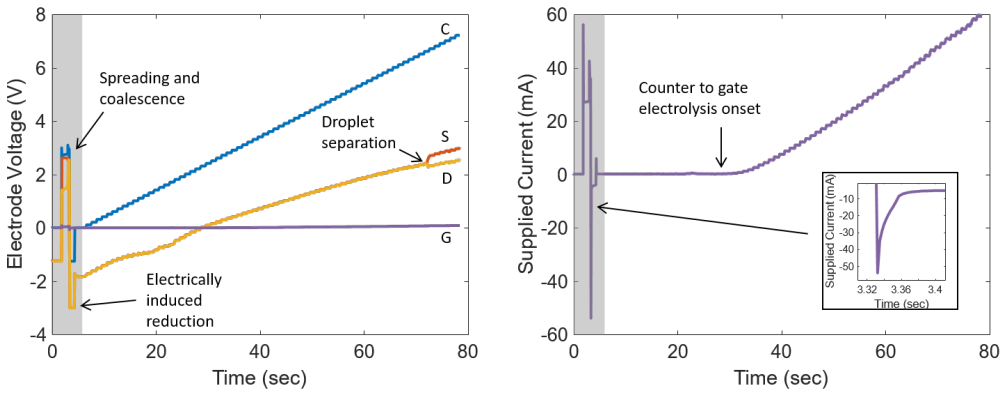

Figure 4.6: Raw voltage and current readings. The gray areas indicate times when spreading and brief reduction is occurring for the coalescence process. Left: Voltage as a function of time for the counter (C), source (S), drain (D), and gate (G). Right: Current as a function of time for the system. The inset is a zoomed-in plot for a current spike.

An example of time versus voltage and time versus current is shown in fig. 4.6. The voltage of the source and drain are initially below 0V due to the difference in electrode potential between EGaIn and copper. Oxidation for coalescence and reduction for oxide removal correspond to the first spikes in the plots. Afterwards, the counter electrode increases steadily in voltage. At approximately 2.1V, electrolysis begins across the counter and gate. Next, droplet movement initiates, though there is clear indication in the electrical data. Instead, data from profile videos must be used to determine motion timestamps. While coalesced, the source and drain are approximately equipotential. After separation at a counter electrode voltage of 6.6V and a supplied current of 50.9 mA, the source and drain voltage diverge due to the significant NaOH resistance now separating them. This feature was used to automate the detection of droplet separation.

Current across the 1 ohm shunt resistor is also plotted in fig. 4.6. From this data, the onset of electrolysis across the counter and gate electrodes can be detected. This data is correlated with voltage data and video data to extract critical currents for movement and separation. There are also spikes and approximately exponential

decays in current that can be identified, indicating the presence of capacitive effects. Since these spikes were not observed when replacing the sample/NaOH bath with resistors, it can be concluded that the capacitance is a result of the formation of a double layer at the surface of the liquid metal. Changing potential rapidly causes a current spike as the double layer capacitor discharges.

4.1.3 Results

Experimental and theoretical results are presented in figs. 4.3 and 4.7. The analysis suggests that the kinetics of oxide growth/removal and droplet motion are influenced by geometry ($\mathscr{V}$, s, D), electrical stimulation (Φ, I) and the electrolytic concentration. Following Faraday's electrochemical laws, greater current increases the oxide growth rate while the solution simultaneously etches away the oxide layer. Current can most easily be adjusted by changing the applied potential, although pad geometry and EGaIn volume can also have an impact. Additionally, the NaOH concentration influences the impedance relationship since it dictates the solution conductivity (σ). Understanding these relationships is important for controlling droplet interaction. In the case of coalescence, if Φ is too small, the LM droplet deformation may be insufficient to induce contact. With too much potential, the oxide growth will be excessive, either providing mechanical resistance to droplet deformation or preventing coalescence even after contact. Also, adequate time is required to allow the droplet to spread and make contact. If the spreading period is too long, the liquid metal might make unwanted contact with the outer electrodes or undergo viscous fingering.

To separate the droplets, a voltage is applied across the counter and gate electrodes. First, we observe (fig. 4.3a) that movement does not initiate until a critical current value I_p (corresponding to $\Delta\Phi_p$) (also see Appendix U). This behavior is reminiscent of electrolysis onset and runs counter to continuous electrowetting (discussed below), which theoretically should have no critical value. We next observe that the

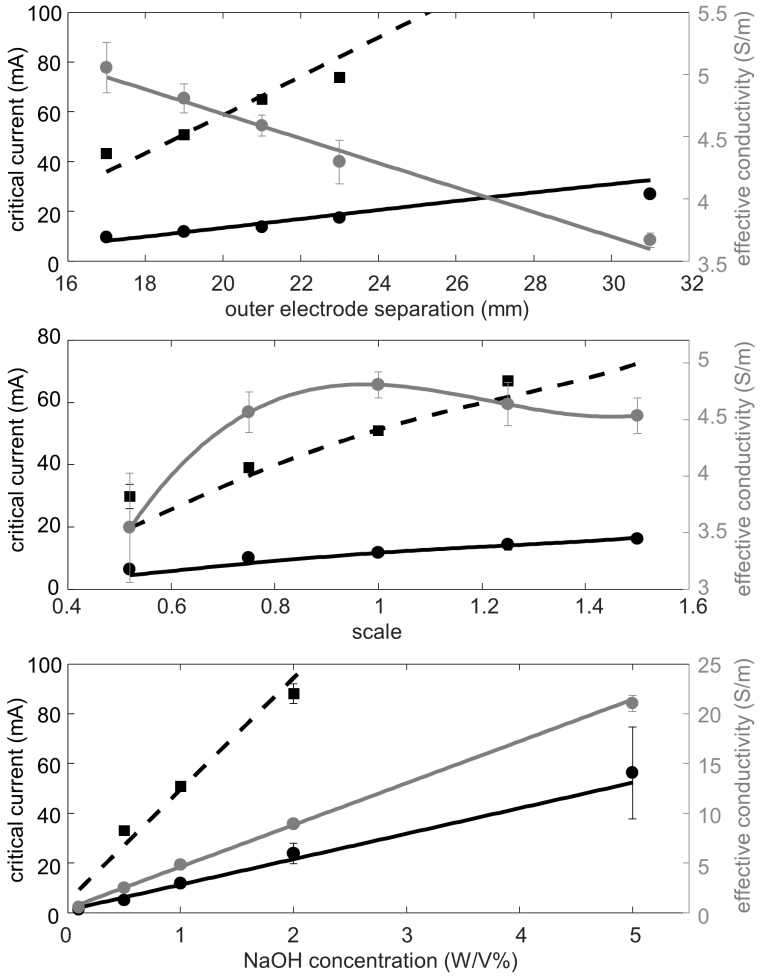

Figure 4.7: Results concerning droplet separation. Experimental data for movement onset I_p (circular) and separation I_c (square) are plotted as points. Theoretical values for movement (solid black) and separation (dashed black) are plotted as lines. The grey points are effective conductivity values fit with a functions (grey lines). Data is reported as a function of outer electrode (gate and counter) separation, overall scale, and NaOH concentration.

coalesced drop shifts towards the grounded gate, which in this case is acting as the cathode (fig. 4.3b,c). This is, again, in contrast to what is typically seen in continuous electrowetting, during which EGaIn droplets in an NaOH solution move towards the anode[75, 218]. Thus, we conclude that bipolar electrochemistry and oxidation must be the driving factor in our experiments. Oxide growth on the anodic pole (facing the gate/cathode) causes the a dramatic lowering of interfacial tension in the affected area while reduction on the cathodic pole (facing the counter/anode) causes interfacial tension to remain high. To minimize the energy of the system, the liquid metal shifts to lower the surface area of the cathodic pole while the area of the anodic pole grows. Alternatively, this behavior can be explained with the Young-Laplace equation, maintaining a constant change in pressure by increasing the mean curvature where interfacial tension is low and decreasing the curvature where interfacial tension is high. If the interfacial tension gradient is sufficient, it becomes more energetically advantageous to have separate drops, breaking the bridge (at I_c and $\Delta\Phi_c$).

To further understand the influence of the interfacial tension gradient on a set of coalesced drops, we ran simulations with Surface Evolver. Our simulation begins with droplets coalesced and in an equilibrium configuration, as seen experimentally. A linear surface energy gradient is then applied, decreasing a normalized surface tension from $\hat{\gamma} = 1$ on one side (M) to $1 - \chi$ on the other (N) ($\hat{\gamma} = \hat{\gamma}(x, \chi)$). As χ increases, the volume shifts towards the side with lower surface energy. At a critical value χ_c, the liquid separates into two droplets. As seen in fig. 4.3, the simulation is qualitatively very similar to what we observe experimentally. The gradient χ represents the constant slope of the imposed surface energy gradient as a function of x (distance from end to end). Experimentally, a supplied current I (or voltage Φ) produces a particular interfacial tension gradient that, while certainly not linear, can be compared qualitatively to χ. Thus, the critical current I_p corresponds to $\chi_p = 0$ for the onset of bipolar electrochemistry, and the critical value I_c corresponds to χ_c

for droplet separation. I_p is approximated experimentally by observing the onset of droplet motion. I_c and χ_c mark the limit-point instability of the system in which the bridge formation is unsustainable.

Reasonable agreement between theory and experiment is also demonstrated in fig. 4.7, which compares predictions from the bipolar electrochemistry model (using equ. (4.2)) with measurements taken during droplet separation. The plots show the effective conductivity and the electrical current supplied to the bath to initiate droplet motion and to cause separation as a function of outer electrode separation (ℓ_{AB}), length scale (scaling pad dimensions, distances, and GaIn volume, but not bath volume), and NaOH concentration. The onset of droplet motion as a metric for bipolar electrolysis onset assumes that movement only occurs when the interfacial tension has been significantly changed by the growth of oxide – an approximation that overestimates current required for bipolar electrolysis since low levels of redox may occur prior to detected motion. Critical values $\Delta\Phi_p$=0.165V and $\Delta\Phi_c$=0.72V were determined experimentally for the reference configuration of outer electrode separation 19 mm, scale 1, and 1% NaOH. These two critical values were used to create curves predicting the movement and break current, respectively.

The distance between the electrodes affects the response of the liquid metal to potential. For example, as the outer electrodes are further separated, the required critical currents for movement and droplet breaking both increase. This is well explained by the theory: the current must flow through a greater length of solution, decreasing the overall electric field strength. Thus, a greater current must be supplied across the counter and gate electrodes to reach the critical $\Delta\Phi$. Like outer electrode separation, increasing scale increases distances, thus increasing the required currents for both movement and separation. It was also assumed that bipolar electrolysis and separation occurs at the same $\Delta\Phi_p$ and $\Delta\Phi_c$, regardless of NaOH concentration. (This is particularly over-simplified for $\Delta\Phi_c$ since concentration influences both electrolysis

rate and the non-voltage induced reduction rate of gallium oxide, thus influencing the interfacial tension gradient.) As indicated by equ. (4.2), a decrease in resistivity should result in an equal increase in required current. (Additional data on power usage and Surface Evolver script are included in Appendices X and Y).

4.1.4 Discussion

The results presented in figs. 4.3 and 4.7 show that applied electrical current, geometry, and electrolytic concentration all have an important role in motion and separation of the coalesced EGaIn droplets. In addition to providing validation for the underlying principles related to equs. (4.1) and (4.2), the experimental measurements suggest that a "LM transistor" could be tailored to respond to a prescribed electric input. For example, closer outer electrodes and smaller scales result in a lower required current for droplet separation.

The effective conductivities reported in fig. 4.7 account for boundary effects due to finite bath size. Experiments were performed in baths of dimensions 50x75x$\sim$17 mm, but equ. (4.2) assumes an infinite half space of uniform conductivity. Thus, conductivity measurements (Appendix V) do not account for areas of essentially infinite resistance and underestimate the true value. However, these effective conductivities coupled with equ. (4.2) more accurately describe the voltage distribution within the bath. Linear fits were applied to the outer electrode separation and NaOH concentration conductivity data, while a cubic polynomial was fitted to the scale conductivity data (see Appendix V.)

There is also a key difference between the two critical voltage drops $\Delta\Phi_p$ and $\Delta\Phi_c$. $\Delta\Phi_p$ is geometry-invariant in the sense that, regardless of outer electrode separation or scale, it should always mark the onset of bipolar electrolysis. The voltage distribution between the endpoints does not influence the fact that redox occurs. On the other hand, $\Delta\Phi_c$ is a less accurate approximation because separation *is* dependent

on the voltage distribution between the endpoints. The same $\Delta\Phi_c$ may be reached for multiple geometries, but the voltage distribution will differ for each, resulting in differing areas oxidation and reduction and differing interfacial tension gradients. In other words, separation occurs when an adequate interfacial tension gradient is achieved, and $\Delta\Phi_c$ provides an approximation for when this gradient is reached.

Experimental deviation from theory was minor and generally explicable. Limitations in our testing circuit (<10V and <100 mA) prevented droplet breaking at the pad distances greater than 23 mm. Moreover, it is still clear from the top plot in fig. 4.7 that the theory (which uses critical voltage drops tailored for a separation of 19 mm) diverges from experimental values at larger electrode separations. Rate effects could be the cause, although experiments were designed to be quasi-static (voltage increased at 0.1 V/s). Alternatively, deviation could be due to the interference of bubbles and turbulence (electrolysis or Marangoni-flow-induced) at close proximity to the electrodes. Geometry could thus influence behavior in ways that are not captured by the basic bipolar electrochemistry formula. We speculate that the geometric influences which caused deviation in the electrode separation are nearly proportionate with dimension, allowing the theory to predict the behavior better with scale. However, separation does not occur reliably at small scales ($0.5\times$) or large scales($\geq 1.25\times$). At smaller scales, the primary reason is interference of bubbles that block current flow. At larger scales the reasoning is less clear, though an upper limit for separation current appears to be the cause (see Appendix W). Separation also fails to occur at low NaOH concentrations (1%), where the ions were insufficient to reach the required interfacial tension gradient. At higher concentrations (5%), separation would occur at currents beyond the range of our testing circuit.

It should be noted that an alternative mechanism for inducing gradients in interfacial tension is through electrocapillarity, which follows the Young-Lippmann equation for relating γ and Φ. This effect has been used to cause fluid motion through so-called

"continuous electrowetting" (CEW) and the Marangoni effect[76]. Assuming that the LM droplet is equipotential (due to its high conductivity), there exists a variation of voltage across the drop due to the relatively low conductivity of the surrounding solution. As suggested by the Young-Lippmann equation, a gradient in interfacial tension develops along the liquid metal, resulting in a forces that can either move the droplet or the surrounding electrolytic solution. Originally, this phenomenon was applied to manipulate mercury slugs [224, 225]. More recently, it has been examined for EGaIn [75, 218] and applied to microfluidic pumping [76] and mixing [226]. For gradients induced by electrocapillarity, EGaIn droplets immersed in NaOH(aq) move towards the anode (positively charged electrode) and the surrounding fluid is pushed in the opposite direction[75, 218]. While also of general interest, electrocapillarity does not achieve the same dramatic interfacial tension change as oxide growth, which can reach interfacial energies of nearly zero J/m^2, as discussed in the literature [227]. Further, as discussed above, our experiments indicate that although it occurs simultaneously with bipolar electrolysis, electrocapillarity is not the driving mechanism in this work.

4.2 Demos and Applications

4.2.1 Simultaneous Control of Multiple Droplets

In this demonstration, I show how multiple sets of drops can be manipulated in a single bath of solution. Three sets of electrodes are arranged to share a single grounded gate electrode, as shown in fig. 4.8. A set of droplets can be coalesced and separated independently or simultaneously with other pairs of droplets. While the input current for a single pair does influence neighboring liquid metal, it is not sufficient to change the bistable state. Note that, for this demo, there is no electrical connection (ignoring NaOH solution) between the droplets and that they are electrically floating during

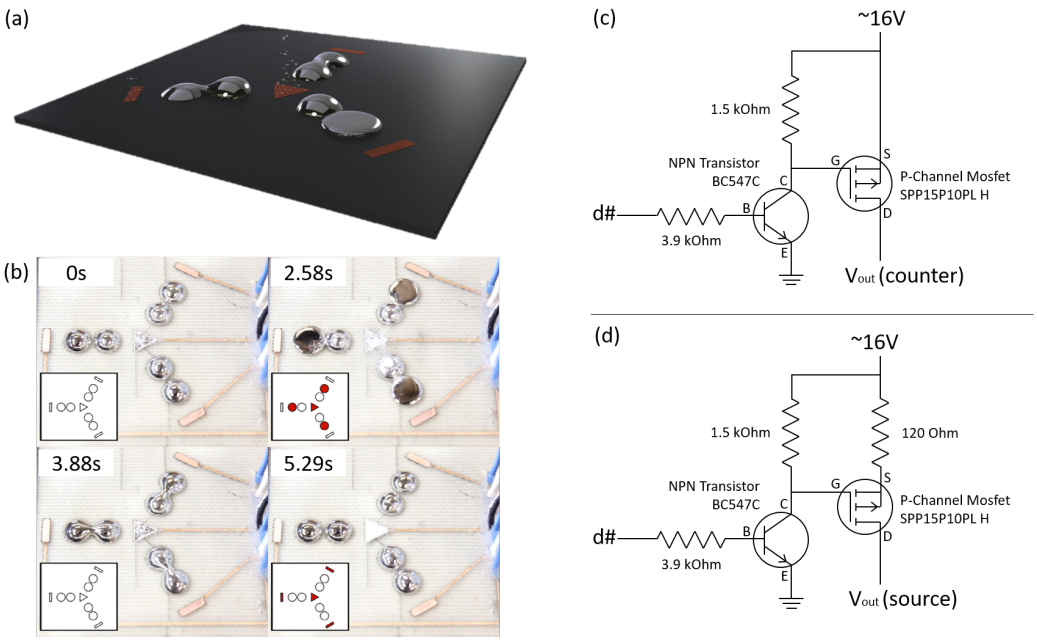

Figure 4.8: 3 droplet manipulation. (a) Rendering of pad and liquid metal orientation. (b) Sample images from video with timestamps. Showing simultaneous control. (c) Circuit for activating counter electrodes for separation. (d) Circuit for activating source electrodes for coalescence.

separation. There is a fundamental limitation to maintaining multiple pairs in a bath if the pairs are electrically connected, such as linking the source of one pair to the drain of another to create an AND gate, then the inputs to one would influence the other. For example, in the case described above, if the source were anodized to spread and coalesce, the drain of the second pair would also spread and possibly coalesce. Careful arrangements, multiple gate electrodes (rather than a single shared electrode), and isolated baths could overcome many of these challenges.

The circuitry used to control multiple droplets is shown in fig. 4.8c,d. The key components are NPN transistors and P-Channel MOSFETs. The transistors act as level shifters between the Arduino UNO R3 microcontroller (which applies input signals to d#) and the MOSFTETs. As stated above, the central gate electrode was continuously grounded, and the drain electrodes were floating. Fig. 4.8c represents

the circuit for controlling a single counter electrode and fig. 4.8d represents the circuit for controlling a single source electrode. The only difference is the addition of a series 120 ohm resistor, which serves to decrease the voltage applied to the source electrode. This is done because spreading and coalescence requires a lesser voltage than separation. The input voltage to the circuit was 16V.

4.2.2 Liquid Metal Transistor

An attractive application for the controlled coalescence and separation of LM is the creation of an electrically-controlled switch. Given the requirements on voltage between source and gate electrodes to achieve spreading and coalescence, we liken this behavior to that of a transistor. The circuit diagram for the liquid metal transistor data is shown in fig. 4.9. The system can be viewed as a high side switch where the source is tied to an input voltage V_{in}, and the drain is then connected to the load a 10 ohm resistor in addition to a 1 ohm shunt resistor (for current readings) in this example. In the off-state when the droplets are separated, current must pass from the gate LM to the NaOH solution to the drain LM, resulting in a high resistance. When coalesced in the on-state, the drain and source are essentially shorted by the LM bridge.

The gate input consists of an N-channel MOSFET (N10L26) with an associated PNP transistor (C9015) for level shifting. When activated by a digital signal from an Arduino R3 microcontroller, a negative voltage V_G is applied to the gate electrode of the liquid metal switch. Current flows from the source to the gate, resulting in oxidation, spreading, and droplet coalescence. Similarly, the counter input consists of a P-channel MOSFET (15P10PL) and an NPN transistor (BC547C), allowing the application of a positive voltage V_C to the counter electrode. Current flows from the counter to the source/drain to the gate, causing droplet separation. The diode attached to the drain prevents the unintentional spreading of the LM of that pad

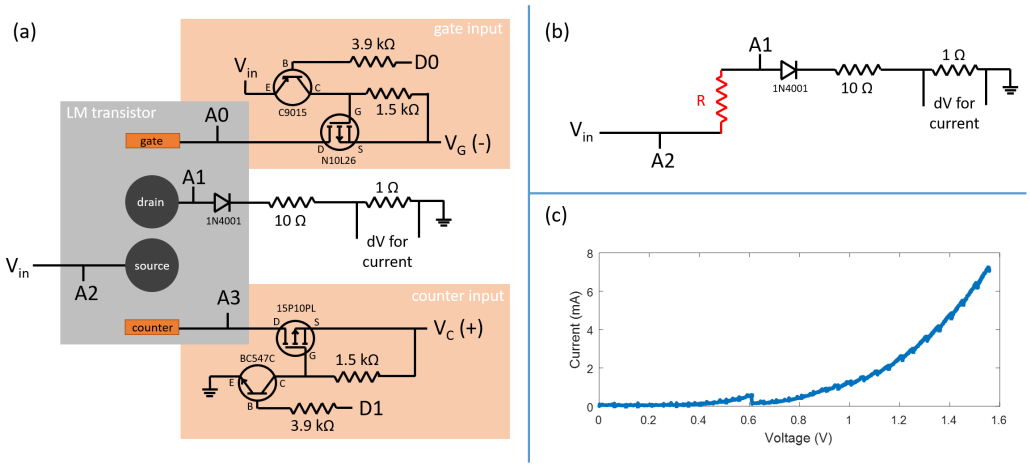

Figure 4.9: Circuit diagrams and data for liquid metal transistor. (a) Overall setup for controlling the liquid metal transistor, including the gate input, counter input, and the LM transistor, itself. (b) The circuit assumed when calculating the drain-source resistance (as marked in red). (c) The current-voltage curve associated with liquid metal on the source and drain.

during gate activation.

As with the general droplet testing described above, voltages (A0, A1, A2, A3) were monitored with the Extended ADC Shield. Rather than the AD8244BRMZ, the signals were buffered with voltage followers created with quad op amps (LM324M). The current was again tracked with the voltage difference across the 1 ohm resistor by using an instrumentation amplifier (AD623). To simplify the calculation of source-drain resistance, the circuit is simplified to fig. 4.9b. Thus, the results (fig. 4.10) contain features as a result of the signals from gate and counter electrodes.

An important byproduct of the LM-NaOH-LM interface is the role of electrolysis. In particular, if V_{in} is too large, the surface will become more electrochemically active as redox increases. fig. 4.9c captures this behavior is a current-voltage relationship for the drain and source with LM (not including the diode or load). The feature around 0.6V seems to coincide with the onset of significant oxide growth, creating additional resistance and lowering the current, but this aspect requires further study. For the transistor, electrolysis results in a decrease in off-state resistance (higher off-state leakage current). If the input voltage is sufficiently high, bubbles (hydrogen) will form on the drain electrode and the source electrode will grow oxide and begin spreading (see fig. 4.10), possibly causing unintentional coalescence. Given this information, testing focused on input voltages between 0.75V and 1V high enough to overcome the forward voltage of the diode ($\sim$0.7V) and low enough to avoid excessive redox. Note that adjusting the control electronics and replacing the standard diode with a Schottky diode (forward voltage of $\sim$0.3V) could improve the off-state resistance.

As shown in fig. 4.10, the on-state allows a current of 12.5 mA with a conductivity of $\sim$2 Siemens (less than an Ohm) while the off-state limits current to about 0.1 mA with a conductivity of $\sim 3 \times 10^{-4}$ Siemens (several kilo-Ohms). The features in current and conductivity are a result of current from the counter/gate during coalescence and separation. During spreading for coalescence, current would flow from drain to

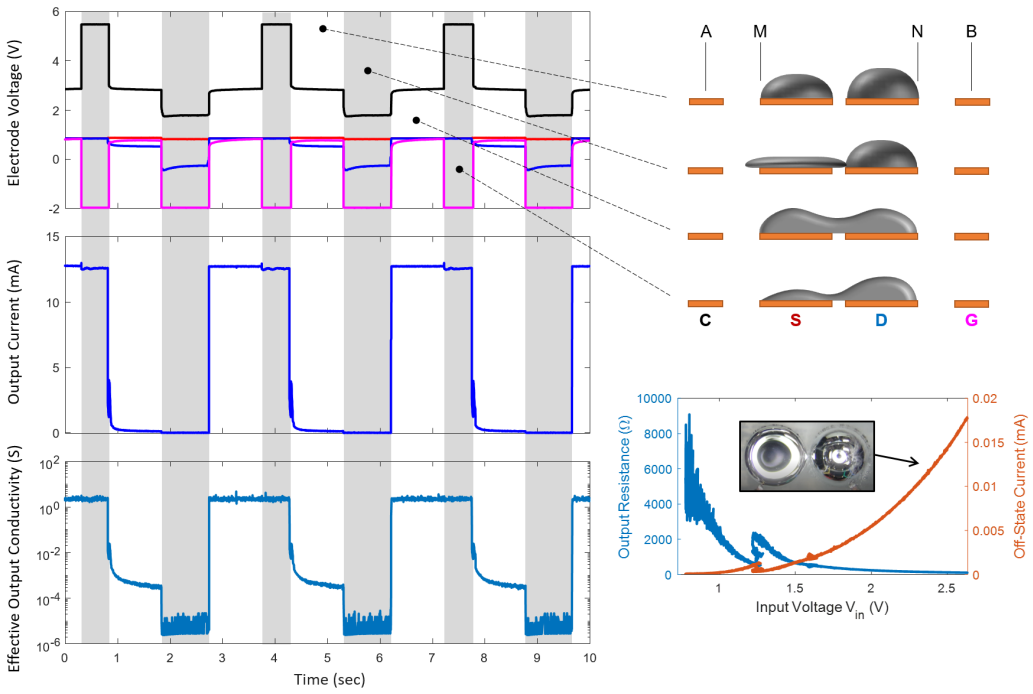

Figure 4.10: General LM transistor behavior. Left: Plots for electrode voltage, output current, and effective conductivity versus time. Electrode voltages including gate (magenta), counter (black), source (red), and drain (blue). Top right: Droplet states associated with the shaded regions of the plots. States include separated, spreading, coalesced, and separating. Bottom right: Off-state output resistance and off-state leakage current as a function of input voltage. The inset shows bubbling on the drain and unintentional spreading of the source due to electrolysis across these two electrodes.

gate (negative in this case) if it were not for the diode. As a result, the current drops to nearly zero and the measuring circuitry has difficulty determining a value for resistivity and conductivity. The off-state output resistance and leakage current are also reported. As expected, the resistance falls and the current rises as the input voltage increases and electrolysis becomes more substantial. The feature at ∼1.25V is reminiscent of the feature showin in the I-V curve in fig. 4.9. Again, this appears to be caused by the onset of significant oxide growth. The voltage is shifted from ∼0.6V to ∼1.25V by the forward voltage of the diode.

There is a significant difference between this liquid metal transistor and the theory discussed for the majority of this paper. Bipolar electrodes (and the samples compared to theory in this paper) are floating in the sense that no charge is applied directly to them. However, for this LM transistor, the source and drain are directly tied to V_{in} during droplet separation. During bipolar electrolysis, oxidation and reduction are equal in terms of charge transfer on either side of the electrode charge in must equal charge out. In this case, however, the direct tie to a voltage source provides an alternative route for charges. Depending on the voltages at the source, gate, and counter, oxidation, reduction, or some ratio of both can occur across the liquid metal. In other words, tying the source to a voltage input gives control over the level of oxidation and reduction across the liquid metal. This is why a negative voltage was required for the gate electrode rather than simply using ground as in other experiments. The situation is elucidated by table 4.1.

For this experiment, the source voltage (V_{in} or V_S) was kept constant as well as the difference between the counter and gate voltages. The potential of the counter and gate were increased progressively while attempting to separate the droplets (held at the source potential V_S) with up to 2 seconds of current flow. When the gate and counter were too high, reduction was excessive and the droplets failed to separate. Likewise, oxidation was excessive and prevented separation when the gate and counter

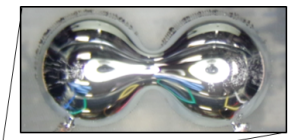

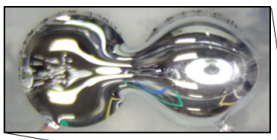

	Trial 1	Trial 2	Trial 3	Trial 4	Trial 5	Trial 6	Trial 7	Trial 8	Trial 9	Floating
Source(V)	0.846	0.845	0.845	0.844	0.842	0.842	0.84	0.839	0.836	2.58
Counter (V)	5.81	5.76	5.71	5.66	5.55	5.51	5.47	5.43	5.33	7.44
Gate (V)	-1.62	-1.67	-1.73	-1.78	-1.83	-1.88	-1.93	-1.97	-2.07	0
Counter-Gate (V)	7.43	7.43	7.44	7.44	7.38	7.39	7.4	7.4	7.4	7.44
Ratio	0.497	0.504	0.511	0.518	0.529	0.535	0.541	0.546	0.559	0.512
Separation?	No	No	Maybe	Yes	Yes	Maybe	Maybe	No	No	Yes

Table 4.1: Table for adjusting the ratio between source, counter, and gate during droplet separation. The images above represent separation attempts with excess reduction (left) and excess oxidation (left).

were to low. In some cases (marked "maybe") separation succeeded and failed in the same trial. We can also look at the following ratio: $(V_S - V_G + E_0)/(V_C - V_G)$, where E_0 is 1.23V for the electrode potential difference between the copper and GaIn. There is a narrow region from approximately 0.511 to 0.541 where separation is possible a range of about 0.2V in this case. It turns out that the ratio for the floating electrode case falls on the lower end of the range, around 0.512. The implication is that the bipolar electrolysis provides an approximately optimal level of oxidation and reduction for droplet separation. Furthermore, the theories presented in this paper are still applicable for this liquid metal transistor. As a side note, it is not known why the ratio does not fall exactly on 0.5 for equal oxidation and reduction. Possible reasons include voltage divider effects due to oxide growth and bubbles or changing electrode potentials as oxidation occurs.

4.3 Summary and Outlook

In this chapter, I presented a fluidic electrical switch that reversibly changes its electrical conductivity by three orders of magnitude in response to moderate applied voltage (∼1-10V). This "liquid transistor" is the first soft-matter electrical switch that operates with voltages similar to that of conventional solid state transistors. LM droplet separation is controlled by a novel fluidic instability that is driven by a field-controlled gradient in interfacial tension and has not before observed in fluidic electrowetting or LM droplet manipulation. Experimental measurements are in good agreement with theoretical predictions based on fluid mechanics and bi-polar electrochemistry. In addition to explaining the observed electro-capillary behavior, the theory can inform the design of physically-reconfigurable liquid metal electronics. Potential applications include field-programmable gate arrays, reconfigurable antennas, and non-volatile memory storage devices that are mechanically soft and highly

deformable. Such advancements could accelerate further progress in the emerging field of LM-based soft microfluidic electronics.

I have demonstrated the controlled coalescence and separation of anchored LM droplets with the application of electric fields and explained the phenomena. Dramatic decreases in LM interfacial tension under direct oxidation enable droplet contact and coalescence. Separation, however, is driven by bipolar electrochemical interactions that induce an oxide gradient and manipulate the interfacial energy between the LM and the electrolytic solution, leading to instabilities. Potential applications of this bistable response include soft-matter switches, reconfigurable electronics, and analogs of solid state circuits in liquid environments. The work presented here primarily focuses on quasi-static behavior, where the limit-point instability is governed by interfacial tension. However, rapid pulses of current introduce inertial effects. In principle, cyclic voltage inputs could be used at the natural frequency of the coalesced drops to further decrease separation voltage and to avoid bubbling at the gate and counter electrodes. Furthermore, typical fluidic phenomena such as Rayleigh instabilities could be leveraged to achieve shape programmability within LM circuits. A truly predictive Surface Evolver simulation could be designed with precise relationships between current input, reaction rates (oxidation and reduction, both electrical and solution-induced), and effective interfacial tension. This is, however, beyond the scope of the work presented here, which instead shows predictions for a variety of designs based on a single set of experimentally gathered critical values ($\Delta\Phi_p$ and $\Delta\Phi_c$).

One area that requires further study is device lifetime. Although the current system is limited by the corrosion of the copper electrodes during oxidation, this could be remedied with more inert electrodes, such as gold. The lifetime would then likely be limited by chemical interactions of gallium. In particular, NaOH slowly converts gallium to gallates like $[Ga(OH)_4]^-$, eventually causing the liquid metal to

lose its eutectic/near-eutectic point [76]. HCl solution is also commonly used with gallium-indium, but would likewise slowly produce gallium chloride [228]. Given this information, further investigation into alternative solutions is warranted.

The onset of LM motion and trends for droplet separation can be predicted with theories from bipolar electrochemistry. Although particularly useful for informing switch design and establishing a general understanding of electrocapillary behavior, more can be learned on the behavior of LM under the influence of applied potentials. Particularly, the proximity of the outer electrodes to the LM droplets appears to have an impact on the bipolar electrochemistry, which is not captured by the theory reported in this paper. Furthermore, models capturing the dynamics of the electrolytic solution (with Marangoni flows and bubbles due to electrolysis) and their interaction with the geometry could produce new and further optimized designs for reconfigurable circuits.

Neutral pH electrolyte baths also present interesting possibilities. In the work presented here, basic NaOH solution was used because the dramatic spreading (particularly for coalescence) is not seen in neutral baths. Instead, oxide rapidly grows too thick, indicating that the competition between electrochemical oxidation and oxide removal through bath chemistry is required [77]. However, if coalescence could be achieved in a neutral bath, the shape would be held by the ever-present oxide layer even at sub-critical volumes of LM. With a sub-critical volume, merely reducing the drops would cause separation as surface area is essentially minimized. In this case, no bipolar electrochemistry or interfacial tension gradient would be required for separation. The above improvements, along with bubble-reducing techniques such specialized electrodes [229, 230], can improve feasibility of these reconfigurable LM microfluidics. Channels could also be used to manipulate the electric field strength. Droplets placed in a narrow channel could increase the required voltage bias due to the higher electrical resistance. Higher resistance can also be achieved with lower

NaOH percents at the cost of higher voltage requirements, slower oxide growth, and slower overall behavior of the system. These trade-offs reflect the importance of furthering our understanding of these systems in order to optimize designs for varying applications in soft-matter electronics and shape-programmable media.

Chapter 5

Conclusions and Future Research

As the fields of soft robotics and wearable devices continue to advance, researchers search for methods to expand functionality of stretchable electronics. Existing soft actuators and recent developments in liquid metal electrochemistry provide techniques and inspiration for developing new active devices which meet my proposed goals: Create devices (i) constructed of soft, condensed matter for integration in stretchable electronics; (ii) capable of low-energy shape programmability for the purpose of achieving electrical switching and reconfiguration; (iii) activated by low voltages (<10V) for use with standard microcontrollers and power supplies. I have explored the electromechanical coupling of a curved DEA, modeled the field-driven deformation of cantilever and fixed-fixed beams under extreme stretch and compression, and created a liquid metal switch activated by low-voltage-induced oxide growth.

Curved cantilever DEAs were fabricated with a PDMS dielectric and liquid metal electrodes. In an effort to predict actuation behavior under high voltages, the elastomer body was modeled as a Neo-Hookean solid and the electrical enthalpy was calculated. Modeling as pure bending (plain-strain) proved to be inadequate as some energy was dissipated into the transverse direction, causing a saddle-like deformation. Instead, a shell theory was introduced, showing strong agreement with experimental

results and reflecting the importance of capturing all (or most) deformation modes. When considering electrostatic cantilever beams created with cPDMS, traditional beam bending and electrostatics theories were sufficient for modeling device behavior, which only included small strains. I developed a novel technique leveraging raster ablation with a CO_2 laser and sacrificial layers of poly(acrylic acid) to create millimeter scale beams with thicknesses and gap heights on the order of hundreds of microns.

Mechanics theory for the manipulation of a hyperelastic beam under extreme stretch was presented and compared to experimental point load tests with great agreement. When simulating electrostatic load, results showed that the additional surface area created by stretch could overcome the additional stresses, maintaining or possibly decreasing the pull-in voltage. On the opposite end of the spectrum, the beams could be compressed. This condition was modeled with a Raleigh-Ritz technique and energy minimization. Although the buckled condition has the added benefit of having bistable conditions, further buckling increases the required load to reach the instability. Given this information, it may be beneficial to construct a soft MEMS beam under pre-stretch. This could result in a more constant pull-in voltage (or magnetic load) and would prevent buckling behavior, which would greatly increase the required input.

A liquid metal switch was fabricated and operated, showing the ability to change the effective conductivity by over three orders of magnitude. The device operates on electrochemically grown oxide layers, which lower the effective interfacial energy of GaIn. Direct growth causes drop spreading and coalescence, and bipolar electrochemistry causes an oxide gradient which splits them apart. Surface Evolver simulations further validate the theory that a interfacial energy gradient can cause such an instability, and electrochemical theory allows for the prediction of required currents for operation. These theories also provide insights which could direct future prototype designs, including the use of channels and proximity of electrodes.

	DEA	Electrostatic Beams	Magnetic Beams	Electrochemical LM Drops
Soft matter construction	✓	✓	✓	✓*
Low-energy reconfiguration	✓	✓		✓
Low voltage activation			✓	✓
Functionality under stretch	?	?	?	?
Other switch metrics	?	?	?	?

Table 5.1: Summary of switch performances. The asterisk indicates the use of a rigid substrate.

In table 5.1, I review the switches covered in this work based on how well they accomplished the original goals. DEAs and electrostatic beams were entirely elastic and low energy ($\sim 10^0$ J/kg DEA activation and $\sim 10^{-1}$ J/kg electrostatic cantilever activation), though operating voltages were still at least 100V. Magnetic beams were similarly soft and could achieve lower voltages, but they required bulky permanent magnets or power-hungry electromagnets. Finally, the electrochemical manipulation of droplets achieved all three goals (bistable states with $\sim 10^3$ J/kg activation), though the substrate was rigid (this is discussed further below). Future endeavors include testing devices under actual stretch. Although functionality may be inferred from theory, none of those constructed here were tested under strains. Furthermore, various switching metrics such as off-state impedance, off-state capacitance, and bandwidth require deeper exploration. Below, I make additional suggestions for possible future research directions. Most of these build on the discoveries presented in this document and further approach the creation of a true stand-alone device for integration in a soft-matter circuit.

5.1 Recommendations for Future Research

5.1.1 Electrostatic Devices

Electrostatics, as demonstrated in MEMS, provides excellent efficiency for creating reconfigurable devices such as switches. Further, they scale well, allowing required voltages to decrease as overall device size is reduced. For the cantilevers presented in this work, beam lengths were on the scale of millimeters, though the low modulus of the rubber material kept required voltages as low as 100V. While this still requires a specialized high voltage supply or transformer, the voltage requirements could be reduced significantly by scaling down the devices. Specifically, reducing the size by 10 times would reduce the required voltage by approximately 10 times. This is true

as well for the fixed-fixed case, even under stretch. Given these factors, the next step would be to develop fabrication techniques for further miniaturization.

Soft Microfabrication Background

Microscale actuators and electronics are typically produced in a cleanroom setting using lithographic techniques. When it comes to soft materials, the counterpart is "soft lithography," a procedure that typically utilizes a mater or negative mold produced with photolithography [231, 232]. Generally, this master is used to cast something like PDMS in order to create a stamp. Because the master can be reused to create multiple stamps, the process is relatively cheap. PDMS stamps can be used for microcontact printing [232, 233] or replica molding [232]. Alternatively, rather than using the casted PDMS (or other elastomer) as a stamp, it can be used directly for creating microfluidic channels [234]. In the field of soft-matter engineering, microfluidic channels are often filled with liquid metal alloys to create electronic parts [33, 235]. Despite its popularity, soft lithography generally is not used to fabricate beams, such as those described in this document, and has remained limited to microfluidics and membranes.

Perhaps the closest existing work related to our goal is work out of Dr. Bergbreiter's lab at University of Maryland [89, 236]. In [236], researchers develop all-soft-matter thermal actuators: a chevron actuator, a heatuator, and a bilayer thermal actuator using cPDMS (with carbon black) and PDMS. In [89], the same lab used MRTV 9, an elastomer from Insulcast, and conductive MRTV 9 (MRTV 9 mixed with carbon black) to fabricate dielectric elastomer actuators. In both cases, the devices were around 500 microns in length - larger than our desired goal, but the fabrication process is still of interest. The fabrication procedure follows that of silicon-on-insulator (SOI). To begin, bare silicon undergoes deep reactive ion etching. The trenches are then filled with conductive elastomer which is allowed to cure. After-

wards, a second round of deep reactive ion etching is performed to create trenches for the non-conductive elastomer. After filling and curing, the entire wafer is attached to a handle wafer with bonding agent. When forced from the fabrication wafer, the handle wafer brings the elastomer device along thanks to the bonding agent. Rinsing with a solvent eliminates the agent, releasing the final product. This process provides a unique freedom of design which could be beneficial to the research proposed in this document.

Nanoscribe

One rapid alternative fabrication method is direct laser writing. Carnegie Mellon's MEMS Chem Lab has obtained a Nanoscribe machine, which is capable of this type of prototyping. The mechanism behind this technology is based on two-photon absorption [237, 238] and is described on the Nanoscribe website. In short, many UV-curable polymers can also be cured when two near-infrared photons are simultaneously absorbed. The Nanoscribe applies this via laser to selectively cure a small region, called a voxel. This technology has been used to create metamaterials [239] and structures for cell growth [240]. Additionally, its artistic capability to create Eiffel Towers on the order of 100 μm in height are shown off online and in magazines.

The Nanoscribe website also describes creating direct-written molds for casting PDMS. These molds can be used similar to those in soft lithography for creating stamps or microfluidic channels. Some preliminary tests have been performed for casting PDMS over Nanoscribe-created structures. Fig. 5.1 shows some results. It should be noted that this was performed while a mirror was misaligned. We have been told that this resulted in only being able to access 40% of the usual laser power. The machine has since been recalibrated.

Perhaps more promising than creating molds with the Nanoscribe is the possibility of directly writing elastomer material. Our lab has already been exploring UV-curable

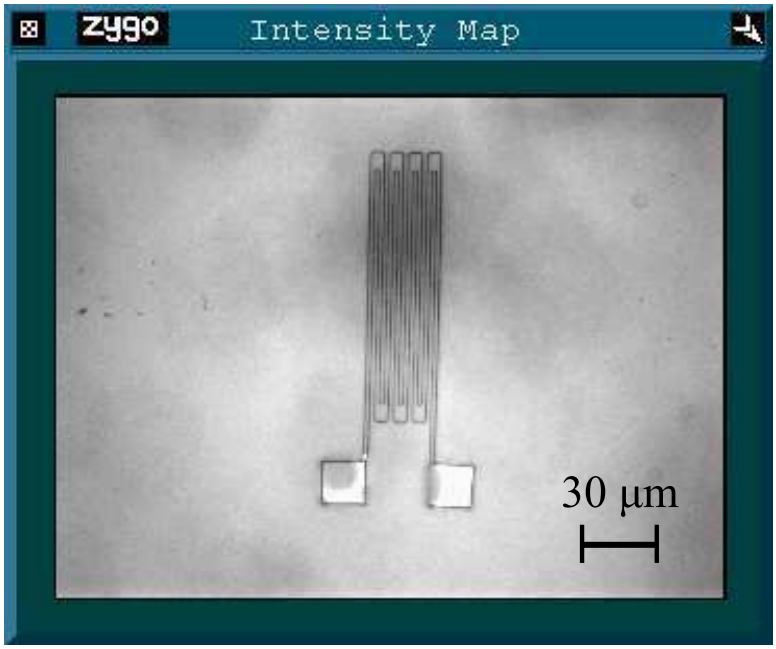

Figure 5.1: Strain gauge mold created with Nanoscribe's photoresist. The total length is approximately 150 microns and the channel height is approximately 2 microns. (Imaged with Zygo Profilometer)

Figure 5.2: Left: Transparency mask on uncured Loctite 3108. Center: Resulting structure after exposure to UV light. Right: Close-up of 500 μm channels.

elastomers in the development of freeze-casting techniques [241]. Another application of UV-curable elastomer has been so-called "benchtop polymer MEMS" [242]. Following the instructions provided (http://www.smela.umd.edu/polymer-mems/benchtop.html), some simple channels for a strain gauge (Fig. 5.2) have been fabricated in their recommended material, Loctite 3108. The hope is that this type of UV-curable material will also work well with the Nanoscribe. While relatively soft and flexible compared to traditional materials, these UV polymers are often more rigid than non-UV counterparts such as PDMS. It would be beneficial to find softer alternatives for use with the Nanoscribe. Further, creating conductive material using fillers could be problematic as some level of transparency is required for thorough UV curing. It should be noted that some success has been achieved with liquid crystal elastomers and the Nanoscribe [243]. This is encouraging and shows that it may be possible to directly write stretchable MEMS structures.

Integration of Gallium-Indium

The application of gallium-indium alloys to soft MEMS presents the possibility of maintaining high conductivity, robustness, and softness. As stated previously, using soft lithography to create microfluidic channels to fill with liquid metal is a popular choice, but this method is not particularly conducive to free standing structures such as beams. Alternatives such as stencil lithography [21] or freeze casting [241] have not yet been developed to produce features fine enough. The microcontact printing

developed in our lab [34] is also too large in scale, though our micro-transfer deposition [118] has been able to produce 2 micron line widths of liquid metal. This technique uses soft lithography to create a PDMS stamp with channels. These channels are filled with gallium-indium ally, and by pressing the stamp against another surface, liquid metal can be transferred. An alternative method is by selectively wetting liquid metal to rubbers sputtered with various metals [244], achieving features as small as 10 microns. While these methods produce features at a satisfactory scale, it could be challenging to apply it to free standing beams and other MEMS designs. As such, this is still very much an open problem.

5.1.2 Electrochemical Manipulation of Liquid Metal

Oxide-driven manipulation of liquid metal allows for large deformations under inputs of less than 10V. In the study reported here, we uniquely apply this phenomenon to achieve bistable coalescence and separation of anchored GaIn droplets. While switching is successfully achieved, there is room for improvement. In particular, further miniaturization and fabrication on stretchable substrates is desirable.

Miniaturization and Bubble Prevention

Miniaturization would be beneficial for several reasons. Two important aspects are the decrease in required currents and the decrease of inertial effects. With regards to the former, the theoretical and experimental work both indicated the decrease in current required for separation as scale was reduced. This translates to a decrease in power requirements, creating a more efficient switch. Regarding reduced inertial effects, gravity would have less of an impact on spreading behavior and the shifting direction of the liquid metal. Because surface forces become dominant at these scales, interfacial-energy-driven actuation should still function. As a result, a liquid metal switch could possibly function correctly regardless of orientation and direction of

applied accelerations. The primary problem that has to be addressed in this case is the bubble formation due to electrolysis. For the work in Chapter 4, a bath was used, allowing bubbles to easily escape. However, at the smallest scales, bubbles still interfered by clinging to the gate and counter electrodes.

Bubble formation is also a significant obstacle in the field of electroosmotics and electrokinetics, where bubble formation inhibits pump flows. Researchers have devised several methods which could be useful to us for overcoming this limitation. One method is to apply alternating currents (AC). [245] used a particular input which resulted in zero net charge current. Another method is to use consumable electrodes such as Ag/Ag_2O [246] that allow for functionality below 1.23V (electrolysis onset of water) or conjugated polymer electrodes which oxidize/reduce in place of water [230]. Palladium presents option since it has a high hydrogen permeability. When used in conjunction with AC signals, hydrogen produced and stored during reduction is consumed during oxidation [229].

AC offers an interesting possibility for liquid metal acting as a bipolar electrode. It is well known that the electrolysis onset of water is around 1.23V. However, based on experiments in Chapter 4, bipolar electrolysis across the liquid metal initiates at end-to-end voltages as low as 0.165V, and separation occurs around 0.75V. In principle, an AC current (rather than DC, as done in Chapter 4) could be applied across the droplets at voltages below 1.23V, avoiding bubble formation. Normally, the lack of electrolysis prevents significant current flow. However, because of the capacitive behavior of the electric double layer, AC signals would produce significant current flows. This same concept was used in [247] to create "ionic cables." Essentially, a sub 1.23V AC signal would not produce reactions at the gate or cathode, but current would flow through the solution producing a sufficient electric field to cause bipolar electrolysis across the liquid metal.

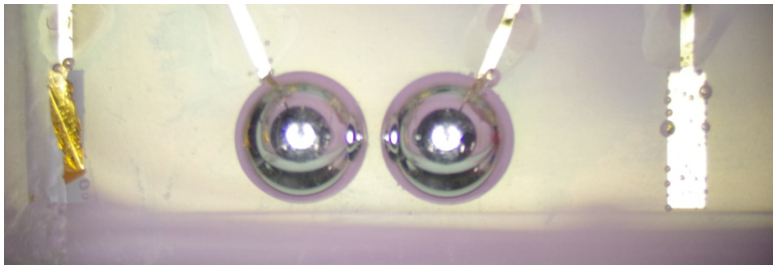

Figure 5.3: Testing with a chromium/gold sputtered sample. Gold lifts off the left electrode as it is oxidized.

Stretchable Substrate

To effectively integrate into other soft matter devices, the rigid PCBs used for fabrication in Chapter 4 would have to be replaced with elastomer alternatives. The challenge is then finding a way to properly anchor the droplets. One possibility is constructing neighboring chambers with finite volume. GaIn could bridge from one to the other through a channel or opening, but the entirety of the liquid metal could never fit in a single chamber. Alternatively, thin layers of metal could be applied to the surface of the rubber, acting as anchor points. Sputtered gold and other metals have (as noted previously [244]) already been used in conjunction with GaIn on PDMS surfaces. In fact, I am working with Kadri Bugra Ozutemiz (Soft Materials Laboratory) to develop a method to create "liquid metal PCBs." As shown in fig. fig:CondMat of Chapter 1 and as reported in [27], we are able to integrate surface mount packages, including land grid array (LGA) and quad flat no-leads (QFN), into robust stretchable circuits. However, there are challenges associated with this process, particularly when involving electrochemical reactions.

For a preliminary test, I applied titanium/gold and chromium/gold to a glass surface and patterned the test structures presented in Chapter 4. The titanium and chromium acted as adhesion layers for gold, which prefers not to remain attached to anything. The titanium sample failed when applying GaIn in NaOH. The surface forces simply peeled the gold off the substrate. In the case of the chromium, everything

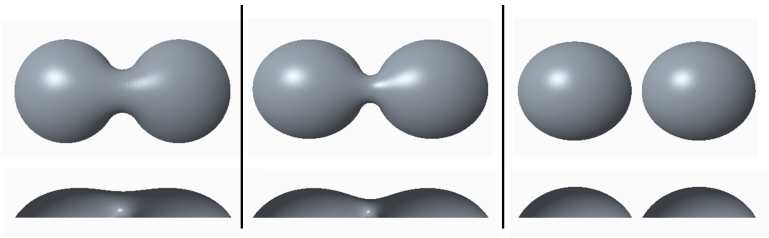

Figure 5.4: Surface Evolver simulation of droplets under 0% (left), 9% (center), and 10% (right) strain.

worked well until current was applied. In particular, the gold on the counter electrode lifted off (see fig. 5.3). I believe that the chromium underneath was oxidized and consumed by the NaOH solution, compromising the adhesion of the gold. More work has to be done to further understand what processes are occurring and what materials are best suited. It is possible that rather than chromium as an adhesion layer, some other material, such as a monolayer capable of adhering to metals, would be optimal.

Another aspect is the behavior of bridging liquid metal when placed under stretch. It is rather intuitive that under enough stretch (lengthwise), two coalesced drops such as those presented in this work would separate. In fact, a quick simulation with Surface Evolver shows that the standard setup used in Chapter 4 would experience instability at around 123 % stretch (see fig. 5.4). Specialized pad geometries or the addition of channels could alleviate this issue. Alternatively, the system could be isolated from strain using stiffer surrounding polymers, similar to the methods used in [248].

5.2 Conclusion

Soft electronics has accelerated in recent years, producing functional circuits comprised of wavy metallic traces, conductive rubbers, and room-temperature liquid alloys. Significant effort has been placed in creating passive circuitry and sensors, though active devices such as relays and transistors are still lacking in the domain.

In particular, there is a need for low energy shape programmability in soft matter devices. The contributions contained in this work provide a step towards creating truly soft and stretchable devices capable of reconfiguring for switching or tuning purposes. The approaches include DEAs, electrostatic/magnetic beams, and electrochemically manipulated liquid metal. Experiments demonstrate feasibility and validate theories which predict device behavior. Future research can focus on applying these theories to optimize designs, particularly with focus on miniaturization for efficiency and ease of integration in soft matter electronics. Soft machines and wearable technology may incorporate a combination of traditional electronics, stretchable interconnects, and - with this work as a foundation - soft, physically reconfigurable devices to create systems that are bio-compatible, mechanically robust, and multi-functional.

References

[1] J. Wissman, L. Finkenauer (co-first author), L. Deseri, and C. Majidi, "Saddle-like deformation in a dielectric elastomer actuator embedded with liquid-phase gallium-indium electrodes," *Journal of Applied Physics*, vol. 116, p. 144905, Oct. 2014.

[2] L. R. Finkenauer, J. Wissman, C. Majidi, and L. Deseri, "Modeling of curved cantilever dielectric elastomer actuator using universal solution in finite bending," in *Proc. Soc. Eng. Sci. 51st Annu. Tech. Meet. Oct. 1-3* (A. Bajaj, P. Zavattieri, M. Koslowski, and T. Siegmund, eds.), (West Lafayette), Purdue University Libraries Scholarly Publishing Services, 2014.

[3] J. Wissman and C. Majidi, "Nonlinear deflection of a fixedfixed hyperelastic beam under extreme stretch," in *Proc. Soc. Eng. Sci. 51st Annu. Tech. Meet. Oct. 1-3* (A. Bajaj, P. Zavattieri, M. Koslowski, and T. Siegmund, eds.), (West Lafayette), Purdue University Libraries Scholarly Publishing Services, 2014.

[4] V. Ramachandran, M. D. Bartlett, J. Wissman, and C. Majidi, "Elastic instabilities of a ferroelastomer beam for soft reconfigurable electronics," *Extrem. Mech. Lett.*, vol. 9, pp. 282–290, dec 2016.

[5] J. Wissman, M. D. Dickey, and C. Majidi, "Field-controlled electrical switch with liquid metal," *under review by Advanced Science*, 2017.

[6] T. Lu, L. Finkenauer, J. Wissman, and C. Majidi, "Rapid Prototyping for Soft-Matter Electronics," *Adv. Funct. Mater.*, vol. 24, pp. 3351–3356, June 2014.

[7] A. Sidpara, "Magnetorheological finishing: a perfect solution to nanofinishing requirements," *Opt. Eng.*, vol. 53, p. 092002, mar 2014.

[8] R. Akhtar, M. J. Sherratt, J. K. Cruickshank, and B. Derby, "Characterizing the elastic properties of tissues," *Mater. Today*, vol. 14, pp. 96–105, mar 2011.

[9] Y. I. Cho and K. R. Kensey, "Effects of the non-Newtonian viscosity of blood on flows in a diseased arterial vessel. Part 1: Steady flows.," *Biorheology*, vol. 28, no. 3-4, pp. 241–62, 1991.

[10] K. Comley and N. A. Fleck, "A micromechanical model for the Young's modulus of adipose tissue," *Int. J. Solids Struct.*, vol. 47, pp. 2982–2990, oct 2010.

[11] C. T. McKee, J. a. Last, P. Russell, and C. J. Murphy, "Indentation Versus Tensile Measurements of Young's Modulus for Soft Biological Tissues," *Tissue Eng. Part B Rev.*, vol. 17, pp. 155–164, jun 2011.

[12] S. Pal, "Mechanical Properties of Biological Materials," in *Des. Artif. Hum. Joints Organs*, vol. 9781461462, pp. 23–40, Boston, MA: Springer US, 2014.

[13] G. Rebeiz and J. Muldavin, "RF MEMS switches and switch circuits," *IEEE Microwave Magazine*, vol. 2, no. 4, pp. 59–71, 2001.

[14] A. J. Baca, J.-H. Ahn, Y. Sun, M. a. Meitl, E. Menard, H.-S. Kim, W. M. Choi, D.-H. Kim, Y. Huang, and J. A. Rogers, "Semiconductor wires and ribbons for high-performance flexible electronics.," *Angewandte Chemie (International ed. in English)*, vol. 47, pp. 5524–42, Jan. 2008.

[15] J. A. Rogers, T. Someya, and Y. Huang, "Materials and mechanics for stretchable electronics.," *Science*, vol. 327, pp. 1603–7, Mar. 2010.

[16] X. Z. Niu, S. L. Peng, L. Y. Liu, W. J. Wen, and P. Sheng, "Characterizing and Patterning of PDMS-Based Conducting Composites," *Advanced Materials*, vol. 19, pp. 2682–2686, Sept. 2007.

[17] M. Kujawski, J. Pearse, and E. Smela, "Elastomers filled with exfoliated graphite as compliant electrodes," *Carbon*, vol. 48, pp. 2409–2417, Aug. 2010.

[18] J. Wissman, A. Perez-Rosado, A. Edgerton, B. M. Levi, Z. N. Karakas, M. Kujawski, A. Philipps, N. Papavizas, D. Fallon, H. a. Bruck, and E. Smela, "New compliant strain gauges for self-sensing dynamic deformation of flapping wings on miniature air vehicles," *Smart Materials and Structures*, vol. 22, p. 085031, Aug. 2013.

[19] J. M. Engel, N. Chen, K. Ryu, S. Pandya, C. Tucker, Y. Yang, and C. Liu, "Multi-layer embedment of conductive and non-conductive PDMS for all-elastomer MEMS," in *The 12th Solid State Sensors, Actuator, and Microsystems Workshop*, (Hilton Head Island), pp. 1–4, 2006.

[20] J. Li, P. C. Ma, C. W. Sze, T. C. Kai, B. Z. Tang, and J.-K. Kim, "PERCOLATION THRESHOLD OF POLYMER NANOCOMPOSITES CONTAINING GRAPHITE NANOPLATELETS AND CARBON NANOTUBES," in *16TH INTERNATIONAL CONFERENCE ON COMPOSITE MATERIALS* (K. Kageyama, T. Ishikawa, N. Takeda, M. Hojo, S. Sugimoto, and T. Ogasawara, eds.), (Kyoto), pp. 1–8, Japan Society for Composite Materials, 2007.

[21] J. Wissman, T. Lu, and C. Majidi, "Soft-Matter Electronics with Stencil Lithography," *Sensors, 2013 IEEE*, pp. 1–4, 2013.

[22] M. Vosgueritchian, D. J. Lipomi, and Z. Bao, "Highly Conductive and Transparent PEDOT:PSS Films with a Fluorosurfactant for Stretchable and Flexible Transparent Electrodes," *Adv. Funct. Mater.*, vol. 22, pp. 421–428, jan 2012.

[23] B. J. Worfolk, S. C. Andrews, S. Park, J. Reinspach, N. Liu, M. F. Toney, S. C. B. Mannsfeld, and Z. Bao, "Ultrahigh electrical conductivity in solution-sheared polymeric transparent films," *Proc. Natl. Acad. Sci.*, vol. 112, no. 46, pp. 14138–14143, 2015.

[24] C. H. Chen, A. Torrents, L. Kulinsky, R. D. Nelson, M. J. Madou, L. Valdevit, and J. C. Larue, "Mechanical characterizations of cast Poly(3,4-ethylenedioxythiophene): Poly(styrenesulfonate)/Polyvinyl Alcohol thin films," *Synth. Met.*, vol. 161, no. 21-22, pp. 2259–2267, 2011.

[25] H. Stoyanov, M. Kollosche, S. Risse, R. Waché, and G. Kofod, "Soft conductive elastomer materials for stretchable electronics and voltage controlled artificial muscles," *Adv. Mater.*, vol. 25, no. 4, pp. 578–583, 2013.

[26] T. Lu, J. Wissman, Ruthika, and C. Majidi, "Soft Anisotropic Conductors as Electric Vias for Ga-Based Liquid Metal Circuits," *ACS Appl. Mater. Interfaces*, vol. 7, pp. 26923–26929, dec 2015.

[27] K. B. Ozutemiz, J. Wissman, B. Ozdoganlar, and C. Majidi, "Lithography-based Fabrication of Liquid Metal Circuits and Integration of Microelectronics," *submitted to Science Advances*, 2017.

[28] R. J. Whitney, "The measurement of volume changes in human limbs," *J. Physiol.*, vol. 121, pp. 1–27, Jan. 1953.

[29] M. D. Dickey, R. C. Chiechi, R. J. Larsen, E. A. Weiss, D. A. Weitz, and G. M. Whitesides, "Eutectic Gallium-Indium (EGaIn): A Liquid Metal Alloy for the Formation of Stable Structures in Microchannels at Room Temperature," *Adv. Funct. Mater.*, vol. 18, pp. 1097–1104, Apr. 2008.

[30] Q. Xu, N. Oudalov, Q. Guo, H. M. Jaeger, and E. Brown, "Effect of oxidation on the mechanical properties of liquid gallium and eutectic gallium-indium," *Phys. Fluids*, vol. 24, no. 6, p. 063101, 2012.

[31] C. Majidi, R. Kramer, and R. J. Wood, "A non-differential elastomer curvature sensor for softer-than-skin electronics," *Smart Mater. Struct.*, vol. 20, p. 105017, Oct. 2011.

[32] S. Cheng, Z. Wu, P. Hallbjorner, K. Hjort, and A. Rydberg, "Foldable and Stretchable Liquid Metal Planar Inverted Cone Antenna," *IEEE Transactions on Antennas and Propagation*, vol. 57, pp. 3765–3771, Dec. 2009.

[33] R. D. Ponce Wong, J. D. Posner, and V. J. Santos, "Flexible microfluidic normal force sensor skin for tactile feedback," *Sensors Actuators A Phys.*, vol. 179, pp. 62–69, jun 2012.

[34] A. Tabatabai, A. Fassler, C. Usiak, and C. Majidi, "Liquid-phase gallium-indium alloy electronics with microcontact printing.," *Langmuir : the ACS journal of surfaces and colloids*, vol. 29, pp. 6194–200, May 2013.

[35] C. Ladd, J.-H. So, J. Muth, and M. D. Dickey, "3D printing of free standing liquid metal microstructures.," *Advanced materials (Deerfield Beach, Fla.)*, vol. 25, pp. 5081–5, Sept. 2013.

[36] J. W. Boley, E. L. White, G. T.-C. Chiu, and R. K. Kramer, "Direct Writing of Gallium-Indium Alloy for Stretchable Electronics," *Adv. Funct. Mater.*, vol. 24, pp. 3501–3507, jun 2014.

[37] A. Fassler and C. Majidi, "Liquid-Phase Metal Inclusions for a Conductive Polymer Composite," *Adv. Mater.*, vol. 27, no. 11, pp. 1928–1932, 2015.

[38] M. D. Bartlett, A. Fassler, N. Kazem, E. J. Markvicka, P. Mandal, and C. Majidi, "Stretchable, High- k Dielectric Elastomers through Liquid-Metal Inclusions," *Adv. Mater.*, vol. 28, pp. 3726–3731, may 2016.

[39] M. D. Bartlett, N. Kazem, M. J. Powell-Palm, X. Huang, W. Sun, J. A. Malen, and C. Majidi, "High thermal conductivity in soft elastomers with elongated liquid metal inclusions," *Proc. Natl. Acad. Sci.*, vol. 114, pp. 2143–2148, feb 2017.

[40] M. Yim, Ying Zhang, and D. Duff, "Modular robots," *IEEE Spectr.*, vol. 39, no. 2, pp. 30–34, 2002.

[41] A. Lyder, R. Garcia, and K. Stoy, "Mechanical design of odin, an extendable heterogeneous deformable modular robot," in *2008 IEEE/RSJ Int. Conf. Intell. Robot. Syst.*, pp. 883–888, IEEE, sep 2008.

[42] A. Kamimura, S. Murata, E. Yoshida, H. Kurokawa, K. Tomita, and S. Kokaji, "Self-reconfigurable modular robot - experiments on reconfiguration and locomotion," in *Proc. 2001 IEEE/RSJ Int. Conf. Intell. Robot. Syst. Expand. Soc. Role Robot. Next Millenn. (Cat. No.01CH37180)*, vol. 1, pp. 606–612, IEEE, 2001.

[43] M. T. Tolley, S. M. Felton, S. Miyashita, D. Aukes, D. Rus, and R. J. Wood, "Self-folding origami: shape memory composites activated by uniform heating," *Smart Mater. Struct.*, vol. 23, p. 094006, sep 2014.

[44] M. Salerno, K. Zhang, A. Menciassi, and J. S. Dai, "A novel 4-DOFs origami enabled, SMA actuated, robotic end-effector for minimally invasive surgery," in *2014 IEEE Int. Conf. Robot. Autom.*, pp. 2844–2849, IEEE, may 2014.

[45] E. Brown, N. Rodenberg, J. Amend, a. Mozeika, E. Steltz, M. R. Zakin, H. Lipson, and H. M. Jaeger, "From the Cover: Universal robotic gripper based on the jamming of granular material," *Proc. Natl. Acad. Sci.*, vol. 107, no. 44, pp. 18809–18814, 2010.

[46] J. Carlson, D. Catanzarite, and K. St. Clair, "COMMERCIAL MAGNETO-RHEOLOGICAL FLUID DEVICES," *Int. J. Mod. Phys. B*, vol. 10, pp. 2857–2865, oct 1996.

[47] J. Z. Chen and W. H. Liao, "Design, testing and control of a magnetorheological actuator for assistive knee braces," *Smart Mater. Struct.*, vol. 19, p. 035029, mar 2010.

[48] S. J. Dyke, B. F. Spencer, M. K. Sain, and J. D. Carlson, "Modeling and control of magnetorheological dampers for seismic response reduction," *Smart Mater. Struct.*, vol. 5, pp. 565–575, oct 1996.

[49] C. Majidi and R. J. Wood, "Tunable elastic stiffness with microconfined magnetorheological domains at low magnetic field," *Appl. Phys. Lett.*, vol. 97, no. 16, p. 164104, 2010.

[50] D. L. Hartsock, "ER fluid requirements for automotive devices," *J. Rheol. (N. Y. N. Y).*, vol. 35, p. 1305, oct 1991.

[51] J. Furusho and M. Sakaguchi, "New Actuators Using ER Fluid and Their Applications to Force Display Devices in Virtual Reality and Medical Treatments," *Int. J. Mod. Phys. B*, vol. 13, pp. 2151–2159, jun 1999.

[52] M. Camacho-Lopez, H. Finkelmann, P. Palffy-Muhoray, and M. Shelley, "Fast liquid-crystal elastomer swims into the dark," *Nat. Mater.*, vol. 3, pp. 307–310, may 2004.

[53] D. K. Shenoy, D. Laurence Thomsen III, A. Srinivasan, P. Keller, and B. R. Ratna, "Carbon coated liquid crystal elastomer film for artificial muscle applications," *Sens Actuators A Phys.*, vol. 96, pp. 184–188, feb 2002.

[54] D. L. Thomsen, P. Keller, J. Naciri, R. Pink, H. Jeon, D. Shenoy, and B. R. Ratna, "Liquid Crystal Elastomers with Mechanical Properties of a Muscle," *Macromolecules*, vol. 34, pp. 5868–5875, aug 2001.

[55] T. H. Ware and T. J. White, "Programmed liquid crystal elastomers with tunable actuation strain," *Polym. Chem.*, vol. 6, no. 26, pp. 4835–4844, 2015.

[56] L. Ionov, "Hydrogel-based actuators: possibilities and limitations," *Mater. Today*, vol. 17, pp. 494–503, dec 2014.

[57] C. Yu, Z. Duan, P. Yuan, Y. Li, Y. Su, X. Zhang, Y. Pan, L. L. Dai, R. G. Nuzzo, Y. Huang, H. Jiang, and J. A. Rogers, "Electronically Programmable, Reversible Shape Change in Two- and Three-Dimensional Hydrogel Structures," *Adv. Mater.*, vol. 25, pp. 1541–1546, mar 2013.

[58] R. F. Shepherd, F. Ilievski, W. Choi, S. A. Morin, A. A. Stokes, A. D. Mazzeo, X. Chen, M. Wang, and G. M. Whitesides, "Multigait soft robot," *Proc. Natl. Acad. Sci. U. S. A.*, vol. 108, pp. 20400–3, dec 2011.

[59] C. D. Onal, X. Chen, G. M. Whitesides, and D. Rus, "Soft mobile robots with on-board chemical pressure generation," in *Int. Symp. Robot. Res.*, (Flagstaff), pp. 1–16, International Foundation for Robotics Research, 2011.

[60] R. V. Martinez, J. L. Branch, C. R. Fish, L. Jin, R. F. Shepherd, R. M. D. Nunes, Z. Suo, and G. M. Whitesides, "Robotic Tentacles with Three-Dimensional Mobility Based on Flexible Elastomers," *Adv. Mater.*, vol. 25, pp. 205–212, jan 2013.

[61] F. Daerden, D. Lefeber, B. Verrelst, and R. Van Ham, "Pleated pneumatic artificial muscles: actuators for automation and robotics," in *2001 IEEE/ASME Int. Conf. Adv. Intell. Mechatronics. Proc. (Cat. No.01TH8556)*, vol. 2, pp. 738–743, IEEE, 2001.

[62] B. Hannaford, "Measurement and modeling of McKibben pneumatic artificial muscles," *IEEE Trans. Robot. Autom.*, vol. 12, no. 1, pp. 90–102, 1996.

[63] Y.-L. Park, B.-r. Chen, C. Majidi, R. J. Wood, R. Nagpal, and E. Goldfield, "Active modular elastomer sleeve for soft wearable assistance robots," *2012 IEEE/RSJ Int. Conf. Intell. Robot. Syst.*, pp. 1595–1602, Oct. 2012.

[64] K. Otsuka and K. Shimizu, "Memory effect and thermoelastic martensite transformation in CuAlNi alloy," *Scripta Metallurgica*, vol. 4, pp. 469–472, June 1970.

[65] J. Madden, N. Vandesteeg, P. Anquetil, P. Madden, A. Takshi, R. Pytel, S. Lafontaine, P. Wieringa, and I. Hunter, "Artificial Muscle Technology: Physical Principles and Naval Prospects," *IEEE Journal of Oceanic Engineering*, vol. 29, pp. 706–728, July 2004.

[66] H.-T. Lin, G. G. Leisk, and B. Trimmer, "GoQBot: a caterpillar-inspired soft-bodied rolling robot.," *Bioinspiration & biomimetics*, vol. 6, p. 026007, June 2011.

[67] Z. Wang, G. Hang, J. Li, Y. Wang, and K. Xiao, "A micro-robot fish with embedded SMA wire actuated flexible biomimetic fin," *Sensors and Actuators A: Physical*, vol. 144, pp. 354–360, June 2008.

[68] M. Shahinpoor, Y. Bar-Cohen, J. O. Simpson, and J. Smith, "Ionic polymer-metal composites (IPMCs) as biomimetic sensors, actuators and artificial muscles - a review," *Smart Materials and Structures*, vol. 7, pp. R15–R30, Dec. 1998.

[69] Y. Jeonga, Y. Taka, and S. Korea, "A ciliary based 8-legged walking micro robot using cast IPMC actuators," in *2003 IEEE International Conference on Robotics and Automation (Cat. No.03CH37422)*, vol. 3, pp. 2940–2945, IEEE, 2003.

[70] R. Pelrine, R. Kornbluh, and J. Joseph, "Electrostriction of polymer dielectrics with compliant electrodes as a means of actuation," *Sens Actuators A Phys.*, vol. 64, no. 97, pp. 77–85, 1998.

[71] R. Pelrine, "High-Speed Electrically Actuated Elastomers with Strain Greater Than 100%," *Science (80-.).*, vol. 287, pp. 836–839, feb 2000.

[72] Q. Pei, M. A. Rosenthal, R. Pelrine, S. Stanford, and R. D. Kornbluh, "Multifunctional electroelastomer roll actuators and their application for biomimetic walking robots," in *SPIE Proc.* (Y. Bar-Cohen, ed.), vol. 5051, (San Diego), pp. 281–290, SRI International, SPIE, jul 2003.

[73] G. Kovacs, P. Lochmatter, and M. Wissler, "An arm wrestling robot driven by dielectric elastomer actuators," *Smart Materials and Structures*, vol. 16, pp. S306–S317, Apr. 2007.

[74] K. Jung, J. C. Koo, J.-d. Nam, Y. K. Lee, and H. R. Choi, "Artificial annelid robot driven by soft actuators.," *Bioinspiration & biomimetics*, vol. 2, pp. S42–S49, June 2007.

[75] S.-Y. Tang, V. Sivan, K. Khoshmanesh, A. P. O'Mullane, X. Tang, B. Gol, N. Eshtiaghi, F. Lieder, P. Petersen, A. Mitchell, and K. Kalantar-zadeh, "Electrochemically induced actuation of liquid metal marbles.," *Nanoscale*, vol. 5, pp. 5949–57, jul 2013.

[76] S.-Y. Tang, K. Khoshmanesh, V. Sivan, P. Petersen, A. P. O'Mullane, D. Abbott, A. Mitchell, and K. Kalantar-zadeh, "Liquid metal enabled pump," *Proc. Natl. Acad. Sci.*, vol. 111, pp. 3304–3309, mar 2014.

[77] M. R. Khan, C. B. Eaker, E. F. Bowden, and M. D. Dickey, "Giant and switchable surface activity of liquid metal via surface oxidation.," *Proc. Natl. Acad. Sci. U. S. A.*, vol. 111, pp. 14047–51, sep 2014.

[78] D. J. Lipomi, M. Vosgueritchian, B. C.-K. Tee, S. L. Hellstrom, J. a. Lee, C. H. Fox, and Z. Bao, "Skin-like pressure and strain sensors based on transparent elastic films of carbon nanotubes.," *Nature nanotechnology*, vol. 6, pp. 788–92, Dec. 2011.

[79] C. Laschi, B. Mazzolai, V. Mattoli, M. Cianchetti, and P. Dario, "Design of a biomimetic robotic octopus arm.," *Bioinspiration & biomimetics*, vol. 4, p. 015006, Mar. 2009.

[80] H.-J. Kim, C. Son, and B. Ziaie, "A multiaxial stretchable interconnect using liquid-alloy-filled elastomeric microchannels," *Applied Physics Letters*, vol. 92, no. 1, p. 011904, 2008.

[81] A. Fassler and C. Majidi, "Soft-matter capacitors and inductors for hyperelastic strain sensing and stretchable electronics," *Smart Mater. Struct.*, vol. 22, p. 055023, may 2013.

[82] J.-H. So, H.-J. Koo, M. D. Dickey, and O. D. Velev, "Ionic Current Rectification in Soft-Matter Diodes with Liquid-Metal Electrodes," *Advanced Functional Materials*, vol. 22, pp. 625–631, Feb. 2012.

[83] L. R. Finkenauer and C. Majidi, "Complaint liquid metal electrodes for dielectric elastomer actuators," *SPIE Proc.*, vol. 9056, p. 90563I, Mar. 2014.

[84] O. A. Araromi, I. Gavrilovich, J. Shintake, S. Rosset, and H. R. Shea, "Towards a deployable satellite gripper based on multisegment dielectric elastomer minimum energy structures," in *Proceedings of SPIE* (Y. Bar-Cohen, ed.), vol. 9056, p. 90562G, Mar. 2014.

[85] R. Zhang, A. Kunz, P. Lochmatter, and G. Kovacs, "Dielectric elastomer spring roll actuators for a portable force feedback device," in *Haptic Interfaces for Virtual Environment and Teleoperator Systems, 2006 14th Symposium on*, pp. 347–353, IEEE, mar 2006.

[86] S. M. C. Abdulla, H. Yagubizade, and G. J. M. Krijnen, "Analysis of resonance frequency and pull-in voltages of curled micro-bimorph cantilevers," *Journal of Micromechanics and Microengineering*, vol. 22, p. 035014, Mar. 2012.

[87] P. Lochmatter, *Development of a Shell-like Electroactive Polymer (EAP) Actuator*. PhD thesis, ETH Zurich, 2007.

[88] S. Rosset, M. Niklaus, P. Dubois, H. R. Shea, and S. Member, "Large-Stroke Dielectric Elastomer Actuators With Ion-Implanted Electrodes," *J. Microelectromech. Syst.*, vol. 18, no. 6, pp. 1300–1308, 2009.

[89] A. P. Gerratt, B. Balakrisnan, I. Penskiy, and S. Bergbreiter, "Dielectric elastomer actuators fabricated using a micro-molding process," *Smart Mater. Struct.*, vol. 23, p. 055004, may 2014.

[90] A. Rajamani, M. D. Grissom, C. D. Rahn, and Q. Zhang, "Wound Roll Dielectric Elastomer Actuators: Fabrication, Analysis, and Experiments," *IEEE ASME Trans. Mechatron.*, vol. 13, pp. 117–124, Feb. 2008.

[91] G. Kovacs, L. Dring, S. Michel, and G. Terrasi, "Stacked dielectric elastomer actuator for tensile force transmission," *Sensors and Actuators A: Physical*, vol. 155, pp. 299–307, Oct. 2009.

[92] W. Lai, A. F. Bastawros, W. Hong, and S.-J. Chung, "Fabrication and analysis of planar dielectric elastomer actuators capable of complex 3-D deformation," *2012 IEEE Int. Conf. Robot. Autom.*, pp. 4968–4973, May 2012.

[93] S. Rosset and H. R. Shea, "Flexible and stretchable electrodes for dielectric elastomer actuators," *Appl. Phys. A Mater. Sci. Process*, vol. 110, pp. 281–307, Nov. 2013.

[94] G.-K. Lau, S. C.-K. Goh, and L.-L. Shiau, "Dielectric elastomer unimorph using flexible electrodes of electrolessly deposited (ELD) silver," *Sensors and Actuators A: Physical*, vol. 169, pp. 234–241, Sept. 2011.

[95] R. Palakodeti and M. Kessler, "Influence of frequency and prestrain on the mechanical efficiency of dielectric electroactive polymer actuators," *Mater. Lett.*, vol. 60, pp. 3437–3440, Dec. 2006.

[96] C. Keplinger, J.-Y. Sun, C. C. Foo, P. Rothemund, G. M. Whitesides, and Z. Suo, "Stretchable, transparent, ionic conductors," *Science*, vol. 341, pp. 984–987, Aug. 2013.

[97] Y. Sun, V. Kumar, I. Adesida, and J. Rogers, "Buckled and Wavy Ribbons of GaAs for High-Performance Electronics on Elastomeric Substrates," *Adv. Mater.*, vol. 18, pp. 2857–2862, Nov. 2006.

[98] R. C. Chiechi, E. A. Weiss, M. D. Dickey, and G. M. Whitesides, "Eutectic gallium-indium (EGaIn): a moldable liquid metal for electrical characterization of self-assembled monolayers.," *Angew. Chem. Int. Ed. Engl.*, vol. 47, pp. 142–144, Jan. 2008.

[99] Y. Liu, M. Gao, S. Mei, Y. Han, and J. Liu, "Ultra-compliant liquid metal electrodes with in-plane self-healing capability for dielectric elastomer actuators," *Appl. Phys. Lett.*, vol. 103, no. 6, p. 064101, 2013.

[100] C. Majidi, Y.-L. Park (co-first author), R. Kramer, P. Bérard, and R. J. Wood, "Hyperelastic pressure sensing with a liquid-embedded elastomer," *J. Micromech. Microeng.*, vol. 20, p. 125029, Dec. 2010.

[101] S. Cheng and Z. Wu, "Microfluidic Electronics," *Lab Chip*, vol. 12, pp. 2782–2791, Aug. 2012.

[102] R. K. Kramer, C. Majidi, and R. J. Wood, "Masked Deposition of Gallium-Indium Alloys for Liquid-Embedded Elastomer Conductors," *Adv. Funct. Mater.*, vol. 23, pp. 5292–5296, Nov. 2013.

[103] S. H. Jeong, A. Hagman, K. Hjort, M. Jobs, J. Sundqvist, and Z. Wu, "Liquid alloy printing of microfluidic stretchable electronics.," *Lab Chip*, vol. 12, pp. 4657–64, nov 2012.

[104] R. M. McMeeking and C. M. Landis, "Electrostatic Forces and Stored Energy for Deformable Dielectric Materials," *J. Appl. Mech.*, vol. 72, no. 4, p. 581, 2005.

[105] M. Wissler and E. Mazza, "Electromechanical coupling in dielectric elastomer actuators," *Sens Actuators A Phys.*, vol. 138, pp. 384–393, Aug. 2007.

[106] Z. Suo, "Theory of dielectric elastomers," *Acta Mech. Solida Sin.*, vol. 23, pp. 549–578, dec 2010.

[107] B.-X. Xu, R. Mueller, A. Theis, M. Klassen, and D. Gross, "Dynamic analysis of dielectric elastomer actuators," *Appl. Phys. Lett.*, vol. 100, no. 11, p. 112903, 2012.

[108] J. Zhu, S. Cai, and Z. Suo, "Resonant behavior of a membrane of a dielectric elastomer," *Int. J. Solids Struct.*, vol. 47, pp. 3254–3262, Dec. 2010.

[109] J. Zhu, S. Cai, and Z. Suo, "Nonlinear oscillation of a dielectric elastomer balloon," *Polym. Int.*, vol. 59, pp. 378–383, Feb. 2010.

[110] D. De Tommasi, G. Puglisi, and G. Zurlo, "Failure modes in electroactive polymer thin films with elastic electrodes," *J. Phys. D. Appl. Phys.*, vol. 47, p. 065502, Feb. 2014.

[111] G. Puglisi and G. Zurlo, "Electric field localizations in thin dielectric films with thickness non-uniformities," *J. Electrostat.*, vol. 70, pp. 312–316, June 2012.

[112] H. S. Park and T. D. Nguyen, "Viscoelastic effects on electromechanical instabilities in dielectric elastomers," *Soft Matter*, vol. 9, no. 4, p. 1031, 2013.

[113] L. R. G. Treloar, "Stresses and Birefringence in Rubber subjected to General Homogeneous Strain," *Proc. Phys. Soc.*, vol. 60, pp. 135–144, Feb. 1948.

[114] M. Mooney, "A Theory of Large Elastic Deformation," *J. Appl. Phys.*, vol. 11, no. 9, p. 582, 1940.

[115] R. S. Rivlin, "Large Elastic Deformations of Isotropic Materials. IV. Further Developments of the General Theory," *Philos Trans R Soc L. A*, vol. 241, pp. 379–397, Oct. 1948.

[116] R. Ogden, "Large deformation isotropic elasticity-on the correlation of theory and experiment for incompressible rubberlike solids," *Proc. R. Soc. Lond. A*, vol. 241, no. 1567, pp. 565–584, 1972.

[117] I. D. Joshipura, H. R. Ayers, C. Majidi, and M. D. Dickey, "Methods to pattern liquid metals," *J. Mater. Chem. C*, vol. 3, no. 16, pp. 3834–3841, 2015.

[118] B. A. Gozen, A. Tabatabai, O. B. Ozdoganlar, and C. Majidi, "High-density soft-matter electronics with micron-scale line width.," *Advanced materials (Deerfield Beach, Fla.)*, vol. 26, pp. 5211–6, Aug. 2014.

[119] P. Roberts, D. D. Damian, W. Shan, T. Lu, and C. Majidi, "Soft-Matter Capacitive Sensor for Measuring Shear and Pressure Deformation," in *2013 IEEE International Conference on Robotics and Automation (ICRA)*, (Karlsruhe), pp. 3529–3534, IEEE, 2013.

[120] D. Kim, Y. Lee, D.-W. Lee, W. Choi, and J.-b. J. B. Lee, "Hydrochloric acid-impregnated paper for liquid metal microfluidics," in *2013 Transducers & Eurosensors XXVII: The 17th International Conference on Solid-State Sensors, Actuators and Microsystems (TRANSDUCERS & EUROSENSORS XXVII)*, (Barcelona), pp. 2620–2623, IEEE, June 2013.

[121] G. Li, M. Parmar, and D.-W. Lee, "An oxidized liquid metal-based microfluidic platform for tunable electronic device applications.," *Lab on a chip*, Nov. 2014.

[122] Z. Wang, A. a. Volinsky, and N. D. Gallant, "Crosslinking effect on polydimethylsiloxane elastic modulus measured by custom-built compression instrument," *J. Appl. Polym. Sci.*, vol. 131, p. 41050, Nov. 2014.

[123] Y. M. Song, Y. Xie, V. Malyarchuk, J. Xiao, I. Jung, K.-J. Choi, Z. Liu, H. Park, C. Lu, R.-H. Kim, R. Li, K. B. Crozier, Y. Huang, and J. a. Rogers, "Digital cameras with designs inspired by the arthropod eye.," *Nature*, vol. 497, pp. 95–99, May 2013.

[124] J. Y. Park, S. J. Yoo, E.-J. Lee, D. H. Lee, J. Y. Kim, and S.-H. Lee, "Increased poly(dimethylsiloxane) stiffness improves viability and morphology of mouse fibroblast cells," *BioChip J.*, vol. 4, pp. 230–236, Sept. 2010.

[125] D. Armani, C. Liu, and N. Aluru, "Re-configurable fluid circuits by PDMS elastomer micromachining," *Tech. Dig. IEEE Int. MEMS 99 Conf. Twelfth IEEE Int. Conf. Micro Electro Mech. Syst. (Cat. No.99CH36291)*, pp. 222–227, 1999.

[126] A. P. Gerratt, I. Penskiy, and S. Bergbreiter, "SOI/elastomer process for energy storage and rapid release," *Journal of Micromechanics and Microengineering*, vol. 20, p. 104011, Oct. 2010.

[127] M. Shalaby, Zhongde Wang, L.-W. Chow, B. Jensen, J. Volakis, K. Kurabayashi, and K. Saitou, "Robust Design of RF-MEMS Cantilever Switches Using Contact Physics Modeling," *IEEE Trans. Ind. Electron.*, vol. 56, pp. 1012–1021, apr 2009.

[128] S. Majumder, N. McGruer, G. G. Adams, P. Zavracky, R. H. Morrison, and J. Krim, "Study of contacts in an electrostatically actuated microswitch," *Sensors and Actuators A: Physical*, vol. 93, pp. 19–26, Aug. 2001.

[129] C. Goldsmith, S. Eshelman, and D. Denniston, "Performance of low-loss RF MEMS capacitive switches," *IEEE Microw. Guid. Wave Lett.*, vol. 8, no. 8, pp. 269–271, 1998.

[130] G. Sathyanarayana, *Computational Analysis of Cantilever Beam Electrostatic MEMS Actuators*. PhD thesis, Indian Institute of Science, 2010.

[131] G. O'Brien, D. J. Monk, and L. Lin, "MEMS cantilever beam electrostatic pull-in model," in *Design, Characterization, and Packaging for MEMS and Microelectronics* (P. D. Franzon, A. P. Malshe, and F. E. Tay, eds.), (Adelaide), pp. 31–41, SPIE, Nov. 2001.

[132] K. Petersen, "Dynamic micromechanics on silicon: Techniques and devices," *IEEE Transactions on Electron Devices*, vol. 25, pp. 1241–1250, Oct. 1978.

[133] V. Linder, B. D. Gates, D. Ryan, B. a. Parviz, and G. M. Whitesides, "Water-soluble sacrificial layers for surface micromachining.," *Small (Weinheim an der Bergstrasse, Germany)*, vol. 1, pp. 730–6, July 2005.

[134] S. R. Oh, K. Yao, and F. E. H. Tay, "Fabrication of piezoelectric P(VDF-TrFE) microcantilevers by wafer-level surface micromachining," *Journal of Micromechanics and Microengineering*, vol. 23, p. 095023, Sept. 2013.

[135] J. Gao, D. Guo, S. Santhanam, Y. Yu, A. J. McGaughey, S.-C. Yao, and G. K. Fedder, "Release and transfer of large-area ultra-thin PDMS," *2014 IEEE 27th International Conference on Micro Electro Mechanical Systems (MEMS)*, pp. 544–547, Jan. 2014.

[136] S. Bhattacharya, a. Datta, J. Berg, and S. Gangopadhyay, "Studies on surface wettability of poly(dimethyl) siloxane (PDMS) and glass under oxygen-plasma treatment and correlation with bond strength," *Journal of Microelectromechanical Systems*, vol. 14, pp. 590–597, June 2005.

[137] K. Tsougeni, N. Vourdas, a. Tserepi, E. Gogolides, and C. Cardinaud, "Mechanisms of oxygen plasma nanotexturing of organic polymer surfaces: from stable super hydrophilic to super hydrophobic surfaces.," *Langmuir : the ACS journal of surfaces and colloids*, vol. 25, pp. 11748–59, Oct. 2009.

[138] D. T. Eddington, J. P. Puccinelli, and D. J. Beebe, "Thermal aging and reduced hydrophobic recovery of polydimethylsiloxane," *Sensors and Actuators B: Chemical*, vol. 114, pp. 170–172, Mar. 2006.

[139] D. Bodas and C. Khan-Malek, "Hydrophilization and hydrophobic recovery of PDMS by oxygen plasma and chemical treatmentAn SEM investigation," *Sensors and Actuators B: Chemical*, vol. 123, pp. 368–373, Apr. 2007.

[140] D. Bodas and C. Khan-Malek, "Formation of more stable hydrophilic surfaces of PDMS by plasma and chemical treatments," *Microelectronic Engineering*, vol. 83, pp. 1277–1279, Apr. 2006.

[141] J. S. Townsend, *Electricity in Gases*. New York: Oxford at the Clarendon Press, 1915.

[142] A. Peschot, N. Bonifaci, O. Lesaint, C. Valadares, and C. Poulain, "Deviations from the Paschen's law at short gap distances from 100 nm to 10 μ m in air and nitrogen," *Appl. Phys. Lett.*, vol. 105, p. 123109, sep 2014.

[143] M. P. de Boer and T. A. Michalske, "Accurate method for determining adhesion of cantilever beams," *J. Appl. Phys.*, vol. 86, no. 2, pp. 817–827, 1999.

[144] L. R. G. Treloar, "The Elasticity of a Network of Long-Chain Molecules. I," *Rubber Chem. Technol.*, vol. 16, pp. 746–751, Dec. 1943.

[145] L. R. G. Treloar, "The Elasticity of a Network of Long-Chain Molecules. II," *Rubber Chem. Technol.*, vol. 17, pp. 296–302, June 1944.

[146] F. B. Fu and R. W. Ogden, eds., *Nonlinear Elasticity: Theory and Applications*. New York: Cambridge University Press, 2001.

[147] B. Kim, S. B. Lee, J. Lee, S. Cho, H. Park, S. Yeom, and S. H. Park, "A comparison among Neo-Hookean model, Mooney-Rivlin model, and Ogden model for chloroprene rubber," *Int. J. Precis. Eng. Manuf.*, vol. 13, pp. 759–764, May 2012.

[148] O. O'Reilly, "On constitutive relations for elastic rods," *Int. J. Solids Struct.*, vol. 35, pp. 1009–1024, Apr. 1998.

[149] S. P. Timoshenko and J. M. Gere, "Beam-Columns," in *Theory Elastic Stab.*, ch. 1, p. 2, Mineola: Dover Publications, inc., 2 ed., 1989.

[150] R. W. Ogden, G. Saccomandi, and I. Sgura, "Fitting hyperelastic models to experimental data," *Comput. Mech.*, vol. 34, pp. 484–502, nov 2004.

[151] J. A. Rogers, T. Someya, and Y. Huang, "Materials and mechanics for stretchable electronics.," *Science*, vol. 327, pp. 1603–7, Mar. 2010.

[152] C. Majidi, "Soft robotics: A perspective - current trends and prospects for the future," *Soft Robotics*, vol. 1, no. 1, pp. 5–11, 2014.

[153] H.-J. Koo, J.-H. So, M. D. Dickey, and O. D. Velev, "Towards all-soft matter circuits: prototypes of quasi-liquid devices with memristor characteristics.," *Advanced Materials*, vol. 23, pp. 3559–64, Aug. 2011.

[154] D.-H. Kim, N. Lu, R. Ma, Y.-S. Kim, R.-H. Kim, S. Wang, J. Wu, S. M. Won, H. Tao, A. Islam, *et al.*, "Epidermal electronics," *Science*, vol. 333, no. 6044, pp. 838–843, 2011.

[155] E. P. Chan, E. J. Smith, R. C. Hayward, and A. J. Crosby, "Surface wrinkles for smart adhesion," *Advanced Materials*, vol. 20, no. 4, pp. 711–716, 2008.

[156] D. R. Paretkar, M. D. Bartlett, R. McMeeking, A. J. Crosby, and E. Arzt, "Buckling of an Adhesive Polymeric Micropillar," *The Journal of Adhesion*, vol. 89, pp. 140–158, Feb. 2013.

[157] J. Y. Chung, J. P. Youngblood, and C. M. Stafford, "Anisotropic wetting on tunable micro-wrinkled surfaces," *Soft Matter*, vol. 3, no. 9, p. 1163, 2007.

[158] Z. Chen, Q. Guo, C. Majidi, W. Chen, D. J. Srolovitz, and M. P. Haataja, "Nonlinear geometric effects in mechanical bistable morphing structures," *Physical Review Letters*, vol. 109, no. 11, p. 114302, 2012.

[159] N. P. Bende, A. A. Evans, S. Innes-Gold, L. A. Marin, I. Cohen, R. C. Hayward, and C. D. Santangelo, "Geometrically controlled snapping transitions in shells with curved creases," *Proc. Nat. Acad. Sci. U.S.A.*, vol. 112, no. 36, p. 1117511180, 2015.

[160] D. P. Holmes, B. Tavakol, G. Froehlicher, and H. a. Stone, "Control and manipulation of microfluidic flow via elastic deformations," *Soft Matter*, vol. 9, no. 29, p. 7049, 2013.

[161] J. Shim, C. Perdigou, E. R. Chen, K. Bertoldi, and P. M. Reis, "Buckling-induced encapsulation of structured elastic shells under pressure," *Proceedings of the National Academy of Sciences*, vol. 109, no. 16, pp. 5978–5983, 2012.

[162] A. Fargette, S. Neukirch, and A. Antkowiak, "Elastocapillary snapping: Capillarity induces snap-through instabilities in small elastic beams," *Physical Review Letters*, vol. 112, no. 13, p. 137802, 2014.

[163] J. T. B. Overvelde, T. Kloek, J. J. A. Dhaen, and K. Bertoldi, "Amplifying the response of soft actuators by harnessing snap-through instabilities," *PNAS*, vol. 112, no. 35, pp. 10863–10868, 2015.

[164] C. Keplinger, T. Li, R. Baumgartner, Z. Suo, and S. Bauer, "Harnessing snap-through instability in soft dielectrics to achieve giant voltage-triggered deformation," *Soft Matter*, vol. 8, no. 2, pp. 285–288, 2012.

[165] D. P. Holmes and A. J. Crosby, "Snapping surfaces," *Advanced Materials*, vol. 19, pp. 3589–3593, 2007.

[166] S. Hhn, A. R. Honerkamp-Smith, P. A. Haas, P. Khuc Trong, and R. E. Goldstein, "Dynamics of a volvox embryo turning itself inside out," *Phys. Rev. Lett.*, vol. 114, no. 17, p. 178101, 2015.

[167] X. Noblin, N. O. Rojas, J. Westbrook, M. Llorens, C. Argentina, and J. Dumais, "The fern sporangium: A unique catapult," *Science*, vol. 335, no. 110, p. 6074, 2012.

[168] Q. Guo, E. Dai, X. Han, S. Xie, E. Chao, and Z. Chen, "Fast nastic motion of plants and bio-inspired structures," *Journal of the Royal Society Interface*, vol. 12, no. 110, p. 20150598, 2015.

[169] P. Seunghoon and H. Dooyoung, "Pre-shaped buckled-beam actuators: Theory and experiments," *Sensors and Actuators, A: Physical*, vol. 148, pp. 186–192, 2008.

[170] E. Dowell, "Comment on "On Dynamic Snap Buckling of Shallow Arches"," *AIAA Journal*, vol. 4, no. 5, pp. 1887–1888, 1966.

[171] J. Zhao, J. Jia, X. He, and H. Wang, "Post-buckling and Snap-Through Behavior of Inclined Slender Beams," *Journal of Applied Mechanics*, vol. 75, no. July, p. 041020, 2008.

[172] M. Vangbo and Y. Bäcklund, "A lateral symmetrically bistable buckled beam," *Journal of Micromechanics and Microengineering*, vol. 8, pp. 29–32, 1999.

[173] M. Vangbo, "An analytical analysis of a compressed bistable buckled beam," *Sensors and Actuators A: Physical*, vol. 69, no. 98, pp. 212–216, 1998.

[174] L. Medina, R. Gilat, and S. Krylov, "Symmetry Breaking Criteria in Electrostatically Loaded Bistable Curved/Prebuckled Micro Beams," *Prog. Opt. Sci., Photonics*, no. July, pp. 679–705, 2013.

[175] Y. Shen, M. F. Golnaraghi, and G. R. Heppler, "Experimental research and modeling of magnetorheological elastomers," *Journal of Intelligent Material Systems and Structures*, vol. 15, no. 1, pp. 27–35, 2004.

[176] M. Yalcintas and H. Dai, "Magnetorheological and electrorheological materials in adaptive structures and their performance comparison," *Smart Materials and Structures*, vol. 8, no. 5, p. 560, 1999.

[177] G. Stepanov, S. Abramchuk, D. Grishin, L. Nikitin, E. Y. Kramarenko, and A. Khokhlov, "Effect of a homogeneous magnetic field on the viscoelastic behavior of magnetic elastomers," *Polymer*, vol. 48, no. 2, pp. 488–495, 2007.

[178] W. Miles, J. Goff, P. Huffstetler, O. Mefford, J. Riffle, and R. Davis, "The design of well-defined pdms–magnetite complexes," *Polymer*, vol. 51, no. 2, pp. 482–491, 2010.

[179] B. A. Evans, B. L. Fiser, W. J. Prins, D. J. Rapp, A. R. Shields, D. R. Glass, and R. Superfine, "A highly tunable silicone-based magnetic elastomer with nanoscale homogeneity," *Journal of magnetism and magnetic materials*, vol. 324, no. 4, pp. 501–507, 2012.

[180] J. D. Carlson and M. R. Jolly, "Mr fluid, foam and elastomer devices," *mechatronics*, vol. 10, no. 4, pp. 555–569, 2000.

[181] J. M. Ginder, M. E. Nichols, L. D. Elie, and J. L. Tardiff, "Magnetorheological elastomers: properties and applications," in *1999 Symposium on Smart Structures and Materials*, pp. 131–138, International Society for Optics and Photonics, 1999.

[182] J. M. Ginder, M. E. Nichols, L. D. Elie, and S. M. Clark, "Controllable-stiffness components based on magnetorheological elastomers," in *SPIE's 7th Annual International Symposium on Smart Structures and Materials*, pp. 418–425, International Society for Optics and Photonics, 2000.

[183] S. Abramchuk, D. Grishin, E. Y. Kramarenko, G. Stepanov, and A. Khokhlov, "Effect of a homogeneous magnetic field on the mechanical behavior of soft magnetic elastomers under compression," *Polymer Science Series A*, vol. 48, no. 2, pp. 138–145, 2006.

[184] S. Ahmed, C. Lauff, A. Crivaro, K. McGough, R. Sheridan, M. Frecker, P. von Lockette, Z. Ounaies, T. Simpson, J.-M. Lien, and R. Strzelec, "Multi-field responsive origami structures: Preliminary modeling and experiments," *Proc. ASME IDETC/CIE*, vol. 6B, no. DETC2013, p. V06BT07A028, 2013.

[185] T. Lu, J. Wissman, Ruthika, and C. Majidi, "Soft anisotropic conductors as electric vias for ga-based liquid metal circuits," *ACS Appl. Mater. & Interfaces*, vol. in press, 2015.

[186] K. Fukui, "The path of chemical reactions-the irc approach," *Accounts of chemical research*, vol. 14, no. 12, pp. 363–368, 1981.

[187] R. C. Gough, A. M. Morishita, J. H. Dang, M. R. Moorefield, W. a. Shiroma, and A. T. Ohta, "Rapid electrocapillary deformation of liquid metal with reversible shape retention," *Micro Nano Syst. Lett.*, vol. 3, p. 4, dec 2015.

[188] M. R. Khan, C. Trlica, and M. D. Dickey, "Recapillarity: Electrochemically Controlled Capillary Withdrawal of a Liquid Metal Alloy from Microchannels," *Adv. Funct. Mater.*, vol. 25, pp. 671–678, feb 2015.

[189] N. A. Bezdenejnykh, J. Meseguer, and J. M. Perales, "Experimental analysis of stability limits of capillary liquid bridges," *Phys. Fluids A Fluid Dyn.*, vol. 4, pp. 677–680, apr 1992.

[190] T.-Y. Chen, J. A. Tsamopoulos, and R. J. Good, "Capillary bridges between parallel and non-parallel surfaces and their stability," *J. Colloid Interface Sci.*, vol. 151, pp. 49–69, jun 1992.

[191] A. Rayleigh, "On the stability or instability of certain fluid motions (iii.)," *Proc. London Math. Soc.*, vol. s1-27, no. 1, pp. 5–12, 1895.

[192] L. Rayleigh, "On The Instability Of Jets," *Proc. London Math. Soc.*, vol. s1-10, pp. 4–13, nov 1878.

[193] J. Qian and C. K. Law, "Regimes of coalescence and separation in droplet collision," *J. Fluid Mech.*, vol. 331, pp. 59–80, 1997.

[194] C. Tang, P. Zhang, and C. K. Law, "Bouncing, coalescence, and separation in head-on collision of unequal-size droplets," *Phys. Fluids*, vol. 24, p. 022101, feb 2012.

[195] M. Abdelgawad and A. R. Wheeler, "The Digital Revolution: A New Paradigm for Microfluidics," *Adv. Mater.*, vol. 21, pp. 920–925, feb 2009.

[196] H. Geng, J. Feng, L. M. Stabryla, and S. K. Cho, "Droplet Manipulations By Dielectrowetting: Creating, Transporting, Splitting, and Merging," in *Micro Electro Mech. Syst. (MEMS), 2017 IEEE 30th Int. Conf.*, (Las Vegas), pp. 113–116, IEEE, 2017.

[197] T. Beerling, "Liquid Metal Switch Emplying Electrowetting for Actuation and Architectures for Implementing Same," 2006.

[198] C. Liu, L. Li, and Q.-H. Wang, "Bidirectional optical switch based on electrowetting," *J. Appl. Phys.*, vol. 113, p. 193106, may 2013.

[199] J. Kim, W. Shen, L. Latorre, and C.-J. Kim, "A micromechanical switch with electrostatically driven liquid-metal droplet," *Sens Actuators A Phys.*, vol. 97-98, pp. 672–679, apr 2002.

[200] R. A. Bilodeau, D. Y. Zemlyanov, and R. K. Kramer, "Liquid Metal Switches for Environmentally Responsive Electronics," *Adv. Mater. Interfaces*, p. 1600913, jan 2017.

[201] J. Zhang, L. Sheng, and J. Liu, "Synthetically chemical-electrical mechanism for controlling large scale reversible deformation of liquid metal objects," *Sci. Rep.*, vol. 4, p. 7116, may 2015.

[202] L. Sheng, J. Zhang, and J. Liu, "Diverse Transformations of Liquid Metals Between Different Morphologies," *Adv. Mater.*, vol. 26, pp. 6036–6042, sep 2014.

[203] L. Hu, L. Wang, Y. Ding, S. Zhan, and J. Liu, "Manipulation of Liquid Metals on a Graphite Surface," *Adv. Mater.*, vol. 28, pp. 9210–9217, nov 2016.

[204] J. Wang, K. Appusamy, S. Guruswamy, and A. Nahata, "Electrolytic reduction of liquid metal oxides and its application to reconfigurable structured devices," *Sci. Rep.*, vol. 5, p. 8637, aug 2015.

[205] M. Wang, C. Trlica, M. R. Khan, M. D. Dickey, and J. J. Adams, "A reconfigurable liquid metal antenna driven by electrochemically controlled capillarity," *J. Appl. Phys.*, vol. 117, p. 194901, may 2015.

[206] J. T. H. Tsai, C.-M. Ho, F.-C. Wang, and C.-T. Liang, "Ultrahigh contrast light valve driven by electrocapillarity of liquid gallium," *Appl. Phys. Lett.*, vol. 95, p. 251110, dec 2009.

[207] B. Yuan, Z. He, W. Fang, X. Bao, and J. Liu, "Liquid metal spring: oscillating coalescence and ejection of contacting liquid metal droplets," *Sci. Bull.*, vol. 60, pp. 648–653, mar 2015.

[208] K. A. Brakke, "The Surface Evolver," *Exp. Math.*, vol. 1, pp. 141–165, jan 1992.

[209] L. M. Yu, B. H. Sur, K. Y. Pyo, W. C. Qing, and Z. Lei, "Simulative Analysis on Factors Influencing Solder Joint Bridging of Fine Pitch Devices," *J. Electron. Packag.*, vol. 126, no. 1, p. 22, 2004.

[210] L. M. Yu and C. Wang, "Simulative Design of Pad Structure for High Density Electronic Interconnection," *J. Mater. Sci. Technol.*, vol. 21, no. 1, pp. 63–67, 2005.

[211] T. J. Singler, X. Zhang, and K. A. Brakke, "Computer Simulation of Solder Bridging Phenomena," *J. Electron. Packag.*, vol. 118, no. 3, p. 122, 1996.

[212] S. E. Fosdick, K. N. Knust, K. Scida, and R. M. Crooks, "Bipolar electrochemistry," *Angew. Chemie - Int. Ed.*, vol. 52, no. 40, pp. 10438–10456, 2013.

[213] F. Mavre, R. K. Anand, D. R. Laws, K.-F. Chow, B.-Y. Chang, J. A. Crooks, and R. M. Crooks, "Bipolar Electrodes: A Useful Tool for Concentration, Separation, and Detection of Analytes in Microelectrochemical Systems," *Anal. Chem.*, vol. 82, pp. 8766–8774, nov 2010.

[214] J. Roche, G. Loget, D. Zigah, Z. Fattah, B. Goudeau, S. Arbault, L. Bouffier, and a. Kuhn, "Straight-forward synthesis of ringed particles," *Chem. Sci.*, vol. 5, no. 5, p. 1961, 2014.

[215] G. Loget and A. Kuhn, "Electric field-induced chemical locomotion of conducting objects," *Nat. Commun.*, vol. 2, p. 535, 2011.

[216] C. Ulrich, O. Andersson, L. Nyholm, and F. Björefors, "Formation of molecular gradients on bipolar electrodes," *Angew. Chemie - Int. Ed.*, vol. 47, no. 16, pp. 3034–3036, 2008.

[217] G. Loget, S. So, R. Hahn, and P. Schmuki, "Bipolar anodization enables the fabrication of controlled arrays of TiO 2 nanotube gradients," *J. Mater. Chem. A*, vol. 2, pp. 17740–17745, sep 2014.

[218] R. C. Gough, A. M. Morishita, J. H. Dang, W. Hu, W. A. Shiroma, and A. T. Ohta, "Continuous Electrowetting of Non-toxic Liquid Metal for RF Applications," *IEEE Access*, vol. 2, pp. 874–882, 2014.

[219] P. H. Rieger, "Electrolytic Conductance," in *Electrochemistry*, ch. 3, pp. 109–150, New York: Chapman & Hall, Inc, 2nd ed., 1994.

[220] S. I. Ibeneme, K. K. Ibe, A. O. Selemo, J. O. Nwagbara, Y. E. Obioha, K. O. Echendu, and B. O. Ubechu, "Geoelectrical Investigation of a Proposed Dam Site in a Sedimentary Terrain: Case Study of Aba River at Amapu-Ideobia, Akanu Ngwa Southeastern Nigeria," *Int. J. Geosci.*, vol. 04, no. 10, pp. 1376–1381, 2013.

[221] P. H. Carpenter, A. Ding, and L. Cheng, "Identifying Groundwater Contamination Using Resistivity Surveys at a Landfill near Maoming, China," *Nat. Educ. Knowl.*, vol. 3, no. 7, p. 20, 2012.

[222] A. Batte, A. Muwanga, P. Sigrist, and M. Owor, "Vertical electrical sounding as an exploration technique to improve on the certainty of groundwater yield in the fractured crystalline basement aquifers of eastern Uganda," *Hydrogeol. J.*, vol. 16, pp. 1683–1693, dec 2008.

[223] L. Valdes, "Resistivity Measurements on Germanium for Transistors," *Proc. IRE*, vol. 42, pp. 420–427, feb 1954.

[224] G. Beni, "Continuous electrowetting effect," *Appl. Phys. Lett.*, vol. 40, no. 10, p. 912, 1982.

[225] J. Lee and C.-j. C. J. Kim, "Surface-tension-driven microactuation based on continuous electrowetting," *J. Microelectromechanical Syst.*, vol. 9, pp. 171–180, jun 2000.

[226] S.-Y. Tang, V. Sivan, P. Petersen, W. Zhang, P. D. Morrison, K. Kalantar-zadeh, A. Mitchell, and K. Khoshmanesh, "Liquid Metal Actuator for Inducing Chaotic Advection," *Adv. Funct. Mater.*, vol. 24, pp. 5851–5858, oct 2014.

[227] C. B. Eaker and M. D. Dickey, "Liquid metal actuation by electrical control of interfacial tension," *Appl. Phys. Rev.*, vol. 3, p. 031103, sep 2016.

[228] K. Doudrick, S. Liu, E. M. Mutunga, K. L. Klein, V. Damle, K. K. Varanasi, and K. Rykaczewski, "Different Shades of Oxide: From Nanoscale Wetting Mechanisms to Contact Printing of Gallium-Based Liquid Metals," *Langmuir*, vol. 30, pp. 6867–6877, jun 2014.

[229] A. Brask, D. Snakenborg, J. P. Kutter, and H. Bruus, "AC electroosmotic pump with bubble-free palladium electrodes and rectifying polymer membrane valves," *Lab Chip*, vol. 6, no. 2, pp. 280–288, 2006.

[230] P. G. Erlandsson and N. D. Robinson, "Electrolysis-reducing electrodes for electrokinetic devices," *Electrophoresis*, vol. 32, pp. 784–790, mar 2011.

[231] Y. Xia and G. M. Whitesides, "SOFT LITHOGRAPHY," *Annual Review of Materials Science*, vol. 28, pp. 153–184, Aug. 1998.

[232] D. Qin, Y. Xia, and G. M. Whitesides, "Soft lithography for micro- and nanoscale patterning.," *Nature protocols*, vol. 5, pp. 491–502, Mar. 2010.

[233] J. L. Wilbur, A. Kumar, E. Kim, and G. M. Whitesides, "Microfabrication by microcontact printing of self-assembled monolayers," *Advanced Materials*, vol. 6, pp. 600–604, July 1994.

[234] P. Kim, K. Kwon, M. Park, S. Lee, S. Kim, and K. Suh, "Soft lithography for microfluidics: a review," *Biochip Journal*, vol. 2, no. 1, pp. 1–11, 2008.

[235] M. Kubo, X. Li, C. Kim, M. Hashimoto, B. J. Wiley, D. Ham, and G. M. Whitesides, "Stretchable microfluidic radiofrequency antennas.," *Advanced materials (Deerfield Beach, Fla.)*, vol. 22, pp. 2749–52, July 2010.

[236] A. P. Gerratt and S. Bergbreiter, "Microfabrication of compliant all-polymer MEMS thermal actuators," *Sensors and Actuators A: Physical*, vol. 177, pp. 16–22, Apr. 2012.

[237] Y.-L. Zhang, Q.-D. Chen, H. Xia, and H.-B. Sun, "Designable 3D nanofabrication by femtosecond laser direct writing," *Nano Today*, vol. 5, no. 5, pp. 435–448, 2010.

[238] J. Fischer, M. Thiel, and M. Wegener, "Matter made to order," *IEEE Spectr.*, vol. 51, pp. 34–58, Feb. 2014.

[239] T. Bückmann, R. Schittny, M. Thiel, M. Kadic, G. W. Milton, and M. Wegener, "On three-dimensional dilational elastic metamaterials," *New J. Phys.*, vol. 16, p. 033032, Mar. 2014.

[240] M. H. Olsen, G. M. Hjortø, M. Hansen, O. Met, I. M. Svane, and N. B. Larsen, "In-chip fabrication of free-form 3D constructs for directed cell migration analysis.," *Lab Chip*, vol. 13, pp. 4800–9, Dec. 2013.

[241] A. Fassler and C. Majidi, "3D structures of liquid-phase GaIn alloy embedded in PDMS with freeze casting.," *Lab Chip*, vol. 13, pp. 4442–50, Nov. 2013.

[242] R. Delille, M. Urdaneta, S. Moseley, and E. Smela, "Benchtop Polymer MEMS," *J. Microelectromech. Syst.*, vol. 15, pp. 1108–1120, Oct. 2006.

[243] H. Zeng, D. Martella, P. Wasylczyk, G. Cerretti, J.-C. G. Lavocat, C.-H. Ho, C. Parmeggiani, and D. S. Wiersma, "High-resolution 3D direct laser writing for liquid-crystalline elastomer microstructures.," *Adv. Mater.*, vol. 26, pp. 2319–22, Apr. 2014.

[244] G. Li, X. Wu, and D.-W. Lee, "Selectively Plated Stretchable Liquid Metal Wires for Transparent Electronics," *Sensors Actuators B Chem.*, vol. 221, pp. 1114–1119, 2015.

[245] P. Selvaganapathy, Yit-shun Leung Ki, P. Renaud, and C. Mastrangelo, "Bubble-free electrokinetic pumping," *J. Microelectromechanical Syst.*, vol. 11, pp. 448–453, oct 2002.

[246] W. Shin, J. M. Lee, R. K. Nagarale, S. J. Shin, and A. Heller, "A Miniature, Nongassing Electroosmotic Pump Operating at 0.5 V," *J. Am. Chem. Soc.*, vol. 133, pp. 2374–2377, mar 2011.

[247] C. H. Yang, B. Chen, J. J. Lu, J. H. Yang, J. Zhou, Y. M. Chen, and Z. Suo, "Ionic cable," *Extrem. Mech. Lett.*, vol. 3, pp. 59–65, 2015.

[248] N. Naserifar, P. R. LeDuc, and G. K. Fedder, "Drop casting of stiffness gradients for chip integration into stretchable substrates," *J. Micromechanics Microengineering*, vol. 27, p. 045018, apr 2017.

[249] N. J. Conway, Z. J. Traina, and S.-G. Kim, "A strain amplifying piezoelectric MEMS actuator," *J. Micromech. Microeng.*, vol. 17, pp. 781–787, Apr. 2007.

[250] G. Fedder and L. Carley, "A low-noise low-offset capacitive sensing amplifier for a 50-/spl mu/g//spl radic/Hz monolithic CMOS MEMS accelerometer," *IEEE J. Solid-State Circuits*, vol. 39, pp. 722–730, May 2004.

[251] S. Alper and T. Akin, "A single-crystal silicon symmetrical and decoupled MEMS gyroscope on an insulating substrate," *J. Microelectromech. Syst.*, vol. 14, pp. 707–717, Aug. 2005.

[252] J. N. Palasagaram and R. Ramadoss, "MEMS-Capacitive Pressure Sensor Fabricated Using Printed-Circuit-Processing Techniques," *IEEE Sens. J.*, vol. 6, pp. 1374–1375, Dec. 2006.

[253] H.-B. Fang, J.-Q. Liu, Z.-Y. Xu, L. Dong, L. Wang, D. Chen, B.-C. Cai, and Y. Liu, "Fabrication and performance of MEMS-based piezoelectric power generator for vibration energy harvesting," *Microelectronics J.*, vol. 37, pp. 1280–1284, Nov. 2006.

[254] R. Mahameed, N. Sinha, M. B. Pisani, and G. Piazza, "Dual-beam actuation of piezoelectric AlN RF MEMS switches monolithically integrated with AlN contour-mode resonators," *Journal of Micromechanics and Microengineering*, vol. 18, p. 105011, Oct. 2008.

[255] M. Glickman, P. Tseng, J. Harrison, T. Niblock, I. B. Goldberg, and J. W. Judy, "High-Performance Lateral-Actuating Magnetic MEMS Switch," *J. Microelectromech. Syst.*, vol. 20, pp. 842–851, Aug. 2011.

[256] M. Daneshmand, S. Fouladi, R. R. Mansour, M. Lisi, and T. Stajcer, "Thermally-actuated latching RF MEMS switch," *2009 IEEE MTT-S International Microwave Symposium Digest*, pp. 1217–1220, June 2009.

[257] J. J. Khazaai and H. Qu, "Electro-Thermal MEMS Switch With Latching Mechanism: Design and Characterization," *IEEE Sensors Journal*, vol. 12, pp. 2830–2838, Sept. 2012.

[258] C. Liu, "Recent Developments in Polymer MEMS," *Advanced Materials*, vol. 19, pp. 3783–3790, Nov. 2007.

[259] J. Streque, A. Talbi, P. Pernod, and V. Preobrazhensky, "New Magnetic Microactuator Design Based on PDMS Elastomer and MEMS Technologies for Tactile Display," *IEEE Transactions on Haptics*, vol. 3, pp. 88–97, Apr. 2010.

[260] G. M. Whitesides, "The origins and the future of microfluidics.," *Nature*, vol. 442, pp. 368–73, July 2006.

[261] C.-X. Liu and J.-W. Choi, "Embedding conductive patterns of elastomer nanocomposite with the assist of laser ablation," *Microsystem Technologies*, vol. 18, pp. 365–371, Dec. 2011.

[262] W. Shan, T. Lu, and C. Majidi, "Soft-matter composites with electrically tunable elastic rigidity," *Smart Mater. Struct.*, vol. 22, p. 085005, aug 2013.

[263] H. Klank, J. P. Kutter, and O. Geschke, "CO(2)-laser micromachining and back-end processing for rapid production of PMMA-based microfluidic systems.," *Lab on a chip*, vol. 2, pp. 242–6, Nov. 2002.

[264] B. a. Fogarty, K. E. Heppert, T. J. Cory, K. R. Hulbutta, R. S. Martin, and S. M. Lunte, "Rapid fabrication of poly(dimethylsiloxane)-based microchip capillary electrophoresis devices using CO2 laser ablation.," *The Analyst*, vol. 130, pp. 924–30, June 2005.

[265] S. Basu and T. DebRoy, "Liquid metal expulsion during laser irradiation," *Journal of Applied Physics*, vol. 72, no. 8, p. 3317, 1992.

[266] T. Liu, P. Sen, and C.-J. Kim, "Characterization of Nontoxic Liquid-Metal Alloy Galinstan for Applications in Microdevices," *Journal of Microelectromechanical Systems*, vol. 21, pp. 443–450, Apr. 2012.

[267] S. S. Antman, *Nonlinear Problems of Elasticity.* New York: Springer Science+Businiess, 1995.

[268] A. E. H. Love, *A treatise on the mathematical theory of elasticity.* New York: Dover Publications, 4 ed., 1944.

[269] J. L. Ericksen and C. Truesdell, "Exact theory of stress and strain in rods and shells," *Arch. Ration. Mech. Anal.*, vol. 1, pp. 295–323, Jan. 1958.

[270] A. E. Green and N. Laws, "A General Theory of Rods," *Proc. R. Soc. A Math. Phys. Eng. Sci.*, vol. 293, pp. 145–155, July 1966.

[271] A. Green, "On the theory of rods. II. Developments by direct approach," *Proc. R. Soc. A Math. Phys. Eng. Sci.*, vol. 337, no. 1611, pp. 485–507, 1974.

[272] A. E. Green, P. M. Naghdi, and M. L. Wenner, "On the Theory of Rods. I. Derivations from the Three-Dimensional Equations," *Proc. R. Soc. A Math. Phys. Eng. Sci.*, vol. 337, pp. 451–483, Apr. 1974.

[273] H. Ramsey, "A theory of thin rods with application to helical constituent wires in cables," *Int. J. Mech. Sci.*, vol. 30, pp. 559–570, Jan. 1988.

[274] F. Schuricht and H. V. D. Mosel, "Euler-Lagrange Equations for Nonlinearly Elastic Rods with Self-Contact," *Arch. Ration. Mech. Anal.*, vol. 168, pp. 35–82, June 2003.

[275] V. G. A. Goss, "Experiments on Snap Buckling, Hysteresis and Loop Formation in Twisted Rods," *Exp. Mech.*, vol. 45, pp. 101–111, Apr. 2005.

[276] J. Diani, B. Fayolle, and P. Gilormini, "A review on the Mullins effect," *Eur. Polym. J.*, vol. 45, pp. 601–612, mar 2009.

[277] T. Tate, "On the magnitude of a drop of liquid formed under different circumstances," *London, Edinburgh, Dublin Philos. Mag. J. Sci.*, vol. 27, no. 181, pp. 176–180, 1864.

[278] Z.-q. Zhang and Y. H. Mori, "Formulation of the Harkins-Brown correction factor for drop-volume description," *Ind. Eng. Chem. Res.*, vol. 32, pp. 2950–2952, nov 1993.

[279] J. P. Garandet, B. Vinet, and P. Gros, "Considerations on the Pendant Drop Method: A New Look at Tate's Law and Harkins' Correction Factor," *J. Colloid Interface Sci.*, vol. 165, pp. 351–354, jul 1994.

[280] D. Huttenlocher, G. Klanderman, and W. Rucklidge, "Comparing images using the Hausdorff distance," *IEEE Trans. Pattern Anal. Mach. Intell.*, vol. 15, no. 9, pp. 850–863, 1993.

[281] M. Wang, Q. Wang, and B. Karki, "Arts of electrical impedance tomographic sensing," *Philos. Trans. R. Soc. A Math. Phys. Eng. Sci.*, vol. 374, p. 20150329, jun 2016.

Appendices

Appendix A

Extra DEA Geometry

A.1 Pure Bending Current Thicknesses

Prior to deformation, a layer has a length-wise cross-sectional area of a_0, as shown in A.1. After deformation, the body takes the shape the area marked by area a_1. Because this is a plain strain bending scenario (width remains constant), it is known that $a_1 = a_0$, thus leading to the following:

$$0.5(r+h)^2\bar{\theta} - 0.5r^2\bar{\theta} = LH, \tag{A.1}$$

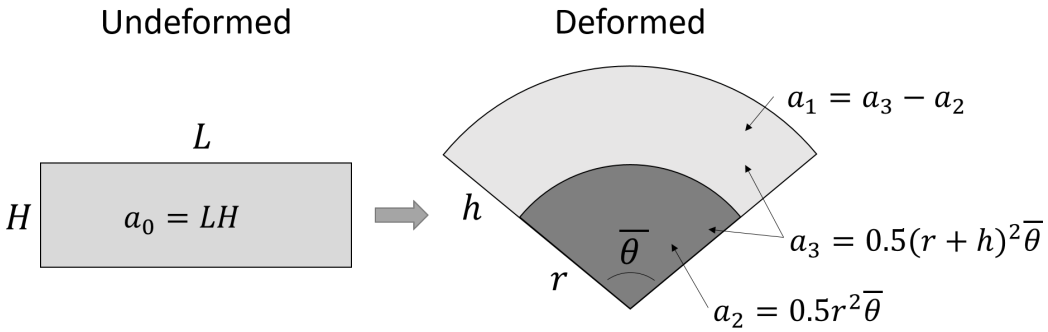

Figure A.1: Geometry and relevant areas before and after deformation.

$$0.5\bar{\theta}h^2 + \bar{\theta}rh - LH = 0, \tag{A.2}$$

$$h = -\bar{\theta}r \pm \sqrt{\frac{\bar{\theta}^2 r^2 + 2\bar{\theta}LH}{\bar{\theta}}}. \tag{A.3}$$

In this case, only the additive option results in a real number. To calculate the thicknesses of various layers, the proper r must be substituted. For example, calculating the thickness of h_3 requires that $r = \rho + h_1 + h_2$. Alternatively, the initial thickness can be calculated as:

$$H = \int_r^{r+h} \frac{dr}{\lambda_z} = \int_r^{r+h} \frac{\bar{\theta}r}{L} dr = \frac{\bar{\theta}}{2L}[(r+h)^2 - r^2], \tag{A.4}$$

where $\lambda_z = L/(\bar{\theta}r)$. Simplifying further results in the same solution as equ. (A.3).

A.2 Saddle Deformation Surface Area

The area of the surface $\mathcal{S}$ is calculated by first determining the lengths of the coordinate lines ℓ_θ and w_ϕ. The length w_ϕ is labeled in A.2, and ℓ_θ is determined by rotating point p about θ (into and out of the page across the total arc $\bar{\theta}$). Thus, $\ell_\theta = R_1\bar{\theta}$ and $w_\phi = R_2\bar{\phi}$, where $R_1 = (\rho_\theta + z) + R_2 - R_2 cos(\phi)$ and $R_2 = \rho_\phi - z$. We can then determine that

$$\ell_\theta = \{(\rho_\theta + z) + (1 - \cos\phi)(\rho_\phi - z)\}\bar{\theta} \tag{A.5}$$

and

$$w_\phi = (\rho_\phi - z)\bar{\phi}. \tag{A.6}$$

An infinitesimal width can be described as $dw_\phi = (\rho_\phi - z)d\bar{\phi}$, and surface area can then be determined by integrating this value along the lengths ℓ_θ:

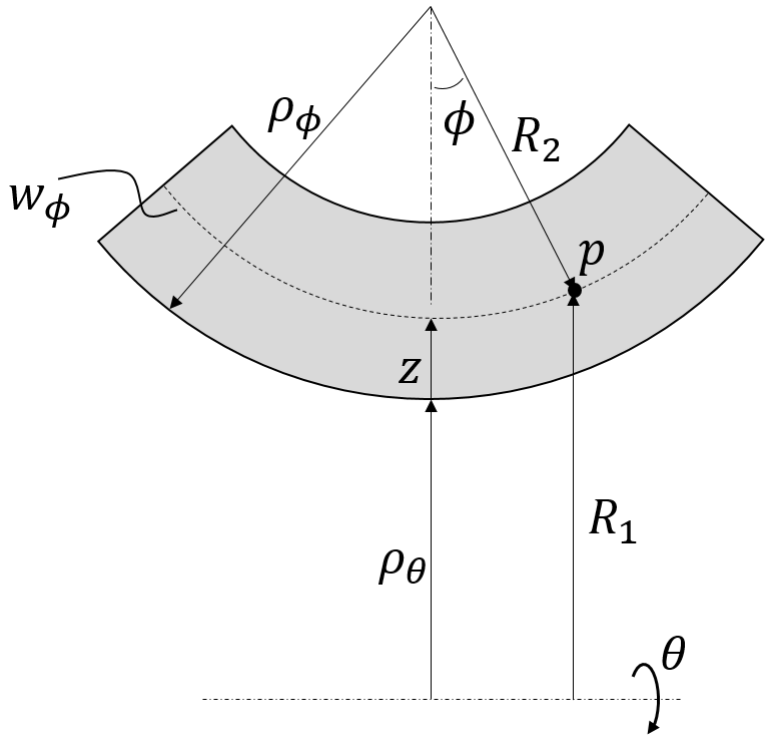

Figure A.2: Dimensions relevant for calculating coordinate line lengths and surface area.

$$a(z) = 2\int_0^{\bar{\phi}/2} \ell_\theta dw_\phi = \left\{ [\rho_\theta + \rho_\phi]\bar{\phi} - 2\,(\rho_\phi - z)\sin\left(\frac{\bar{\phi}}{2}\right) \right\} \bar{\theta}(\rho_\phi - z)\,. \tag{A.7}$$

Appendix B

Pure Bending DEA MATLAB Code

```
%% pure_bending.m
% This code determines the deformation of a DEA composite undergoing ...
   pure
% bending (plain strain)

syms Y bt r z L1 L2 L3 C1 W b H1 H2 H3 V er e0

%% Inputs
type1 = 0; % 0 - Current condition strain energy integrals, 1 - ...
   Unstrained integrals
type2 = 0; % 0 - Maxwell's equation energy, 1 - Capacitor approximation

Vtrange = 0:100:5000; % Range of voltage inputs (V)
angle = ones(length(Vtrange),1); % Allocate space for results

Yv = 1e6;    % Elastic modulus  (Pa) (PDMS ~1 MPa)

L1v = 20e-3;    % Length of undeformed layer 1 (m)
L2v = L1v;      % Length of undeformed layer 2 (m) (same as layer 1)
L3v = L1v*1.06; % Length of undeformed layer 3 (m)

bv = 0.75e-3;  % Width of border surrounding the electrodes (m)

H1v = 163e-6;  % Height (thickness) of undeformed layer 1 (m)
H2v = 85e-6;   % Height of undeformed layer 2 (m)
H3v = 490e-6;  % Height of undeformed layer 3 (m)

Wv = 6.5e-3;   % Width of undeformed layers (m)

erv = 2.72;      % Dielectric constant
e0v = 8.85e-12;  % Vacuum permittivity

%% Get energy functions
if type1 == 0
```

```
    [f1,f2] = symbolic_solving_current;  % Current condition strain ...
       energy integral
    f1 = subs(f1,[Y L1 L2 L3 b H1 H2 H3 W e0 er],[Yv L1v L2v L3v bv ...
       H1v H2v H3v Wv e0v erv]); % Maxwell
    f2 = subs(f2,[Y L1 L2 L3 b H1 H2 H3 W e0 er],[Yv L1v L2v L3v bv ...
       H1v H2v H3v Wv e0v erv]); % Capacitor

else
    [f1,f2] = symbolic_solving_unstrained; % Unstrained condition ...
       strain energy integral
    f1 = subs(f1,[Y L1 L2 L3 b H1 H2 H3 W e0 er],[Yv L1v L2v L3v bv ...
       H1v H2v H3v Wv e0v erv]); % Maxwell
    f2 = subs(f2,[Y L1 L2 L3 b H1 H2 H3 W e0 er],[Yv L1v L2v L3v bv ...
       H1v H2v H3v Wv e0v erv]); % Capacitor

end

%% Convert symbolic into matlab functions
if type2 == 0
    fun = matlabFunction(f1,'Vars',{V [bt r]});
else
    fun = matlabFunction(f2,'Vars',{V [bt r]});
end


%% Minimum energy solving
options=optimset('MaxFunEvals',10000,'MaxIter',10000,'TolFun',1e-12,...
    'TolX',1e-12); % Options for fminsearch
i=0;
for Vt = Vtrange
    i = i + 1;
    sol = fminsearch(@(x)fun(Vt,x),[1 .1],options);
    angle(i) = sol(1)/2*180/pi; % Convert angles to degrees
end


%% Plot data
plot(Vtrange/1000,angle)
xlabel('Voltage (kV)')
ylabel('Actuator Angle (deg)')
```

```
%% symbolic_solving_current.m
% The function describing the potential energy of the pure bending ...
   DEA can
% be expressed analytically. This function pulls out the necessary ...
   MATLAB
% functions to minimize numerically.
%
% This version integrates across the current volume to calculate strain
% energy.

function [f1,f2] = symbolic_solving_current
```

```
syms Y bt r z L1 L2 L3 C1 W b H1 H2 H3 h1 h2 h3 V er e0

% Assumptions
assume(r>0)
assume(h1>0)
assume(h2>0)
assume(h3>0)

C1 = Y/6;  % Material constant (Y is elastic modulus)

% Stretches
lam1 = bt*(r + z)/L1; % Stretch of layer 1
lam2 = bt*(r + z)/L2; % Stretch of layer 2
lam3 = bt*(r + z)/L3; % Stretch of layer 3

% Current thicknesses in terms of r, by, and given values
% Note: It is easier to set assumptions on h1 h2 h3 and substitute the
% below values later.
h1s = (-r*bt + sqrt(2*L1*H1*bt+r^2*bt^2))/bt;                  % ...
    Deformed layer 1 thickness
h2s = (-(r+h1)*bt + sqrt(2*L2*H2*bt+(r+h1)^2*bt^2))/bt;        % ...
    Deformed layer 2 thickness
h2s = subs(h2s,h1,h1s);
h3s = (-(r+h1+h2)*bt + sqrt(2*L3*H3*bt+(r+h1+h2)^2*bt^2))/bt;  % ...
    Deformed layer 3 thickness
h3s = subs(h3s,h2,h2s);
h3s = subs(h3s,h1,h1s);

% Energy density functions (Neo-Hookean)
psi1 = C1*(lam1^2+lam1^(-2)-2); % Strain energy density function of ...
    layer 1
psi2 = C1*(lam2^2+lam2^(-2)-2); % Strain energy density function of ...
    layer 2
psi3 = C1*(lam3^2+lam3^(-2)-2); % Strain energy density function of ...
    layer 3

% Strain energy
U1 = int(psi1*(r+z)*W*bt,z,0,h1);           % Strain energy of layer 1
U2 = int(psi2*(r+z)*W*bt,z,h1,h1+h2);       % Strain energy of layer 2
U3 = int(psi3*(r+z)*W*bt,z,h1+h2,h1+h2+h3); % Strain energy of layer 3
U1 = subs(U1,[h1 h2 h3],[h1s h2s h3s]);
U2 = subs(U2,[h1 h2 h3],[h1s h2s h3s]);
U3 = subs(U3,[h1 h2 h3],[h1s h2s h3s]);

% Electrical enthalpy - Using Maxwell's equations
E = V/((r+z)*log((r+h1+h2)/(r+h1)));                    % Electric field
Uel1 = -int(0.5*er*e0*E^2*(r+z)*bt*(W-2*b),z,h1,h1+h2); % Energy
Uel1 = subs(Uel1,[h1 h2 h3],[h1s h2s h3s]);

% Electrical enthalpy - Capacitor approximation
lamt = bt*(r + h1 + h2/2)/L2;  % Stretch at halfway through dielectric
lD = L2*lamt;                  % Length at halfway through dielectric
C = er*e0*(W-2*b)*lD/h2;       % Capacitance
```

```
Uel2 = -0.5*C*V^2;              % Energy
Uel2 = subs(Uel2,[h1 h2 h3],[h1s h2s h3s]);

f1 = U1 + U2 + U3 + Uel1; % Function with Maxwell's
f2 = U1 + U2 + U3 + Uel2; % Function with capacitor
```

```
%% symbolic_solving_unstrained.m
% The function describing the potential energy of the pure bending ...
    DEA can
% be expressed analytically. This function pulls out the necessary ...
    MATLAB
% functions to minimize numerically.
%
% This version integrates across the unstrained volume to calculate ...
    strain
% energy.

function [f1,f2] = symbolic_solving_unstrained

syms Y l k bt r z L1 L2 L3 C1 W b H1 H2 H3 h1T h2T V er e0 h1 h2 h3

% Assumptions
assume(k>0)
assume(H1>0)
assume(H2>0)
assume(H3>0)
assume(h1T>0)
assume(h2T>0)

C1 = Y/6;  % Material constant (Y is elastic modulus)

% Stretches
lam1 = l/L1*(1+k*z); % Stretch of layer 1
lam2 = l/L2*(1+k*z); % Stretch of layer 2
lam3 = l/L3*(1+k*z); % Stretch of layer 3

% Current thicknesses in terms of r, by, and given values
% Note: It is easier to set assumptions on h1 h2 h3 and substitute the
% below values later.
h1s = (-r*bt + sqrt(2*L1*H1*bt+r^2*bt^2))/bt;                  % ...
    Deformed layer 1 thickness
h2s = (-(r+h1)*bt + sqrt(2*L2*H2*bt+(r+h1)^2*bt^2))/bt;        % ...
    Deformed layer 2 thickness
h2s = subs(h2s,h1,h1s);
h3s = (-(r+h1+h2)*bt + sqrt(2*L3*H3*bt+(r+h1+h2)^2*bt^2))/bt;  % ...
    Deformed layer 3 thickness
h3s = subs(h3s,h2,h2s);
h3s = subs(h3s,h1,h1s);

% Energy density functions (Neo-Hookean)
psi1 = C1*(lam1^2+lam1^(-2)-2); % Strain energy density function of ...
    layer 1
```

```
psi2 = C1*(lam2^2+lam2^(-2)-2); % Strain energy density function of ...
    layer 2
psi3 = C1*(lam3^2+lam3^(-2)-2); % Strain energy density function of ...
    layer 3

% Strain energy
U1 = int(psi1*W*L1,z,0,H1);           % Strain energy of layer 1
U2 = int(psi2*W*L2,z,H1,H1+H2);       % Strain energy of layer 2
U3 = int(psi3*W*L3,z,H1+H2,H1+H2+H3); % Strain energy of layer 3

% Electrical enthalpy - Using Maxwell's equations
E = V/((r+z)*log((r+h1+h2)/(r+h1)));                    % Electric field
Uel1 = -int(0.5*er*e0*E^2*(r+z)*bt*(W-2*b),z,h1,h1+h2); % Energy
Uel1 = subs(Uel1,[h1 h2 h3],[h1s h2s h3s]);

% Electrical enthalpy - Capacitor approximation
lamt = bt*(r + h1 + h2/2)/L2;  % Stretch at halfway through dielectric
lD = L2*lamt;                  % Length at halfway through dielectric
C = er*e0*(W-2*b)*lD/h2;       % Capacitance
Uel2 = -0.5*C*V^2;             % Energy
Uel2 = subs(Uel2,[h1 h2 h3],[h1s h2s h3s]);

f1 = U1 + U2 + U3 + Uel1; % Function with Maxwell's
f2 = U1 + U2 + U3 + Uel2; % Function with capacitor

kre = 1/r;   % Curvature in terms of radius
lre = r*bt;  % Length in terms of radius and angle theta bar

% Functions in terms of radius and angle
f1 = subs(f1,[k l],[kre lre]);
f2 = subs(f2,[k l],[kre lre]);
```

Appendix C

Saddle Deformation MATLAB Code

```
%% saddle.m
% This code solves for the deformation of a saddle-shaped DEA under a
% prescribed range of voltages.
%
% Uses energy minimization

global E L1 L2 L3 W1 W2 W3 b H1 H2 H3 V eps


%% Inputs

Type = 0;   % 0 -- Uniaxial pre-stretch, 1 -- Plain strain pre-stretch

n = 20;                   % Number of voltages to test
Vs = linspace(0,5e3,n);  % Input voltage range (V)

E = 1e6;    % Elastic modulus  (Pa) (PDMS ~1 MPa)

L1 = 20e-3;   % Length of undeformed layer 1 (m)
L2 = L1;      % Length of undeformed layer 2 (m) (same as layer 1)
L3 = L1*1.06; % Length of undeformed layer 3 (m)

b = 0.75e-3;  % Width of border surrounding the electrodes (m)

H1 = 163e-6;  % Height (thickness) of undeformed layer 1 (m)
H2 = 85e-6;   % Height of undeformed layer 2 (m)
H3 = 490e-6;  % Height of undeformed layer 3 (m)

W1 = 6.5e-3;  % Width of undeformed layer 1 (m)
W2 = W1;      % Width of undeformed layer 2 (m)
% Width of undeformed layer 3
if Type == 0
    W3 = W1/sqrt(L3/L1); % Uniaxial (m)
else
```

```
    W3 = W1; % Plain strain (m)
end

eps = 2.72*8.85e-12;  % Dielectric constant times vacuum permittivity


%% Setup for iterations
% Initial guesses for solver (note that these get updated)
ktheta0 = 100;   % Curvature in theta direction
L0 = L1*1.03;    % Length in theta direction
kphi0 = 100;     % Curvature in phi direction
w0 = W3*1.03;    % Length in phi direction

% Allocate space for solutions
ktheta = ones(n,1);   % Curvature in theta direction
L = ones(n,1);        % Length in theta direction
kphi = ones(n,1);     % Curvature in phi direction
w = ones(n,1);        % Length in phi direction


%% Iterate through voltages
for i = 1:n
    V = Vs(i); % Voltage input

    x0 = [ktheta0 L0 kphi0 w0]; % Initial guesses
    options=optimset('Display','iter','TolFun',1e-10); % Options for ...
       fminsearch
    x = fminsearch(@potential,x0,options);  % Minimum energy search

    % Extract
    ktheta(i) = x(1);  % Curvature in theta direction
    L(i) = x(2);       % Length in theta direction
    kphi(i) = x(3);    % Curvature in phi direction
    w(i) = x(4);       % Length in phi direction

    ktheta0 = ktheta(i); % Curvature in theta direction
    L0 = L(i);           % Length in theta direction
    kphi0 = kphi(i);     % Curvature in phi direction
    w0 = w(i);           % Length in phi direction

end


%% Plot the results
theta = (ktheta.*L/2)*(180/pi); % Calculate angle theta

figure(1); hold on
plot(Vs*1e-3,theta,'k--');
xlabel('Voltage (kV)')
ylabel('(Half) Angle of Deflection (deg)')

figure(2); hold on
plot(Vs*1e-3,ktheta,'k-o',Vs*1e-3,kphi,'k-^');
xlabel('Voltage (kV)')
```

```
ylabel('Curvature (m^{-1})')
legend('\kappa_{\theta} (axial)','\kappa_{\phi} (transverse')
```

```
%% potential.m
% Calculates the potential energy of the saddle DEA based on 4 parameter
% inputs.

function y = potential(x)

global L1 L2 L3 W1 W2 W3 b H1 H2 H3 V eps ktheta L kphi w

ktheta = x(1); % Curvature in theta direction
L = x(2);      % Length in theta direction
kphi = x(3);   % Curvature in phi direction
w = x(4);      % Length in phi direction

%bt = ktheta*L; % theta bar (arc angle)
bp = kphi*w;    % phi bar   (arc angle)

%% Approximate layer thicknesses
a1 = get_area(0);  % Calculating the area at z = 0
h1 = W1*L1*H1/a1;  % Approximate h1 based on a1

a2 = get_area(h1); % Calculating the area at z = h1
h2 = W2*L2*H2/a2;  % Approximate h2 based on a2

a3 = get_area(h1+h2); % Calculating the area at z = h1 + h2
h3 = W3*L3*H3/a3;     % Approximate h3 based on a3


%% Integrate to calculate potential energy
U1 =  dblquad(@density1,0,h1,-bp/2,bp/2);           % Strain energy ...
    layer 1
U2 =  dblquad(@density2,h1,h1+h2,-bp/2,bp/2);       % Strain energy ...
    layer 2
U3 =  dblquad(@density3,h1+h2,h1+h2+h3,-bp/2,bp/2); % Strain energy ...
    layer 3

chi = (W2 - 2*b)*(L2 - 2*b)/(W2*L2);   % Scaling for electrode size
Uel = -eps*chi*a2*V^2/(2*h2);          % Electrical enthalpy

y = U1 + U2 + U3 + Uel;  % Total energy
```

```
%% get_area.m
% Calculates the area of the saddle shape at some z position.

function a = get_area(z)

global ktheta L kphi w

bt = ktheta*L; % theta bar (arc angle)
```

```
bp = kphi*w;   % phi bar   (arc angle)

rt = 1/ktheta; % rho_theta  (theta radius)
rp = 1/kphi;   % rho_phi    (phi radius)

a = ((rt + rp)*bp - 2*(rp-z)*sin(bp/2))*bt*(rp-z); % Area
```

```
%% density1.m
% Potential energy density (Neo-Hookean) of layer 1

function y = density1(z, phi)

global E L1 W1 ktheta L kphi w

bt = ktheta*L; % theta bar (arc angle)
bp = kphi*w;   % phi bar   (arc angle)

rt = 1/ktheta; % rho_theta  (theta radius)
rp = 1/kphi;   % rho_phi    (phi radius)

Ltheta = ((rt+z) + (1-cos(phi))*(rp-z))*bt; % theta arc length
wphi = (rp-z)*bp;                           % phi arc length

lt = Ltheta/L1; % Stretch in theta direction
lp = wphi/W1;   % Stretch in phi direction

psi = (E/3)*(lt.^2 + lp.^2 + (lt.*lp).^(-2) - 3); % Energy density ...
    (Neo-Hookean)

y = psi.*Ltheta.*(rp-z); % Geometry components for integral
```

```
%% density2.m
% Potential energy density (Neo-Hookean) of layer 2

function y = density2(z, phi)

global E L2 W2 ktheta L kphi w

bt = ktheta*L; % theta bar (arc angle)
bp = kphi*w;   % phi bar   (arc angle)

rt = 1/ktheta; % rho_theta  (theta radius)
rp = 1/kphi;   % rho_phi    (phi radius)

Ltheta = ((rt+z) + (1-cos(phi))*(rp-z))*bt; % theta arc length
wphi = (rp-z)*bp;                           % phi arc length

lt = Ltheta/L2; % Stretch in theta direction
lp = wphi/W2;   % Stretch in phi direction

psi = (E/3)*(lt.^2 + lp.^2 + (lt.*lp).^(-2) - 3); % Energy density ...
```

```
    (Neo-Hookean)

y = psi.*Ltheta.*(rp-z); % Geometry components for integral
```

```
%% density3.m
% Potential energy density (Neo-Hookean) of layer 3

function y = density3(z, phi)

global E L3 W3 ktheta L kphi w

bt = ktheta*L; % theta bar (arc angle)
bp = kphi*w;   % phi bar   (arc angle)

rt = 1/ktheta; % rho_theta  (theta radius)
rp = 1/kphi;   % rho_phi    (phi radius)

Ltheta = ((rt+z) + (1-cos(phi))*(rp-z))*bt; % theta arc length
wphi = (rp-z)*bp;                           % phi arc length

lt = Ltheta/L3; % Stretch in theta direction
lp = wphi/W3;   % Stretch in phi direction

psi = (E/3)*(lt.^2 + lp.^2 + (lt.*lp).^(-2) - 3); % Energy density ...
    (Neo-Hookean)

y = psi.*Ltheta.*(rp-z); % Geometry components for integral
```

Appendix D

Further MEMS Background

While stretchable semiconductor technology may be difficult to achieve, MEMS is a field which can easily contribute to soft-matter engineering and provide a starting point for designing stretchable activated devices. MEMS devices are generally on the scale of hundreds of microns or smaller, and have been designed for tasks such as actuation [249] and acceleration [250], orientation [251], and pressure [252] sensing. Work has also been invested in developing MEMS for energy harvesting [253]. All of these designs have the potential to contribute to soft and stretchable equivalents.

Another popular area of MEMS is switching. These switches are widely used for radio-frequency circuits, offering low insertion loss and, thanks to the use of air gaps, low off-state capacitances [13]. Piezoelectric [254], electromagnetic [255], and thermal [256, 257] MEMS switches have been created, but electrostatic is currently the most common. Electrostatic switches generally consist of a stationary pull-in electrode which is charged and attracts a floating fixed-free [127, 128] or fixed-fixed beam [129]. This actuation can be used to directly complete a connection [127, 128] or to form a capacitor [129].

While MEMS can inspire new stretchable electronic devices, novel uses of soft materials can have an impact on and improve MEMS. In fact, hyperelastic components

have already been integrated into MEMS for sensing [258], actuation [259], and energy storage [126]. PDMS is a popular choice due to low costs, optical transparency, and ease of use, though it is also common for biological microfluidic devices because of its gas permeability [258, 260]. In general, as is the case with the aforementioned examples, soft materials are used in conjunction with rigid metals and silicon. However, there are a instances of all polymer and fluid MEMS style devices in the literature, including pressure sensors [19] and thermal [236] and electrostatic [89] actuators. Soft lithography techniques and the micro-molding described for the actuators [89, 236] could be valuable assets for future fabrication.

While MEMS can inspire new stretchable electronic devices, novel uses of soft materials can have an impact on conventional MEMS. In fact, hyperelastic components

have already been integrated into MEMS for sensing [258], actuation [259], and energy storage [126]. PDMS is a popular choice due to low costs, optical transparency, and ease of use, though it is also common for biological microfluidic devices because of its gas permeability [258, 260]. In general, as is the case with the aforementioned examples, soft materials are used in conjunction with rigid metals and silicon. However, there are a instances of all polymer and fluid MEMS style devices in the literature, including pressure sensors [19] and thermal [236] and electrostatic [89] actuators. Soft lithography techniques and the micro-molding described for the actuators [89, 236] could be valuable assets for future fabrication.

Appendix E

Electrostatic Cantilever MATLAB Code

```
%% CantileverIterate.m
%
% This code iterates over length values to and tracks the pull-in ...
   voltage
% of a rectangular cantilever beam.
%
% Used with ElectroCantilever.m

%% Input values
LRange = 0.002:0.0005:0.005;    % Range of lengths (m)
PhiRange = 1:2000;    % Range of voltage (V)

W   = 0.001;        % Width (m)
H   = 0.0002;       % Thickness (m)
D   = 0.0003;       % Gap (m)
E   = 840000;       % Elastic modulus (Pa)
I   = W*H^3/12;     % Moment of inertia (m^4)
eps = 8.85*10^-12; % Vacuum permittivity


%% Prep values
endposition = ones(length(PhiRange),1); % Allocate space for end ...
   position data
PIs         = ones(length(LRange),1); % Allocate space for pull-in ...
   voltages
EPs         = ones(length(LRange),1); % Allocate space for pull-in ...
   positions
j = 1; % Index for L values



%% Iterate over lengths and voltages
for L = LRange
```

```
    solinit = bvpinit(linspace(0,L,20),[0,0,0,0]); % Initial guess ...
       for beam solution (flat)

    i = 1; % Index for endposition

    for Phi = PhiRange
        try
            [x,ysol,solinit] = ...
               ElectroCantilever(Phi,L,W,D,E,I,eps,solinit);
            endposition(i) = ysol(1,end);
            % Plots the beam deflections. Only enable for small ...
               LRange and VRange
            % figure(j + 1)
            % plot(x*1000,ysol(1,:)*1000)
            % hold on
        catch
            endposition(i) = NaN;
            break
        end
        i = i + 1; % Increase index
    end

    % Uncomment if plotting beam deflections
    % xlabel('x (mm)')
    % ylabel('y (mm)')
    % title(['Deflection -- Length: ',num2str(L*1000),' mm'])
    % legend(num2str(PhiRange(1:i-1)'))

    % Find pull in point based on curvature
    loc = find(diff(diff(endposition(1:i-1)))>0,1,'first')+1;
    if isempty(loc) % If curvature never positive, assume last value ...
       is PI
        loc = i-1;
    end
    PIs(j) = PhiRange(loc); % Store pull-in voltage
    EPs(j) = endposition(loc); % Stores position at pull-in

    % Plot end position as a function of voltage with pull in point
    figure(1)
    plot(PhiRange(1:i-1),endposition(1:i-1)*1000,'linewidth',2)
    hold on
    j = j + 1;

end

% Pull in position and labels for position vs voltage plot
plot(PIs,EPs*1000,'^k','MarkerFaceColor', 'k')
xlabel('Voltage (V)')
ylabel('Tip Deflection (mm)')
legend(strcat(num2str(LRange'*1000),' mm'))
set(gca,'fontsize',14)

% Plot pull-in voltage as a function of beam length
figure
```

```
plot(LRange*1000,PIs,'linewidth',2)
xlabel('Length (mm)')
ylabel('Pull-In Voltage (V)')
set(gca,'fontsize',14)

% Plot modified pull-in voltage term as a function of beam length
figure
plot(LRange*1000,(10*eps*PIs.^2)/(3*E*H^3*D^3)/1000^4,'linewidth',2)
xlabel('Length (mm)')
ylabel('(10\epsilon_0\Phi_P_I^2)/(3EH^3G^3)  (mm^-^4)')
set(gca,'fontsize',14)
```

```
%% ElectroCantilever.m
%
% This code solves for the deformation of a cantilever beam under
% electrostatic loading.
%
% Used in conjunction with CantileverIterate.m
%
% Governing equations:
% y'''' = - q/(IE)
% q = -eps*Phi^2*W/(2(D+y(x))^2)
%
% Governing equation as system of first order ODEs:
% y1' = y2  (= y')
% y2' = y3  (= y'')
% y3' = y4  (= y''')
% y4' = -eps*V^2*W/(2*(D+y1)^2)  (= -eps*V^2*W/(2(D+y)^2))
%
% Boundary conditions:
% y(1)    = 0
% y'(1)   = 0
% M(end)  = y''(end)  = 0
% v(end)  = y'''(end) = 0
%

function [x,ysol,sol] = ElectroCantilever(Phi,L,W,D,E,I,eps,solinit)

x = linspace(0,L,100); % Values for x

% Boundary value problem solver
sol     = bvp4c(@(x,y)mat4ode(x,y,eps,Phi,E,I,W,D),@mat4bc,solinit);

ysol = deval(sol,x); % Extract Solution

    % Governing equation (system of first order ODEs)
    function dydx = mat4ode(~,y,eps,Phi,E,I,W,D)
        dydx = [y(2) y(3) y(4) -(eps*Phi^2*W)/(2*E*I*(D+y(1))^2)];
    end

    % Boundary conditions
    function res = mat4bc(ya,yb)
```

```
        res = [yb(4) ya(2) yb(3) ya(1)];
    end

end
```

Appendix F

Extra Cantilever Data

F.1 cPDMS True Stress vs Strain

The 15% cPDMS used for electrostatic cantilever experimentation was characterized on an Instron tensile tester (model 5969). The data from two dogbone samples is reported in fig. F.1. Both samples were approximately 4.4 mm wide and consisted

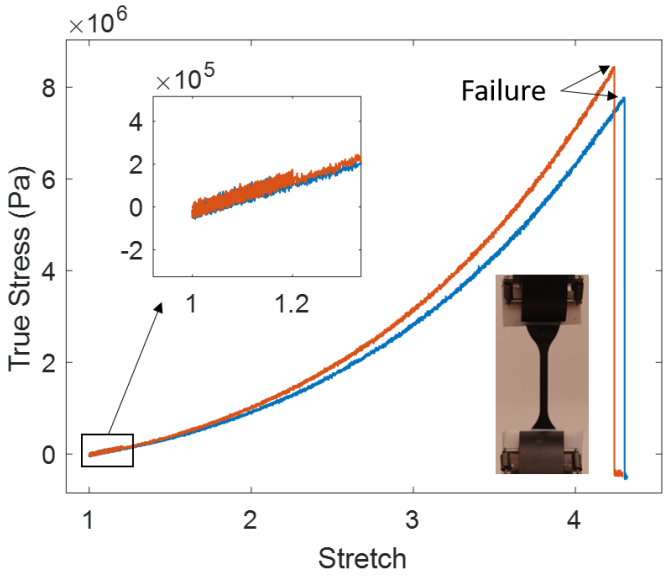

Figure F.1: Data from Instron tensile tests for two dog-bone samples of 15% cPDMS (red - 0.2 mm thick, blue - 0.22 mm thick). Top left inset: magnification of first 120% stretch. Bottom right inset: image from testing.

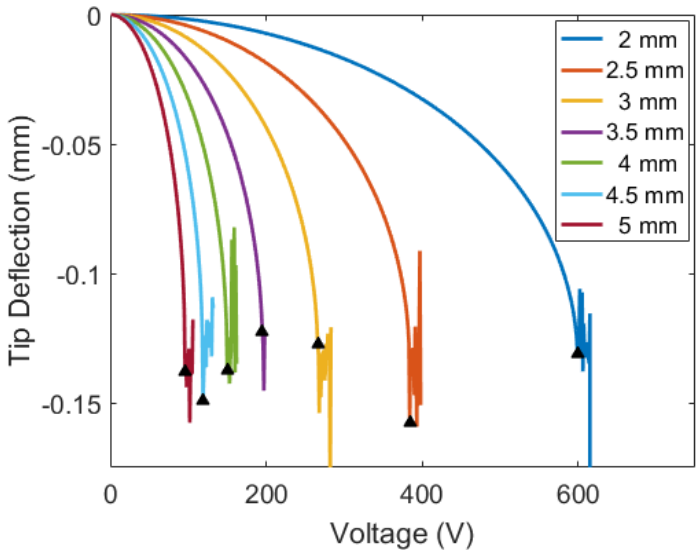

Figure F.2: Tip deflection as a function of applied voltage. The legend indicates the beam length. The black triangles mark the location of pull-in.

of about 50 mm exposed between the testing clamps. One sample was 0.2 mm thick and the second was 0.22 mm. Before stretching to failure, each sample under went 3 stretches to 120% (shown in the figure inset). All tests were performed at a rate of 10 mm/min. The both samples failed after stretching over 3 times their original length. Based on the first 7% strain during the failure cycle, the 0.2 mm thick sample had an elastic modulus of 896 kPa and the 0.22 mm thick sample had 793 kPa. For theoretical purposes, the modulus was assumed to be 840 kPa.

F.2 Cantilever Numerical Simulation

Fig. F.2 is an example output from the numeric code for determining pull-in of an electrostatic cantilever. As voltage increases, the displacement at the end of the beam increases. Eventually, pull-in occurs and the solver becomes unstable. These simulations were run for a beam of width 1 mm, thickness 0.2 mm, air gap 0.3 mm, and elastic modulus 840 kPa.

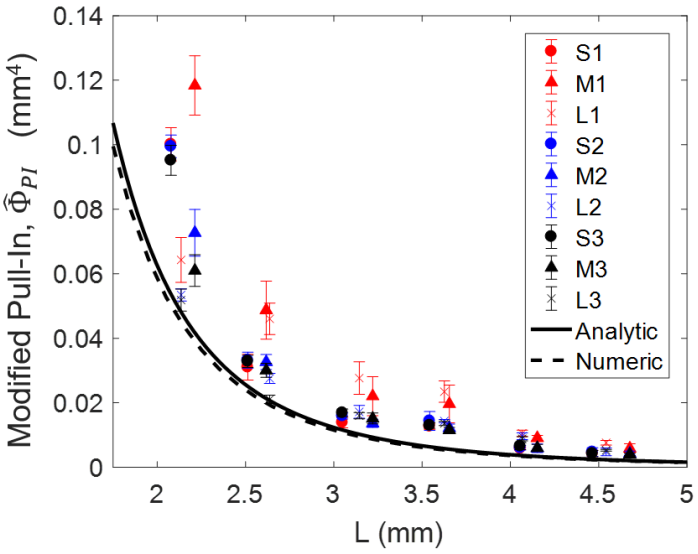

Figure F.3: Comparison of 3 sets of experimental results to theory. Widths of 0.46 (circles), 0.94 (triangles), and 1.43 mm (crosses) are plotted separately. Set 1 is plotted in red, set 2 in blue, and set 3 in black. The theory, $1/L^4$, is plotted as a solid line. Numeric results are plotted as a dashed line.

F.3 Additional Pull-In Data

Fig. F.3 is extra data from electrostatic cantilever experiments. A total of three sets of experimental data (each containing 6 values for each beam) were taken. The first set, in particular, appears to be an outlier. We suspect there may have been additional capacitive effects introduced by leads contacting part of the metal test stand. Set 2 and 3 display very similar results. Since we were most confident in the setup during set 3, that data was reported in the main document.

Appendix G

Extra Fabrication with PAA

For testing purposes, I coated a thin layer (about 60 μm) of PAA (Sigma-Aldrich, 523925) on a metallic plate. After hardening in an oven or on a hot plate, the PAA can be ablated away using raster or vector settings on a CO_2 laser engraver. Multiple passes may be needed. This essentially creates a mold on which we can cast PDMS or elastomers. As long as the elastomer is thick enough to avoid tearing, it can be

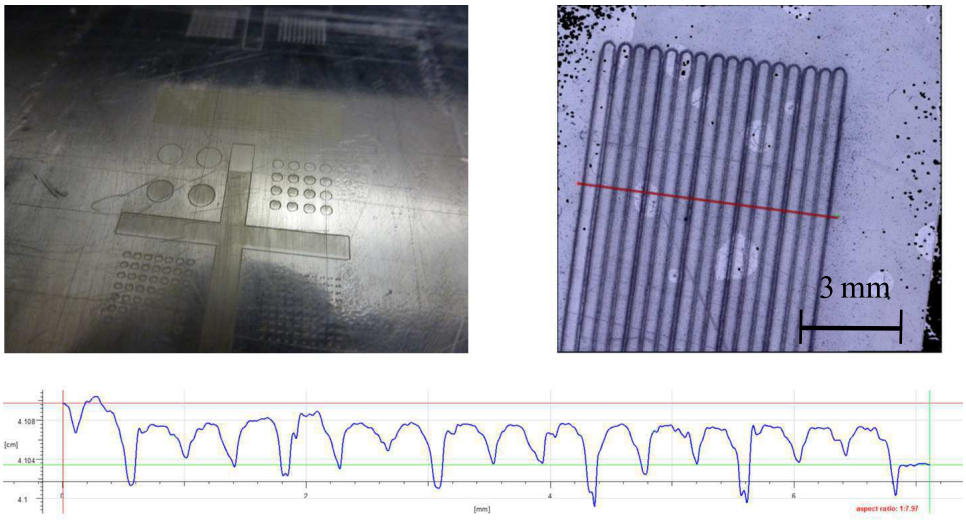

Figure G.1: Top left: PAA on a metallic plate after partially ablating away a pattern. Top right: A series of ridges in PDMS after peeling away from the PAA mold. Bottom: Profile measurements (Alicona Optical Profilometer) of the ridges. The height of each ridge is approximately 60 μm.

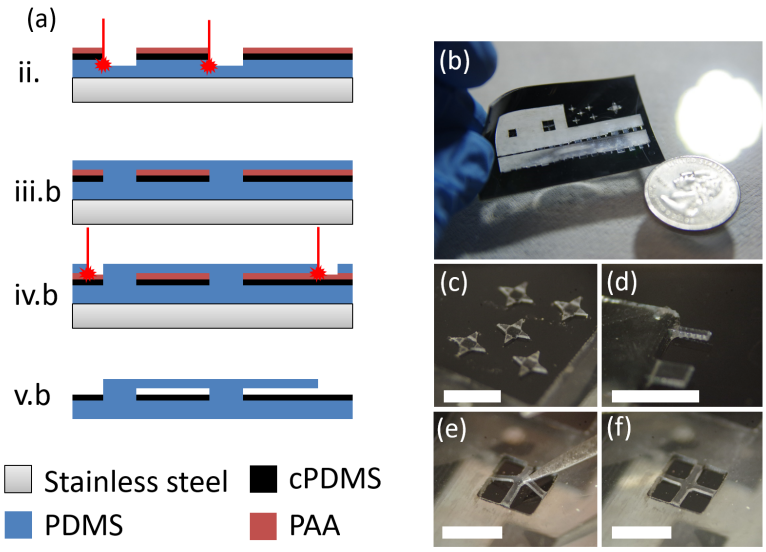

Figure G.2: Fabrication of free hanging PDMS structures with PAA. a) Fabrication process similar to that presented in chapter 2. b) A bulk fabrication of beams and other structures. c) Star shaped cantilevers. d) Rectangular cantilevers. e) Deformation of a free hanging structure with tweezers. f) Undeformed structure. All scale bars represent 3 mm.

simply peeled away from the metal and PAA. Fig. G.1 shows a sample of partially laser patterned PAA and the resulting PDMS sample. The fabrication method here provides an additional way to fabricated parts such as microfluidic channels and membranes. Only a single metallic plate is required since the laser has little effect on its surface and the PAA can be washed off with water when a new mold must be created. While the fabrication process described above may be useful, the true goal was to create free standing structures. One option is to create membranes with the method above and bond them to stretchable substrates via oxygen plasma or some other technique. However, it would be beneficial to avoid tedious bonding steps if possible.

The fabrication presented in fig. G.2a is nearly identical to that presented in chapter 2. The primary difference is the lack of a second layer of cPDMS. Instead, step iii is replaced with iii.b, which simply coats the entire surface with regular PDMS.

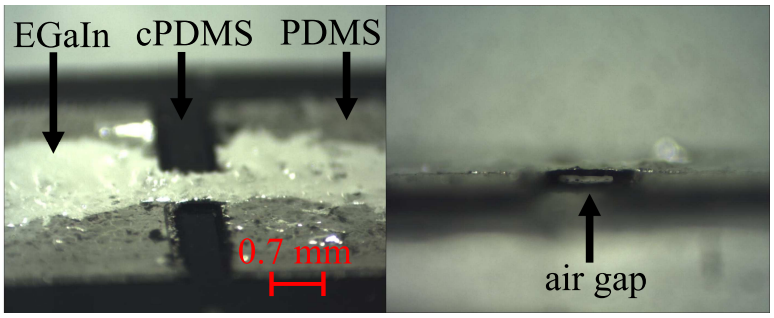

Figure G.3: Preliminary fixed-fixed beams fabricated using PAA.

Similar laser settings were used for patterning the structures. Fig. G.2 also shows some sample structures, demonstrating the resolutions capable with a CO_2 laser and PAA sacrificial layers. These processes for creating suspended bodies could be easily extended to created manual electrical switches that do not require the conductivity of the human body for activation, as required by devices in [6].

Using materials different from those presented in chapter 2 could also allow for the creation of fixed-fixed hyperelastic electrostatic beams. Because cPDMS tends to be extremely viscoelastic, it would be best to avoid it as a material for the actuating beam (particularly when experiencing large changes in stretch). Instead, for testing purposes, ordinary PDMS can be used in conjunction with eutectic gallium-indium (EGaIn). An example is shown in Fig. G.3, where the beam was manually coated with EGaIn on its top surface using a scrap piece of elastomer. This fabrication method has not yet been perfected, and testing of the electrostatic beams has not yet been performed. An alternate material which may be tested in the future work is EGaIn-PDMS composites [37].

Appendix H

Signal Cantilever Beams

The following work was performed with the goal of creating a functional electrostatic cantilever switch. As shown in Fig. H.1, the cantilever beam contains of two cPDMS traces. One is a grounded electrode which is parallel to a stationary pull-in electrode. The second trace carries the signal. When the stationary electrode is charged, the beam deforms, causing the signal carrying trace to make contact with a conductive pad on the body of the device. This completes the circuit. It was hoped that, after releasing the charge, the beams elastic restoring force would return the device to its original, off-state position.

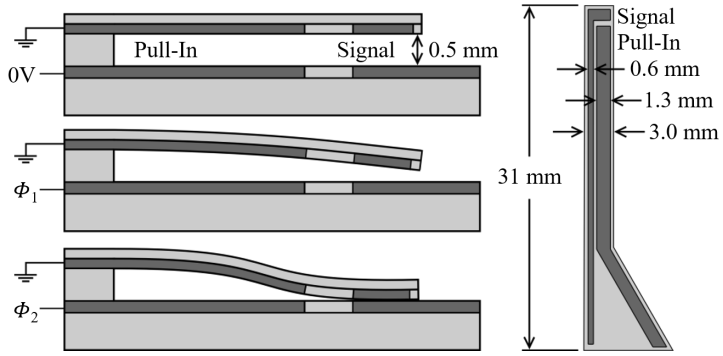

Figure H.1: Device with approximate dimensions. The light grey is PDMS and the dark grey is cPDMS. Left: Actuation functionality (not to scale). Right: Top view of beam (drawn to scale).

H.1 Method

H.1.1 Rapid Prototyping for Soft-Matter Electronics [6]

The following research for rapid prototyping with a CO_2 laser was lead by Tong Lu of the Soft Materials Laboratory. While reliable, many existing methods for soft-circuit fabrication typically require photolithography or customized printing hardware and can be costly and time consuming. An exception is the method presented in [261] in which a commercial excimer laser (wavelength, $\lambda = 248$ nm) is used to produce molds for casting cPDMS. Another approach is stencil lithography, which has been recently applied to liquid GaIn [103, 119, 262] and is discussed in Chapter 2. However, although it is rapid and inexpensive, stencil lithography can only be used to produce a limited range of circuit geometries.

CO_2 laser ablation has been previously used to produce microfluidic channels in PMMA [263] and PDMS [264]. Polymers are typically patterned through a combination of vaporization and the displacement of molten polymer. Molten polymer is displaced when the pressure of the escaping vapor (recoil force) exceeds the surface tension of the liquid. We introduce a method for producing soft-matter electronic circuits by patterning thin films of cPDMS and liquid-phase EGaIn alloy with a CO2 laser (10.6 μm wavelength). This rapid prototyping approach to fabrication eliminates the need for photolithography or customized printing hardware. Moreover, we demonstrate the ability to laser-pattern EGaIn through a mechanism that exploits the unique moldability of the liquid alloy. After the excess EGaIn and elastomer are removed, the patterned film is sealed in additional PDMS.

Patterning of cPDMS is essentially a three step process. First, we coat cPDMS on a metallic surface via spin coater or thin-film applicator. After curing, patterns can be cut with the CO_2 laser, and excess material can be peeled away. The metallic surface is not easily affected by the CO_2 laser, making it an appropriate work substrate.

Finally, the exposed conductive traces can be coated in PDMS. After curing and any additional cuts to shape the final product, we peel the entire film up (PDMS and cPDMS joined together). This process was used to create the beams described in this chapter and is described in more depth in [6].

In contrast to elastomers, liquid-phase GaIn metal alloys cannot be ablated with a CO_2 laser. As with other metals, EGaIn would require a high-energy UV radiation source for photochemical ablation. Instead, we postulate that EGaIn is removed with the same liquid metal expulsion mechanisms used in CO_2 laser beam welding (LBW) [265]. However, whereas stainless steel, titanium, and other solid metals require a high power to initiate melting (>1 kW for CO_2 lasers), GaIn alloys are already molten at room temperature and, as with molten polymer, can be displaced by pressure from the vapor escaping the PDMS beneath. If GaIn is applied as a sufficiently thin layer (around 20 μm or less), the heat generated from the laser will be enough to vaporize underlying elastomer. The pressure from the vaporized elastomer exceeds the surface tension of the GaIn, allowing the vapor to puncture the liquid metal film. The surface tension of GaIn alloys includes a surface oxide of Ga_2O_3 that prevents the liquid from flowing back into the laser-patterned region. In other words, this property of "moldability" enabled by the oxide skin [29, 98, 101, 266] allows the liquid to retain its shape after it has been patterned. Since they have both low fluidic viscosity and a high surface tension, GaIn alloys can simultaneously behave like a solid and a liquid at sub-millimeter length scales. This unique combination of properties enables the rare ability to pattern a metal alloy with an inexpensive laser engraving system that operates at relatively high wavelengths (10.6 μm) and low power (1-30 W).

To pattern thin films of liquid EGaIn alloy, we begin by spin coating a layer of PDMS on a brass cutting sheet. Next, we use an elastomeric roller to deposit a 10-20 μm thin layer of EGaIn; a minimum thickness of 10 μm has been measured with optical profilometry (Zygo NewView 7300 Optical Profilometer). An extra layer of PDMS

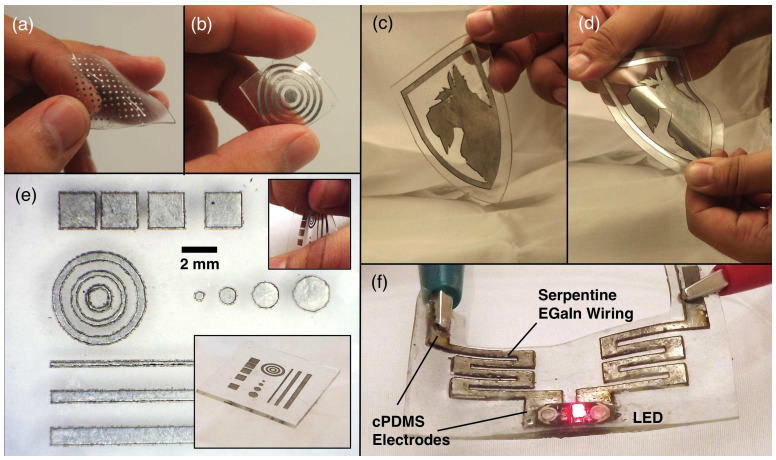

Figure H.2: Samples [6]. a,b) PDMS embedded with laser-patterned inclusions of EGaIn. c,d) Large area sample. e) Miniaturized features: 2 mm 2 mm squares spaced 0.25, 0.5, and 1 mm apart; concentric rings with diameters of 1.5, 3, and 5 mm and widths of 0.25, 0.35, and 0.5 mm, respectively; circles with diameters of 0.5, 1, 1.5, and 2 mm; rectangular strips with widths of 0.3, 0.7, and 1 mm. f) LED circuit containing laser-patterned (Ag/Ni)cPDMS and EGaIn.

is spun-coated on the GaIn alloy and cured before patterning the alloy and underlying PDMS substrate with a CO_2 laser. This extra layer of PDMS serves to prevent the EGaIn from oxidizing and getting coated in debris during laser-patterning. Next, we remove the excess material and seal the patterned circuit. After the sealing layer has cured, we peel the circuit from the brass cutting sheet. This approach to EGaIn patterning exploits the alloys liquid state and strong surface tension, which allows it to hold its shape after being cut with a CO_2 laser. The samples presented in Figs. H.2a-e demonstrate the versatility of this approach to rapidly pattern liquid GaIn with millimeter-scale resolution over a large area. Fig. H.2f presents an integrated circuit composed of laser-patterned EGaIn and conductive elastomer electrodes (NuSil R-2637) used to mount an LED and connect the circuit to an external power supply. This sample demonstrates the ability to pattern multiple conductive materials and maintain conductivity. This prototyping technique has not yet been applied to the active soft MEMS described in this document, but it my prove useful in the future.

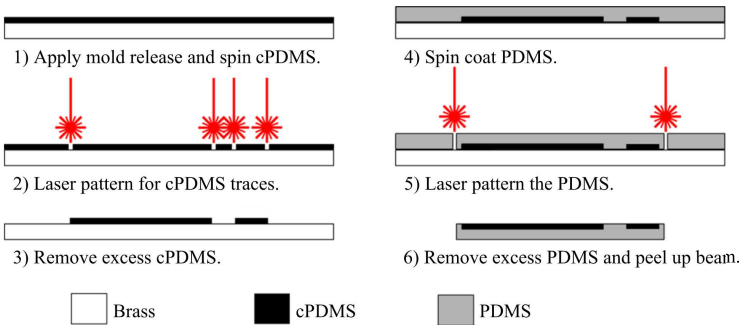

Figure H.3: Beam fabrication process.

H.1.2 Beam Fabrication

The cPDMS recipe and the beam fabrication method (Fig. H.3) were derived from [6], which is described above. To create the cPDMS, 1.85 g of carbon black (SigmaAldrich, Inc), 10.5 g of 20:1 PDMS (Sylgard 184, Dow Corning, Inc), and at least 13 g of hexane (SigmaAldrich, Inc) were combined in a small sealed cup. This resulted in cPDMS with 15% carbon by weight. The hexane decreased the viscosity, aiding in the dispersion of carbon particles and facilitating subsequent spin coating or spreading with a thin film applicator. A magnetic stirrer (Isotemp, Fisher Scientific, Inc) was used to mix the uncured conductive elastomer for at least 3 hours at 700 rpm.

A thin brass sheet served as the substrate for spinning thin layers of polymer. Before spin coating the cPDMS, mold release (Ease Release 200, Mann Release Technologies, Inc) was applied to the surface of the brass. The mold release is unnecessary but may prevent tearing as the device is peeled off the substrate. The first spin cycle was set at 1000 rpm for 9 seconds. For best results with the cPDMS, the uncured polymer was placed on the spinning sheet during this first cycle. The second cycle was set at 2000 rpm for 20 seconds. The cPDMS could then be cured on a hot plate (Isotemp, Fisher Scientific, Inc) at 85^{o}C for about 45 minutes.

After fully curing the cPDMS, a laser engraver (VLS3.50, Universal Laser Systems, Inc) was used to cut out the shapes for the pull-in electrode and the signal path. The

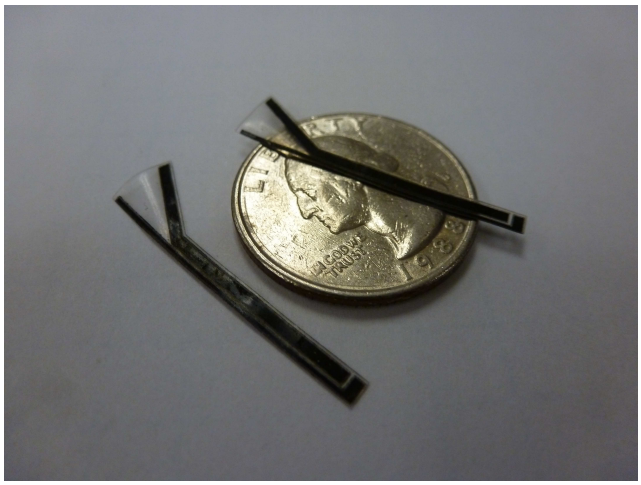

Figure H.4: Fabricated signal beams.

laser, set at about 3% power and 5% speed, is capable of ablating thin layers of PDMS and cPDMS without significantly singing the surrounding area, but its wavelength is too large to affect the brass. Multiple passes were performed in some cases to ensure a clean cut. Afterwards, the surrounding cPDMS was removed manually, leaving behind the electrode and signal path.

10:1 PDMS spun on top of the cPDMS traces using the same two spin settings. This was cured on the hot plate at 85^{o}C for about 45 minutes. Two sets of samples were created. For second set, another layer of 10:1 PDMS was added using the same process. The first set of samples were approximately 100 μm thick and the second set were about 140 μm. The laser engraver was then used to cut through the PDMS layer around the cPDMS traces, forming the beam and the connection points. After manually removing the surrounding PDMS, the beams were carefully peeled up by hand with the use of tweezers and razors. Sample final signal beams can be seen in Fig. H.4.

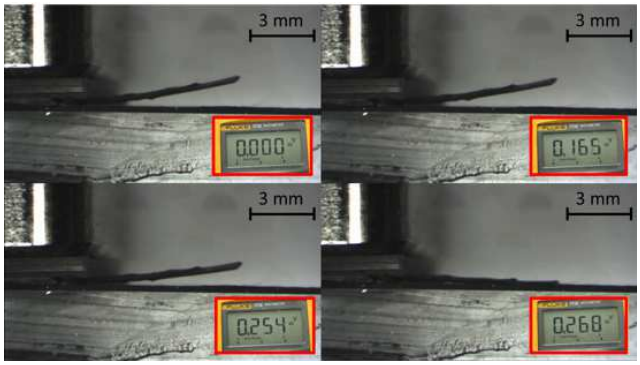

Figure H.5: Actuation of a signal beam. The voltages are 0 V, 165 V, 254 V, and 268 V.

H.1.3 Experimental Setup

To test actuation, the beams were clamped (Fig. H.5) at one end to a 4 mm thick block of PDMS. The block of PDMS had a thin coating of cPDMS which functioned as the stationary pull-in electrode. A thin (350 μm) layer of PDMS acts as an insulator between the beam and the surface, also providing the initial distance, d. A high voltage power supply (6209B, Hewlett-Packard, Inc) was used to ground the beam while applying charges to the stationary surface.

H.2 Results

The signal path on the beam, unfortunately, provided a resistance of 10s to 100s of mega-ohms. This made testing for completed circuits impractical. Specifically, cPDMS samples (170 μm by 9.5 mm cross-section) demonstrated a lengthwise (between 24 and 84 mm) resistivity of 0.7 Ω-m. Further, the value through the thickness was about 3000 Ω-m. For reference, the resistivity of copper is $1.7*10^{-8}$ Ω-m. At the moment, it is unclear why the resistivity through the thickness differs, though it could be due to percolation probabilities at small length scales.

Although this level of resistivity is unacceptable for completing circuits, it is suit-

able for electrostatics where little to no current is required. Despite initial curvatures due to residual stresses, actuation could typically be achieved in less than 300 V for beam lengths of 5 mm or longer. Figure H.5 demonstrates the actuation of a signal beam. The initial curvature is evident in the upper left image, where 0 V is applied.

Appendix I

Rod Theory History

The following elastic rod history is described in greater detail within Antman's Nonlinear Problems of Elasticity [267]. By 1732, initial work by Bernoulli and Euler resulted in a set of inextensible beam equations defined based on moment balance and Hooke's law. The internal bending moment of a beam undergoing planar deflections was shown to vary linearly with curvature. Euler expanded the elastica theory and included force balance in 1771 and 1774. With this theory, large deformations can be considered as long as strains remain small. It was not until the mid-1800s that St. Venant accounted for twist and scholars such as Kirchhoff and Love contributed to the understanding of strains. A thorough source for the work up until this point is A Treatise on the Mathematical Theory of Elasticity by Love [268]. What we now refer to as directors were introduced by the Cosserat brothers in work from 1907 and 1909. With this directed model, each point along the curve of the beam is defined with a set of deformable vectors.

Most models today take a directed rod approach, particularly after 1958 when Ericksen and Truesdell [269] dedicated a paper to the Cosserat brothers. Their paper clarifies and builds on work by the Cosserats and other scholars regarding rod and shell stress and strain theory. In a paper from 1966, Green and Laws created a general

theory for rods [270], and the theory was further developed by Green, Naghdi, and Wenner based on three-dimensional continuum mechanics in 1974 [271, 272]. Since then, these theories have been widely applied to helical wires [273], self-contacting elastic rods [274], and loop formation [275].

Appendix J

Ecoflex 0030 Tensile Data

Fig. J.1 displays tensile data (Instron, 33R 4442) from three separate beams. After the first loading, the second and third settle out on a particular path. This behavior is known as the Mullins effect [276]. Data was taken from the third set for each beam and averaged to acquire the curve used for fitting constitutive models in Chapter 3.

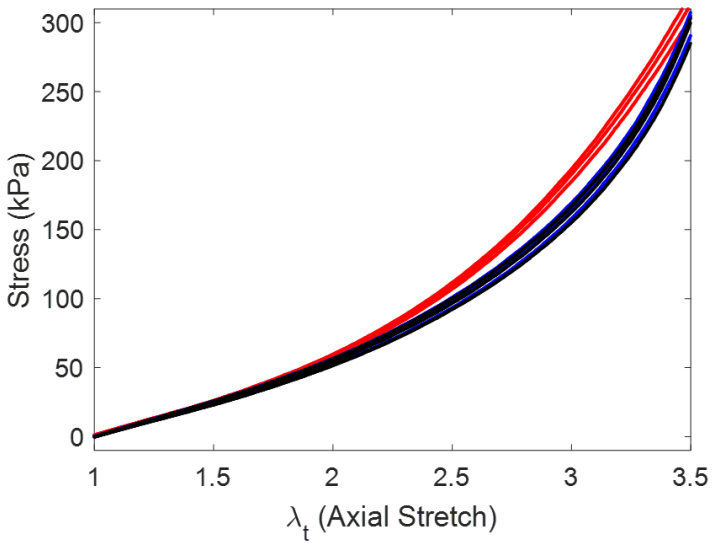

Figure J.1: Instron data from 3 separate Ecoflex 0030 beams (each of dimension 70 mm x 20 mm x 4 mm). The first loading (unloading was not included) is shown in red. The second is blue, and the third is black.

Appendix K

Visualization for Fixed End Algorithms

The following describes the algorithms for maintaining beam ends which maintain fixed positions. Specifically, these represent the process for point load (centered). They can be extended to distributed loads and other conditions.

K.1 Solving for $\theta(s)$

This algorithm (fig. K.1) is used for

$$\frac{d^2\theta}{ds^2} = \frac{F}{I^*E^*}\sin(\theta) + \frac{V}{I^*E^*}\cos(\theta). \tag{K.1}$$

Additional stretch is applied to the beam until the deformed beam (under point load) has the same end to end length as the reference condition. The beam bending is solved with MATLAB's *bvp4c* and the comparison of the beam center was performed with *fsolve*.

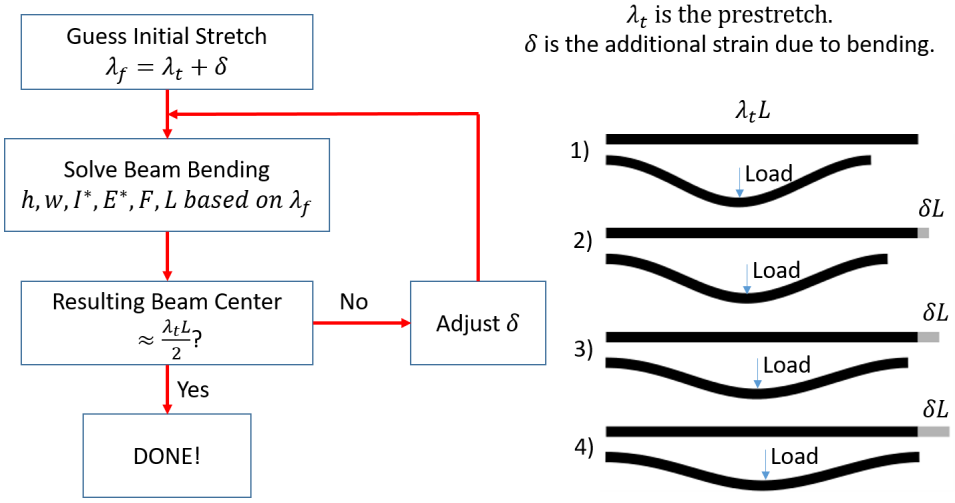

Figure K.1: Process for acquiring fixed end positions when solving for $\theta(s)$.

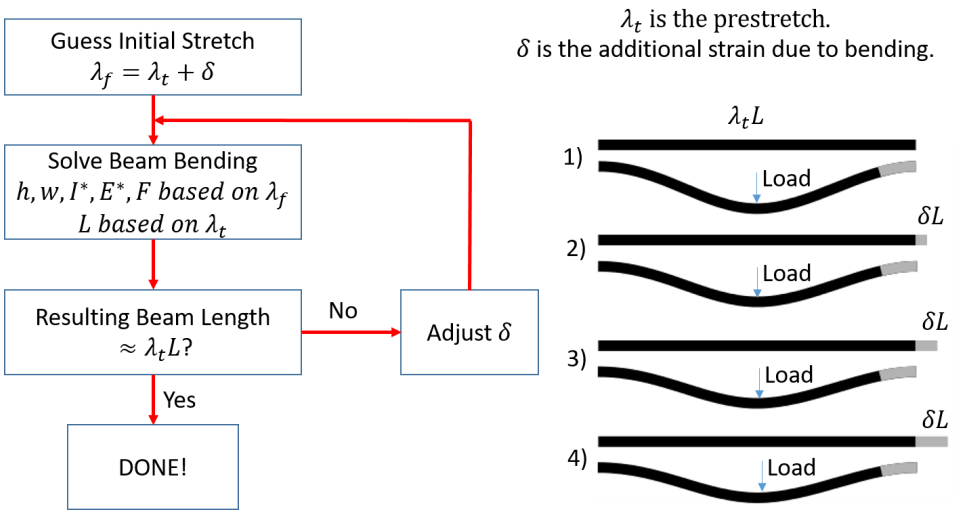

Figure K.2: Process for acquiring fixed end positions when solving for $y(x)$.

K.2 Solving for $y(x)$

This algorithm (fig. K.2) is used for

$$\frac{d^4y}{dx^4} = \frac{F}{I^*E^*}\frac{d^2y}{dx^2} - \frac{q}{I^*E^*}. \tag{K.2}$$

Additional stretch is applied to the beam until the beam length before and after point load are identical. The beam bending is solved with MATLAB's *bvp4c* and the comparison of the beam length was performed with *fsolve*.

Appendix L

BVP Re-Formulation for MATLAB

MATLAB's *BVP4C* requires that the problem be described as a system of 1st order ODEs. Below, I describe the process for obtaining these equations based on the stretched fixed-fixed beam governing equations. Here we consider electrostatic loading. This can be extended to the cantilever beams, different loading conditions, and other examples.

We begin with the governing equation:

$$\frac{d^2\theta}{ds^2} = \frac{F}{I^*E^*}\sin(\theta) + \frac{V}{I^*E^*}\cos(\theta). \tag{L.1}$$

We also note that:

$$\frac{dV}{ds} = -q(s) \tag{L.2}$$

and that

$$q = -\frac{\epsilon_0\Phi^2 w}{2(d+y)^2}. \tag{L.3}$$

In this case, q is in terms of y, but the rest of the governing equation is in terms

of θ. To handle this case, we apply

$$y = \int_0^s sin(\theta) ds. \tag{L.4}$$

With the Second Fundamental Theorem of Calculus, we know that

$$y' = sin(\theta). \tag{L.5}$$

With the above, we have all the information required to define a system of 1st order ODEs describing the governing equation. To start, we define that $f_1 = \theta$, $f_3 = V$, $f_4 = y$, and

$$f_1' = \theta' = f_2, \tag{L.6}$$

$$f_2' = \theta'' = \frac{F}{I^* E^*} \sin(f_1) + \frac{f_3}{I^* E^*} \cos(f_1), \tag{L.7}$$

$$f_3' = -q = \frac{\epsilon_0 V^2 w}{2(f + f_4)^2}, \tag{L.8}$$

$$f_4' = sin(f_1) = y'. \tag{L.9}$$

To accompany these four 1st order ODEs, we require four boundary conditions. With the fixed-fixed beam problem definition, we define:

$$f_1(0) = \theta(0) = 0, \tag{L.10}$$

$$f_1(l_f) = \theta(l_f) = 0, \tag{L.11}$$

$$f_4(0) = y(0) = 0, \tag{L.12}$$

$$f_4(l_f) = y(l_f) = 0. \tag{L.13}$$

This system of equations can be plugged into *BVP4C* to reach a numeric solution.

Below are posted the 1st order ODEs and boundary conditions when solving for

$$\frac{d^4y}{dx^4} = \frac{F}{I^*E^*}\frac{d^2y}{dx^2} - \frac{q}{I^*E^*}. \tag{L.14}$$

1st order ODES, after setting $g_1 = y$:

$$g_1' = y' = g_2, \tag{L.15}$$

$$g_2' = y'' = g_3, \tag{L.16}$$

$$g_3' = y''' = g_4, \tag{L.17}$$

$$g_4' = y'''' = \frac{F}{I^*E^*}\frac{d^2y}{dx^2} - \frac{q(g_1)}{I^*E^*}. \tag{L.18}$$

Boundary conditions:

$$g_1(0) = y(0) = 0, \tag{L.19}$$

$$g_1(l) = y(l) = 0, \tag{L.20}$$

$$g_2(0) = y'(0) = 0, \tag{L.21}$$

$$g_2(l) = y'(l) = 0. \tag{L.22}$$

Appendix M

Fixed-Fixed Point Load MATLAB Code

```
%% PointLoadIterate.m
% Iterates through a point load being applied to a hyperelastically
% stretched beam. Can assume beam has fixed ends in terms of ...
   position or
% can assume that a constant force F is stretching the beam.
%
% Currently approximating Ecoflex 0030

%% Beam dimensions, conditions, and properties
% Currently assumed to be rectangular cross-section...
W = 0.02;    % Beam width (m)
H = 0.004;   % Beam thickness (m)
L = 0.07/2;  % Beam length (m) (/2 because load at center  of beam)

fix   = 0; % 0-Constant force F (constant stretch, lam), 1-Ends are ...
   fixed.
type1 = 1; % 0-Deflection d is varied (only for y(x) solver), ...
   1-Point load is varied
type2 = 0; % 0-y(x) solver, 1-theta(s) solver
model = 3; % 0-NeoHookean, 1-Mooney-Rivlin, 2-2 Param Ogden, 3-3 ...
   Param Ogden


%% Iteration inputs
lambda_trange = [1 1.02 1.05 1.1 1.25 1.5 2 2.5 2.75 3];    % Input ...
   stretch range

% Note - if these meshes aren't fine enough, the solver will have ...
   trouble
% finding a solution when considering the fixed end case. (Extra stretch
% delta appears to be causing instabilities)
drange   = 0:0.00025:0.007;     % Deflection range (m)
Loadrange   = 0:0.001:0.6;       % Load range (N) (note this is ...
   halved for each half of the beam)
```

```
dlimit = 0.007; % Limit in deflection when varying load.
Loadlimit = 0.6; % Limit in load when varying deflection.


%% Constitutive equations
% Total stretch (delta is additional stretch due to fixed ends)
lambda_f = @(lambda_t,delta) lambda_t + delta;

if model == 0 % Neo-Hookean
    % Material constants
    alpha1 = 2;
    E = 50000; % Elastic moduls (Pa)
    C1 = E/6;
    mu1 = C1*alpha1;

    % Stress as a function of stretch: sigma = f(lam)
    sigma_t = @(lambda_t,delta) ...
       mu1*(lambda_f(lambda_t,delta).^(alpha1) -...
        lambda_f(lambda_t,delta).^(-0.5*alpha1));

    % Effective modulus as a function of stretch: effective E = ...
       sigma_t'(lam) = effE(lam)
    effE = @(lambda_t,delta) ...
       mu1*(alpha1*lambda_f(lambda_t,delta).^(alpha1-1) + ...
        0.5*alpha1*lambda_f(lambda_t,delta).^(-0.5*alpha1-1));

elseif model == 1 % Mooney-Rivlin
    % Material constants
    alpha1 = 2;
    alpha2 = -2;
    C1 = 6.8824e+03;
    C2 = 1.4509e+03;
    mu1 = C1*alpha1;
    mu2 = C2*alpha2;


    % Stress as a function of stretch: sigma = f(lam)
    sigma_t = @(lambda_t,delta) ...
       mu1*(lambda_f(lambda_t,delta).^(alpha1) -...
        lambda_f(lambda_t,delta).^(-0.5*alpha1)) + ...
        mu2*(lambda_f(lambda_t,delta).^(alpha2) - ...
        lambda_f(lambda_t,delta).^(-0.5*alpha2));

    % Effective modulus as a function of stretch: effective E = ...
       sigma_t'(lam) = effE(lam)
    effE = @(lambda_t,delta) ...
       mu1*(alpha1*lambda_f(lambda_t,delta).^(alpha1-1) + ...
        0.5*alpha1*lambda_f(lambda_t,delta).^(-0.5*alpha1-1)) + ...
        mu2*(alpha2*lambda_f(lambda_t,delta).^(alpha2-1) + ...
        0.5*alpha2*lambda_f(lambda_t,delta).^(-0.5*alpha2-1));

elseif model == 2 % 2 Param Ogden
    % Material constants
```

```
    alpha1 = 2.2083;
    alpha2 = 10.9755;
    mu1 = 1.3111e+04;
    mu2 = 0.0968;

    % Stress as a function of stretch: sigma = f(lam)
    sigma_t = @(lambda_t,delta) ...
       mu1*(lambda_f(lambda_t,delta).^(alpha1) -...
        lambda_f(lambda_t,delta).^(-0.5*alpha1)) + ...
        mu2*(lambda_f(lambda_t,delta).^(alpha2) - ...
        lambda_f(lambda_t,delta).^(-0.5*alpha2));

    % Effective modulus as a function of stretch: effective E = ...
       sigma_t'(lam) = effE(lam)
    effE = @(lambda_t,delta) ...
       mu1*(alpha1*lambda_f(lambda_t,delta).^(alpha1-1) + ...
        0.5*alpha1*lambda_f(lambda_t,delta).^(-0.5*alpha1-1)) + ...
        mu2*(alpha2*lambda_f(lambda_t,delta).^(alpha2-1) + ...
        0.5*alpha2*lambda_f(lambda_t,delta).^(-0.5*alpha2-1));

elseif model == 3 % 3 Param Ogden
     % Material constants
    alpha1 = 1.2140;
    alpha2 = -8.1327;
    alpha3 = 16.9936;
    mu1 = 2.2889e+04;
    mu2 = -956.2478;
    mu3 = 2.6390e-05;

    % Stress as a function of stretch: sigma = f(lam)
    sigma_t = @(lambda_t,delta) ...
       mu1*(lambda_f(lambda_t,delta).^(alpha1) -...
        lambda_f(lambda_t,delta).^(-0.5*alpha1)) + ...
        mu2*(lambda_f(lambda_t,delta).^(alpha2) - ...
        lambda_f(lambda_t,delta).^(-0.5*alpha2)) + ...
        mu3*(lambda_f(lambda_t,delta).^(alpha3) - ...
        lambda_f(lambda_t,delta).^(-0.5*alpha3));

    % Effective modulus as a function of stretch: effective E = ...
       sigma_t'(lam) = effE(lam)
    effE = @(lambda_t,delta) ...
       mu1*(alpha1*lambda_f(lambda_t,delta).^(alpha1-1) + ...
        0.5*alpha1*lambda_f(lambda_t,delta).^(-0.5*alpha1-1)) + ...
        mu2*(alpha2*lambda_f(lambda_t,delta).^(alpha2-1) + ...
        0.5*alpha2*lambda_f(lambda_t,delta).^(-0.5*alpha2-1)) + ...
        mu3*(alpha3*lambda_f(lambda_t,delta).^(alpha3-1) + ...
        0.5*alpha3*lambda_f(lambda_t,delta).^(-0.5*alpha3-1));
end


%% Other functions
% Effective area moment of inertia
effI = @(lambda_t,delta) W*H^3/12/lambda_f(lambda_t,delta)^2;
```

```
% Effective horizontal force at ends
F = @(lambda_t,delta) ...
    sigma_t(lambda_t,delta)*W*H/lambda_f(lambda_t,delta);


%% Setup for iterations
if type1 == 0 % Varying d
    Load = ones(length(drange),length(lambda_trange)).*NaN; % ...
       Allocate space for shear force (N)
else % Varying V
    Load = ones(length(Loadrange),length(lambda_trange)).*NaN; % ...
       Allocate space for shear force (N)
end

d = Load; % Allocate space for displacement (mm)
j = 1; % Index for lambda_t


%% Iterate over stretches and deflections
for lambda_t = lambda_trange

    %%%% Intial guesses which are updated by numeric solutions
    if type2 == 0 % y(x) solver
        solinit = bvpinit(linspace(0,L*lambda_t,10),[0 0 0 0]);  % ...
           Initial guess for beam solution (flat)
    else % theta(s) solver
        solinit = bvpinit(linspace(0,L*lambda_t,10),[0 0]);      % ...
           Initial guess for beam solution (flat)
    end
    deltainit = 0; % Initial guess for additional stretch due to ...
       deflection


    %%%% Varying d
    if type1 == 0
        d(:,j) = drange;
        if type2 == 0 % y(x) solver
            for i = 1:length(drange)
                disp(['Stretch: ',num2str(lambda_t),', d: ...
                   ',num2str(drange(i)),' mm'])
                [x,y,solinit,deltainit,Load(i,j)] = PointLoad_y_d(L, ...
                   lambda_t, drange(i), solinit, deltainit, ...
                   lambda_f, effE, effI, F, fix);
                y = y(1,:);
                if Load(i,j) > Loadlimit  % Limit in load
                    break
                end
                % Plots the beam deflections. Only enable for small ...
                   drange/Loadrange and lambda_trange
                %  figure(j+1)
                %  plot(x,y)
                %  hold on
            end
        else % theta(s) solver
```

```
            error('Varying d only available for y(x) solver (type1 = ...
                0)')
        end


    %%%% Varying V
    else
        Load(:,j) = Loadrange;
        for i = 1:length(Loadrange)
            disp(['Stretch: ',num2str(lambda_t),', Load: ...
                ',num2str(Loadrange(i)),' N'])
            if type2 == 0 % y(x) solver
                [x,yfin,solinit,deltainit] = PointLoad_y_V(L, ...
                    lambda_t, Loadrange(i)/2, solinit, deltainit, ...
                    lambda_f, effE, effI, F, fix);
                y = yfin(1,:);
                if d(i,j) > dlimit  % Limit in deflection
                    break
                end
            else % theta(s) solver
                [s,thetafin,solinit,deltainit] = ...
                    PointLoad_theta_V(L, lambda_t, Loadrange(i)/2, ...
                    solinit, deltainit, lambda_f, effE, effI, F, fix);
                n = length(s);
                ds = s(2)-s(1);
                x = tril(ones(n,n))*(cos(thetafin(1,:)))'*ds; % ...
                    Approximate x
                y = tril(ones(n,n))*(sin(thetafin(1,:)))'*ds; % ...
                    Approximate y
                if d(i,j) > dlimit  % Limit in deflection
                    break
                end
            end
            d(i,j) = -y(end);
            % Plots the beam deflections. Only enable for small ...
                drange/Loadrange and lambda_trange
            % figure(j+1)
            % plot(x,y)
            % hold on
        end
    end


    % Uncomment if plotting beam deflections
    %  xlabel('x (mm)')
    %  ylabel('y (mm)')
    %  title(['Stretch: ',num2str(lambda_t)])
    %  if type1 == 0
    %      legend(num2str(drange'))
    %  else
    %      legend(num2str(Loadrange'))
    %  end
    %  set(gca,'fontsize',14)
```

```
    % Plots load (shear force) as a function of deflection
    figure(1)
    plot(d(:,j)*1000,Load(:,j),'k')
    hold on
    j = j + 1;

end

% Label for results plot
xlabel('Deflection (mm)')
ylabel('Force (N)')
legend(num2str(lambda_trange'))
axis([0 8 0 0.6])
set(gca,'fontsize',14)
```

```
%% PointLoad_y_V.m
%
% This code solves for the deformation of a fixed-fixed beam under a ...
   point
% load (generally centered). The function is solved in terms of y. The
% input is shear force (applied point load) V.
%
% Used in conjunction with PointLoadIterate
%
% Governing equations:
% y'''' = F/(effE*effI)*y''' - q/(effE*effI)
% [FOR q = 0: y'''' = F/(effE*effI)*y''']
%
% Governing equation as system of first order ODEs:
% y1' = y2 (= y')
% y2' = y3 (= y'')
% y3' = y4 (= y''')
% y4' = F/(effE*effI)*y3 (= F/(effE*effI)*y''')
%
% Boundary conditions:
% y(1)      = 0
% y'(1)     = 0
% y'(end)   = 0
% y'''(end) = V/(eff*effI)
%
% Fixed ends condition:
% During deflection, fixed ends causes an additional stretch of delta.
% Deformed beam length bl = L*lambda_f
%

function [x,yfin,solfin,deltafin] = ...
    PointLoad_y_V(L,lambda_t,V,solinit,delta,lambda_f,effE,effI,F,fix)

x = linspace(0,L*lambda_t,1000); % Values for x
options = optimset('TolFun',1e-8, 'TolX',1e-8); % Options for fsolve

% Boundary value problem solver
```

```
sol = @(lambda_t,delta) bvp4c(@(x,y)fourode(x, y, F(lambda_t,delta), ...
    effI(lambda_t,delta), effE(lambda_t,delta)), ...
    @(ya,yb)fourbc(ya,yb,V,effI(lambda_t,delta), ...
    effE(lambda_t,delta)), solinit);

if fix == 1
    % Solves such that fixed ends condition is met (solves for ...
       required delta)
    deltafin = fsolve(@(delta)beamlength(sol(lambda_t,delta),x)- ...
       L*lambda_f(lambda_t,delta),delta,options);
else
    % Assumes constant force (F and lam constant [delta = 0] with ...
       deformation)
    deltafin = 0;
end

% Pulls out final solutions
solfin = sol(lambda_t,deltafin);
yfin = deval(solfin,x);


    % Governing equation (system of first order ODEs)
    function dydx = fourode(~,y,F,effI,effE)
        dydx = [y(2);y(3);y(4);F/effI/effE*y(3)];
    end

    % Boundary conditions
    function res = fourbc(ya,yb,V,effI,effE)
        res = [ya(1);ya(2);yb(2);yb(4)-V/(effI*effE)];
    end

    % Calculating the length of the deformed beam
    function bl = beamlength(sol,x)
        y = deval(sol,x);
        bl = sum(sqrt(diff(y(1,:)).^2+diff(x).^2));
    end


end
```

```
%% PointLoad_y_d.m
%
% This code solves for the deformation of a fixed-fixed beam under a ...
   point
% load (generally centered). The function is solved in terms of y. The
% input is displacement d.
%
% Used in conjunction with PointLoadIterate
%
% Governing equations:
% y'''' = F/(effE*effI)*y''' - q/(effE*effI)
% [FOR q = 0: y'''' = F/(effE*effI)*y''']
```

```
%
% Governing equation as system of first order ODEs:
% y1' = y2 (= y')
% y2' = y3 (= y'')
% y3' = y4 (= y''')
% y4' = F/(effE*effI)*y3 (= F/(effE*effI)*y''')
%
% Boundary conditions:
% y(1)    = 0
% y(end)  = -d
% y'(1)   = 0
% y'(end) = 0
%
% Fixed ends condition:
% During deflection, fixed ends causes an additional stretch of delta.
% Deformed beam length bl = L*lambda_f
%

function [x,yfin,solfin,deltafin,V] = PointLoad_y_d(L, lambda_t, d, ...
    solinit, delta, lambda_f, effE, effI, F, fix)

x = linspace(0,L*lambda_t,1000); % Values for x
options = optimset('TolFun',1e-12, 'TolX',1e-12); % Options for fsolve

% Boundary value problem solver
sol = @(lambda_t,delta) bvp4c(@(x,y)fourode(x, y, F(lambda_t,delta), ...
    effI(lambda_t,delta), effE(lambda_t,delta)), ...
    @(ya,yb)fourbc(ya,yb,d), solinit);

if fix == 1
    % Solves such that fixed ends condition is met (solves for ...
       required delta)
    deltafin = fsolve(@(delta)beamlength(sol(lambda_t,delta),x)- ...
       L*lambda_f(lambda_t,delta),delta,options);
else
    % Assumes constant force (F and lam constant [delta = 0] with ...
       deformation)
    deltafin = 0;
end

% Pulls out final solutions
solfin = sol(lambda_t,deltafin);
yfin = deval(solfin,x);

% The shear force is the applied load (for point load case)
V = yfin(4,end)*effI(lambda_t,deltafin)*effE(lambda_t,deltafin)*2; % ...
    Calculate shear force (~y'''*effI*effE). Doubled for each half ...
    of beam.)

    % Governing equation (system of first order ODEs)
    function dydx = fourode(~,y,F,effI,effE)
        dydx = [y(2);y(3);y(4);F/effI/effE*y(3)];
    end
```

```
    % Boundary conditions
    function res = fourbc(ya,yb,d)
        res = [ya(1);yb(1)+d;ya(2);yb(2)];
    end

    % Calculating the length of the deformed beam
    function bl = beamlength(sol,x)
        y = deval(sol,x);
        bl = sum(sqrt(diff(y(1,:)).^2+diff(x).^2));
    end


end
```

```
%% PointLoad_theta.m
% This code solves for the deformation of a fixed-fixed beam under a ...
   point
% load (generally centered). The function is solved in terms of ...
   theta. The
% input is shear force (applied point load) V.
%
% Used in conjunction with PointLoadIterate
%
% Governing equations:
% theta'' = F/(effE*effI)*sin(theta) + V/(effE*effI)*cos(theta)
%
% Governing equation as system of first order ODEs:
% theta1' = theta2 (= theta')
% theta2' = F/(effE*effI)*sin(theta1) + V/(effE*effI)*cos(theta1)
%    (= F/(effE*effI)*sin(theta + V/(effE*effI)*cos(theta)))
%
% Boundary conditions:
% theta(1)    = 0
% theta(end)  = 0
%
% Fixed ends condition:
% During deflection, fixed ends causes an additional stretch of delta.
% Deformed beam center midpoint = L*lambda_t
%

function [sfin,thetafin,solfin,deltafin] = PointLoad_theta_V(L, ...
   lambda_t, V, solinit, delta, lambda_f, effE, effI, F, fix)

s = @(lambda_t,delta) linspace(0,L*lambda_f(lambda_t,delta),1000); % ...
   Values for s (note these depend on the new delta value)
options = optimset('TolFun',1e-11, 'TolX',1e-11); % Options for fsolve


% Boundary value problem solver
sol = @(lambda_t,delta) ...
   bvp4c(@(s,theta)fourode(s,theta,F(lambda_t,delta), ...
   effI(lambda_t,delta), effE(lambda_t,delta),V), ...
```

```
    @(thetaa,thetab)twobc(thetaa,thetab), ...
    solinitNu(solinit,L,lambda_f(lambda_t,delta)));

if fix == 1
    % Solves such that fixed ends condition is met (solves for ...
       required delta)
    deltafin = ...
       fsolve(@(delta)midpoint(sol(lambda_t,delta),s(lambda_t,delta)) ...
       -L*lambda_t,delta,options);
else
    % Assumes constant force (F and lam constant [delta = 0] with ...
       deformation)
    deltafin = 0;
end

% Pulls out final solutions
sfin   = s(lambda_t,deltafin);
solfin = sol(lambda_t,deltafin);
thetafin = deval(solfin,sfin);


    % Governing equation (system of first order ODEs)
    function dthetadx = fourode(~,theta,F,effI,effE,V)
        dthetadx = [theta(2);F/(effE*effI)*sin(theta(1)) + ...
           V/(effE*effI)*cos(theta(1))];
    end

    % Boundary conditions
    function res = twobc(thetaa,thetab)
        res = [thetaa(1);thetab(1)];
    end

    % Calculating the x position of the middle of the beam
    function midp = midpoint(sol,s)
        theta = deval(sol,s);
        ds = s(2)-s(1);
        n = length(s);
        x = tril(ones(n,n))*(cos(theta(1,:)))'*ds; % Approximate x
        midp = x(end)-x(1);
    end

    % Create new intial guess by stretching the previous solution
    function solinit = solinitNu(solinit,L,lambda_f)
        xs = solinit.x;
        solinit.x = solinit.x*(L*lambda_f/xs(end)*1.000001); % A bit ...
           of extra stretch to account for numerical inaccuracies ...
           (I think...)
    end


end
```

Appendix N

Fixed-Fixed Electrostatic Load MATLAB Code

```
%% ElectrostaticLoadIterate.m
% Iterates through an electrostatic load being applied to a
% hyperelastically stretched beam. Can assume beam has fixed ends in ...
   terms
% of position or can assume that a constant force F is stretching ...
   the beam.
%
% Currently approximating Ecoflex 0030

%% Beam dimensions and conditions
% Currently assumed to be rectangular cross-section...
% W = 0.5*10^-3;     % Beam width (m)
% H = 0.01*10^-3;    % Beam thickness (m)
% L = 0.7*10^-3;     % Beam length (m)
% D = 0.1*10^-3;    % Gap height (m)
W = 0.5*10^-3;     % Beam width (m)
H = 0.05*10^-3;    % Beam thickness (m)
L = 0.7*10^-3;     % Beam length (m)
D = 0.05*10^-3;    % Gap height (m)

fix   = 0; % 0-Constant force F (constant stretch, lam), 1-Ends are ...
   fixed.
fixd  = 1; % 0-d is not fixed, 1-d is fixed (d = D)
type1 = 0; % 0-y(x) solver, 1-theta(s) solver
model = 3; % 0-NeoHookean, 1-Mooney-Rivlin, 2-2 Param Ogden, 3-3 ...
   Param Ogden


%% Iteration inputs
lambda_trange = [1 1.01 1.02 1.03 1.05 1.07 1.1 1.15 1.2 1.25 1.3 ...
   1.4 1.5 1.75 2 2.25 2.5 2.75 3];    % Input stretch range

% Note - if these meshes aren't fine enough, the solver will have ...
   trouble
```

```
% finding a solution when considering the fixed end case. (Extra stretch
% delta appears to be causing instabilities)
Phirange   = 0:0.2:12000;          % Load range (V)


%% Constitutive equations
% Total stretch (delta is additional stretch due to fixed ends)
lambda_f = @(lambda_t,delta) lambda_t + delta;

if model == 0 % Neo-Hookean
    % Material constants
    alpha1 = 2;
    E = 50000; % Elastic moduls (Pa)
    C1 = E/6;
    mu1 = C1*alpha1;

    % Stress as a function of stretch: sigma = f(lam)
    sigma_t = @(lambda_t,delta) ...
       mu1*(lambda_f(lambda_t,delta).^(alpha1) -...
        lambda_f(lambda_t,delta).^(-0.5*alpha1));

    % Effective modulus as a function of stretch: effective E = ...
       sigma_t'(lam) = effE(lam)
    effE = @(lambda_t,delta) ...
       mu1*(alpha1*lambda_f(lambda_t,delta).^(alpha1-1) + ...
        0.5*alpha1*lambda_f(lambda_t,delta).^(-0.5*alpha1-1));

elseif model == 1 % Mooney-Rivlin
    % Material constants
    alpha1 = 2;
    alpha2 = -2;
    C1 = 6.8824e+03;
    C2 = 1.4509e+03;
    mu1 = C1*alpha1;
    mu2 = C2*alpha2;


    % Stress as a function of stretch: sigma = f(lam)
    sigma_t = @(lambda_t,delta) ...
       mu1*(lambda_f(lambda_t,delta).^(alpha1) -...
        lambda_f(lambda_t,delta).^(-0.5*alpha1)) + ...
        mu2*(lambda_f(lambda_t,delta).^(alpha2) - ...
        lambda_f(lambda_t,delta).^(-0.5*alpha2));

    % Effective modulus as a function of stretch: effective E = ...
       sigma_t'(lam) = effE(lam)
    effE = @(lambda_t,delta) ...
       mu1*(alpha1*lambda_f(lambda_t,delta).^(alpha1-1) + ...
        0.5*alpha1*lambda_f(lambda_t,delta).^(-0.5*alpha1-1)) + ...
        mu2*(alpha2*lambda_f(lambda_t,delta).^(alpha2-1) + ...
        0.5*alpha2*lambda_f(lambda_t,delta).^(-0.5*alpha2-1));

elseif model == 2 % 2 Param Ogden
    % Material constants
```

```
    alpha1 = 2.2083;
    alpha2 = 10.9755;
    mu1 = 1.3111e+04;
    mu2 = 0.0968;

    % Stress as a function of stretch: sigma = f(lam)
    sigma_t = @(lambda_t,delta) ...
       mu1*(lambda_f(lambda_t,delta).^(alpha1) -...
        lambda_f(lambda_t,delta).^(-0.5*alpha1)) + ...
        mu2*(lambda_f(lambda_t,delta).^(alpha2) - ...
        lambda_f(lambda_t,delta).^(-0.5*alpha2));

    % Effective modulus as a function of stretch: effective E = ...
       sigma_t'(lam) = effE(lam)
    effE = @(lambda_t,delta) ...
       mu1*(alpha1*lambda_f(lambda_t,delta).^(alpha1-1) + ...
        0.5*alpha1*lambda_f(lambda_t,delta).^(-0.5*alpha1-1)) + ...
        mu2*(alpha2*lambda_f(lambda_t,delta).^(alpha2-1) + ...
        0.5*alpha2*lambda_f(lambda_t,delta).^(-0.5*alpha2-1));

elseif model == 3 % 3 Param Ogden
     % Material constants
    alpha1 = 1.2140;
    alpha2 = -8.1327;
    alpha3 = 16.9936;
    mu1 = 2.2889e+04;
    mu2 = -956.2478;
    mu3 = 2.6390e-05;

    % Stress as a function of stretch: sigma = f(lam)
    sigma_t = @(lambda_t,delta) ...
       mu1*(lambda_f(lambda_t,delta).^(alpha1) -...
        lambda_f(lambda_t,delta).^(-0.5*alpha1)) + ...
        mu2*(lambda_f(lambda_t,delta).^(alpha2) - ...
        lambda_f(lambda_t,delta).^(-0.5*alpha2)) + ...
        mu3*(lambda_f(lambda_t,delta).^(alpha3) - ...
        lambda_f(lambda_t,delta).^(-0.5*alpha3));

    % Effective modulus as a function of stretch: effective E = ...
       sigma_t'(lam) = effE(lam)
    effE = @(lambda_t,delta) ...
       mu1*(alpha1*lambda_f(lambda_t,delta).^(alpha1-1) + ...
        0.5*alpha1*lambda_f(lambda_t,delta).^(-0.5*alpha1-1)) + ...
        mu2*(alpha2*lambda_f(lambda_t,delta).^(alpha2-1) + ...
        0.5*alpha2*lambda_f(lambda_t,delta).^(-0.5*alpha2-1)) + ...
        mu3*(alpha3*lambda_f(lambda_t,delta).^(alpha3-1) + ...
        0.5*alpha3*lambda_f(lambda_t,delta).^(-0.5*alpha3-1));
end


%% Other functions
% Effective area moment of inertia
effI = @(lambda_t,delta) W*H^3/12/lambda_f(lambda_t,delta)^2;
```

```
% Effective horizontal force at ends
F = @(lambda_t,delta) ...
    sigma_t(lambda_t,delta)*W*H/lambda_f(lambda_t,delta);

% Final width for electrostatics
w = @(lambda_t,delta) W/sqrt(lambda_f(lambda_t,delta));

% Reference (pre-stretched) gap dimensions for electrostatics
if fixd == 0
    d = @(lambda_t) D/sqrt(lambda_t);
else
    d = @(lambda_t)D;
end


%% Setup for iterations
Phi = ones(length(Phirange),length(lambda_trange)).*NaN; % Allocate ...
    space for shear force (N)

md  = Phi; % Allocate space for midpoint displacement (mm)
j   = 1; % Index for lambda_t
PIs = ones(length(lambda_trange),1); % Allocate space for pull-in ...
    voltages
EPs = ones(length(lambda_trange),1); % Allocate space for pull-in ...
    positions


%% Iterate over stretches and deflections
for lambda_t = lambda_trange

    %%%% Intial guesses which are updated by numeric solutions
    solinit = bvpinit(linspace(0,L*lambda_t,20),[0 0 0 0]);  % ...
        Initial guess for beam solution (flat)
    deltainit = 0; % Initial guess for additional stretch due to ...
        deflection


    %%%% Varying Phi
    Phi(:,j) = Phirange;
    for i = 1:length(Phirange)
        disp(['Stretch: ',num2str(lambda_t),', Phi: ...
            ',num2str(Phirange(i)),'V'])
        try
            if type1 == 0 % y(x) solver
                [x,yfin,solinit,deltainit] = Electrostatic_y(L, w, ...
                    d(lambda_t), lambda_t,Phirange(i),solinit, ...
                    deltainit, lambda_f, effE, effI, F, fix);
                y = yfin(1,:);
            else
                [s,thetafin,solinit,deltainit] = ...
                    Electrostatic_theta(L, w, d(lambda_t), lambda_t, ...
                    Phirange(i), solinit, deltainit, lambda_f, effE, ...
                    effI, F, fix);
                n = length(s);
```

```
                ds = s(2)-s(1);
                x = tril(ones(n,n))*(cos(thetafin(1,:)))'*ds; % ...
                    Approximate x
                y = tril(ones(n,n))*(sin(thetafin(1,:)))'*ds; % ...
                    Approximate y
            end
            md(i,j) = y(end/2);
            if i > 1
                if md(i,j)>md(i-1,j) % Ends if beam starts moving ...
                    upwards
                    break
                end
            end
        catch
            break
        end
        % Plots the beam deflections. Only enable for small Phirange ...
            and lambda_trange
        % figure(j+1)
        % plot(x,y)
        % hold on
    end



    % Uncomment if plotting beam deflections
    % xlabel('x (mm)')
    % ylabel('y (mm)')
    % title(['Stretch: ',num2str(lambda_t)])
    % legend(num2str(Phirange'))
    % set(gca,'fontsize',14)

    % Find pull in point based on curvature (this sometimes fails)
    loc = find(diff(diff(md(1:i-1,j)))>0,1,'first')+1;
    if isempty(loc) % If curvature never positive, assume last value ...
        is PI
        loc = i-1;
    end
    PIs(j) = Phi(loc,j); % Store pull-in voltage
    EPs(j) = md(loc,j);  % Stores position at pull-in

    % Plots load (voltage) as a function of deflection
    figure(1)
    plot(Phi(:,j),md(:,j)*1000,'--')
    hold on
    j = j + 1;
end

% Pull in position and labels for position vs voltage plot
plot(PIs,EPs*1000,'^k','MarkerFaceColor', 'k')
xlabel('Voltage (V)')
ylabel('Deflection (mm)')
legend(num2str(lambda_trange'))
set(gca,'fontsize',14)
```

```
% Plot pull-in voltage as a function of beam length
figure
plot(lambda_trange,PIs,'--','linewidth',2)
xlabel('Stretch')
ylabel('Pull-In Voltage (V)')
set(gca,'fontsize',14)
```

```
%% Electrostatic_y.m
% This code solves for the deformation of a fixed-fixed beam ...
   electrostatic
% loading. The function is solved in terms of y. The input is voltage.
%
% Used in conjunction with ElectrostaticLoadIterate.m
%
% Governing equations:
% y'''' = F/(effE*effI)*y''' - q/(effE*effI)
% [FOR q = (eps*Phi^2*w)/(2*effE*effI*(d+y)^2)]
%
% Governing equation as system of first order ODEs:
% y1' = y2 (= y')
% y2' = y3 (= y'')
% y3' = y4 (= y''')
% y4' = F/(effE*effI)*y3 - (eps*Phi^2*w)/(2*effE*effI*(d+y1)^2)
%          (= F/(effE*effI)*y'''- (eps*Phi^2*w)/(2*effE*effI*(d+y)^2))
%
% Boundary conditions:
% y(1)    = 0
% y'(1)   = 0
% y(end)  = 0
% y'(end) = 0
%
% Fixed ends condition:
% During deflection, fixed ends causes an additional stretch of delta.
% Deformed beam length bl = L*lambda_f
%

function [x,yfin,solfin,deltafin] = Electrostatic_y(L, w, d, ...
   lambda_t, Phi, solinit, delta, lambda_f, effE, effI, F, fix)

x = linspace(0,L*lambda_t,1000); % Values for x
options = optimset('TolFun',1e-13, 'TolX',1e-13); % Options for fsolve


% Boundary value problem solver
sol = @(lambda_t,delta) bvp4c(@(x,y)fourode(x, y, F(lambda_t,delta), ...
   effI(lambda_t,delta), effE(lambda_t,delta), Phi, ...
   w(lambda_t,delta), d), @(ya, yb)fourbc(ya, yb), solinit);

if fix == 1
    % Solves such that fixed ends condition is met (solves for ...
       required delta)
```

```
    deltafin = fsolve(@(delta)beamlength(sol(lambda_t, delta), ...
       x)-L*lambda_f(lambda_t, delta), delta, options);
else
    % Assumes constant force (F and lam constant [delta = 0] with ...
       deformation)
    deltafin = 0;
end

% Pulls out final solutions
solfin = sol(lambda_t,deltafin);
yfin = deval(solfin,x);


    % Governing equation (system of first order ODEs)
    function dydx = fourode(~, y, F, effI, effE, Phi, w, d)
        eps = 8.85*10^-12;
        dydx = [y(2); y(3); y(4); F/effI/effE*y(3) - ...
            (eps*Phi^2*w)/(2*effE*effI*(d+y(1))^2)];
    end

    % Boundary conditions
    function res = fourbc(ya,yb)
        res = [ya(1);ya(2);yb(1);yb(2)];
    end

    % Calculating the length of the deformed beam
    function bl = beamlength(sol,x)
        y = deval(sol,x);
        bl = sum(sqrt(diff(y(1,:)).^2+diff(x).^2));
    end

end
```

```
%% Electrostatic_theta.m
% This code solves for the deformation of a fixed-fixed beam ...
   electrostatic
% loading. The function is solved in terms of theta. The input is ...
   voltage.
%
% Used in conjunction with ElectrostaticLoadIterate.m
%
% Governing equations:
% theta'' = F/(effE*effI)*sin(theta) + V/(effE*effI)*cos(theta)
% q = dV/ds = (eps*Phi^2*w)/(2*effE*effI*(d+y)^2)
% y = int(sin(theta),s,0,L*lambda_f)  ->  dy/ds = sin(theta)
%
% Governing equation as system of first order ODEs:
% fun1' = fun2 (= theta')
% fun2' = F/(effE*effI)*sin(fun1) + fun3/(effE*effI)*cos(fun1)
%       (= F/(effE*effI)*sin(theta) + V/(effE*effI)*cos(theta)))
% fun3' = q = (eps*Phi^2*w)/(2*effE*effI*(d+fun4)^2)
% fun4' = sin(fun1)
```

```
%
% Boundary conditions:
% fun1(1)     = 0    (theta(1)    = 0)
% fun1(end)   = 0    (theta(end)  = 0)
% fun4(1)     = 0    (y(1)        = 0)
% fun4(end)   = 0    (y(end)      = 0)
%
% Fixed ends condition:
% During deflection, fixed ends causes an additional stretch of delta.
% Deformed beam endpoint endp = L*lambda_t
%

function [sfin,thetafin,solfin,deltafin] = Electrostatic_theta(L, w, ...
    d,lambda_t, Phi, solinit, delta, lambda_f, effE, effI, F, fix)

s = @(lambda_t,delta) linspace(0,L*lambda_f(lambda_t,delta),1000); % ...
    Values for s (note these depend on the new delta value)
optionsbvp = bvpset('RelTol',1e-8,'AbsTol',1e-8,'NMax',2500); % ...
    Options for bvp4c
options = optimset('TolFun',1e-13, 'TolX',1e-13); % Options for fsolve


% Boundary value problem solver
sol = @(lambda_t,delta) bvp4c(@(s,theta)fourode(s, theta, ...
    F(lambda_t,delta), effI(lambda_t,delta), effE(lambda_t,delta), ...
    Phi, w(lambda_t,delta),d), @(funa,funb)fourbc(funa,funb), ...
    solinitNu(solinit,L,lambda_f(lambda_t,delta)), optionsbvp);

if fix == 1
    % Solves such that fixed ends condition is met (solves for ...
       required delta)
    deltafin = fsolve(@(delta)(endpoint(sol(lambda_t,delta), ...
       s(lambda_t,delta))-L*lambda_t),delta,options);
else
    % Assumes constant force (F and lam constant [delta = 0] with ...
       deformation)
    deltafin = 0;
end

% Pulls out final solutions
sfin   = s(lambda_t,deltafin);
solfin = sol(lambda_t,deltafin);
thetafin = deval(solfin,sfin);


    % Governing equation (system of first order ODEs)
    function dthetadx = fourode(~,fun,F,effI,effE,Phi,w,d)
        eps = 8.85*10^-12;
        dthetadx = [fun(2); ...
           F/(effE*effI)*sin(fun(1))+fun(3)/(effE*effI)*cos(fun(1)); ...
           -(eps*Phi^2*w)/(2*(d+fun(4))^2); sin(fun(1))];
    end

    % Boundary conditions
```

```
    function res = fourbc(funa,funb)
        res = [funa(1);funb(1);funa(4);funb(4)];
    end

    % Calculating the x position of the middle of the beam
    function endp = endpoint(sol,s)
        theta = deval(sol,s);
        ds = s(2)-s(1);
        n = length(s);
        x = tril(ones(n,n))*(cos(theta(1,:)))'*ds; % Approximate x
        endp = x(end)-x(1);
    end

    % Create new intial guess by stretching the previous solution
    function solinit = solinitNu(solinit,L,lambda_f)
        xs = solinit.x;
        solinit.x = solinit.x*(L*lambda_f/xs(end)*1.000001); % A bit ...
           of extra stretch to account for numerical inaccuracies ...
           (I think...)
    end


end
```

Appendix O

Additional Electrostatic Load Data

Fig. O.1 demonstrates the simulated deflection vs voltage behavior of an Ecoflex 0030 beams of length L =700 μm, width W =500 μm, and height H =10 μm. The initial height between the beam and pull-in electrode was D =100 μm. The applied pre-stretch force, F, remains constant. Fig. O.2 shows the same beam under the condition of fixed end positions (F increases as the beam deflects). In particular, the fixed ends condition changes the behavior of the beam under low stretches (~100%),

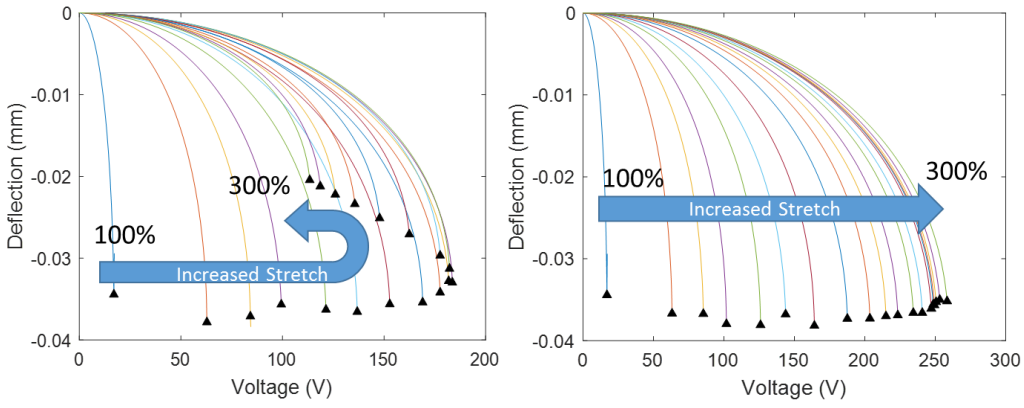

Figure O.1: Assuming the pre-stretch force remains constant. Pull-in data from MATLAB simulations for $d = D/\sqrt{\lambda_t}$ on the left and $d = D$ on the right. Each line represents the same beam at a different pre-stretch value. The pull-in voltage/displacement is marked by black rectangles.

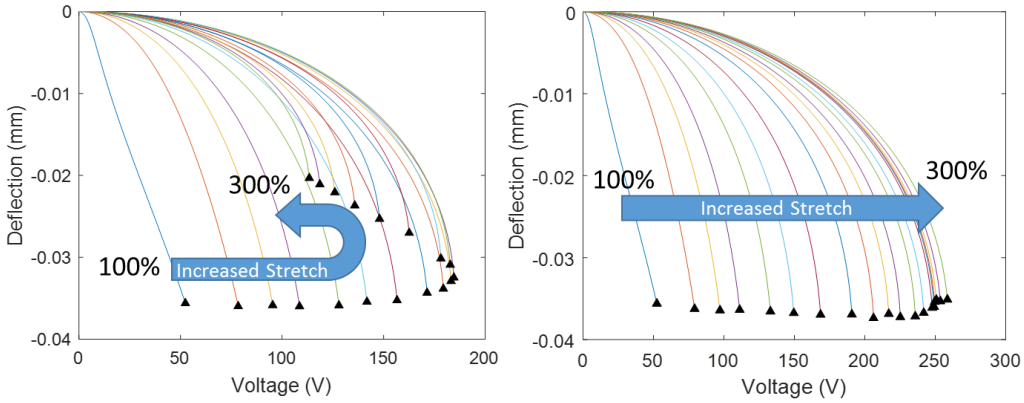

Figure O.2: Assuming the end positions remain constant. Pull-in data from MATLAB simulations for $d = D/\sqrt{\lambda_t}$ on the left and $d = D$ on the right. Each line represents the same beam at a different pre-stretch value. The pull-in voltage/displacement is marked by black rectangles.

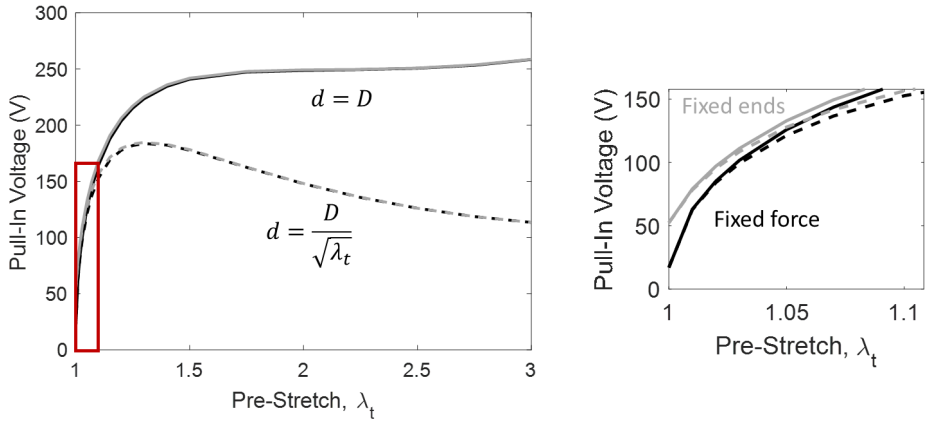

Figure O.3: Pull-in voltage as a function of pre-stretch for when dimension d remains constant ($d = D$) (solid) and for when dimension d changes with pre-stretch ($d = D/\sqrt{\lambda_t}$) (dashed). Black is for the fixed force condition and grey is for the fixed end position condition. On the right, a zoomed in region of low stretch values, highlighting the difference between fixed force and fixed ends.

increasing the pull-in voltage. This is a result of the beam undergoing the change from beam bending to membrane type behavior over the course of deflect. This is further reflected in fig. O.3, which shows a substantial difference between the fixed force and fixed position pull-in voltages when stretch values are small. This difference diminishes as pre-stretch increases.

Appendix P

Magnetic Field Measurement

The force $\mathbf{F_m} = F_m \mathbf{e}_z$ due to the external magnetic field causes a pre-buckled beam to snap-through from one stable configuration to another. As shown in fig. P.1, the magnet is centered a distance d above the beam supports and has a N/S orientation aligned with the beam's minor axis ($\mathbf{e}_z$). The magnetic force at this nominal distance is expected to scale with $y^{-3/2}$, i.e. $F_m = \beta_F / y^{3/2}$, where $y = d - w$ and β_F is a fitting

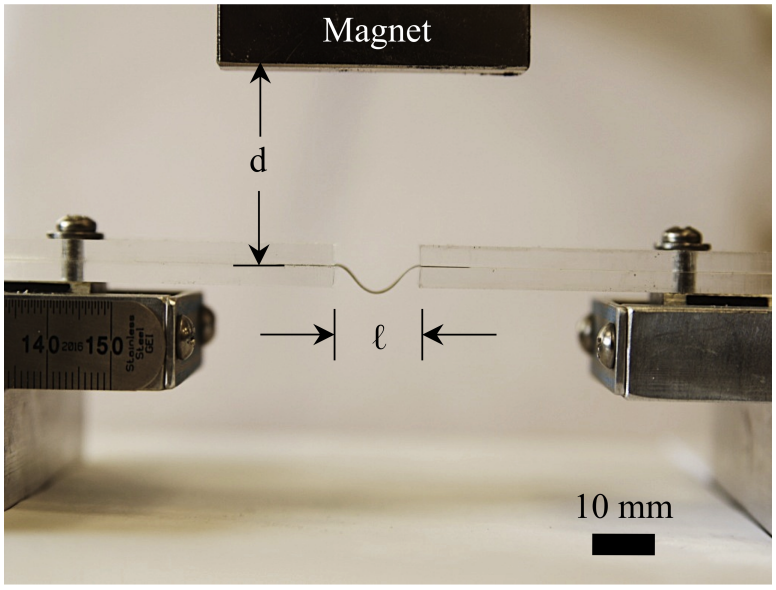

Figure P.1: A magnet is placed a distance d above the beam supports. The length ℓ corresponds to the horizontal distance between the supports.

parameter associated with the choice of permanent magnet. Since the width of the magnet is over 2× greater than L_0 and y, we assume that β_F is uniform along the length of the beam. Therefore, the only variation in F_m is due to the vertical beam deflection w.

For this study, we used a 2"x2"x1/4" NdFeB magnet (K&J Magnetics, Inc.) that was mounted to the travel head of a materials testing system (Instron 5969). The magnetic force F_m was measured for prescribed values of y using a 10 N load cell and a ferromagnetic sample of volume $V = 12.205$ mm^3, with the same composition as the beam. As expected, the magnetic force F_m due to the field was measured to approximately scale as $\beta_F/y^{3/2}$, where β_F is a proportionality constant obtained curve fitting. Field was measured below the center of the 50.8 mm wide magnet. To use this result for beams of different cross-sections, we define the magnetic force density f as the magnetic force F_m divided by the volume of ferromagnetic material V to obtain $\mathbf{f} = f\mathbf{e}_z$. Note that $f = F_m/V$, so $\beta = \beta_F/V$. Reasonable fitting against snap-through values was obtained with $\beta = 550$ N·m$^{-3/2}$. thus we calculate that β_F = 6.7128*10^{-}6 N·m$^{3/2}$.

Appendix Q

Buckled Beam Potential and Basis Functions

The potential Π is composed of the elastic strain energy (from bending), and the energy associated with gravity and magnetic field.

$$\Pi = \int_0^{L_0} \left\{ \frac{1}{2} D w_{,xx}^2 + q_g w - \frac{2 q_m}{(d-w)^{1/2}} \right\} dx \,. \tag{Q.1}$$

We approximate w using a pair of linearly independent basis functions ϕ_1 and ϕ_2: $w \approx \alpha\phi_1 + \alpha_2\phi_2$ and $w_{,xx} \approx \alpha_1\phi_1'' + \alpha_2\phi_2''$. We consider the following basis functions that are in qualitative agreement with the deflection modes that we observe experimentally.

$$\begin{aligned} \phi_1 &= \frac{1}{2}\left\{1 - \cos\left(\frac{2\pi x}{L_0}\right)\right\}, \\ \phi_2 &= \frac{4}{3\sqrt{3}} \sin\left(\frac{2\pi x}{L_0}\right)\left\{1 - \cos\left(\frac{2\pi x}{L_0}\right)\right\} . \end{aligned} \tag{Q.2}$$

Differentiating ϕ_1 and ϕ_2 twice with respect to x , we obtain:

$$\begin{aligned}\phi_1'' &= \frac{1}{2}\left(\frac{2\pi}{L_0}\right)^2 \cos\left(\frac{2\pi x}{L_0}\right), \\ \phi_2'' &= \frac{4}{3\sqrt{3}}\left(\frac{2\pi}{L_0}\right)^2 \left\{2\sin\left(\frac{4\pi x}{L_0}\right) - \sin\left(\frac{2\pi x}{L_0}\right)\right\}.\end{aligned} \tag{Q.3}$$

The Taylor series expansion of $\{1-(w/d)\}^n$ about $w/d = 0$ up to order 3 is expressed as:

$$\begin{aligned}\left(1-\frac{w}{d}\right)^n \approx & 1 + \frac{n}{1!}\left(-\frac{w}{d}\right) + \frac{n(n-1)}{2!}\left(-\frac{w}{d}\right)^2 \\ & + \frac{n(n-1)(n-2)}{3!}\left(-\frac{w}{d}\right)^3.\end{aligned} \tag{Q.4}$$

Substituting (Q.2) and (Q.3) in (Q.1), employing (Q.4), and dropping the terms in Π which are independent of α_1 and α_2:

$$\begin{aligned}\Pi \approx & \frac{D\pi^4}{L_0^3}\left(\alpha_1^2 + \frac{320}{27}\alpha_2^2\right) + \frac{L_0 q_g \alpha_1}{2} \\ & - \frac{L_0 q_m}{d^{3/2}}\left\{\frac{\alpha_1}{2} + \frac{1}{288d}\left(81\alpha_1^2 + 80\alpha_2^2\right) + \frac{5\alpha_1}{1152d^2}\left(45\alpha_1^2 + 112\alpha_2^2\right)\right\}).\end{aligned} \tag{Q.5}$$

This analytic expression approximates the numerical calculation of the potential energy better for higher values of $\hat{\lambda}$ i.e., $\hat{\lambda} \to 1$. For lower values of $\hat{\lambda}$ and subcritical distances ($d < d_{cr}$), as shown in fig. Q.1, the numerical model predicts the symmetric bifurcation of the local minimum at $\alpha_1 = \alpha_1^*, \alpha_2 = 0$, to two local minima having non zero α_2 values. As shown in the inset, the analytic model does not capture the bifurcation. This artifact might point to the possiblity of the beam being capable of possessing effective mode-shapes with non-zero α_2 values at equilibrium. This is also captured in fig. Q.2, where the numeric solution includes an inflection point, indicating the onset of non-zero α_2 prior to snap through. Note that the numeric solution only works until around $\hat{\lambda} = 0.8$ because the basis functions become undefined when

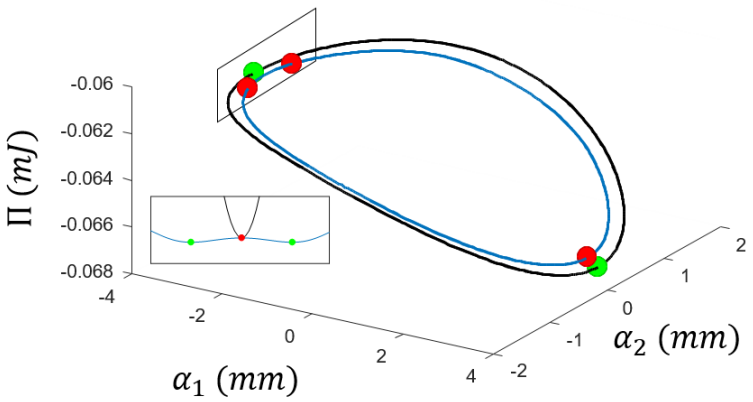

Figure Q.1: Numerical (blue) and analytical (black) results for the relative variation in the potential energy along the "valley" under sub-critical magnetic load with local and global minima indicated; numerical (red dot) and analytical (green dot) for $\hat{\lambda} = 0.85$ at a separation $d = 20.5$ mm.

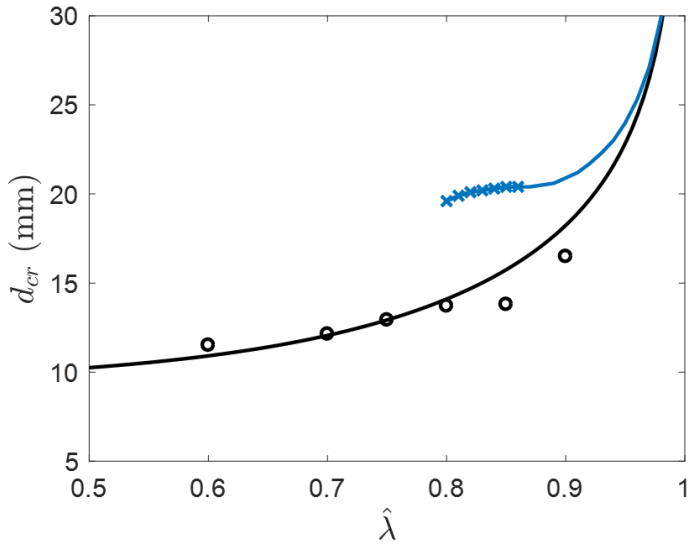

Figure Q.2: Numeric (blue line), analytic (black line), and experimental (black circles). The blue x markers indicate where the second basis function became non-zero prior to snap-through in the numeric solution.

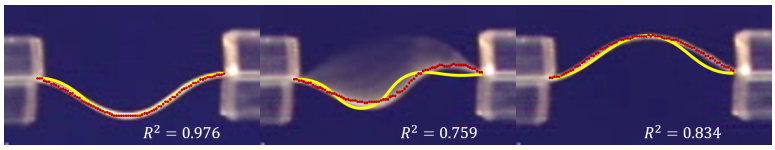

Figure Q.3: Least Squares fit of the two parameter representation for the deflection w of the beam undergoing snap through (left to right) from one stable configuration to the other under the influence of an increasing external magnetic field. The approximate beam shape is indicated by the solid yellow line and the actual beam shape is traced by the red dots.

used in conjunction with the isoperimetric constraint. Lastly, fig. Q.3 shows the least squares fitting of the two parameter representation of the beam deflection w to the video data for $\hat{\lambda} = 0.9$ as the beam transitions from being buckled downward initially, undergoing snap-through to being buckled upwards ultimately.

Appendix R

Magnetic Composite Tensile Data

Fig. R.1 is tensile data to determine the Young's modulus of the magnetic beam composite. The samples were approximately 51x10x0.13 mm in dimension. Testing was performed on an Instron (model 5969) at 10 mm/min.

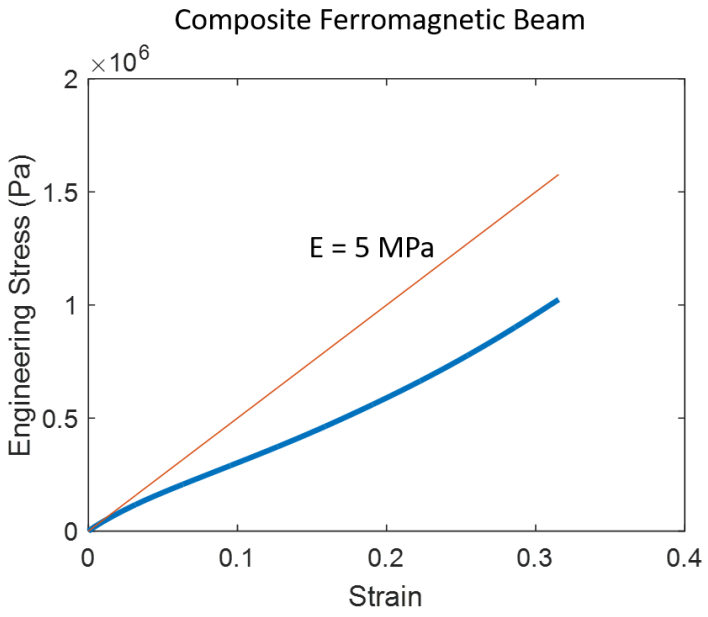

Figure R.1: Tensile data (blue) for magnetic composite beam - an average of 3 samples. The red line is a fit for Young's modulus.

Appendix S

Buckled Beam Magnetic Load MATLAB Code

```
%% AnalyticBeamEquOnly.m
%
% Only uses the analytic equation to solve for critical snap-through
% distance.
%

%% Primary inputs

lamrange = 0.99:-0.01:0.5;     % Buckle stretch range


%% Allocate space for outputs

d_NU  = zeros(1,length(lamrange)); % Numeric snap distance
d_AN  = d_NU;                      % Analytic snap distance
d_AN2 = d_NU;                      % Analytic snap distance version 2
k_NU  = d_NU;                      % Numeric number of mins prior to ...
   snap
k_AN  = d_NU;                      % Analytic number of mins prior ...
   to snap


%% Input dimensions, properties, etc...

L0 = 15.4e-3;      % Initial beam length (m)
w = 5e-3;          % Beam width (m)
h = 0.11e-3;       % Beam thickness (m)

I = w*h^3/12;      % Area moment of inertia (m^4)
A = w*h;           % Cross-sectional area (m^2)

E = 5e6;           % Beam modulus (Pa)

g = 9.81;          % Gravity (m/s^2)
```

```
%% Density

k = 0.8;                                % Weight fraction of particles ...
    (filler)
rhom = 8000;                            % Density of iron (kg/m^3)
rhoe = 965;                             % Density of PDMS (kg/m^3)

rhoeff = 1/((k/rhom) + ((1-k)/rhoe));   % Effective Density of mix


%% Load distributions

beta = 550;     % Magnetic coefficient (N-m^(-3/2)
pm = -1.50;     % Magnetic exponent
qm = beta*A;    % Magnetic load (N-m^(1/2))

qg = rhoeff*A*g;    % Gravitational load (N/m)


j = 1;

%% Iterate through lambda values

for lam = lamrange

    % Assuming a2 = 0 in analytic model
    d_AN2(j) = fsolve(@(d)-32*pi/27*qm/d^(3/2)*(1-lam)^(-1/2) + ...
        19/9*qm/(d^(3/2))*L0/d ...
        - 65/18*qm/(pi*d^(3/2))*(L0/d)^2*(1-lam)^(1/2)...
        + 32/27*E*w*h^3*pi^4/L0^3 + 32*pi/27*qg*(1-lam)^(-1/2),...
        10^-3);

    j = j + 1;

end

%% Plot results

figure
plot(lamrange,d_AN2*1000)

xlabel('$\hat{\lambda}$','Interpreter','Latex', ...
    'FontSize',18,'FontName','Times New Roman')
ylabel('$d_{cr}$ (mm)','Interpreter','Latex', ...
    'FontSize',18,'FontName','Times New Roman')
```

```
%% MagneticBeamPotential.m
%
% Plots potential energy as a function of a1 and a2 (alpha_1 and ...
    alpha_2).
```

```
%
% Calls MagneticBeam_Numeric.m and MagneticBeam_Analytic.m
%

%% Primary inputs

lam = 0.9;      % Buckle stretch
d   = 25*1e-3;  % Nominal gap (m)


%% Input dimensions, properties, etc...

L0 = 15.4e-3;     % Initial beam length (m)
w = 5e-3;         % Beam width (m)
h = 0.11e-3;      % Beam thickness (m)

I = w*h^3/12;     % Area moment of inertia (m^4)
A = w*h;          % Cross-sectional area (m^2)

E = 5e6;          % Beam modulus (Pa)

g = 9.81;         % Gravity (m/s^2)


%% Density

k = 0.8;                          % Weight fraction of particles ...
    (filler)
rhom = 8000;                      % Density of iron (kg/m^3)
rhoe = 965;                       % Density of PDMS (kg/m^3)

rhoeff = 1/((k/rhom) + ((1-k)/rhoe));   % Effective Density of mix


%% Load distributions

beta = 550;    % Magnetic coefficient (N-m^(-3/2)
pm = -1.50;    % Magnetic exponent
qm = beta*A;   % Magnetic load (N-m^(1/2))

qg = rhoeff*A*g;   % Gravitational load (N/m)


%% Define range of alphas (weighting coefficients) and ell  to test

al1_max = L0/2*(1.4-lam^2); % Approximate maximum alpha_1
al2_max = al1_max*0.8;      % Approximate maximum alpha_2

% Use an odd number of values (to fall on zero)
a1range = linspace(-al1_max,al1_max,301); % Range of alpha1 to test
a2range = linspace(-al2_max,al2_max,301); % Range of alpha2 to test

ell = lam*L0;     % Final end-to-end distance
```

```
%% Calculate energy

% Numeric
[a1sNU, a2sNU,PisNU] = ...
    MagneticBeam_Numeric(L0,ell,d,I,E,qg,qm,pm,a1range,a2range);
% Analytic approximation
[a1sAN, a2sAN,PisAN] = ...
    MagneticBeam_Analytic(L0,lam,d,I,E,qg,qm,pm,a1range,a2range);


%% Prepare results

% Scale data
a1sNU = a1sNU*1e3; % Convert to mm
a2sNU = a2sNU*1e3; % Convert to mm
PisNU = PisNU*1e3; % Convert to mJ
a1sAN = real(a1sAN)*1e3; % Convert to mm
a2sAN = real(a2sAN)*1e3; % Convert to mm
PisAN = PisAN*1e3; % Convert to mJ

% Remove extra values (where alpha ranges went too far)
PisNU(logical([abs(a2sNU(1:2,:)) < ...
    max(max(a2sNU))*0.1;zeros(2,length(a2sNU))])) = NaN;
PisNU(logical([zeros(2,length(a1sNU));abs(a1sNU(3:4,:)) < ...
    max(max(a1sNU))*0.1])) = NaN;
PisAN(logical([abs(a2sAN(1:2,:)) < ...
    max(max(a2sAN))*0.1;zeros(2,length(a2sAN))])) = NaN;
PisAN(logical([zeros(2,length(a1sAN));abs(a1sAN(3:4,:)) < ...
    max(max(a1sAN))*0.1])) = NaN;

% Shift analytic solution to align with numeric
loc1 = find(abs(a2sNU) < 10^-7);
loc2 = find(abs(a2sAN) < 10^-7);
PiDiff = max(PisNU(loc1)) - max(PisAN(loc2));
if ~isnan(PiDiff)
     PisAN = PisAN + PiDiff;
end


%% Find local/global mins

[~,locs3] = findpeaks(-PisNU(3,:));
[~,locs4] = findpeaks(-PisNU(4,:));
[~,locs5] = findpeaks(-PisAN(3,:));
[~,locs6] = findpeaks(-PisAN(4,:));


%% Plot results

% Numeric
figure(1)
plot3(a1sNU(1,:),a2sNU(1,:),PisNU(1,:))
hold on
plot3(a1sNU(2,:),a2sNU(2,:),PisNU(2,:))
```

```
plot3(a1sNU(3,:),a2sNU(3,:),PisNU(3,:))
plot3(a1sNU(4,:),a2sNU(4,:),PisNU(4,:))

plot3(a1sNU(3,locs3),a2sNU(3,locs3),PisNU(3,locs3),'*')
plot3(a1sNU(4,locs4),a2sNU(4,locs4),PisNU(4,locs4),'*')

xlabel('\alpha_1 (mm)')
ylabel('\alpha_2 (mm)')
zlabel('\Pi (mJ)')
title('Numeric (solid) vs Analytic (dash)')

figure(2)
plot(a2sNU(4,:),PisNU(4,:))
hold on
plot(a2sNU(4,locs4),PisNU(4,locs4),'*')

xlabel('\alpha_2 (mm)')
ylabel('\Pi (mJ)')
title('Numeric (solid) vs Analytic (dash)')

% Analytic
figure(1)
plot3(a1sAN(1,:),a2sAN(1,:),PisAN(1,:),'--')
hold on
plot3(a1sAN(2,:),a2sAN(2,:),PisAN(2,:),'--')
plot3(a1sAN(3,:),a2sAN(3,:),PisAN(3,:),'--')
plot3(a1sAN(4,:),a2sAN(4,:),PisAN(4,:),'--')

plot3(a1sAN(3,locs5),a2sAN(3,locs5),PisAN(3,locs5),'*')
plot3(a1sAN(4,locs6),a2sAN(4,locs6),PisAN(4,locs6),'*')

figure(2)
plot(a2sAN(4,:),PisAN(4,:),'--')
hold on
plot(a2sAN(4,locs6),PisAN(4,locs6),'*')
```

```
%% MagneticBeamSnap.m
%
% Determines critical distance for snap-through of a buckled ...
   magnetic beam
% over a range of buckle stretch values.
%
% Calls MagneticBeam_Numeric.m and MagneticBeam_Analytic.m
%

%% Primary inputs

lamrange = 0.99:-0.01:0.5;      % Buckle stretch range
drange   = 37*1e-3:-0.1e-3:0;   % Nominal gap (m) range


%% Allocate space for outputs
```

```
d_NU  = zeros(1,length(lamrange)); % Numeric snap distance
d_AN  = d_NU;                      % Analytic snap distance
d_AN2 = d_NU;                      % Analytic snap distance version 2
k_NU  = d_NU;                      % Numeric number of mins prior to ...
   snap
k_AN  = d_NU;                      % Analytic number of mins prior ...
   to snap


%% Input dimensions, properties, etc...

L0 = 15.4e-3;     % Initial beam length (m)
w = 5e-3;         % Beam width (m)
h = 0.11e-3;      % Beam thickness (m)

I = w*h^3/12;     % Area moment of inertia (m^4)
A = w*h;          % Cross-sectional area (m^2)

E = 5e6;          % Beam modulus (Pa)

g = 9.81;         % Gravity (m/s^2)


%% Density

k = 0.8;                           % Weight fraction of particles ...
   (filler)
rhom = 8000;                       % Density of iron (kg/m^3)
rhoe = 965;                        % Density of PDMS (kg/m^3)

rhoeff = 1/((k/rhom) + ((1-k)/rhoe));   % Effective Density of mix


%% Load distributions

beta = 550;    % Magnetic coefficient (N-m^(-3/2)
pm = -1.50;    % Magnetic exponent
qm = beta*A;   % Magnetic load (N-m^(1/2))

qg = rhoeff*A*g;   % Gravitational load (N/m)


j = 1;


for lam = lamrange


    %% Define range of alphas (weighting coefficients) and ell  to test

    al1_max = L0/2*(1.4-lam^2);   % Approximate maximum alpha_1
    al2_max = al1_max*0.8;        % Approximate maximum alpha_2
```

```
% Use an odd number of values (to fall on zero)
a1range = linspace(-al1_max,al1_max,301); % Range of alpha1 to test
a2range = linspace(-al2_max,al2_max,301); % Range of alpha2 to test

ell = lam*L0;      % Final end-to-end distance
i = 1;             % Index

for d = drange

    disp(['lambda: ',num2str(lam),', d: ',num2str(d)])

    %% Calculate energy

    % Numeric
    if lam >= 0.8
        [a1sNU, a2sNU,PisNU] = ...
           MagneticBeam_Numeric(L0,ell,d,I,E,qg,qm,pm,a1range, ...
           a2range);
    else
        a1sNU = ones(4,length(a1range))*NaN;
        a2sNU = a1sNU;
        PisNU = a1sNU;
    end
    % Analytic approximation
    [a1sAN, a2sAN,PisAN] = ...
       MagneticBeam_Analytic(L0,lam,d,I,E,qg,qm,pm,a1range,a2range);


    %% Prepare results

    % Scale data
    a1sNU = a1sNU*1e3; % Convert to mm
    a2sNU = a2sNU*1e3; % Convert to mm
    PisNU = PisNU*1e3; % Convert to mJ
    a1sAN = real(a1sAN)*1e3; % Convert to mm
    a2sAN = real(a2sAN)*1e3; % Convert to mm
    PisAN = PisAN*1e3; % Convert to mJ

    % Remove extra values (where alpha ranges went too far)
    PisNU(logical([abs(a2sNU(1:2,:)) < ...
       max(max(a2sNU))*0.1;zeros(2,length(a2sNU))])) = NaN;
    PisNU(logical([zeros(2,length(a1sNU));abs(a1sNU(3:4,:)) < ...
       max(max(a1sNU))*0.1])) = NaN;
    PisAN(logical([abs(a2sAN(1:2,:)) < ...
       max(max(a2sAN))*0.1;zeros(2,length(a2sAN))])) = NaN;
    PisAN(logical([zeros(2,length(a1sAN));abs(a1sAN(3:4,:)) < ...
       max(max(a1sAN))*0.1])) = NaN;

    % Shift analytic solution to align with numeric
    loc1 = find(abs(a2sNU) < 10^-7);
    loc2 = find(abs(a2sAN) < 10^-7);
    PiDiff = max(PisNU(loc1)) - max(PisAN(loc2));
    if ~isnan(PiDiff)
        PisAN = PisAN + PiDiff;
```

```
        end


        %% Find local/global mins (in upper portion of curve)

        [~,locs3] = findpeaks(-PisNU(3,:));
        [~,locs4] = findpeaks(-PisNU(4,:));
        [~,locs5] = findpeaks(-PisAN(3,:));
        [~,locs6] = findpeaks(-PisAN(4,:));


        %% Record local min count and find snap-through

        k_NU(j) = max([k_NU(j),length(locs4)]); % Number of numeric mins
        k_AN(j) = max([k_AN(j),length(locs6)]); % Number of analytic ...
           mins

        % If there is no local min, snap through has occurred
        if isempty(locs4)
            if ~isnan(PiDiff)
                d_NU(j) = max([d_NU(j),d]);
            else
                d_NU(j) = NaN;
            end
        end
        if isempty(locs6)
            d_AN(j) = max([d_AN(j),d]);
            break
        end

        i = i +1 ;

    end

    % Assuming a2 = 0 in analytic model
    d_AN2(j) = fsolve(@(d)-32*pi/27*qm/d^(3/2)*(1-lam)^(-1/2) + ...
        19/9*qm/(d^(3/2))*L0/d ...
        - 65/18*qm/(pi*d^(3/2))*(L0/d)^2*(1-lam)^(1/2)...
        + 32/27*E*w*h^3*pi^4/L0^3 + 32*pi/27*qg*(1-lam)^(-1/2),...
        d_AN(j));


    drange = drange(find(drange == max([d_NU,d_AN])):end);
    j = j + 1;

end

%% Plot results

plot(lamrange,d_NU*1000)
hold on
plot(lamrange,d_AN*1000,'--')
plot(lamrange,d_AN2*1000,'-.')
```

```
plot(lamrange(k_NU>1),d_NU(k_NU>1)*1000,'o') % a2~=0 before snapping
plot(lamrange(k_AN>1),d_AN(k_AN>1)*1000,'o') % a2~=0 before snapping


xlabel('$\hat{\lambda}$','Interpreter','Latex', ...
    'FontSize',18,'FontName','Times New Roman')
ylabel('$d_{cr}$ (mm)','Interpreter','Latex', ...
    'FontSize',18,'FontName','Times New Roman')
legend('Numeric', 'Analytic \Pi', 'Analytic Equation', 'Numeric ...
    \alpha_2 != 0')
```

```
%% MagneticBeam_Numeric.m
%
% Numerically minimizes energy to solve beam shape based on magnetic ...
    load
% and dimensions.
%
% Runs 4 quadrants (positive/negative a1 and a2) in order to have higher
% resolution.
%

function [a1s, a2s,Pis] = ...
    MagneticBeam_Numeric(L0,ell,d,I,E,qg,qm,pm,a1range,a2range)

options2 = ...
    optimset('TolFun',1.0e-12,'TolX',1.0e-12,'FunValCheck','on', ...
    'Display','off');

a1s = ones(4,length(a1range)); % Allocate space for a1 values
a2s = a1s;                     % Allocate space for a2 values
Pis = a2s;                     % Allocate space for energy values

% Prepare for calculating derivative of w
xx = linspace(0,L0,1001);
phi1_x = 0.5*(2*pi/L0)*(sin(2*pi*xx/L0));                          % ...
    Derivative of first shape function
phi2_x = (4/3^1.5)*(2*pi/L0)*(cos(2*pi*xx/L0) - cos(4*pi*xx/L0)); % ...
    Derivative of second shape function


%% Iterate a1 values
% Positive a2 values
for i = 1:length(a1range)

        a1 = a1range(i);  % Set alpha_1

        % Potential energy
        Pi_exact = ...
            @(a2)(integral(@(x)Lagrangian(x,a1,a2,L0,d,E,I,qm,qg,pm), ...
            0,L0));

        % Problem is undefined when dw/dx>1. Find a valid initial guess.
```

```
        for a2_0 = -a2range
            w_x = a1*phi1_x + a2_0*phi2_x; % Derivative of w
            if max(w_x.^2)<1
                break % Use first acceptable a2 value as initial ...
                    point for fsolve
            end
        end

        % Solve isoperimetric constraint to get alpha_2
        try  % fsolve may fail (if dw/dx<1)
            a2sol = fsolve(@(a2)get_a(a1,a2,L0,ell),a2_0,options2);
            a1s(1,i) = a1;              % Store a1
            a2s(1,i) = a2sol;           % Store a2
            Pis(1,i) = Pi_exact(a2sol); % Store energy
        catch
            a1s(1,i) = NaN; % Store a1
            a2s(1,i) = NaN; % Store a2
            Pis(1,i) = NaN; % NaN if a2 is not defined
        end

end

% Negative a2 values (based on symmetry)
a1s(2,:) = a1s(1,:);
a2s(2,:) = -a2s(1,:);
Pis(2,:) = Pis(1,:);


%% Iterate a2 values
% Positive a1 values
for i = 1:length(a1range)

        a2 = a2range(i);  % Set alpha_2

        % Potential energy
        Pi_exact = ...
            @(a1)(integral(@(x)Lagrangian(x,a1,a2,L0,d,E,I,qm,qg,pm), ...
            0,L0));

        % Problem is undefined when dw/dx>1. Find a valid initial guess.
        for a1_0 = -a1range
            w_x = a1_0*phi1_x + a2*phi2_x; % Derivative of w
            if max(w_x.^2)<1
                break % Use first acceptable a2 value as initial ...
                    point for fsolve
            end
        end

        % Solve isoperimetric constraint to get a1
        try  % fsolve may fail (if dw/dx<1)
            a1sol = fsolve(@(a1)get_a(a1,a2,L0,ell),a1_0,options2);
            a1s(3,i) = a1sol;           % Store a1
            a2s(3,i) = a2;              % Store a2
            Pis(3,i) = Pi_exact(a1sol); % Store energy
```

```
        catch
            a1s(3,i) = NaN;
            a2s(3,i) = NaN;
            Pis(3,i) = NaN;
        end

end

% Negative a1 values
for i = 1:length(a1range)

        a2    = a2range(i);  % Set alpha_1

        % Potential energy
        Pi_exact = ...
            @(a1)(integral(@(x)Lagrangian(x,a1,a2,L0,d,E,I,qm,qg,pm), ...
            0,L0));

        if ~isnan(a1s(3,i)) % fsolve may fail (if dw/dx<1)
            a1sol = -a1s(3,i);   % Get alpha_2 (based on symmetry)
            a1s(4,i) = a1sol;           % Store a1
            a2s(4,i) = a2;              % Store a2
            Pis(4,i) = Pi_exact(a1sol); % Store energy
        else
            a1s(4,i) = NaN;
            a2s(4,i) = NaN;
            Pis(4,i) = NaN;
        end

end


%-- Lagrangian (energy summation)
function lagr = Lagrangian(x,a1,a2,L0,d,E,I,qm,qg,pm)

phi1 = 0.5*(1 - cos(2*pi*x/L0));             % Basis function 1
phi1_xx = 0.5*((2*pi/L0)^2)*cos(2*pi*x/L0);  % Second derivative

phi2 = (4/3^1.5)*sin(2*pi*x/L0).*(1 - cos(2*pi*x/L0)); ...
                    % Basis function 2
phi2_xx = (4/3^1.5)*((2*pi/L0)^2)*(-sin(2*pi*x/L0) + ...
    (2*sin(4*pi*x/L0))); % Second derivative

w = a1*phi1 + a2*phi2;            % Beam shape
w_xx = a1*phi1_xx + a2*phi2_xx;   % Second derivative

% Bending + gravitational + magnetic energy
lagr = 0.5*E*I*w_xx.^2 + qg*w - 2*qm./(((d - w).^(-pm - 1)));


%-- Isoperimetric constraint -> res should be 0
function res = get_a(a1,a2,L0,ell)

% Integrate ds (in terms of x) to get ell_hat
```

```
ell_hat = integral(@(x)get_ds(x,a1,a2,L0),0,L0);
res = (ell_hat - ell);


%--  Find ds in terms of x
function ds = get_ds(x,a1,a2,L0)
% Note: ds = sqrt(1 - (dw/dx)^2)*dx

% Derivatives of basis functions
phi1_x = 0.5*(2*pi/L0)*(sin(2*pi*x/L0));
phi2_x = (4/3^1.5)*(2*pi/L0)*(cos(2*pi*x/L0) - cos(4*pi*x/L0));

% Derivative of beam shape
w_x = a1*phi1_x + a2*phi2_x;

ds = sqrt(1 - w_x.^2);
```

```
%% MagneticBeam_Analytic.m
%
% Uses an analytic approximation of energy to solve beam shape based on
% magnetic load and dimensions.
%
% Runs 4 quadrants (positive/negative a1 and a2) in order to have higher
% resolution.
%

function [a1s, a2s,Pis] = ...
   MagneticBeam_Analytic(L0,lam,d,I,E,qg,qm,pm,a1range,a2range)

a1s = ones(4,length(a1range)); % Allocate space for a1 values
a2s = a1s;                     % Allocate space for a2 values
Pis = a2s;                     % Allocate space for energy values


%% Iterate a1 values
% Positive a1 values
for i = 1:length(a1range)

        a1 = a1range(i);  % Set alpha_1

        % Potential energy
        Pi_app = @(a)((-L0*qm*((a(1)/2) + ((1/(288*d))*( ...
            (81*(a(1)^2)) + ...
             (80*(a(2)^2)) ))  +  ((5*a(1)/(1152*(d^2)))*( ...
                (45*(a(1)^2)) + ...
             (112*(a(2)^2)) ))  )/(d^(-pm))) + (L0*qg*a(1)/2) + ...
             (E*I*pi^4*(27*a(1)^2 + 320*a(2)^2)/(27*L0^3))  - ...
             (2*L0*qm/d^0.5)) ;

        % Solve isoperimetric constraint to get alpha_2
        a2 = (3/(8*pi))*(((-1.5*(pi^2)*(a1^2)) + (6*(L0^2)*(1 - ...
            lam)))^0.5);
```

```
        a1s(1,i) = a1;              % Store a1
        a2s(1,i) = a2;              % Store a2
        Pis(1,i) = Pi_app([a1,a2]); % Store energy

end

% Negative a2 values (based on symmetry)
a1s(2,:) = a1s(1,:);
a2s(2,:) = -a2s(1,:);
Pis(2,:) = Pis(1,:);


%% Iterate a2 values
% Positive a2 values
for i = 1:length(a1range)

        a2 = a2range(i);  % Set alpha_2

        % Potential energy
        Pi_app = @(a)((-L0*qm*((a(1)/2) + ((1/(288*d))*( ...
            (81*(a(1)^2)) + ...
             (80*(a(2)^2)) ))  +  ((5*a(1)/(1152*(d^2)))*( ...
                (45*(a(1)^2)) + ...
             (112*(a(2)^2)) ))  )/(d^(-pm))) + (L0*qg*a(1)/2) + ...
             (E*I*pi^4*(27*a(1)^2 + 320*a(2)^2)/(27*L0^3))    -  ...
             (2*L0*qm/d^0.5)) ;

        % Solve isoperimetric constraint to get alpha_1
        a1 = (2/(3*pi))*(((-(32/3)*(pi^2)*(a2^2)) + (9*(L0^2)*(1 - ...
            lam)))^0.5);

        a1s(3,i) = a1;              % Store a1
        a2s(3,i) = a2;              % Store a2
        Pis(3,i) = Pi_app([a1,a2]); % Store energy

end

% Negative a2 values
for i = 1:length(a1range)

        a2 = a2range(i);  % Set alpha_2

        % Potential energy
        Pi_app = @(a)((-L0*qm*((a(1)/2) + ((1/(288*d))*( ...
            (81*(a(1)^2)) + ...
             (80*(a(2)^2)) ))  +  ((5*a(1)/(1152*(d^2)))*( ...
                (45*(a(1)^2)) + ...
             (112*(a(2)^2)) ))  )/(d^(-pm))) + (L0*qg*a(1)/2) + ...
             (E*I*pi^4*(27*a(1)^2 + 320*a(2)^2)/(27*L0^3))    -  ...
             (2*L0*qm/d^0.5));

        a1 = -a1s(3,i);   % Get alpha_1 (based on symmetry)
```

```
        a1s(4,i) = a1;              % Store a1
        a2s(4,i) = a2;              % Store a2
        Pis(4,i) = Pi_app([a1,a2]); % Store energy

end
```

Appendix T

GaIn Volume Creation and Measurement

Precise volumes of GaIn were produced by quasi-statically dispensing droplets into a bath of 1% W/V NaOH solution (fig. T.1). This was performed with a Harvard Apparatus syringe pump (PHD 2000) and dispensing needles (C-U Innovations) of various gauge, ranging from 14G to 27G. While varying the flowrate with a single needle produces a range of droplet volumes, we found that quasi-static production was more repeatable. The volume of an individual drop is determined by the competition between gravitational and surface tension forces. The instability point, when the droplet falls, can be approximated with $2\pi R\gamma = (\rho_G - \rho_s)Vg$, where γ is the GaIn/solution interfacial tension, R is the inner radius of the syringe, ρ_G is the density of GaIn, ρ_S is the density of the solution, V is the volume of the GaIn droplet, and g is gravitational acceleration. This equation is referred to as Tates law and is commonly used to determine surface tension values [277–279].

After creating repeatable droplets, the actual volume had to be determined. Images were taken with an optical stereoscope to extract values for droplet diameter. Assuming spherical droplets was insufficient due to the substantial volume and den-

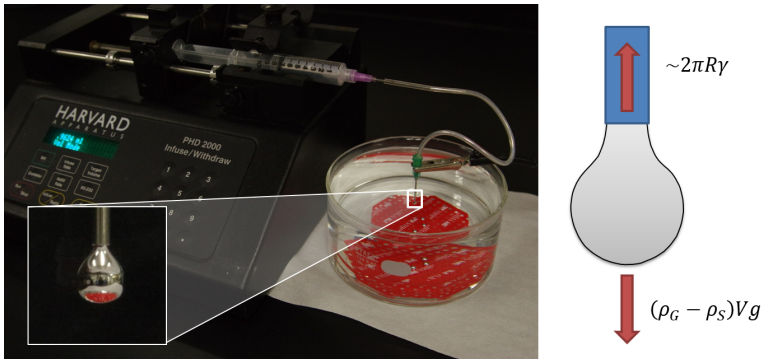

Figure T.1: Left: Setup for creating repeatable GaIn volumes. Left inset: Profile of GaIn droplet deposited from a deposition needle. Right: Schematic laying out the forces governing droplet volume.

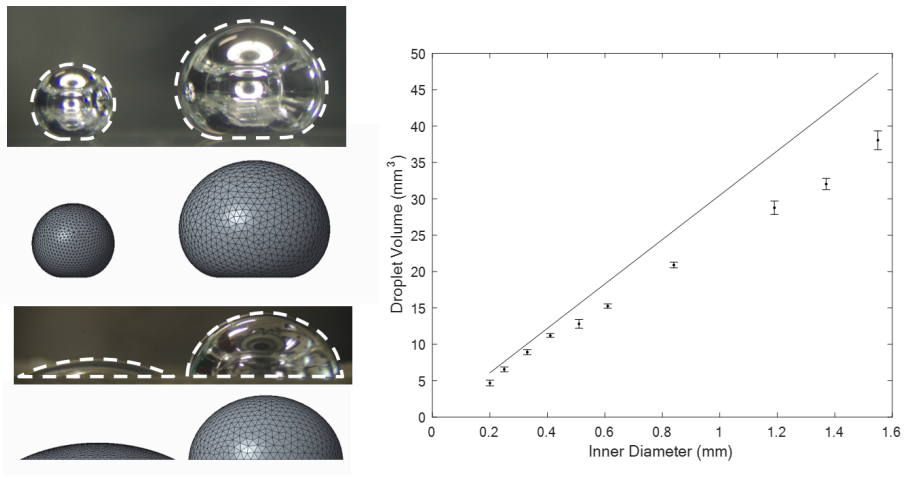

Figure T.2: Left: Comparison of experimental images to Surface Evolver results. The small droplet is approximately 7.3 mm^3 and the large droplet is 39.8 mm^3, according to Surface Evolver. The small cap and large cap are 7.8 mm^3 and 37.8 mm^3, respectively. Right: Experimental results (points) for creating droplet volumes based on needle inner diameter (ID) compared to simplified theory based on weight and surface tension (line). Flowrates: 0.2 mm ID 100 μL/min, 0.25 to 0.41 mm ID 250 μL/min, 0.51 to 0.84 mm ID 500 μL/min, 1.19 to 1.55 mm ID 1000 μL/min.

sity. Instead, experimental measurements were compared to simulated results from Surface Evolver, taking γ as 500 mJ/m^2, ρ_G as 6.25 g/cm^3, and ρ_S as 1 g/cm^3. The comparison and results from trials with varying needle diameter are reported in fig. T.2. The theory described above generally overestimates the experimental results by about 20%, likely due the approximation that separation occurs at the tip of the needle. Several groups have applied corrections to Tates law [278, 279], increasing prediction accuracy, but none were used for this study since measured values were sufficient. In most cases, desired volumes of liquid metal were produced by combining two or more droplets from a single or multiple needles.

Appendix U

Visual Droplet Monitoring and Image Analysis

Visual data was required for determining the onset of droplet deformation and to quantify the system behavior. Top-down videos provided information on bridge width, but profile videos proved to be more informative by more clearly indicating the shift of mass during droplet separation. Profile videos of droplet deformation were recorded through a stereo microscope (Carton SPZT 50) with a Pentax K3 digital SLR. The overall setup is shown in U.1a. To acquire a profile view of the liquid metal, a 1st surface mirror was placed at approximately 45°, and the sample was backlit to increase contrast. The experiment could then be magnified and viewed live on a computer monitor through an HDMI connection. In most cases, 4 videos were taken for every 10 tests on the 1st, 2nd, 5th, and 10th.

To quantify data from video recordings, frames (15 per second) were systematically processed (fig. U.1b-f) using MATLABs (2016b) Image Processing Toolbox. First frames were extracted, cropped, and straightened. The images were then converted to greyscale (*rgb2gray*), followed by a conversion to black and white with a specified luminance threshold. Irrelevant objects such as bubbles separated from the main

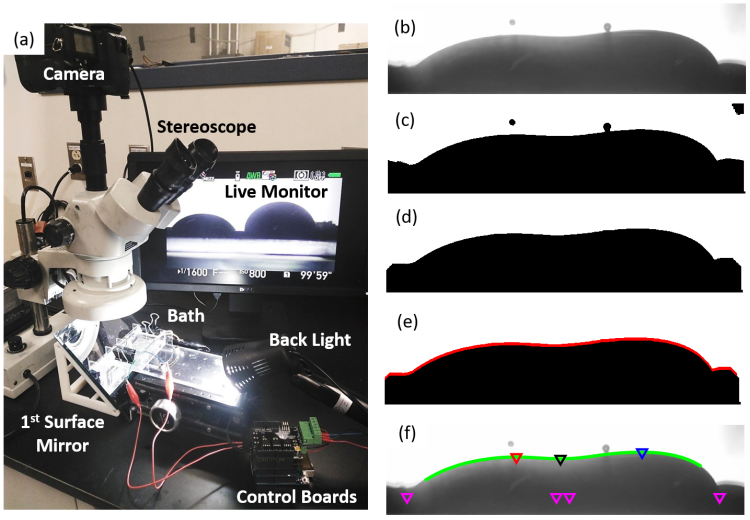

Figure U.1: (a) Experimental setup. (b) Cropping and straightening of video. (c) Thresholding to acquire a black and white image. (d) Removal of bubbles and extraneous pixels with morphological functions. (e) Identification of top surface in red. (f) Fitting of polynomial curve and identification of min and max points. Pad edges are marked with magenta.

body were removed using a filter for connected pixels (*bwareaopen*), and bubbles attached to the surface of the liquid metal could be removed using morphological dilation followed by erosion (combined into one MATLAB function: *imclose*). The top surface of the droplet could then be identified and points could be extracted. Finally, a polynomial curve was fitted (*polyfit*) to the extracted points to smooth any roughness due to pixilation and to facilitate the extraction of minimum and maximum liquid metal height values.

A number of approaches were taken to determine the onset of droplet motion. First, the motion of points of interest (such maximum height locations) along the profile could be tracked. Plots such as those shown in fig. 4.3 of Chapter 4 could be used to approximate when and at what current input the liquid metal begins to shift. Alternatively, the polynomial profile curve can be compared to a reference. The profile under zero deformation works as a useful reference (green line in lower image

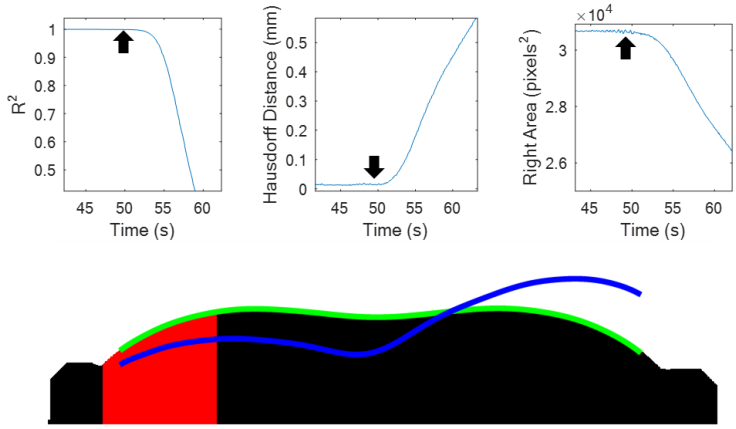

Figure U.2: Methods for determining droplet motion. The arrows in the plots approximate where motion begins. (Top left) R squared value for comparing the non-deformed (green line) and deformed (blue line) shapes. (Top middle) Hausdorff distance associated with the same two curves. (Top right) Change in pixel area, indicated by the area shaded in red.

of fig. U.2) for most comparisons. The deformed profile (blue line in lower image of fig. U.2) can then be compared to the reference using root mean square (RMS) distance, coefficient of determination R2, or Hausdorff distance [280]. Tracking the area of a particular section of the profile (such as that shaded in red in fig. U.2) can also provide information for determining timestamps coinciding with movement. However, deviations due to bubbles and changing light conditions caused noise that made it difficult to locate small deformations, particularly impacting samples with slower responses (large outer electrode separation, low NaOH concentration, etc.). As a result, the most reliable and repeatable method was visual inspection of the videos or video frames. Syncing camera data with voltage/current data from the electronic setup allowed for the determination of current

Appendix V

NaOH Conductivity

Conductivity of a material is usually determined using Ohms law. However, the electrochemical interface of bulk solution and electrodes complicates the system [219], Wang2016]. A single electrochemical cell, consisting of solution and two electrodes, is approximated as a circuit in fig. V.1a. At each interface, an electric double layer forms which behaves like a capacitor (C). A Faradaic impedance, involving mass and electron transport, is represented as a component (Z) in parallel. It should be noted that while the bulk resistance R follows Ohms law, the Faradaic impedance does not. Finally, the electrode potential is represented with U. To calculate the solution conductivity, the resistance R is required, but the interface effects interfere. In many cases, conductivity measurements are taken by applying alternating currents and simplifying the circuit to a single capacitor and a single resistor in series. However, given that all experiments were performed with direct current, a direct current approach [281] was taken, as seen in fig. V.1b. If the electrodes and probes are all the same material, the equivalent circuit can be simplified to fig. V.1c. The electrode potentials then cancel each other out, simplifying the problem. The resistance R2 is then a function of the current I and the potential difference $\Delta\Phi$, which can be determined directly with the two probes. The conductivity is then a function of the measured

resistance and dimensions of the solution and electrodes.

Theoretical modeling with the given geometry was non-trivial due to the fact that a bath and co-planar electrodes were used rather than a simple tube filled with solution and 4 copper electrodes. With this in mind, equations from vertical electrical sounding (VES) were used, as described in the main document. Equation (4.2) can be rearranged to solve for the conductivity. Test electrodes (examples shown in fig. V.2) were used to gather the necessary data. All samples were created with the same FR4 board, laser patterning techniques, and sealing/insulating methods as described previously. The most general design (fig. V.2a) was created to match the dimensions used for the parametric testing of liquid metal bipolar electrochemistry. However, instead of having a source and drain pad, copper pads were placed where the outer edges of liquid metal would be located. As with the bipolar electrochemistry testing, these sample dimensions were adjusted, scaled, and tested in various NaOH concentrations. Typical testing procedure involved increasing the voltage in steps of 0.1 V/sec across the outer electrodes while recording current and the voltage between the two inner probes. Plotting the difference voltage difference between the probes versus current reveals a linear increase, starting from 0V at 0 mA. This information is then plugged into equation (2) along with dimensions to determine conductivity.

In bipolar electrochemistry, it is generally assumed (though often ignored) that the bipolar electrode (liquid metal in this case) will influence the electric field [213]. Specifically, the high conductivity of the electrode results in a decrease in electric field strength across its physical area. This is a result of the high conductivity and near-equipotential of the electrode. In order to test this, the designs in fig. V.2b and c were implemented to measure the potential difference in the same relative locations as fig. V.29a (the outer edge of liquid metal). In fig. V.2c, liquid metal is included. Fig. V.2b is identical except for the lack of liquid metal. Any large influence of the bipolar electrode should appear as a difference in measured conductivity. However,

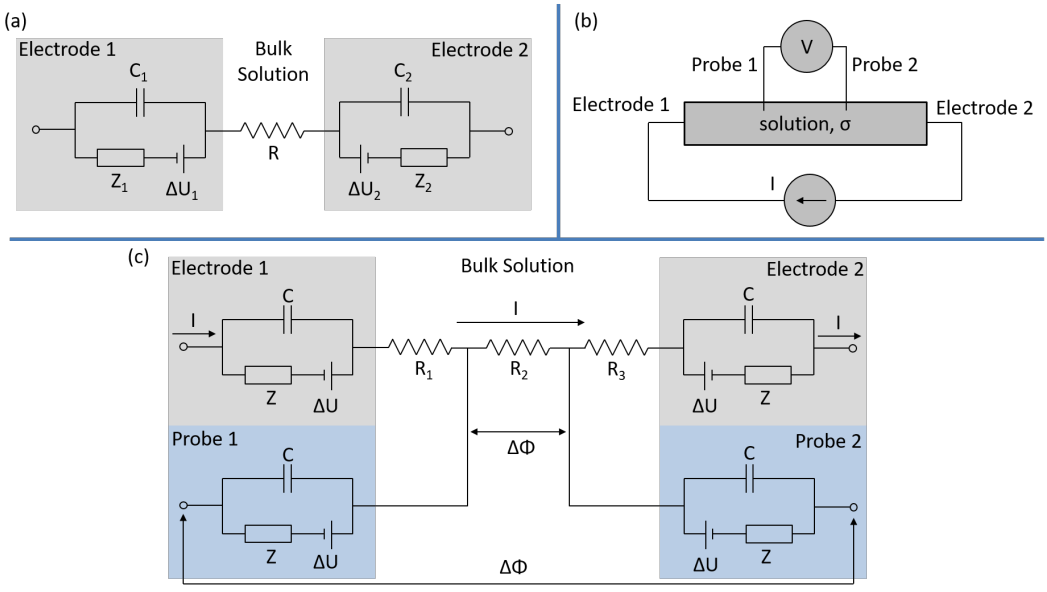

Figure V.1: Electrochemical circuitry. (a) A simple electrode-electrode-electrolyte system. (b) The general approach for determining solution conductivity using direct current. (c) The circuit equivalent of (b).

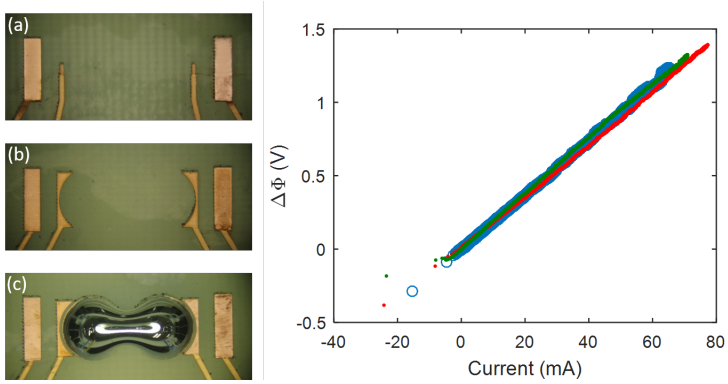

Figure V.2: Various testing pads for determining conductivity and their experimental output. (a) Pad design for use with theory (plotted in blue). (b) Arcs for comparison to samples with liquid metal (plotted in red). (c) Arcs with liquid metal to simulate actual experimental conditions (plotted in green).

as shown by the plot in fig. V.2, there was no significant difference. Given this information, the influence of the liquid metal conductivity was not considered during theoretical calculations. If a narrow tube were used instead of a bath, however, the liquid metal (then taking up a sizeable cross-sectional area) could have a far larger impact and would possibly have to be included for theoretical accuracy.

Although the VES approach provided a good measurement for "effective" conductivity, the finite dimensions of the bath caused inaccuracies with regards to the "true solution" conductivity. The smaller bath resulted in underestimations in solution conductivity, particularly when large outer electrode separations were used. This is due to the fact that the conductivity deeper into the solution (and further from the electrodes) has a larger impact when the electrode separation is increased. When separations are large, the conductivity outside the bath (essentially zero) has a larger influence. The conductivities measured in the small bath ("effective" conductivities) were used for the bipolar electrolysis onset and droplet separation theory in order to remain self-consistent. The following fits were used in conjunction with experimental

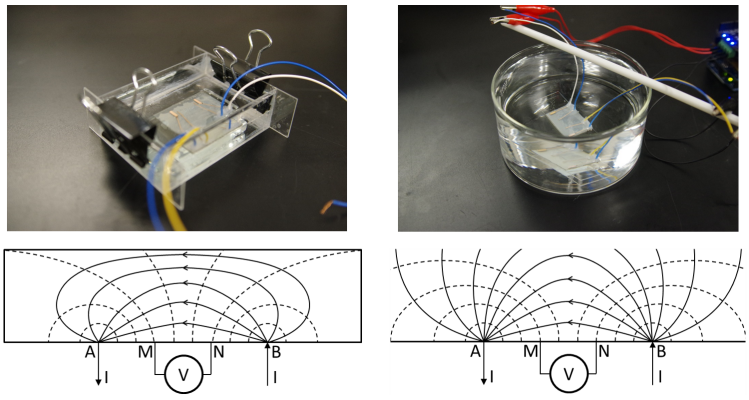

Figure V.3: Conductivity tests in various bath sizes. (Left) Small bath. (Right) Large bath. (Below) Approximated current paths (solid lines) and equipotential lines (dotted lines) for each situation.

conductivity data:

$$G_{OES} = -0.0986(l_{AB} - 1.5) + 6.5094, \tag{V.1}$$

$$G_{SC} = 5.263X_{scale}^3 - 19.1416X_{scale}^2 + 22.3067X_{scale} - 3.6195, \tag{V.2}$$

$$G_C = 4.2069C + 0.4475, \tag{V.3}$$

where G_{OES}, G_{SC}, and G_C are the conductivities (S/m) for outer electrode separation, length scale, and NaOH concentration, respectively. l_{AB} is the outer electrode separation (mm), X_{scale} is the length scale, and C is the weight per volume concentration of NaOH. No particular constraints were applied during fitting. The length scale curve is nonlinear because bubble production decreases effective conductivity at small scales (bubbles block electrodes) and finite bath size limits effective conductivity at large scales. A max effective conductivity then falls somewhere around a scale of 1.

Measurements were taken in a larger bath (125 mm diameter by 65 mm height, PYREX 3140-125) to gauge the difference in behavior, as seen in fig. V.3. The results for both baths are compared to values from EXW Foxboro, Massachusetts (http://myweb.wit.edu/sandinic/Research/conductivity%20v%20concentration.pdf).

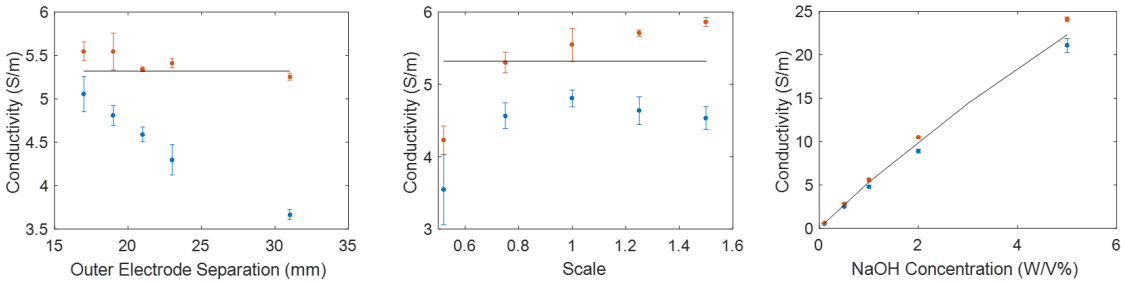

Figure V.4: Comparison between conductivity measurements in the small (blue points) and large (red points) baths. Values from literature are reported as a black line. Data is shown for (left) outer electrode separation, (center) scale, and (right) NaOH concentration.

The outer electrode separation plot in fig. V.4 emphasizes how the small bath results in underestimated conductivity. Even in the larger bath, bubble interference causes an under approximation when the scale is small. In general, however, this method appears to overestimate conductivity, particularly as scale is increased in the large bath. This is likely because the theory assumes point sources while the true pads are rectangular. The average distance from all points on the outer electrodes to the center of the probes (smaller pads of copper) is greater than the distance from center to center. This results in an inflated value for conductivity.

Appendix W

Progressive Decrease of Voltage for Droplet Separation

This experiment was implemented with the same circuitry and methods as the general testing described above. However, instead of increasing the voltage during separation, the ∼9V was immediately applied and decreased by 0.1V per second. Of particular interest were the larger scales, such as x1.25, where successful separation only occurred in 11 out of 20 attempts during parametric testing. The plots shown in fig. W.1 are for a x1.25 sample. In the first 9 trials, no separation occurred. However, from trial 10 onwards, the LM droplets successfully separated. During the 14th trial, separation occurred with a counter electrode voltage of 6.72V and a current of 68.0 mA. On the 15th trial, the test process was reverted to the original method of increasing voltage until separation. Interestingly, separation occurred at a voltage of 6.85 and a current of 69.5 mA. The proximity of the values between these two trials indicates that there is a narrow region in which separation occurs. It is unclear why an upper limit exists, though it could be a result of countering surface tension effects from continuous electrowetting.

This data also suggests that the solution, electrodes, or liquid metal are somehow

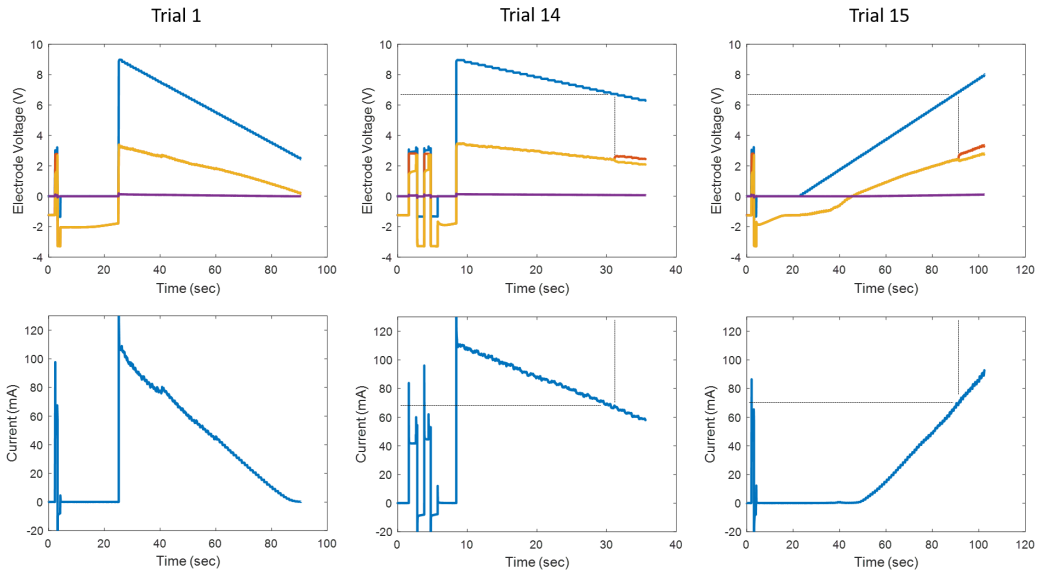

Figure W.1: Plots for voltage (blue counter, red source, yellow drain, purple gate) and applied current of a x1.25 scale sample. Left column: The 1st trial. Middle column: The 14th trial. Right column: The 15th trial, increasing voltage and current instead of decreasing.

being altered during testing. While this was kept to a minimum during experimentation by limiting testing cycles, using fresh NaOH solution, and testing on multiple PCB electrodes, it is an aspect that needs further exploration. It should be noted that after excessive testing, copper electrodes are consumed, likely the result of copper oxidation followed by corrosion by the NaOH solution. Inert platinum or gold electrodes would be preferential for future experiments and prototyping.

The same experiment was performed on a scale x1 sample. The very first sample separated with a voltage of 8.02V and a current of 73.0 mA. By the third trial, separation occurred immediately at 9.41V and 90.4 mA. Note that separation on the upward ramp generally required about 50.9 mA for separation. We conclude that increasing the scale decreases the upper limit for separation. At a scale of x1.5, there is no window for successful switching. The reason for this behavior is unclear, but the fact that scaling down the device does not suffer from this limitation is promising.

It should be noted that, as shown in fig. W.2, initial simulations with Surface Evolver indicate that increasing the scale increases the interfacial tension gradient required for separation. At larger scales, the dominance of gravitational forces prevent separation as the droplets simply flatten under their own weight. In fact, separation failed in the simulations at x1.5 due to excessive spreading which led to an instability. At smaller scales, the gravitational forces vanish, and the required gradient appears to level out.

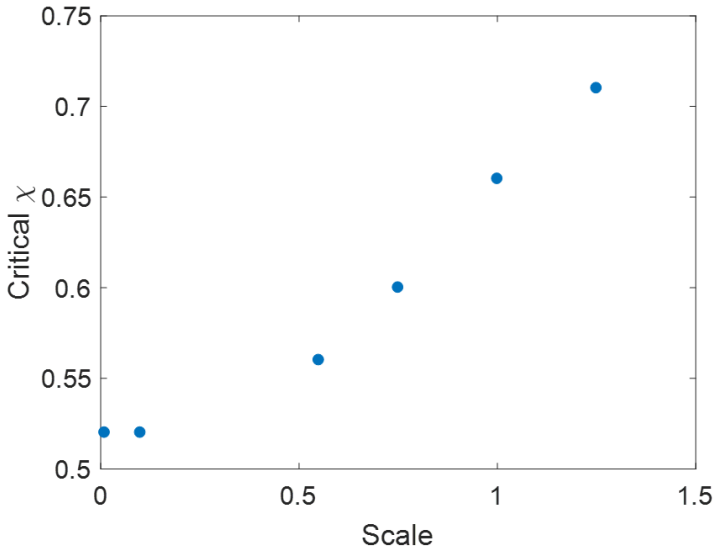

Figure W.2: Surface Evolver results for scale verses interfacial tension gradient, χ, required for separation.

Appendix X

Droplet Separation Power Requirements

Of particular interest in fig. X.1 are the power requirements. A number of approaches can be taken to improve efficiency. According to experimental results, decreasing outer electrode separation drives down both voltage and current. Essentially, current has to flow through less solution as gaps are decreased. However, as electrodes are placed in closer proximity, interference from bubbling and turbulence at the outer electrodes could become an obstacle. Scale has a similar effect on power. Interestingly, voltage requirements remain nearly constant until a scale of 0.5. The constant voltage requirements is a result of the electric field scaling approximately inversely with distance (distance decreases, electric field increases, and voltages stay constant). However, bubble formation drastically increases resistance and voltage requirements at small scales. Finally, decreased NaOH concentration decreases power, as well. Again, voltage requirements remain fairly constant, this time due to the constant dimensions. The drawback here is that lower concentrations leads to slower overall functionality (both separation and coalescence). At 0.1%, separation failed altogether due to apparent lack of ionic species (lack of conductivity).

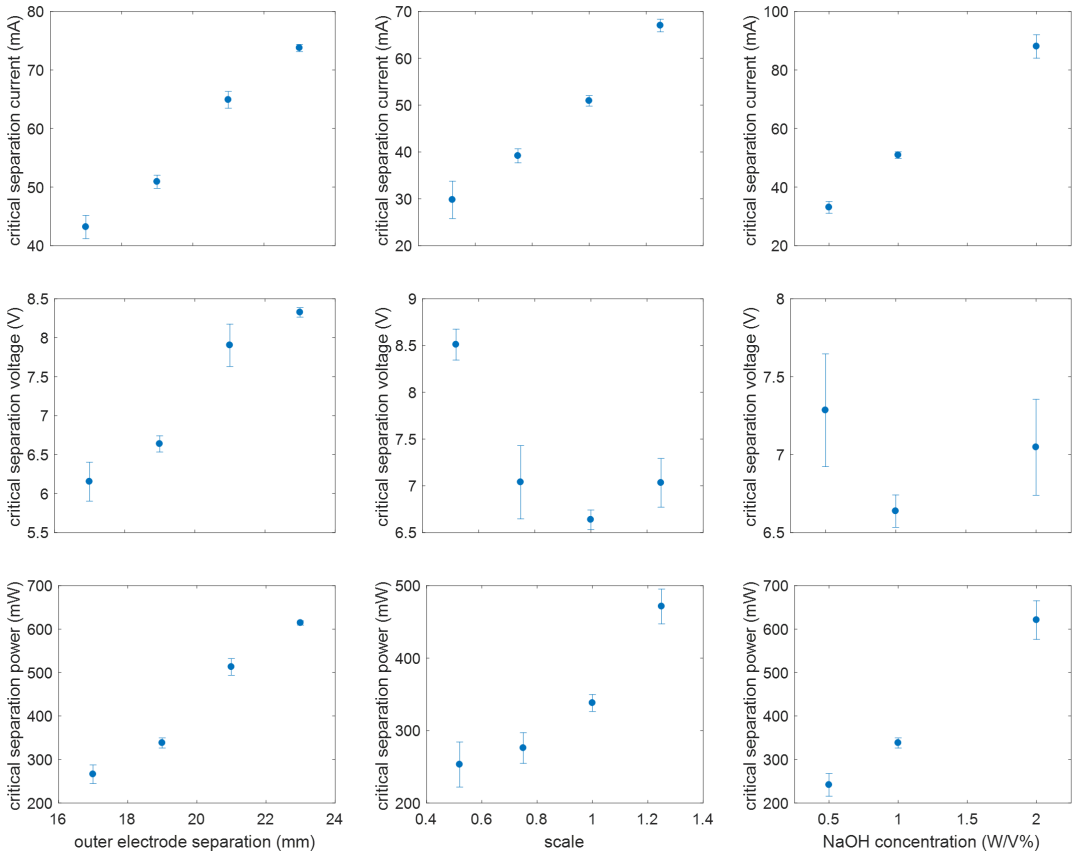

Figure X.1: Data for voltage, current, and power requirements for droplet separation under various outer electrode separations, length scales, and NaOH concentrations.

Appendix Y

Surface Evolver Script for Droplet Separation

The following scripts were used to simulate droplet separation, determine droplet volume based on diameter, and determine droplet volume based on cap height when alloyed to a circular pad. These scripts should run properly by simply entering "start" into the command line. To produce STL files, command code was stored in C:/Evolver/extra/. The code (file name: stl.cmd) is shown below (credit: Ken Brakke):

```
// stl.cmd

// Surface Evolver command to produce STL format text file from
//    surface.
// Evolver command line usage:
//    read "stl.cmd"
//    stl >>> "filename.stl"
// Programmer: Ken Brakke, brakke@susqu.edu,
//    http://www.susqu.edu/brakke

stl := {
   local mag,inx;
   printf "solid\n";
   foreach facet ff do
```

```
   { mag := sqrt(ff.x^2+ff.y^2+ff.z^2);
     printf "facet normal %f %f %f\n",ff.x/mag,ff.y/mag,ff.z/mag;
     printf "   outer loop\n";
     for ( inx := 1 ; inx <= 3 ; inx += 1 )
       printf "     vertex %f %f %f\n",ff.vertex[inx].x,
         ff.vertex[inx].y,ff.vertex[inx].z;
     printf "   endloop\n";
     printf "  endfacet\n";
   };
   printf "endsolid\n";
}
```

Y.0.1 Droplet Separation

```
// Simulation for separation of liquid metal droplets
// Normalization notes: 10=10x smaller (mm to cm)
//                      2.821=2.821mm radious
//                      1=1x larger

PARAMETER sc  = 10/(2.821*1.0)  // Scaling factor
PARAMETER gap = 0.1772          // Normalized gap (0.05 cm)
PARAMETER rad = 1               // Normalized radius (0.2821 cm)
PARAMETER hi   = 0.4            // Normalized height
PARAMETER chi = 0               // Initial surface tension gradient
#define TENS 1                  // Normalized surface tension
                                // (500 mJ/m^2)

gravity_constant (980*sc)/500   // Normalized gravity (980 cm/s^2)

// Boundary for droplet 1
boundary 1 parameter 1
x1: rad*cos(p1) - gap/2 - rad
x2: rad*sin(p1)
x3: 0

// Boundary for droplet 2
boundary 2 parameter 1
x1: rad*cos(p1) + gap/2 + rad
x2: rad*sin(p1)
x3: 0

// Constraint for substrate (can't pass through substrate)
constraint 1 nonnegative
formula: z+0.00001
```

```
//----Surface tension gradients----//
// If coalesced, apply gradient across entire surface
quantity vtens energy method facet_scalar_integral global
scalar_integrand: (body_count == 1)*-chi*(x+0.5892*sc)/(2*0.5892*sc)

// If separated, apply separate gradient for each drop
quantity vtens1 energy method facet_scalar_integral global
scalar_integrand: (body_count == 2)*((x < 0)*-chi*(x+0.5892*sc)/
(2*0.5892*sc)+(x > 0)*-chi*(x-0.025*sc)/(2*0.5892*sc))
//----Surface tension gradients----//

vertices
1   5*pi/4 boundary 1 fixed
2   7*pi/4 boundary 2 fixed
3   1*pi/4 boundary 2 fixed
4   3*pi/4 boundary 1 fixed
5   7*pi/4 boundary 1 fixed
6   5*pi/4 boundary 2 fixed
7   3*pi/4 boundary 2 fixed
8   1*pi/4 boundary 1 fixed
9   rad*cos(5*pi/4)-gap/2-rad    rad*sin(5*pi/4)    hi constraint 1
10  rad*cos(7*pi/4)+gap/2+rad    rad*sin(7*pi/4)    hi constraint 1
11  rad*cos(1*pi/4)+gap/2+rad    rad*sin(1*pi/4)    hi constraint 1
12  rad*cos(3*pi/4)-gap/2-rad    rad*sin(3*pi/4)    hi constraint 1


edges
1 1 5 boundary 1  fixed
2 5 8 boundary 1  fixed
3 8 4 boundary 1  fixed
4 4 1 boundary 1  fixed
5 6 2 boundary 2  fixed
6 2 3 boundary 2  fixed
7 3 7 boundary 2  fixed
8 7 6 boundary 2  fixed
9 5 6 constraint 1
10 7 8 constraint 1
11 1 9 constraint 1
12 2 10 constraint 1
13 3 11 constraint 1
14 4 12 constraint 1
15 9 10 constraint 1
16 10 11 constraint 1
17 11 12 constraint 1
```

```
18 12 9 constraint 1


faces
1 1 9 5 12 -15 -11 color blue density TENS constraint 1
2 -12 6 13 -16 color red density TENS constraint 1
3 7 10 3 14 -17 -13 color blue density TENS constraint 1
4 11 -18 -14 4 color red density TENS constraint 1
5 -10 8 -9 2 density TENS constraint 1
6 15 16 17 18 density TENS constraint 1


bodies
1 1 2 3 4 5 6 volume 2.2718 density 5.25/sc^3

read
// New command: start
// Begins iterating for a solution
start:={U;     // Toggle conjugate gradient method
u;     // Equiangulate
V 100; // Vertex averaging 100x
u;     // Equiangulate
g 250; // Iterate 250 times
V 100; // Vertex averaging 100x
u;     // Equiangulate
r;     // Refine
r;     // Refine
refine edges where on_boundary 1 or on_boundary 2;
refine edges where on_boundary 1 or on_boundary 2;
ii := 0; // Index
jj := 0; // Index
tval := min(edge,length);       // Value for removing tiny edges
Vval := min(edge,length)^2/1.3; // Value for weeding out small
                                // triangles

// Iterate through gradients
for (chi:= 0; chi < 0.8; chi+=0.01)
{
old := 1000;             // Filler for older energy
dif := old-total_energy; // Energy difference

// Iterate until the the difference in energy is sufficiently small
while (dif > 10^-8) do {
ii := ii + 1;  // Increase index
jj := jj + 1;    // Increase index
```

```
// Occasionally run the following mesh tailoring
if (ii > 500) then {u;V 5;ii := 0;};
if (jj > 20) then { O;o; O;w Vval; t tval;O;o; O;K 0.1;
O;o; jj := 0; rebody;};
old:=total_energy;
exec sprintf "printf \"%f\t%f\\n\" >> \"testwrite.txt\"",
clock,total_energy; // Print energy
g; // Iterate once
dif:=abs(old-total_energy); // Calculate energy difference
};

u;    // Equiangulate
V 10; // Vertex averaging 10x
// Prepare for stl writing
exec sprintf "read \"C:/Evolver/extra/stl.cmd\"";
// Write stl file
exec sprintf "stl >>> \"Chi_%d.stl\"", chi*1000;
};
}
r
r
s
q
```

Y.0.2 Droplet on Surface

```
// Simulation for liquid drop on a surface

PARAMETER sc  = 1/0.0002  // Scaling factor
PARAMETER VT  = 0.0002    // Initial volume
PARAMETER VT2 = 1         // Normalized volume VT*sc

#define TENS 1            // Normalized surface tension (500 mJ/m^2)

gravity_constant (980*sc^(1/3))/500  // Normalized gravity
 // (980 cm/s^2)

// Constraint for substrate (can't pass through substrate)
constraint 1 nonnegative
formula: z-0.00001

vertices
1  0.0 0.0 0.0 constraint 1
2  1.0 0.0 0.0 constraint 1
3  1.0 1.0 0.0 constraint 1
```

```
4  0.0 1.0 0.0 constraint 1
5  0.0 0.0 1.0 constraint 1
6  1.0 0.0 1.0 constraint 1
7  1.0 1.0 1.0 constraint 1
8  0.0 1.0 1.0 constraint 1

edges  /* given by endpoints and attribute */
1   1 2 constraint 1
2   2 3 constraint 1
3   3 4 constraint 1
4   4 1 constraint 1
5   5 6 constraint 1
6   6 7 constraint 1
7   7 8 constraint 1
8   8 5 constraint 1
9   1 5 constraint 1
10  2 6 constraint 1
11  3 7 constraint 1
12  4 8 constraint 1

faces  /* given by oriented edge loop */
1   1 10 -5  -9 density TENS constraint 1
2   2 11 -6 -10 density TENS constraint 1
3   3 12 -7 -11 density TENS constraint 1
4   4  9 -8 -12 density TENS constraint 1
5   5  6  7   8 density TENS constraint 1
6  -4 -3 -2  -1 density TENS constraint 1

bodies  /* one body, defined by its oriented faces */
1   1 2 3 4 5 6  volume VT2 density 5.25/sc

read
// New command: start
// Begins iterating for a solution
start:={U;       // Toggle conjugate gradient method
u;       // Equiangulate
V 100;   // Vertex averaging 100x
u;       // Equiangulate
g 250;   // Iterate 250 times
V 100;   // Vertex averaging 100x
u;       // Equiangulate
r;       // Refine
r;       // Refine
r;       // Refine
r;       // Refine
```

```
ii := 0; // Index
tval := min(edge,length);     // Value for removing tiny edges
Vval := min(edge,length)^2/2; // Value for weeding out small
  // triangles

// Iterate through volumes
for (VT:= 0.0002; VT < 0.05; VT+=0.0002)
{
sc:=1/VT; // New scaling factor
G (980*sc^(1/3))/500; // New scaled gravity
set body[1].density 5.25/sc; // New scaled density
u;     // Equiangulate
V 10;  // Vertex averaging 10x
g 100; // Iterate 10x
u;     // Equiangulate
V 10;  // Vertex averaging 10x
old := 1000;  // Filler for older energy
dif:=old-total_energy; // Energy difference

// Iterate until the the difference in energy is sufficiently small
while (dif > 10^-9) do {
ii := ii + 1; // Increase index
// Occasionally run the following mesh tailoring
if (ii > 1000) then { w Vval; t tval; o; O; u; V; ii := 0; rebody;};
old:=total_energy;
exec sprintf "printf \"%f\t%f\\n\" >> \"testwrite.txt\"",
clock,total_energy; // Print energy
g; // Iterate once
dif:=abs(old-total_energy); // Calculate energy difference
};

// Prepare for stl writing
exec sprintf "read \"C:/Evolver/extra/stl.cmd\"";
// Write stl file
exec sprintf "stl >>> \"Vol_%d.stl\"", VT*10000;
};
}
s
q
```

Y.0.3 Droplet on Pad

```
// Simulation liquid metal drop on a single pad
// Normalization notes: 10=10x smaller (mm to cm)
//                      2.821=2.821mm radious
```

```
//                      1=1x larger

PARAMETER sc  = 10/(2.821*1.0)  // Scaling factor
PARAMETER rad = 1               // Normalized radius (2.821 mm)
PARAMETER hi   = 0.01           // Normalized height
PARAMETER VT  = 0.01            // Normalized volume
#define TENS 1                  // Normalized surface tension
// (500 mJ/m^2)

gravity_constant (980*sc)/500   // Normalized gravity (980 cm/s^2)


// Boundary for pad
boundary 1 parameter 1
x1: rad*cos(p1)
x2: rad*sin(p1)
x3: 0

// Constraint for substrate (can't pass through substrate)
constraint 1 nonnegative
formula: z+0.00001

vertices
1   1*pi/4 boundary 1 fixed
2   3*pi/4 boundary 1 fixed
3   5*pi/4 boundary 1 fixed
4   7*pi/4 boundary 1 fixed
5   rad*cos(1*pi/4)    rad*sin(1*pi/4)    hi constraint 1
6   rad*cos(3*pi/4)    rad*sin(3*pi/4)    hi constraint 1
7   rad*cos(5*pi/4)    rad*sin(5*pi/4)    hi constraint 1
8   rad*cos(7*pi/4)    rad*sin(7*pi/4)    hi constraint 1

edges
1   1 2 boundary 1 fixed
2   2 3 boundary 1 fixed
3   3 4 boundary 1 fixed
4   4 1 boundary 1 fixed
5   5 6 constraint 1
6   6 7 constraint 1
7   7 8 constraint 1
8   8 5 constraint 1
9   1 5 constraint 1
10  2 6 constraint 1
11  3 7 constraint 1
12  4 8 constraint 1
```

```
faces  /* given by oriented edge loop */
1   1 10 -5  -9 density TENS constraint 1
2   2 11 -6 -10 density TENS constraint 1
3   3 12 -7 -11 density TENS constraint 1
4   4  9 -8 -12 density TENS constraint 1
5   5  6  7   8 density TENS constraint 1
//6  -4 -3 -2  -1 density TENS constraint 1

bodies  /* one body, defined by its oriented faces */
1   1 2 3 4 5  volume VT density 5.25/sc^3

read
// New command: start
// Begins iterating for a solution
start:={U;     // Toggle conjugate gradient method
u;     // Equiangulate
V 100; // Vertex averaging 100x
u;     // Equiangulate
g 250; // Iterate 250 times
V 100; // Vertex averaging 100x
u;     // Equiangulate
r;     // Refine
r;     // Refine
r;     // Refine
quadratic; // Using quadratic mesh
refine edges where on_boundary 1;
ii := 0; // Index
tval := min(edge,length);     // Value for removing tiny edges
Vval := min(edge,length)^2/2; // Value for weeding out small
  // triangles

// Iterate through volumes
for (VT:= 0.01; VT < 4; VT+=0.01)
{
set body[1].target VT; // Change volume
u;     // Equiangulate
V 10;  // Vertex averaging 10x
g 100; // Iterate 100x
u;     // Equiangulate
V 10;  // Vertex averaging 10x
old := 1000; // Filler for older energy
dif:=old-total_energy; // Energy difference

// Iterate until the the difference in energy is sufficiently small
```

```
while (dif > 10^-10) do {
ii := ii + 1;  // Increase index
// Occasionally run the following mesh tailoring
if (ii > 300) then { w Vval; t tval; o; 0; u; V; ii := 0; rebody;};
old:=total_energy;
exec sprintf "printf \"%f\t%f\\n\" >> \"testwrite.txt\"",
clock,total_energy; // Print energy
g; // Iterate once
dif:=abs(old-total_energy); // Calculate energy difference
};

// Prepare for stl writing
exec sprintf "read \"C:/Evolver/extra/stl.cmd\"";
// Write stl file
exec sprintf "stl >>> \"Vol_%d.stl\"", VT*100;
};
}
s
q
```